Quasi One Dimensional GaN Nanostructures: Growth Kinetics, Physical Properties, and Applications

By

Prasana Kumar Sahoo

Enrolment No: PHYS02200704020
Indira Gandhi Centre for Atomic Research, Kalpakkam, India

A thesis submitted to the Board of Studies in Physical Sciences,
In partial fulfilment of requirements
For the Degree of

DOCTOR OF PHILOSOPHY

of

HOMI BHABHA NATIONAL INSTITUTE, MUMBAI

June 2012

HOMI BHABA NATIONAL INSTITUTE

Recommendations of the Viva Voce Board

As members of the Viva Voce Board, we certify that we read the dissertation prepared by **Mr. Prasana Kumar Sahoo** entitled **"Quasi One Dimensional GaN Nanostructures: Growth Kinetics, Physical Properties and Applications"** and recommend that it may be accepted as fulfilling the dissertation requirement for the Degree of Doctor of Philosophy.

Chairperson – **Prof. A. K. Tyagi** Date:

Supervisor/Convenor – **Prof. Sitaram Dash** Date:

Member 1 – External examiner – Date:

Member 2 – **Prof. A. K. Arora** Date:

Member 3 – **Prof. K. G. M. Nair** Date:

Technology Advisor – **Shri. N. Murali** Date:

Final approval and acceptance of this dissertation is contingent upon the candidate's submission of the final copies of dissertation to HBNI.

I hereby certify that I have read this dissertation prepared under my direction and recommend that it may be accepted as fulfilling the dissertation requirement.

Date:

Place: Indira Gandhi Centre for Atomic Research, Kalpakkam

STATEMENT BY AUTHOR

This dissertation has been submitted in partial fulfillment of requirements for an advanced degree at Homi Bhaba National Institute (HBNI) and is deposited in the library to be made to borrowers under rules of the HBNI.

Brief quotations from this dissertation are allowable without special permission, provided that accurate acknowledgement of source is made. Requests for permission for extended quotation from or reproduction of this manuscript in whole or in part may be granted by the Competent Authority of HBNI when in his or her judgement the proposed use of the material is in the interest of scholarship. In all other instances, permission must be obtained from the author.

Kalpakkam **(Prasana Kumar Sahoo)**

June 2012

DECLARATION

I, hereby declare that the investigation presented in the thesis has been carried out by me. The work is original and has not been submitted earlier as a whole or in part for a degree / diploma at this or any other Institution / University.

Kalpakkam **(Prasana Kumar Sahoo)**

June 2012

Epigraph

". .. … from there I came
who taught me in all meanderings
to discover a way out
to reach there again… .. . "

Dedicated to

All

Visionaries, Philosophers & Natural Scientists

A space for

My Parents, My Brother

&

My friends: Seshadev & Satyanarayan

ACKNOWLEDGEMENT

First and foremost, I would like to express my deep and sincere gratitude to Dr. Sandip Dhara, MSG, IGCAR, for his constant encouragement, caring, and insightful guidance all the way leading to the completion of my PhD work. His sharpness, enthusiasm, experience, and friendliness have made my research life more smooth and enjoyable. I specially thank him a lot, and place my admiration on record.

I thank the Director, IGCAR for providing me the opportunity to continue the research work at IGCAR. I thank the Director, MSG for facilitating the research activities. I also convey my hearty thanks to Dr. M. Sai Baba, the Associate Director, RMG, IGCAR for his support.

I am deeply indebted to Dr. Sitaram Dash, MSG, IGCAR, for his encouragement and providing timely advice on thesis work. I truly appreciate his willingness and sharing his best scientific and technical knowledge through discussions and suggestions. It is my pleasure to thank Dr. A. K. Tyagi, Dr. A. K. Arora, Dr. K. G. M. Nair of MSG, IGCAR, and Mr. N. Murali of EIG, IGCAR for advising me timely on my thesis work. I do appreciate the amenities and environment created by former Director Dr. Baldev Raj, for research scholars and for his encouragement in pursuing high-end research.

I especially thanks to my collaborators Prof. Monica Cotta, D. UNICAMP, Brazil for KPFM study. I convey my deep gratitude Dr. S. Murthy, and Ms. S. Sumathi, WSCD, BARCF for antibacterial and EIS studies, respectively. I also deeply thank Dr. J. Basu, Dr. A. Dasgupta, of PMG, IGCAR; Dr. S. Amirthapandian, Dr. M. Kamruddin of MSG, IGCAR and Prof. C. P. Lu of NCKU, Tainan, Taiwan for their valuable contribution in microscopic studies. I would like to thank all the members in SND and MSG, IGCAR.

I deeply express my heartfull thanks to all of my colleagues, Dr. A. Das, Mr. Avinash Patsha, Mr. Kishore Kumar, and Dr. A. K. Prasad for valuable discussion and sharing our scientific adventures.

I would like to express my boundless gratitude to all M.Tech. students Sandeep, Arunya, Garima, and Satish for their valuable contribution while working with me. I also thank Christy and Silambu working effortlessly with me during their M.Sc. summer project work.

I owe my great pleasure to thank Prof. G. N. Dash, Sambalpur University. I would not forget the love, care and inspiration that he bestowed upon me during my M.Sc. studies.

It is my pleasure to keep a special line for my dearer Bishnu. I owe my great pleasure to have around Saravana, Kalpataru, Kamalakanta, Akshaya, Sachindra, Rama and Nihar for sharing most of my valuable thoughts, philosophy and knowledge, and for bearing all my tough teasing- making fun out of nothing. My special gratitude to my close intimates Satendar, Satya, Alok, Maneesha, Pravati, Soumee, Ashit, Satyaprakash, Karunakar, Joysankar, Herojit, Varghese, Haribabu, Baban, Rahul, Sorb, Pradeep, Sudhansu, Bonu, Subhrat, Susil, Subhra, Rajini, Devasmita, Madhusmita, and all research scholar friends for making my life more amiable and charming during my stay at JRF Enclave, Kalpakkam.

I pass my biggest gratitude of my career to my two friends, Satyanarayan and Seshadev. I have no word to express the value they have added to my life in terms of love, care and friendliness. I also thank Mr. Nigamanada Bhuyan, Mr. Santosh Sahoo, Silu and Somanath all the way they filled courage in my tough time.

I would like to express my heartiest gratitude and honor to my parents, Mrs. Padmabati Sahoo and Mr. Birakishor Sahoo, my brother, Mr. Pramod Sahoo and all other family members for their love, compassion, caring nature and patience in the walkway of my life.

Finally yet importantly- how I forget from where I came, what is that force doing all these, and what for I am delving- It is my admiration and deepest gratitude to this unbound “Nature” from whom I am learning the essence of life and its very cause.

(Prasana Kumar Sahoo)

SYNOPSIS

This dissertation summarizes experimental effort undertaken towards synthesis, characterization and demonstration of some of the potential applications of one dimensional GaN nanostructures. An atmospheric-pressure thermal chemical vapor deposition technique is developed for the growth of GaN nanostructures using liquid Ga metal as a source and NH_3 as a reactant gas. Different growth mechanism are employed to synthesize various nanostructures, such as, 1) GaN nanowires of hexagonal, triangular, square and wurtzite/zinc-blende biphase homostructures via vapor-solid-liquid method, 2) nanotips, nanoparticles, and hierarchical nanostructures by vapor-solid method, 3) GaN nanotubes by quasi vapor-solid process and 4) core-shell Ga_2O_3@GaN microbelts by self-catalytic method. The detail morphological, structural and optical properties are used to arrive upon the possible growth mechanisms for these nanostructures. All the as-grown GaN nanostructures are composed of dominating wurtzite phase and show distinct UV luminescence properties.

Microscopic study reveals that all the core-shell Ga_2O_3@GaN microbelts possess distinct shape with self-affine nanoprotrusions on their surface. The wetting properties of this ideal surface are investigated and correlated with a mathematical model. A superhydrophobic state is observed in a single microbelt, which has been attributed to the presence of spatial air-trapped nanocavities within the vicinity of nanoprotrusions. In addition, the nanoprotruded microbelt is much more sensitive to the presence of moisture than their thin film counterparts. This has been demonstrated by measuring the variation of surface potential using Kelvin probe force microscopy. A dissociative pathway for the reaction mechanism of water molecules on GaN surfaces has been worked out.

Functionalization of GaN nanotubes using Pt nanoclusters carried out via a green chemistry route brings about novel laser assisted catalytic properties. Gas sensing behaviour

of GaN NTs co-catalysed by Pt nanoclusters has been studied over a wide range of temperatures. Pt nanocluster functionalized nanotube shows superior response to H_2 sensing. The recorded sensitivity extends down to 25 ppm concentration at room temperature.

A label free ultra sensitive impedimetric DNA biosensor has been demonstrated using GaN nanowires. The necessary reagents, experimental techniques and subsequent characterizations used during the process are discussed. A series of functionalization steps on GaN nanowires are employed to covalently immobilize single stranded DNA as a probe molecule. The amine-terminated dendrimer (PAMAM) has been employed as a linker molecule between nanowire and probe DNA. In-situ monitoring of the DNA hybridization process in GaN-PAMAM-probe indicates excellent sensitivity of these nano-matrices over 10^{-9} to 10^{-19} molar target concentrations. In addition, this sensor shows excellent selectivity and specificity. A detailed mechanism for DNA sensing is proposed.

GaN NPs induced toxicity and inhibition of biofilm formation in both gram positive (*Staphylococcus aureus)* and gram negative (*Escherichia coli, Pseudomonas aeruginosa and Pseudomonas putida)* bacterial cells over a wide range of nanoparticle concentrations (0.25 - 100 µg/mL) have been demonstrated. The erosion of intracellular material, localized protein exudation site and extent of cellular damages upon exposure with GaN NPs has been investigated in detail to probe the dynamics prevailing at the nano-bio interface by confocal laser Raman microscopy. These studies addressed the interactions at both single and multi-cellular levels.

CONTENTS

Title **Page No.**

CHAPTER 1

CHAPTER 2

CHAPTER 3

CHAPTER 4

SINGLE-STEP GROWTH DYNAMICS AND PHYSICOCHEMICAL PROPERTIES OF CORE–SHELL Ga_2O_3@GaN MICROBELTS 79

CHAPTER 5

GROWTH AND FUNCTIONALIZATION OF GaN NANOTUBES FOR CATALYTIC AND GAS SENSING APPLICATION 111

CHAPTER 6

CHAPTER 7

CHAPTER 8

List of Figures

List of Tables

List of Abbreviation

1D -One Dimensional

3D -Three dimensional

AFM- Atomic Force Microscopy

BB- Blue band

CLRS- Confocal Micro-Raman Spectroscopy

CNT- Carbon Nanotubes

CVD- Chemical Vapor Deposition

DAP- Donor-Accepter-Pair

DNA- Deoxyribonucleic Acid
p-DNA- Probe DNA
t-DNA- Target DNA
ct-DNA- Complementary Target DNA
sm-DNA- Single Mismatch DNA
EC- Escherichia coli
EDX- Energy Dispersive X-Ray Spectroscopy
EDC- Ethyl-3-(3-dimethylaminopropyl) carbodimide
EFGS- Exposure Facility for Gas Sensor
EIS- Electrochemical Impedance Spectroscopy
FB- Free-to-Bound
FESEM- Field Emission Electron Microscopy
FFT- Fast Fourier Transform
FIB- Focused Ion Beam
G3-PAMAM- Third Generation Poly-(amidoamine)-Dendrimer
H1N1- Human Influenza A
HOMO- Highest Occupied Molecular Orbital
HOPG- Highly Ordered Pyrolytic Graphite
HRTEM- High Resolution Electron Microscopy
IDB- Inversion Domain Boundaries
IDP- Interface Dipole Layer
KPFM- Kelvin Probe Force Microscopy
LB-Luria Bertini
LED- Light Emiting Diode
LO- Longitudinal Optical
LUMO- Lowest Unoccupied Molecular Orbital
MBE- Molecular Beam Epitaxy
NBE- Near Band Edge
NP- Nanoparticle
NT- Nanotube
NW- Nanowire
OCP- Open Circuit Potential
PA- Pseudomonas aeuriginosa
PA01-Pseudomonas aeuriginosa

PL- Photoluminescence

Q- Constant Phase Element

RT- Room Temperature

R_p - Polarization Resistance

R_s - Solution Resistance

SA- Staphylococcus aureus

SAED- Selected Area Electron Diffraction

SERS- Surface Enhanced Raman Scattering

SMB- Stacking Mismatch Boundaries

SO- Surface Optical

SP- Surface Potential

TO- Transverse Optical

VLS- Vapor– Liquid–Solid

VS- Vapor-Solid

WZ- Wurtzite

YL- Yellow Luminescence

ZB- Zone Boundary

CHAPTER 1

INTRODUCTION

General interest in reducing the size of a material to nanometer scale arises from the manifestation of properties distinct from their three dimensional (3D) counterparts. The nanoscale is not only the middle ground between molecular and macroscopic levels but also a dimension that is specifically probed over the last decade. This investigative process has unraveled fascinating phenomena that eventually interweaved disciplines like physics, chemistry, biomedicine, analytical science and engineering.[1-6] Certain materials in reduced length scale of few nanometers exhibit several unexpected properties, such as energy quantization, ballistic transport, single electron tunneling, metastable phase formation, plasmonic coupling, magnetic/electric behavior, and superhydrophobicity.[7-9] Magnitude of these nanoscale phenomena far exceed those found in corresponding bulk materials. It is worthwhile to mention that these intrinsic properties of a nano-material can be modulated as a function of length scale. Such scale dependency is gainfully utilized to achieve miniaturization of structural components. However, size alone is not the only determining parameter to obtain the desired properties. More specifically, it is rather the surface area to volume ratio which brings in an upsurge of nanoscale phenomena during the scaling down process of materials. As a matter of fact, particles with constant volume but variable shape can differ significantly in their physical and chemical properties. Thus, vigorous experimental efforts are still being continued worldwide for the synthesis of new types of materials with a high degree of shape anisotropy. Such materials are obtained in the form of wires, rods, tubes, tips and other multimodal structures. Apart from the control over the size and shape of a material, other associated parameters such as depletion of crystal defects, modulation of surface roughness and selected exposure of crystal facets also contribute significantly to the enhanced functionality appearing at nanoscale.[10-13]

Nanomaterials are classified into three important categories depending on the spatial confinement of carrier. These are quantum well (2D), quantum wire (1D) and quantum dot (0D). In the long run, 1D semiconductor nanostructures have emerged as one of the promising classes of functional materials owing to their large surface to volume ratio, ultra high aspect ratio and possession of unidirectional conduction channels. The tremendous progress in research has led to a multitude of applications of single crystalline 1D nanostructures in the fabrication of noble LEDs,[14] lasers,[15] waveguides,[16] photo detectors,[3] solar cells,[17] communication devices, ultra-small gas sensors, and bio-medical devices.[2,18] Full functionality of 1D nanostructure based devices is expected with further miniaturization and better functionality in this era of nanotechnology.

Recent progress in 1D nanostructures such as nanowires (NW) or nanorod growth techniques, including both physical (thermal evaporation, laser ablation and metal organic vapor phase epitaxy) and chemical deposition techniques [chemical vapor deposition (CVD), molecular beam epitaxy (MBE) and hydride vapor phase epitaxy (HVPE)] have allowed development of a broad range of inorganic NW compositions including group III–V, II–VI compounds and alloy crystal structures.[2,19] A typical “bottom up” NW synthesis process involves vapor– liquid–solid (VLS) or vapor-solid (VS) growth mechanism. The versatility of these techniques allows one to exercise control over a wide range of NW materials, superlattices and branched structures. In this regard, VLS mechanism is quite popular as it promotes seeding and directional growth by incorporating catalytic liquid alloy phase which helps in the rapid conversion of vapor to supersaturation levels.[20] Although understanding of the VLS growth mechanism has become very successful in making semiconductor NWs with a wide range of compositions, the use of metal during growth unavoidably introduces the potential problem of contamination and formation of defects. It becomes a hindrance for large scale use of NWs in the optoelectronic industry. The problem has been mitigated by efforts devoted towards NW growth without using catalyst support. Significant progress has been made in realizing catalyst-free growth of compound semiconductor NWs by several methods. These catalyst-free growths can be driven by the VS growth mechanism, self catalytic VLS mechanism,[21] dislocation-driven process[22] or by oxide-assisted methods.[23]

The human quest for alternative renewable energy sources and attempt to realize miniaturized efficient optoelectronic devices has brought excitement among researchers to fabricate new and promising nanostructures bestowed with a high degree of shape anisotropy.

1.1 Promising Wide Band Gap Material:

Every now and then, a new semiconductor material comes along that appears promising for varieties of applications in the field of optoelectronics.[24] GaN is one such compound, known for its potential use in future high-performance, high-power optoelectronic devices with high carrier mobility, high electrical breakdown voltage, high melting point and low chemical reactivity.[2] It has an unusual capacity to emit green, blue and ultraviolet light. This aspect has generated considerable interest over past decades. However, much of the potential of GaN is yet to be realized.

1.1.1 Gallium Nitride (GaN):

GaN is a semiconductor having a wide band gap value of ~ 3.47 eV at 0 K.[25] The band gap of the GaN can be tuned with suitable alloying with other group III elements. Thus, it is possible to get access to entire visible spectrum and a large part of the ultraviolet region which makes it a very exciting optoelectronic material system.[25-27] At ambient temperature and pressure, the stable equilibrium structure of GaN is wurtzite (*WZ*) 2H polytypes and under certain non-equilibrium conditions, they can exist as a zinc-blende 3C polytype structure. Moreover, a rock salt or NaCl structure of GaN can be induced at high pressure

(~37 GPa). The *WZ*-nitrides are most widely grown, studied and reported.[25,26] The *WZ* structure consists of two interpenetrating hexagonal-close-packed lattices, each displaced from the other by an extent of 0.375 (c_0) as represented schematically in figure 1.1(a). The *WZ* lattice is characterized by three distinct parameters: the edge length of the basal hexagon (a_0), the height of the hexagonal lattice cell (c_0), and the cation-anion bond length ratio (u_0) along the [0001] axis in units of c_0 at equilibrium. In an ideal case, the c_0/a_0 ratio is 1.633 and u_0 is 0.375. The unit cell of *WZ* structure contains six group III metal atoms and six group V nitrogen atoms and the structure belongs to P63mc (c_{6v}^4) space group symmetry with *ABABAB* type stacking sequence along [0001] direction. The different crystallographic orientations and stacking sequence of atoms in *WZ* structure are shown in figure 1.1(b) The non-centrosymmetric nature of *WZ* structure exhibits properties such as piezoelectricity and pyroelectricity, which are absent in centrosymmetric crystals. A comparison of the major properties of GaN with other widely used semiconductors is summarized in table 1.1.

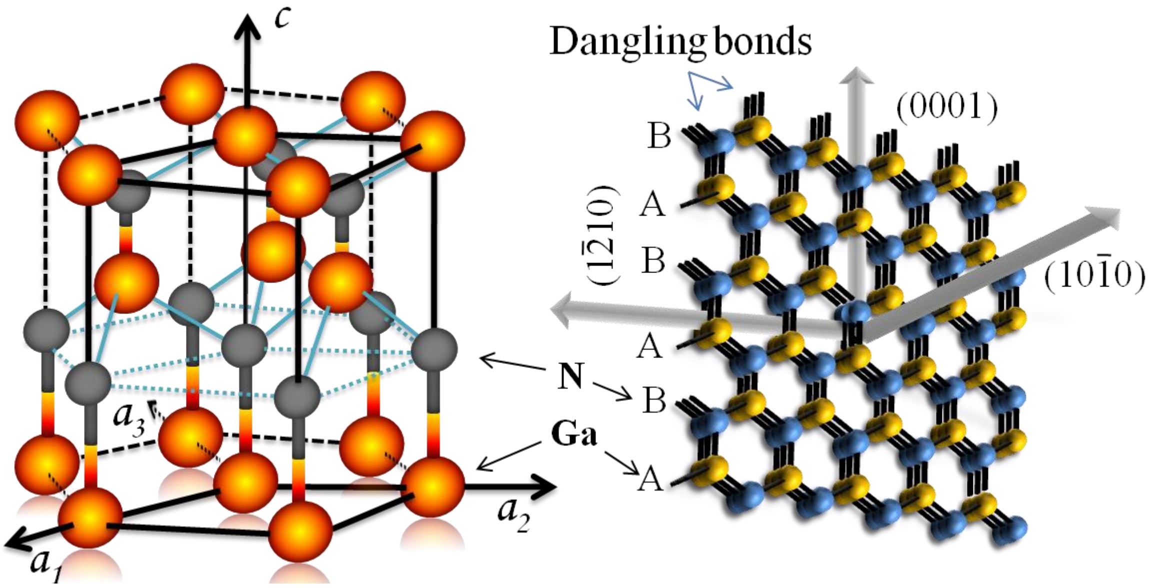

Fig. 1.1 (a) Schematic diagram of a hexagonal wurtzite crystal structure; The primitive unit cell is represented by the thick solid line between the three axial vectors, (b) represents the different crystallographic plane orientation in the *WZ* structure along the [0001] direction.

Table 1.1 Comparison of basic physical properties between GaN and other widely used semiconductors.[25-28]

Property	**GaN**	**InN**	**AlN**	**GaAs**	**Si**	**ZnO**	**Diamond**
Energy gap (eV)	3.4	0.6-0.7	6.2	1.4	1.1	3.37	5.47 eV
Exciton binding energy (meV)	22	3	57	-4.8	--	60	80
Bohr radius (nm)	2.9	5	1.9	14	5	1.4	1.5
Transition n type (10^7 V cm^{-1})	direct	direct	direct	direct	indirect	direct	indirect
Breakdown field (MV/cm)	3.0	2.0	1.8	0.4	0.3	--	4.0
Saturation electron Velocity (X 10^7cm/s)	2.5	4.2	2.0	2.0	1.0	--	2.5
Electron Mobility (cm^2/V.s)	1,200	4,000	--	8,500	1,500	2000	1,800
Thermal conductivity (W/cm.K)	2.1	0.8	2.9	0.5	1.5	0.6-1	20.9
Relative dielectric constant, (ε_r)	8.9	15	8.5	12.8	11.8	--	5.5

GaN is generally grown by a thin film deposition process, more popularly, by metal organic chemical vapor deposition (MOCVD) and MBE techniques. These techniques normally employ certain foreign substrate such as sapphire, and often introducing an additional buffer layer on arbitrary substrates. GaN grown over foreign substrates possess a high density of threading dislocations (~10^{10} cm^{-1}) owing to the larger mismatch in lattice constant and thermal expansion coefficient, which have been long regarded as a critical issue to improve the efficiency and lifetime of GaN based thin film devices. Notably, GaN NWs or nanorods and their heterojunctions are usually dislocation-free and can readily accommodate large lattice mismatches. Therefore, NWs can be directly integrated with silicon technology as it is also compatible with conventional thin film technology.

1.1.2 Progress and Prospects of 1D GaN Nanostructures:

Sustained research effort on 1D GaN has resulted synthesis of several nanostructures, such as NWs, nanotubes (NTs), nanotips, nanobelts, and nanoparticles (NPs).[2] As the diameter (*d*) of a material approaches to its exciton Bohr radius, band gap energy can increase along with exciton binding energy and oscillatory strength. Phonon dispersion in the reduced dimension can also be modified resulting in drastically different transport properties. This happens when *d* of the material becomes comparable with the mean free path of phonon (~ 100 nm for GaN).[25] In this context, 1D nanostructures of GaN with small diameter, high surface area, high aspect ratio, and tunable electrical and optical properties, makes it as good candidates for various applications including optoelectronics, photovoltaic, photocatalysis, gas and biosensing.[2] The potential research areas pertaining to 1D GaN nanostructure are summarized in table 1.2.

Table 1.2 Summarizes potential research area pertaining to 1D GaN nanostructures.

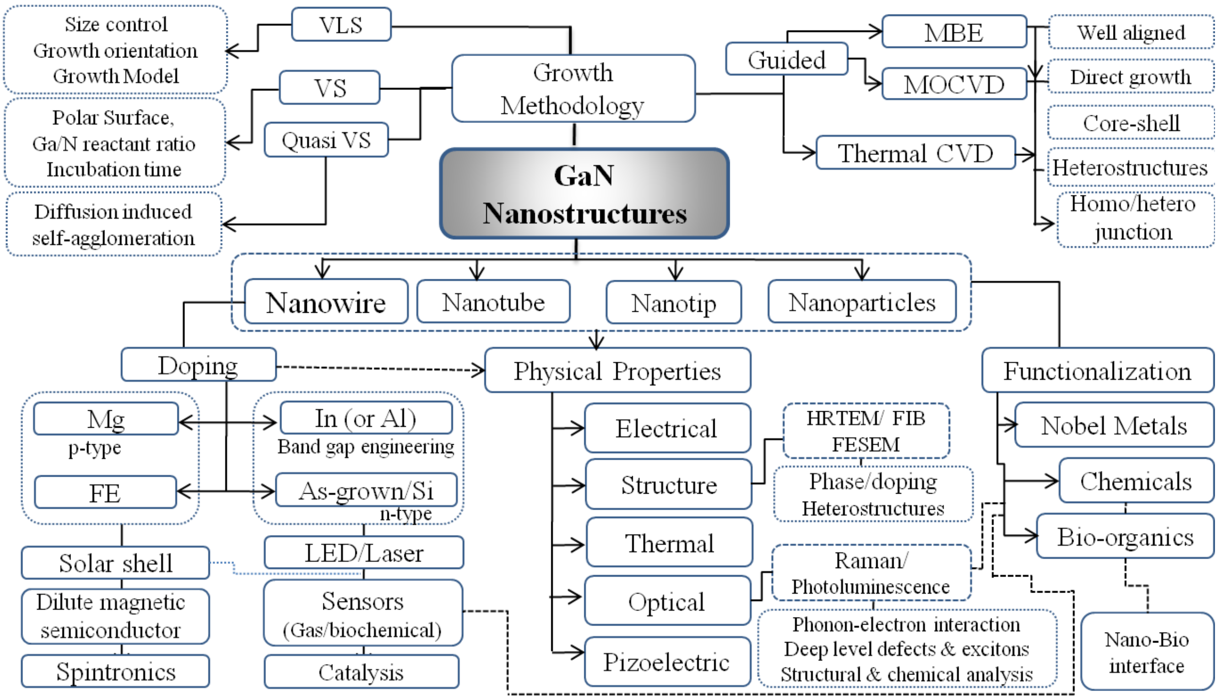

It was Han et al. who first reported the synthesis of GaN NWs by employing carbon nanotubes as templates, Ga/Ga_2O_3 as source materials and NH_3 as a reactant gas in a thermal CVD technique.[29] The first VLS growth of the GaN NW was reported by Duan et al.[30] using a laser ablation technique followed by Chen et al.[31] who employed thermal CVD. The relatively simpler instrumentation and operation of thermal CVD technique has made it attractive and widely useful. Meanwhile, progress in VLS/VS based growth of various other forms of 1D GaN nanostructures, NWs, NTs, nanobelts and nanotips, is being pushed forward on several fronts.[2] Moreover, from a bottom-up perspective, the ability to synthesize complex nanoscale objects with hybrid architecture and composition appear to be a formidable challenge in CVD based techniques. Optimization of various parameters in understanding the growth mechanism in the CVD technique is essential to ensure reproducibility.

High flexibility in designing of new optoelectronics devices is due to tunability of intrinsic properties coupled to miniaturization. Advances in optical devices made from planar GaN and other related semiconductor alloys have already shown success in realizing first ever fabrication of high-brightness blue LED, green laser diode, novel solar cells, high electron mobility transistor (HEMT) - that can amplify signals at a frequency of 300 GHz, smart grid, and ultra small transistor to detect DNA, detection of pH and identification of protein associated with breast cancer.[2,24-27] However, success story of 1D GaN based devices is continuing at a rapid pace. These pertain to optically pumped single GaN NW laser, multi quantum well NR array based super bright LEDs for lighting and full color displays, coaxial NR heterostructures based flexible blue LEDs, photovoltaics, wafer level photocatalysis for hydrogen generation with better performance than TiO_2 and ZnO NWs and gas/biochemical/DNA sensing.[2,32-34] Applications pertaining to biomedical and chemical sensors are still in their infancy, but progress in nitride based electronics is bringing them steadily closer to reality. Nevertheless, in the nanoscale miniaturization process, 1D GaN is expected to outperform the better known silicon optoelectronic components in the long run.

1.2 Overview of the Thesis:

Chapter 1 provides the motivation for the study of one-dimensional semiconductor nanostructured materials with a comprehensive review of recent progress and a discussion on underlying prospects. The basic physical properties of GaN, various 1D GaN nanostructures and their importance, recent developmental effort, key material parameters and other issues dealing with potential applications are presented.

Chapter 2 briefly covers the experimental and characterization techniques used in the present thesis work. The development of an atmospheric-pressure thermal CVD technique is detailed. Various characterization tools, such as, field emission scanning electron microscopy (FESEM) for morphological, high resolution transmission electron microscopy (HRTEM) for structural, Raman and photoluminescence (PL) spectroscopy for optical properties are briefly discussed. Kelvin probe force microscopy (KPFM) and impedimetric spectroscopic techniques are also covered as these were used for measuring surface and interfacial electronic properties.

Chapter 3 deals with the growth of various forms of GaN nanostructures using liquid Ga metal as a source and NH_3 as a reactant gas in thermal CVD technique. Initially, the process parameters to synthesize high quality GaN NWs of particular shape and size are optimized by interplaying with the incubation time in VLS technique. A simple steady state model has been used to correlate the NW growth morphology with the size of the liquid catalyst. VS type catalyst free process is used for the growth of various other forms of GaN, such as, nanotips, and NPs having a high degree of shape anisotropy. FESEM, HRTEM, Raman and PL studies are performed to explore the underlying growth mechanism of these GaN nanostructures.

The self-catalytic growth and physicochemical properties of core-shell Ga_2O_3@ GaN microbelts are presented in Chapter 4. The nanoprotruded surface topographic features of the microbelts are explored by FESEM study. The interface of the core-shell structures is characterized in detail by focused ion beam (FIB) cross sectioning, HRTEM, and Raman imaging techniques. The GaN microbelt shows superhydrophobic properties as a result of the formation of inbuilt air-trapped nanocavity within the vicinity of surface protrusion and correlated with a mathematical model. High degree of dangling bonds and native defects on the nanoprotruded surface of the microbelts has shown enhanced sensitivity to moisture levels present in atmosphere as compared to thin film counterparts. This has been monitored by measuring the variation of surface potential using KPFM technique. A dissociative pathway for the reaction mechanism of water molecules on GaN surfaces is presented.

Chapter 5 covers the growth and functionalization of GaN NTs for catalytic oxidation and gas sensor application. GaN NTs are synthesized employing a quasi-VS process. In this case, Au is used to initiate the nucleation process to form a layer of GaN nanoparticulates that drives the further growth of NTs. Functionalization of NTs with Pt nanoclusters via a green chemistry route is performed. Laser assisted localized oxidation and photo-fragmentation of a single as well as GaN NT arrays is demonstrated and discussed in detail. Gas sensing behavior of NTs, co-catalyzed by Pt nanoclusters has been studied for a wide range of operating temperature, room temperature (RT) to 300 ^{o}C. Pt functionalized NTs show superior response to H_2, down to 25 ppm concentration at RT.

Chapter 6 deals with the development of an ultra sensitive DNA biosensing technique, which utilizes the advantage of narrow conduction channels being present in GaN NWs. The necessary reagents, experimental techniques, and subsequent characterization methods used during the process are described. A series of functionalization steps undertaken for GaN NWs to covalently immobilize single stranded DNA as a probe molecule is presented. This approach uses established molecules like amine terminated dendrimer (PAMAM) for obtaining specific probes linkages to NWs. In-situ monitoring of the hybridization in GaN-PAMAM-probe indicates excellent sensitivity over 10^{-9} to 10^{-19} molar target DNA concentration. The presence of single, triple mismatch, and radiation induced damage target-DNA base pair can be delineated in the hybridization process. This demonstrates the excellent selectivity and specificity of PAMAM modified probes. A detail mechanism of DNA sensing is proposed which is based on observed band bending at the interface between the semiconductor and electrolyte that takes place during surface modification steps.

Chapter 7 briefly covers the recent trend in understanding the physicochemical interactions at the nano-bio interface, which is essential to trace the safe use of nanomaterials. GaN NPs induced toxicity and inhibition of biofilm formation in both gram positive (*Staphylococcus aureus)* and gram negative (*Escherichia coli, Pseudomonas aeruginosa and Pseudomonas putida)* bacterial cells over a wide range of NPs concentrations (0.25 -100 µg/mL) are demonstrated. The erosion of intracellular material, localized protein exudation site and extent of cellular damage upon exposure to GaN NP have been investigated in detail by confocal laser Raman microscopy. These studies cover both single and multi-cellular levels.

A brief summary of this thesis along with the future prospective is given in Chapter 8.

1.3 References:

1. Mann, S.; *Angew Chem. Int. Ed. Engl.* **2008**, 47, 5306.
2. Sahoo, P.; Dhara, S.; Dash, S.; Tyagi, A. K. *Nanoscience & Nanotechnology-Asia* **2011**, 1, 140.
3. Yan, R.; Gargas D.; Yang, P.; *Nat. Photonics* **2009**, 3, 569.
4. M. Ferrari, *Nat. Rev. Cancer* **2005**, 5, 161.
5. Niemeyer, C. M. *Angew Chem. Int. Ed.* **2001**, 40, 4128.
6. G. A. Ozin, L. Cademartiri, *Small* **2009**, 5, 1240.
7. Ferry, D. K.; Goodnick, S. M. *Transport in Nanostructures* **2009**, ISBN: 0521877482.

8. Dupas, C.; Houdy, P.; Lahmani, M. *Nanoscience: Nanotechnologies and Nanophysics* **2007**, Springer, ISBN-10 3-540-28616-0.
9. Sahoo, P.; Dhara, S.; Dash, S.; Raj, B.; Manna, I.; Tyagi, A. K. *Appl. Phys. Lett.* **2011**, 98, 043103.
10. Sahoo, P.; Dhara, S.; Amirthapandian, S.; Kamruddin, M.; Dash, S.; Tyagi, A. K. *Cryst. Growth Des.* **2012**, 12, 2375.
11. Sahoo, P.; Oliveira, D. S.; Cotta, M. A.; Dhara, S.; Dash, S.; Tyagi, A. K.; Raj, B. *J. Phys. Chem. C* **2011**, 115, 5863.
12. Sahoo, P.; Basu, J.; Dhara, S.; Fang, H.C.; Liu, C-P.; Ravindran, T. R.; Dash, S.; Tyagi, A.K. *J. Mater. Sci.* **2012**, 47, 3447.
13. Li, M.; Schnablegger, H.; Mann, S. *Nature* **1999,** 402, 393.
14. Waltereit, P.; Brandt, O.; Trampert, A.; Grahn, H. T.; Menniger, J.; Ramsteiner, M.; Reiche, M.; Ploog, K. H. *Nature* **2000**, 406, 865; Kim, H. M.; Cho, Y. H.; Lee, H.; Kim, S. I.; Ryu, S. R.; Kim, D. Y.; Kang, T. W.; Chung, K. S. *Nano Lett.* **2004**, 4, 1059.
15. Huang, M. H.; Mao, S.; Feick, H.; Yan, H.; Wu, Y.; Kind, H.; Weber, E.; Russo, R.; Yang, P.; *Science* **2001**, 292, 1897.
16. Sirbuly, D. J.; Law, M.; Pauzauskie, P.; Yan, H.; Maslov, A. V.; Knutsen, K.; Ning, C. Z.; Saykally, R. J.; P. Yang, *Proc Natl. Acad. Sci.* **2005**, 102,7800.
17. Law, M.; Greene, L. E.; Johnson, J. C.; Saykally, R.; Yang, P. *Nat. Mater.* **2005**, 4, 455.
18. Yan, R.; Park, J. H.; Choi, Y.; Heo, C. J.; Yang, S. M.; Lee, L. P.; Yang, P. *Nat. Nanotechnology* **2012**, 7, 191.
19. Johansson, J.; Karlsson, L. S.; Svensson, C. P. T.; Rtensson, T.; Wacaser, B. A.; Deppert, K.; Samuelson, L.; Seifert, W. *Nat. Mater.* **2006,** 5, 574.
20. Mohammad, S. N. *Nano Lett.* **2008**, 8, 1532.
21. Mohammad, S. N. *J Chem. Phys. C* **2007**, 127, 244702.
22. Bierman, M. J.; Lau, Y. K. A.; Kvit, A. V.; Schmitt A. L.; Jin, S. *Science* **2008**, 320, 1060.
23. Schumann, T.; Gotschke, T.; Limbach, F.; Stoica T.; Calarco, R. *Nanotechnology* **2011**, 22, 095603.
24. Service, R. F. *Science* **2010**, 327, 1598.
25. Takahashi, K.; Yoshikawa, A.; Sandhu, A. *Wide Bandgap Semiconductors; Fundamental Properties and Modern Photonic and Electronic Devices,* ISBN-10 3-540-47234-7, ISBN-10: 3642079946.
26. Feng, Z. C.; *III-Nitride Semiconductor Material, Imperial College London*, **2006**, ISBN-1-86094-636-4.
27. Nam, C-Y.; *Gallium Nitride Nanowire: Synthesis, Resonant Electrochemical Properties, Ion Beam Disorder Effects on Contact Conduction, and Heterojunction Fabrication,* **2007**, UMI Number: 3260956.

28. Yao, T.; Hong, *S-K.;Oxide and Nitride Semiconductors: Processing, Properties, and Applications* **2009**, ISBN: 978-3-540-88846-8.
29. Han, W.; Fan, S.; Li, Q.; Hu, Y.; *Science* **1997,** 277, 1287.
30. Duan, X.; Lieber, C. M. *J. Am. Chem. Soc.* **2000**, 122, 188.
31. Chen, C. C.; Yeh, C. C. *Adv. Mater.* **2000**, 12, 738.
32. Chattopadhyay, S.; Ganguly, A.; Chen, K. H.; Chen, L. C. *Critical Reviews in Solid State and Materials Sciences* **2009**, 34, 224.
33. Jung, H. S.; Hong, Y. J.; Li, Y.; Cho, J.; Kim, Y. J.; Yi, G. C. *ACS Nano* **2008**, 2, 637.
34. Sofikiti, N.; Chaniotakis, N.; Grandal, J.; Utrera, M.; S.García, M. A.; Calleja, E. *Mater. Lett.* **2010**, 64, 1332.

CHAPTER 2

EXPERIMENTAL AND CHARACTERIZATION TECHNIQUES

Growth of GaN nanostructures, chemical functionalization and their characterization processes were performed using a variety of experimental methodologies. Each method provides in depth information about the crystal structure, growth mechanism, and their associated surface, optical and electronic properties. This chapter describes each methodology employed for growth, characterization, and application of GaN nanostructures, and delineates the merits and demerits associated with each technique.

2.1 Growth Techniques

2.1.1 Introduction:

There are dozens of deposition techniques available to realize a wide variety of nanomaterials and their complexes.[1,2] The concern here is with deposition method, which can be made simpler by limiting the number of technologies to be considered as well as classifying the task of comparison of physical properties of the resulting materials. In general, the growth of nanostructure via catalytic or self-catalytic deposition method consists of statistical process of nucleation, surface diffusion controlled growth of 3D nuclei and the subsequent ingress of incoming vapor phase species. The differential growth rate among the different atomic facets/planes results in a high degree of shape anisotropy. By controlling the thermodynamic parameters of the deposited materials and the substrate surface, the initial nucleation stage could be monitored that decides where an incoming adatom species will get attached. Various important parameters associated with the adatom migration process are listed as follows; [2]

1. The mean residence time of adatoms: $\tau_s = \tau_v \, exp\left(\frac{E_{ad}}{kT}\right)$ (1)

where τ_v is a period of vibration perpendicular to the surface assumed to be almost $1/v$ (= 10^{-13} s), where v ($\sim 10^{13}$ Hz) is a frequency of lattice thermal vibration, and E_{ad} is the adsorption energy of adatoms on the substrate (= 0.1 to 1 eV).

2. The thermal equilibrium time of the adatoms: $\tau_e = \tau_s\, exp\left(\frac{-E_{ad}}{kT}\right)$ (2)

3. The mean travelling distance of the adatoms: $X = a_0 \exp\left(\frac{E_{ad}-E_d}{2kT}\right)$ (3)

where a_0 denotes a lattice spacing of surface atoms of the substrates and E_d is the surface diffusion energy for the adatoms against the potential barrier on the substrate surface..

The necessary condition for the adatom is to stay at the surface of substrate is E_{ad} >> kT, where τ_s >> τ_e otherwise it may disrobe out of the substrate. In case of epitaxial or VS growth mode, the initial growth stage of a material is governed by the surface energy content of the initial films (γ_f), the surface energy of substrates (γ_s) and the interfacial energy between thin films and substrates (γ_{fs}). The island growth will be predominant at (γ_s - γ_{fs}) < γ_f which is a necessary condition for anisotropic growth proceeding towards formation of 1D nanostructures. In all these cases, the key variable influencing evaporation rate is temperature since it has a profound effect on equilibrium vapor pressures. On the other hand, growth of materials via a VLS process depends strongly on the catalyst particles as well as other messoscopic parameters, which are discussed in detail in Chapter 3. In the present work, we have employed chemical and physical vapor deposition methods for the growth of GaN nanostructures with varying aspect ratios.

2.1.2 Thermal Chemical Vapor Deposition (CVD):

When a volatile compound of a material of interest to be deposited is vaporized, and subsequently decomposed into atoms or molecules, and/or reacted with other gas/vapor species, or liquids on the substrate surface to generate non-volatile reactant products on the substrate, the process is termed as thermal chemical vapor deposition (CVD). In contrast, physical vapor deposition (PVD) technique is based on material transfer process from condensed-phase evaporant or sputter target sources to substrate surface. The fundamental sequential steps that occur in every CVD process can be outlined as follows;

1. Convective and diffusive transport of reactant species to the reaction zone,
2. Transport of the reactant products from chemical to the substrate surface,
3. Heterogeneous reactions of these species the substrate surface by means of adsorption diffusion, and desorption process leading to nucleation,
4. Further rational attachment of reactant species leading to growth of nuclei,
5. Transport of volatile substances and the reaction by-products away from the reaction zone.

Important components of the CVD system for the growth of nanostructures:

The experimental setup for the growth of various forms of GaN nanostructures is described schematically in figure 2.1. The important components of the system are listed as follows:

1) High Temperature Vacuum Tube Furnace (GSL-1300X, MTI Corporation, USA): Maximum temperature inside furnace can reach 1400 °C under vacuum or flowing gas. The furnace temperature profile can be set up by 51 segments and run automatically by the 708p type advanced PID temperature controller. This system has additional features including,

   - ✓ Heating element: SiC rod
   - ✓ Constant temperature zone: 100 mm
   - ✓ Power: 2.5 KW and Voltage: AC 220~240 V (single phase 50/60 Hz)
   - ✓ Thermocouples: S type Pt-Rh

2) Quartz tube reactor of diameter ~2.7 cm, length of ~130 cm and thickness 2 mm

3) Rotary vacuum evaporator (*Edwards RV3 50L/m two-stage rotary pump with oil mist filter*) for pre-evacuation of the chamber down to 1 mbar pressure

4) High pure NH_3 gas (99.99 %) source

5) Mass Flow controller (GFC 57/67/77): 1-100 sccm for NH_3 and 10-1000 sccm for N_2 gas

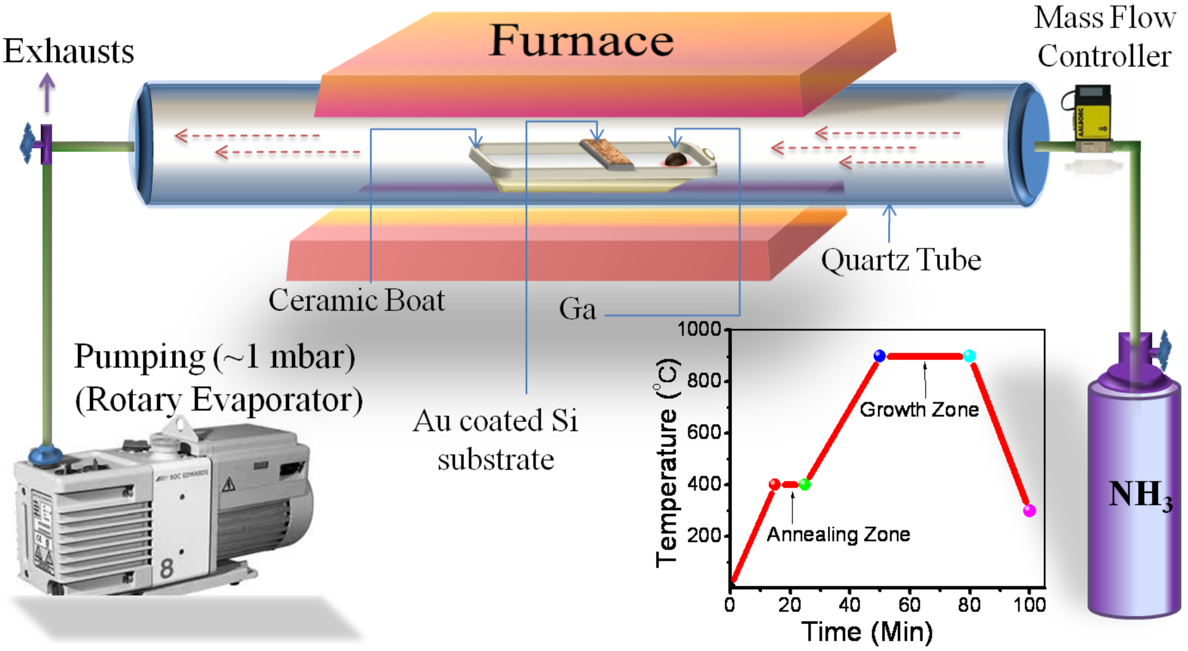

Fig. 2.1 Schematic representation of the thermal CVD system used for the growth of various forms of GaN nanostructure; Inset shows the typical temperature profile maintained during the growth process.

6) Pirani Vacuum Gauge: to monitor vacuum inside the chamber in the range of 1000 to 1 x 10^{-3} mbar.

The thermal CVD has been used for the growth of GaN nanostructures. Typical temperature profile in the CVD system employed for our growth of various GaN nanostructures is shown in the inset in figure 2.1.

Advantages:

1) Ability to produce a large variety of films and coatings of metals, semiconductors, and inorganic as well as organic compounds

2) Ability to control stoichiometry of films

3) Affordable cost of the equipment and operating expenses,

4) Suitability and compatibility with other growth processing steps

Limitations:

1) Controlled and aligned growth of nanostructures

2) Maintaining the stoichiometric ratio of the precursors during growth

3) Difficulties in controlling the various process parameters dependent anisotropic growth aspect

2.1.3 Thermal Physical Vapor Deposition:

The PVD process is divided into two categories: (1) thermal evaporation and (2) sputtering. Thermal evaporation or vacuum deposition techniques are still widely used in the laboratory and in industry for depositing metal and metal alloys. The important steps involved in the thermal evaporation process include; (*i*) generation of reactant vapors by boiling or subliming a source material in a vacuum chamber pressure with $p < 1 \times 10^{-6}$ Torr, (*ii*) transfer of vapor phase species to the substrate, and (*iii*) condensation of vapors on the substrate leading to the formation of a solid film. The resistive heating process is most commonly used to evaporate source materials for thin film deposition. The heating elements are either in the form of filaments or boat, generally made of refractory metals such as W, Mo, or Ta. The thermal evaporation system (Model 15F6, HINDHIVAC) used for our study facilitates coating of single and multilayer films along with Ion cleaning (bombardment) and film thickness monitoring. This is a versatile and flexible unit suitable to produce a simple metallic film for research.

Important components of the thermal evaporation system:

1) Vacuum pumping system:

- ✓ Diffusion pump type and speed: OD-150, 300 Lit/Sec
- ✓ Rotary vacuum pump type and speed: ED-21, 350 Lit/Min.
- ✓ Vacuum gauge : Analog, Pirani, Penning gauge (with sensors to measure vacuum in the range of 0.5 mbar to 1×10^{-3} mbar and 10^{-3} to 10^{-6} mbar)

2) Power: 230V AC, 50Hz, 1 Phase

3) Chamber gadgetories:

- ✓ LT Evaporation: 3 sets- (200 Amps, 10 V) or (100A, 20V)
- ✓ Ion Bombardment: 1 set, 3.5 KV, 200 mA
- ✓ Work holder size (flat): 340 mm dia (nominal)

We have employed this technique to deposit Au films of 3-10 nm thickness on Si or sapphire substrates for the growth of NWs and nanotubes. In addition, metal films of single (Pd, Pt, or Al) and multilayer (Ti/Au or Cr/Au) are deposited by this system for sensor fabrication.

2.1.4 DC Sputtering:

Generally, deposition of material in the sputtering process involves the bombardment of energetic ion particles on a solid surface. Among the different sputtering systems available, such as rf diode, magnetron, and ion-beam, DC sputtering system is relatively simple. The DC sputtering system is composed of a pair of planar electrodes where one of the electrodes is a cold cathode and the other one is an anode. The top plasma-facing surface of the cathode is covered with a target material of interest whereas substrates are placed in the anode. When the sputtering chamber is maintained at 0.1 torr of argon gas, several kilovolts of dc voltage with a series resistance of 1 to 10 kΩ are applied between the electrodes, which initiate the formation of the glow discharge. The air ions in the glow discharge region are accelerated towards the cathode, and sputter the target resulting in the deposition of thin film on the substrates. The film-growth rate (G) during DC sputtering can be calculated with the help of following equation;[2]

$$G\ (cm/s) = \frac{P_d\ \langle x_{th} \rangle}{g\rho\ (1+\gamma_e)\ E} \tag{4}$$

P_d refers to the discharge power-density (W/cm^2), $\langle x_{th} \rangle$ is the mean distance from the cathode where sputtered atoms travel before they become thermalized, g is the distance between the cathode and anode, ρ is the atomic density (atoms/cm^3), γ_e is the secondary-electron emission coefficient and E is the average sputtering energy.[2] This expression reflects that the deposition rate depends directly with applied power and inversely with electrode spacing. Pressure and cathode voltages are assumed constant. We have employed this technique to deposit Pd, Pt or Ag films of various thicknesses for sensor application.

2.2 Structural and Morphological Characterization

It is essential to understand and ultimately control the properties of the material. To achieve this characterizing the detailed material structure down to the atomic level is required. Imaging, measuring, modelling, and manipulating matter at dimensions of roughly 1 to 100 nm can be accomplished with the help of emerging nanocharacterization techniques such as AFM, TEM, STM, and FESEM with the capability to achieve high spatial and analytical resolution. [3]

2.2.1 Electron Microscopes:

Electron microscopes were developed because of the limited image resolution in light microscopes imposed by their wavelength range. From the Rayleigh criterion, the smallest distance (δ) that can be resolved, is approximately by $\delta \approx 0.61 \frac{\lambda}{\mu sin\,\beta}$, where λ is the wavelength of light, μ the refractive index of the viewing medium, and β the semi-angle of collection of the magnifying lens. The resolution limit of a microscope depends on the wavelength used to form the image. Short wavelength provides higher resolution than long wavelength in otherwise identical systems. The wavelength of an electron can be calculated by

$$\lambda = \frac{h}{\left[2m_0\, eV\left(1+\frac{eV}{2m_0\, c^2}\right)\right]^{1/2}} \qquad (5)$$

where h is Plank's constant, p is momentum, m_0 is the mass of the electron, e is the charge of the electron and V is the applied electric potential. The $\left(1+\frac{eV}{2m_0c^2}\right)^{1/2}$ is the relativistic correction term applied when the incident electron energy is $\geq$100 keV.

All electron microscopes take advantage of the wave and particle like behavior of electrons to obtain high-resolution images. The electron scattering process is a succession of particle nature, while electron diffraction is treated by a wave theory. In the scattering process, those electrons do not deviate far from the incident-electron direction gives us the information we seek about the internal structure and chemistry of the specimen. TEM construction allows gathering of these electrons. Another form of scattering where electrons are scattered though large angle (e.g. Backscattering electron) and electrons ejected from the specimen (e.g. Secondary electrons) are of much greater interest in the SEM. These electrons provide atomic number contrast, surface-sensitivity and topographic images.

2.2.1.1 Transmission Electron Microscopy (TEM):

TEM comprises a range of different instruments that make use of the properties of electrons, both as particles and as wave.[3] The TEM generates a wide range of signals which can be processed to obtain atomic resolution images, diffraction patterns (DP), and different kinds of spectra from the small region of the specimen. It produces a much localized electron probe, typically < 5 nm and at best, < 0.1 nm in diameter. The beam current can be as high as ~0.1-1 µA. The wavelength of an electron accelerated by a 200 kV potential (a typical TEM operating parameter) is 2.51 pm which is five orders of magnitude smaller than the wavelength of visible light. It provides valuable information about specimen chemistry and crystallography. TEM comes in wide variants namely high resolution transmission electron microscope (HRTEM), scanning transmission electron microscope (STEM), Analytical Electron Microscope (AEM), high voltage electron microscopy (HVEM) and intermediate voltage electron microscopy (IVEM).

Important Components:

The TEM is divided into three important components: the illumination system, the objective lens\stage, and the imaging system. A schematic diagram of the TEM is given in the figure 2.2. The illumination system comprises the gun and the condenser lenses and its role is to take the electrons from the source and transfer them to the specimen. It can be operated in two principal modes; parallel beam [for TEM and selected area electron diffraction (SAED)] and convergent beam [for STEM, analysis via X-ray and electron spectrometer, and convergent beam electron diffraction (CBED)]. The objective lens/stage system is the heart of the TEM, which extends over a distance of 10 mm at the center of the

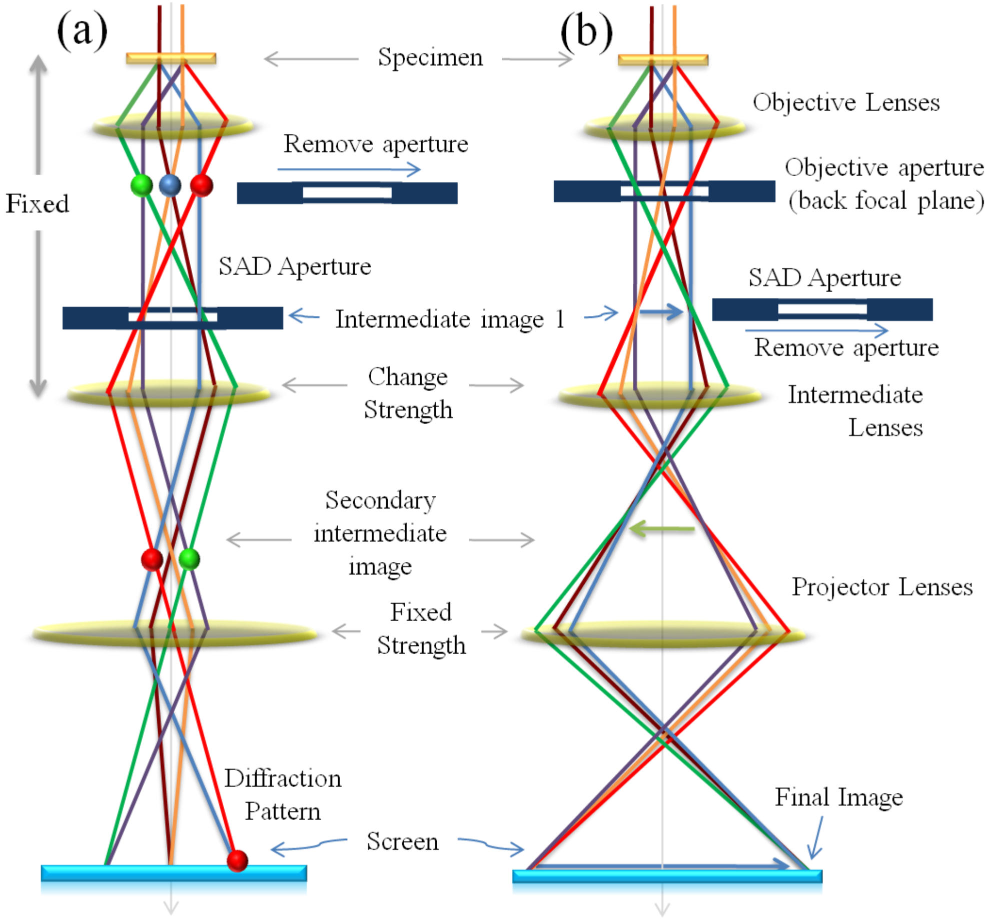

Fig. 2.2 The highly simplified diagram showing two basic operations of the TEM imaging system involving (a) diffraction mode where the DP was projected onto the viewing screen, and (b) image mode where the images were projected onto the onto the viewing screen. In each case the intermediate lens selects either the back focal point (a) or the image plane (b) of the objective lens as its object.

column. In this critical region, beam specimen interactions take place and the two fundamental TEM operations occur. These pertain to the creation of various images and DPs that are subsequently magnified for viewing and recording. The imaging system uses several lenses to magnify the image or DP produced by the objective lens and to focus these on the viewing screen through a detector, charge coupled detector (CCD), or TV camera.

Principle of Operation:

When beams of electrons are sent through the thin sample within the column of a TEM, the atoms in the sample diffract the electrons. If the Bragg condition ($2dsin(\theta) \approx n\lambda$) is satisfied for the diffracted electrons from different planes of the specimen, then the waves will constructively interfere. Either, depending on how the electro-magnetic lenses are focused, interference patterns (the image of the sample) or the DP can be observed. HRTEM can image samples at an atomic resolution, which are formed by allowing many diffracted beams as well as the transmitted beam to contribute to the image. However, we are not seeing the individual atoms while looking at an HRTEM image. When the beams are combined they are constructively and destructively interfere resulting in the phase contrast image, which can be described by:

$$T\ (\hat{u}) = 2A(\hat{u})\ \sin\big(\chi(\hat{u})\big), \qquad (6)$$

where u is a reciprocal lattice vector, $A(u)$ is the aperture function, and $\chi(\hat{u})$ is the phase-distortion function by taking into account of the fact that spherical aberration, astigmatism, and defocus affect the phase of each beam. When T(u) is positive, a negative phase contrast results, meaning that atoms would appear bright against a dark background.

The DP of a specific area of the sample can be obtained by putting an aperture around a selected area of the sample while in imaging mode, and then switching the TEM to diffraction mode. This process is known as SAED, which provides crystallographic structure in reciprocal space. Indexing the SAED, by comparing the relative distances and angles between the diffraction spots, the crystal structure, symmetry, and the orientation of the sample at a particular region can be derived. The SAED contains a bright central spot that corresponds to the direct-beam electrons and some scattered electrons, the distribution of which will depend on the nature of the specimen. Direct beam can be selected to form a bright field image or electrons that are not in the direct beam can be collected to form a dark filed image. There is a limit to the size of the area that can be selected with an aperture due to the spherical aberration of the objective lens. In cases where the area of interest is too small to be imaged using SAED, a fast Fourier transform (FFT) can be applied to an HRTEM image of the area of interest to get a pattern similar to the SAED pattern. The Fourier transform switches between real space *(x)* and reciprocal space *(1/x)*. The mathematical processing of the interference pattern of an HRTEM image results in the same pattern of spots that would be expected from an SAED of the crystal structure.

Limitation:

1) Thin specimen and maximum sampling capability no more than 10^3 mm^3
2) Projection limitation
3) Poor depth sensitivity
4) Damage to specimen by high energy electrons

However, there has been progress in overcoming these limitations, which was much more of a problem for biologists interested in the shape of complex molecules, cells, and other natural structures. Recently, there has been a rapid improvement to create a 3D image using electron tomography that uses a sequence of images taken at different tilts.

In this thesis work, a Libra 200 Zeiss HRTEM was used to substantiate the growth process of various GaN nanostructures and their associated crystallographic information.

2.2.1.2 Scanning Electron Microscopy (SEM):

Scanning Electron Microscopy is used to produce real space magnified images of the surface showing texture, shape, and size of particles by using a beam of electrons. An electron beam with primary electron energy typically 0.5 keV to 40 keV is focused by an electromagnetic lens system onto a spot of 0.4 to 5 nm in diameter on the sample surface. The main difference between a TEM and an SEM is that in a TEM, the electrons go through the sample and in an SEM the electrons only interact with the surface of the sample. The specimen preparation for SEM studies is rather easy.

To acquire an SEM image, the electron beam is rastered across a selected area of the sample. The high energy electrons from the electron beam transfer some of their energy to electrons of the sample's atoms, causing emission of back scattered electron by elastic scattering and secondary electrons by inelastic scattering along with other electromagnetic radiations. Each of these can be detected by specialized detectors and the number of electrons detected is translated into intensity for each pixel on a computer monitor. Because electrons near sharp corners or edges can more easily escape the sample and get to the electron detector, SEM images have a 3D appearance. The two most common materials used for electron emitting filaments are Tungsten (W) and lanthanun hexaboride (LaB_6). Traditional SEM normally uses a thermionic electron gun, where electrical heating of a filament emits electrons. Thermionic sources have relatively low brightness, high evaporation of cathode material and thermal drift during operation. These aspects hinder the resolution limits of a conventional SEM. However, adopting field emission gun (FEG) in the SEM provides us with a high contrast image having low electrostatic distortion and spatial resolution < 2 nm. The FEG has used a tungsten wire with sharp tip of radius ~100 nm. When FEG equipped with focused-ion-beam (FIB), it can perform multiple works like TEM sample preparation, electrode deposition, in-situ annealing and pattern formation. [3]

In this study, a FESEM (Model Zeiss SUPRA 40) was used to examine the morphology, interface structure of various GaN nanostructures grown under different conditions. It was also used to substantiate the growth mechanism as well as the connectivity of nanostructures to the substrate.

2.3 Optical and Electronic Properties

Raman and Photoluminescence spectroscopy are standard optical characterization techniques for studying various aspects of solids such as lattice and electronic properties, and for direct detection of molecular species. In this dissertation, the optoelectronics properties of the as-grown GaN nanostructures were studied by Raman spectroscopy, Photoluminescence (PL), and Kelvin probe force microscopy (KPFM).

2.3.1 Raman Scattering Spectroscopy:

Raman scattering is an inelastic scattering process of photon that occurs essentially as a result of modulation of the electronic polarizability induced by various elementary excitations in a material such as phonons and plasmons.[4,5] Stokes scattering corresponds to the emission of a phonon, while anti-Stokes scattering corresponds to phonon absorption. Generally, Raman scattering intensity *I* can be expressed as:

$$I(\omega_I) \propto \omega_s^4 \, |\hat{e}_s \; .R. \; \hat{e}_I|^2 \left|\sum\nolimits_{\alpha\beta} \frac{1}{(E_\alpha - \hbar\omega_I)(E_\beta - \hbar\omega_\beta)}\right|^2 \qquad (7)$$

ω_I (wave vector $\boldsymbol{k_1}$) and ω_s (wave vector $\boldsymbol{k_2}$) are the incoming and scattering light frequencies respectively. E_α and $E_{\boldsymbol{\beta}}$ are the energy of the intermediate states available (e.g. band gap energy, exciton, impurity state levels etc.). R is the Raman tensor. $\hat{e}_s$ and $\hat{e}_I$ are the polarization vectors of the scattered and incident lights, respectively. In this equation, the first term represents the dipole transition radiation, the middle term represents the Raman selection rule that is related to the change of polarizability and the crystal symmetry, and the last term contributes to the resonance effects.[5]

During the scattering process, conservation of energy during the interaction requires that $\omega_I = \omega_S + \Omega$, while conservation of momentum gives; $\boldsymbol{k_1} = \boldsymbol{k_2} \pm \boldsymbol{q}$, where Ω phonon frequency (wave vector $\boldsymbol{q}$). The maximum phonon frequency of a typical crystal is about 10^{12} - 10^{13} *Hz* that is approximately two orders of magnitude smaller than the frequency of a photon in the visible spectral region. The maximum possible value of $|\boldsymbol{q}|$ $\{=\boldsymbol{k_1} - (-\boldsymbol{k_2}) = 2n\omega/c\}$ occurs for the backscattering geometry in which the outgoing photon is emitted in the direction backward to the source.[6] The maximum value of q that can be accessed in an inelastic light scattering experiment is of order 10^7 m^{-1}. This is very small compared to the size of the Brillouin zone in a typical crystal (~ 10^{10} m^{-1}). Inelastic light scattering is thus able to probe small wave vector phonons with $q \approx 0$. Therefore, Raman scattering gives little information about the dispersion of optical phonons, and its main use is to determine the frequencies of the LO and TO modes near the Brillouin zone center. In addition, the momentum transfer from a photon to a phonon is negligible, and hence only the zone-center phonons will be Raman active (first-order Raman scattering, $q = 0$). However, in reduced dimension such as in nanomaterials, the momentum conservation is often relaxed. In this case, the off-centered phonons can be Raman active and are named as a second-order scattering, $q \neq 0$, which is related to the continuum of phonon density of state and the specific second-order scattering process (e.g. overtone and combination).

Raman scattering has many advantages when compared with other spectroscopic techniques, such as non-destructiveness, contactlessness, and requires no special sample preparation technique such as thinning or polishing. However, Raman based techniques like resonance Raman scattering (RRS), surface enhance Raman scattering (SERS), tip enhanced Raman scattering (TERS), time-resolved Raman scattering (TR^{2}S), nonlinear Raman scattering (NRS), coherent anti-stokes Raman scattering (CARS) and stimulated Raman scattering (SRS) are also very popular as non-invasive techniques that offer chemical and structural information pertaining to a variety of materials inclusive of biomaterials.

2.3.1.1 Major Components of micro-Raman Spectrometer:

The micro-Raman spectrometer (inVia, Renishaw, UK) used for this work is facilitated with the following important components:

1) Excitation source, which is generally a continuous wave laser: Ar^+ laser with 524.5 and 488 nm excitation (maximum laser power ~ 40 mW), He-Cd Laser (UV - 325.5 nm, Power 10 mW), and 788 nm NIR laser.

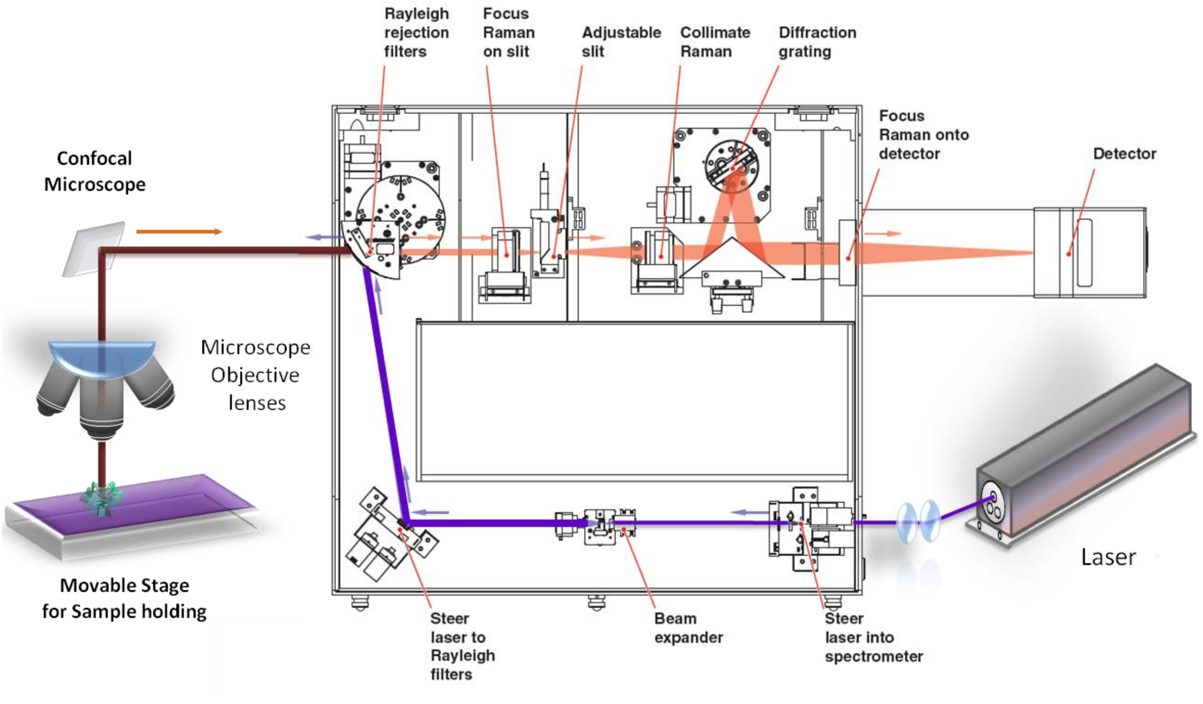

Fig. 2.3 Schematic arrangement of the micro-Raman spectrometer along with detailed internal and external components, laser, and confocal microscopy.

2) Sample illumination via Leica microscope equipped with 5X, 20X, 50X and 100X objective lenses. Standard and confocal modes of operation and collection system is in backscattering configuration are available.

3) Wavelength selector and diffraction gratings of 600, 1800, 2400 and 3000 gr.mm^{-1}

4) Thermoelectric cooled CCD in visible and InGaAs detectors in the near IR range.

5) Computerized data processing systems along with additional facilities including optical elements for Polarization measurement, Linkum liquid N_2 stage for low temperature measurement and XYZ movable stage with step size of 0.1 µm capabilities are available.

A schematic ray diagram of the typical arrangement of these components is shown in figure 2.3. The spectrometer provides true confocal capability by adjusting the detector slit and pinhole aperture. According to the Abbe's formula ($0.63\lambda/NA$ where λ is the wavelength and NA the numerical aperture of the objective), the theoretical lateral resolution using 100X objective (NA~ 0.85) is about 385 nm.

2.3.1.2 Raman Imaging and Mapping Study:

In Raman mapping, Raman spectra are measured at various spatial locations. After data acquisition, it is possible to display individual components of Raman spectra for each spatial location or to display a false color image based on the intensities at a selected Raman frequency. Three modes of scanning can be used as per the requirement, namely static, extended and confocal modes. In static mode, the number of spectra in one image can be acquired in less time without the movement of the grating, whereas in extended scanning mode the grating moves in order to cover a larger range of wave number resulting in longer acquisition times. The spectrometer facilitates mapping of different phase, elemental distribution and stress analysis in various hybrid systems including bimolecular and GaN nanostructures. The mapping study was performed in a raster scan mode (static/confocal) with minimum of 0.1 µm step size and 1 s integration time.

Generally, Raman scattering efficiency is higher in covalent crystals than in ionic crystals, because the valence electrons are less localized and larger fluctuation of the polarizability can be induced by lattice vibration. From this perspective, GaN is suitable for Raman scattering studies, since the chemical bonding is a mixture of covalent and ionic bonding. In addition, GaN is generally robust and stand up well to laser irradiation, which is another advantage of Raman scattering studies.

2.3.2 Photoluminescence Spectroscopy:

Photoluminescence (PL) is a process of re-emission of light after absorbing a photon of higher energy.[6,7] This is a radiative recombination process among excited carriers, such as, electrons/holes or excitons in semiconductor during external optical excitation process. Typical band diagram representation of the PL process in a direct gap material is shown in figure 2.4. Photons of energy $(\hbar\omega_I)$ from an excitation source such as a laser or lamp, when impinge on a semiconductor of band gap E_g $(E_g; \leq (\hbar\omega_I))$, inject electrons into the conduction band and holes in the valence band. While absorbing a photon, initially the electron from the valence band creates a state high up in the conduction band. It rapidly loses energy by emitting phonons as indicated by the cascade of transition lines within the conduction band as shown in figure 2.4(a). The emitted phonon preserves all conservation laws of energy and momentum. This process of electron-phonon coupling in most solids is

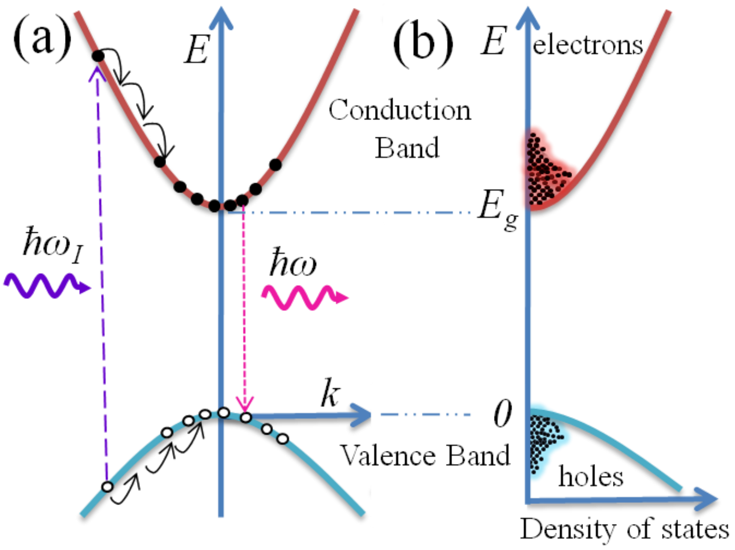

Fig. 2.4 (a) Schematic diagrams of the PL processes happening in case of a direct gap semiconductor after optical excitation, (b) Density of states and level occupancies for the electrons and holes which obey the Boltzmann distribution functions.

very strong that takes place for a short time scale (~ 100 fs). This time scale is much faster than the radiative lifetimes of electrons/holes, which has typical values in the range of 10^{-8} - 10^{-9} s. Therefore, the electrons accumulate at the bottom of the conduction band long before they have had time to emit photon by the radiative recombination process. The similar relaxation process applies for holes in the valence band. Since the momentum of the photon is very small compared to the momentum of the electron, the electron and hole that take part in the recombination process must have the same k vector. Therefore, the emission takes place near k = 0 that corresponds to a photon of energy E_g. No matter how the electrons and holes are excited in the first place, we always obtain luminescence at energies close to the band gap of a material of interest. The luminescence property of a material is also strongly affected by the presence of native defects, impurity, dopants and absolved molecular species. The shape of the band-to-band PL spectra can be calculated. Assuming a direct band gap semiconductor with low carrier density, the PL intensity can be expressed as:

$$I_{PL}(\hbar\omega) = (\hbar\omega - E_g)^{\frac{1}{2}} \exp\left(-\frac{\hbar\omega - E_g}{k_B T}\right) \tag{8}$$

The first term arises from the joint density of states in the interband transition and the second factor arises from the Boltzmann distribution of the electron and holes.[6] The luminescence efficiency of direct band gap semiconductors is relatively higher compared to indirect band gap materials. In typical direct gap semiconductors, the optical transitions between the valence and conduction bands are dipole-allowed and have large matrix elements. Apart from the band-edge transition, there are other possible pathways for the excited carriers to take part in the radiative transition process. The following possibilities exist:[7]

1) **Free-to-bound (FB) transition**: FB radiative recombination process involves a transition from a free carrier (electron) to a charge (hole) bound to an impurity (shallow acceptor) state.

2) **Donor-accepter-pair (DAP) transitions**: Quite often, a semiconductor may contain both donors and acceptors like states. When electrons from the neutral donors (D^o) state recombine

radiatively with holes in the neutral acceptors (A^o) state, this is known as DAP transition. The energy of the emitted photon in a DAP transition is given by following expression:

$$\hbar\omega = E_g - E_A - E_D + e^2/4\pi\varepsilon_0\varepsilon_r R \qquad (9)$$

where E_g is the band gap energy and E_D and E_A are the donor and acceptor binding energies, respectively. The last term is appeared from coulomb energy provided that the distance (R) between two charge states (D^+ and A^-) is much larger than the lattice constant, otherwise zero.

3) **Free and bound exciton emission:** In high purity and high quality semiconductors, the photo-excited electrons and holes are often formed as excitons by Coulomb interaction. The emission produced during the radioactive annihilation of exciton is so-called free exciton emission. However, the emission arising from the exciton attached at the neutral donors or acceptor states is called bound exciton emission. It commonly occurs at low temperature.

PL spectroscopy is a potential tool in the semiconductor research with an objective to develop electroluminescent devices such as light-emitting diodes and lasers. The experimental arrangement is same as for Raman spectrometer as shown in figure 2.3. In this dissertation, the PL studies of GaN nanostructures were carried out using 325.5 nm excitation line of He-Cd UV Laser. Low temperature PL measurements were carried out by a liquid N_2 stage (Linkam).

2.3.3 Kelvin Probe Force Microscope (KPFM):

Kelvin probe force microscopy is based on the principle of an atomic force microscopy that uses a conducting tip.[8] In KPFM mode, the contact potential between sample and tip is compensated by applying external bias voltages and thus facilitating the simultaneous acquisition of topography and surface potential (SP) images. It is based on a two-pass technique. In the first pass the topography is acquired using standard semi-contact mode (mechanical excitation of the cantilever). In the second pass this topography is retraced at a set lift height from the sample surface to detect the electric surface potential $\varphi(x)$. During this second pass the cantilever is no longer excited mechanically but electrically by applying a voltage (V_{tip}) to the tip, which contains both *dc* and *ac* components; $V_{tip}=V_{dc} + V_{ac}\sin(\omega_{ac}t)$

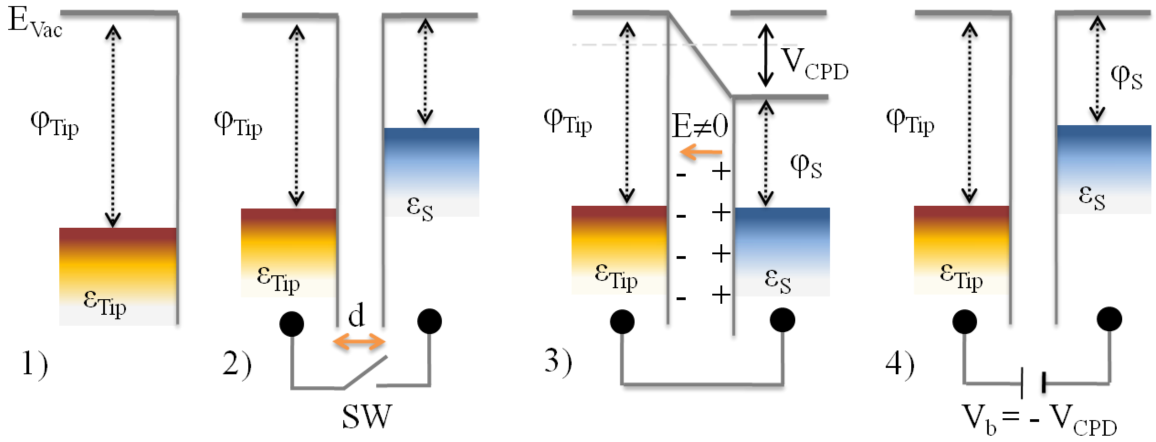

Fig. 2.5 Schematic band diagram of the KPFM process steps (1 to 4) of measuring the surface potential of a surface using metal tip.

The *ac* voltage produces an electrostatic force between the tip and the sample and causes the tip to oscillate at the fundamental *ac* bias frequency (ω_{ac}). The resulting capacitive force F_{cap} between the tip and a surface at potential V_s is [9]

$$F_{cap} =(1/2)\,(V_{tip} - \varphi(x))^2(\mathrm{dC/dz}) \qquad (10)$$

where C and z are the capacitance and the distance between the tip and sample, respectively. The first harmonic force expressed as

$$F_{cap\,\omega} = (\mathrm{dC/dz}(V_{dc}- \varphi(x)V_{ac})\sin(\omega_{ac}t) \qquad (11)$$

leads to suitable cantilever oscillations. In KPFM, an additional bucking voltage (V_{dc}) is applied to the tip to null out the ω_{ac} component of the cantilever (and accordingly ω_{ac} component of the tip-force). The *dc* bias $V_{dc}(x)$ is then equal to $\varphi(x)$. The KPFM process for SP measurements is depicted schematically in figure 2.5. So mapping $V_{dc}(x)$ reflects the distribution of the SP along the sample surface, which is equal to SP = $\Delta\varphi/e$. Here, $\Delta\Phi$ is the difference between tip and sample work functions, and e is the electron charge. If no special tip-sample bias voltage is applied, this distribution becomes a Contact Potential Difference (CPD) distribution.

In this study, topography and SP images of GaN samples were acquired simultaneously using an Agilent 5500 with a three-lock-in amplifier in the amplitude modulation KPFM. For the measurements, V_{AC} bias at frequencies in the range 10-15 kHz plus a DC bias, V_{DC}, were applied between tip and sample. The change in the SP values with moisture level in the environment was correlated to the specific material properties.

2.4. Electrochemical Impedance Spectroscopy (EIS):

Electrochemical impedance spectroscopy (EIS) is a valuable method for the characterization of surfaces, functional layers or membranes as well as the exchange and diffusion processes by analyzing the complex electrical resistance at the interface at different frequencies.[10,11] In the field of biosensor, it is particularly very sensitive to the detection of a variety of target analytes, such as DNAs, proteins, antigens, or antibodies. Impedance based biosensors measures the electrical impedance of an interface in the *AC* steady state with the constant *DC* bias condition. The impedance is a complex value that can be determined by applying a sinusoidal voltage of small amplitude (± 10 mV) and simultaneously detecting the current response.[11] The impedance can be expressed by

$$Z = \frac{\mathrm{V(t)}}{I(\mathrm{t})} = \frac{V_0\ \mathrm{Sin}(\omega\mathrm{t})}{I_0\ Sin\ (\omega\mathrm{t} - \varphi)}$$

where V_0 and I_0 are the maximum amplitude of voltage and current, respectively. ω is the angular frequency, t the time, φ the phase shift between the voltage–time and current–time functions. It can be represented in two different ways: 1) using a Bode plot which plots $log|Z|$ and φ as a function of $log\ \omega$; or 2) using a Nyquist plot which plots imaginary impedance $Z''(\omega)$ vs real impedance $Z'(\omega)$. Depending upon the nature of current flow across the interface, all electrochemical sensors are broadly divided into two categories, 1) *Faradic* type (charge transferred across the interface) and 2) *non-Faradic* type (transient currents can flow without charge transfer).

An Eco Chemie Autolab PG STAT 30 model potentiostat was used for our study belongs to a conventional three-electrode system as shown in figure 2.6(a). Here, functional GaN NWs were used as working electrodes, a platinum foil as a counter electrode and a saturated calomel electrode as a reference electrode through a luggin capillary. Impedance spectra were recorded at open circuit potential by applying a sinusoidal voltage of small amplitude (± 10 mV) in the frequency range of 10^6- 0.005 Hz. Typical impedance spectrum was often represented by the Nyquist plot as shown in figure 2.6(b) which is constituted of a semicircle at low frequency side (electron-transfer-dominated process) and a 45^o inclined line at higher frequency side (diffusion-limited process). The area under the curve represents the polarized resistance (R_P) whereas the 45° line indicates Warburg-limited behaviour whose value can be determined by extrapolating to the real axis. For the situation of an electrode in contact with an electrolyte, the so-called Randles circuit were used [as shown in Fig. 2.6(b)], comprising of the solution resistance (R_s), polarization resistance (R_p), a constant phase

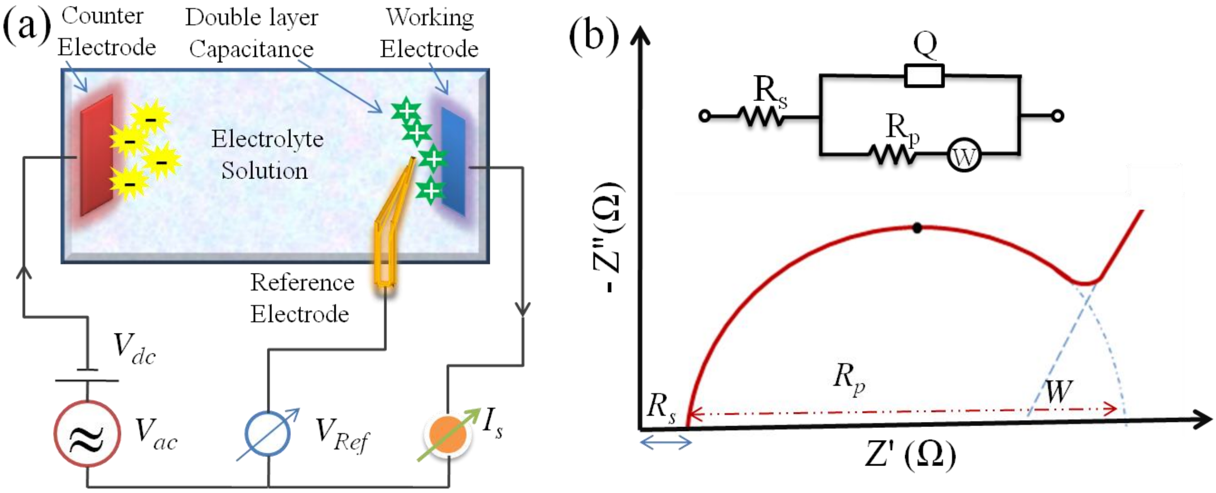

Fig. 2.6 Schematic representation and working methodology of a three-electrodes based EIS technique, (b) typical Randles' equivalent circuit and Nyquist plot for an electrode in contact with an electrolyte (used for our study).

element (Q) and Warburg impedance (W). Constant phase element (CPE), denoted here as Q, was used for better fitting for some of the elements instead of true capacitance. The CPE reflects non-homogeneity of the layer and the extent of deviation from the Randles model. The CPE is a special element whose impedance value is a function of the angular frequency ω and whose phase is independent of the frequency. Impedance due to CPE is expressed as $Z_{\mathrm{CPE}} = 1/Y_o(j\omega)^{-n}$ where Y_o is the magnitude of the CPE, ω is the angular frequency and n is the exponential term of the CPE. This technique has been employed for in-situ detection of DNA undergoing hybridization event.

2.5. Gas Sensor Measurement System:

The gas sensing properties of functionalized GaN nanostructures were studied using a custom-built exposure facility for gas sensor (EFGS) testing system. The schematic diagram of the EFGS system is shown in figure 2.7. The important components of the system include double walled stainless steel chamber, heater stage (which also acts as sample holder), scroll pumps, residual gas analyzer (RGA), flow controllers, pressure gauges, readout system, gas delivery lines and pneumatically actuated valves. The vacuum is maintained by using dry scroll pumps. Gas flow and temperature are controlled by mass flow controller (MFC) and PID controller respectively. The entire operation of the exposure facility system can be controlled externally using Supervisory Control and Data Acquisition (SCADA) software. A residual gas analyzer is used to monitor the gases inside the chamber. The sensor response upon exposure to gases manifests as a change in resistance of the sample. This resistance or other electrical output can be recorded on a PC via GPIB interface which is configured to acquire data at user-defined intervals. The parameters that can be varied are vacuum inside the chamber, operation temperature and gas mass flow ratios.

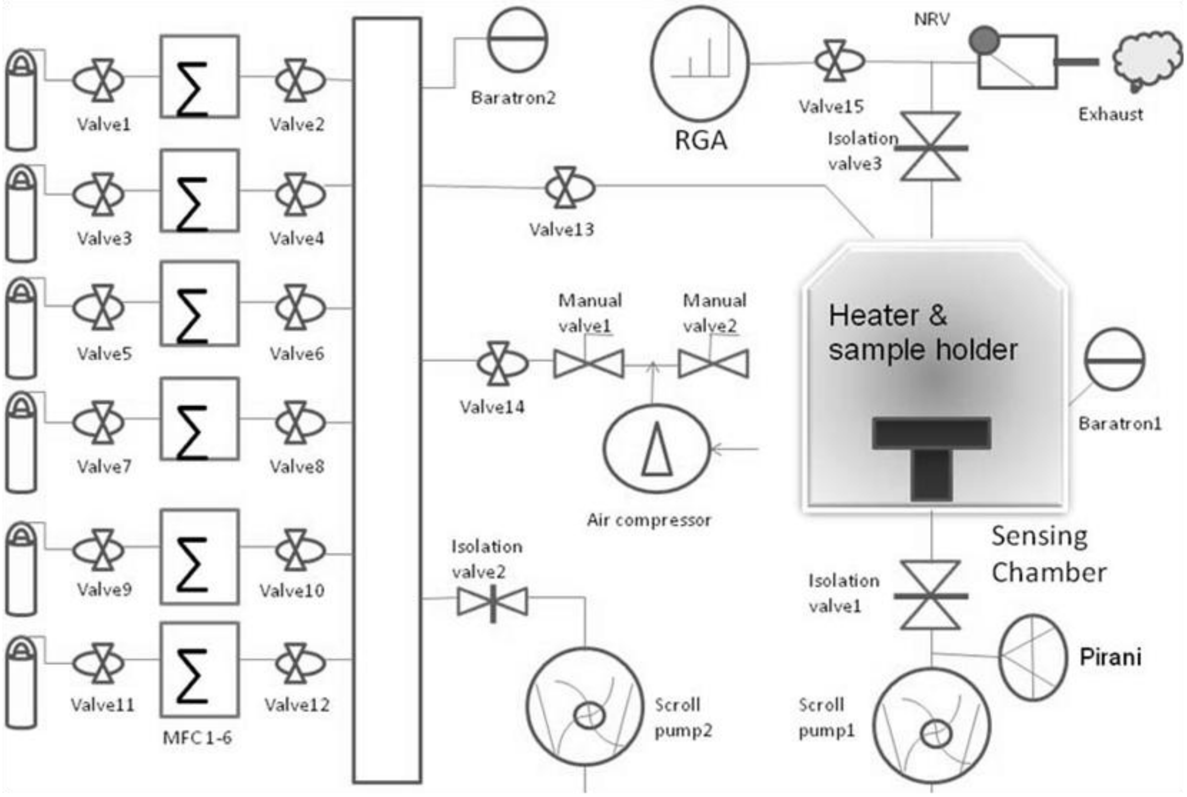

Fig. 2.7 Schematic representation of the exposure facility for gas sensor (EFGS) system.

2.6 Summary:

This chapter highlights experimental methodologies used for growth, characterization of GaN nanostructures. Several solid state and microscopic analytical techniques were used to obtain structure property correlations in nanometer scale. Application potential involving hydrophobicity, gas sensing response, and DNA detection capability was studied by using techniques like KPFM, EFGS, and EIS, respectively. Brief outline on each analytical method is given with appropriate references.

2.7 Reference:

1. Ohring, M. *Material Science of thin films*, **2002**, Academic Press, ISBN: 0-12-524975-6.
2. Wasa, K.; Kitabatake, M.; Adachi, H.; *Thin film materials technology: Sputtering of compound materials*, **2004**, William Andrew, Inc. ISBN: 0-8155-1483-2.

3. Williams, D. B.; Carter, C. B. *Transmission Electron Microscopy*, **2009**, Springer, ISBN 978-0-387-76502-0
4. Ferraro, J. R.; Nakamoto K.; Brown, C. W. *Introductory Raman Spectroscopy,* **2003**, Elsevier, ISBN: 978-0-12-254105-6.
5. Weber, W. H.; Merline, R. *Raman scattering in material science*, **2000**, Springer, ISBN 3-540-67223-0.
6. Fox, M. *Optical Properties Solids*, **2001,** Oxford University Press, ISBN 0-19-850613-9.
7. Yu, P. Y.; Cardona, M. *Fundamentals of Semiconductors: Physics and Materials Properties,* **2010**, Springer-Verlag Berlin, ISSN 1868-4513.
8. Mironov, V. L. *Fundamentals of scanning probe microscopy*, **2004,** NT-MDT.
9. Nonnenmacher, M.; O'Boyle, M. P.; Wickramasinghe, H. K. *Appl. Phys. Lett.* **1991**, 58, 2921.
10. Daniels, J. S.; Pourmand, N. *Electroanalysis* **2007**, 12, 1239.
11. Lisdat, F.; Schafer, D. *Anal. Bioanal. Chem.* **2008**, 391, 1555.

CHAPTER 3

GENERAL ROUTE OF SYNTHESIS FOR 1D GaN NANOSTRUCTURES, CHARACTERIZATION, AND GROWTH DYNAMICS

3.1 Introduction:

Several prototype devices have already been realized using GaN and GaN-based alloy III-V compounds.[1] However, large scale applications of 1D GaN nanostructures based devices are limited because of the cost and efforts involved in developing there nanostructures with necessary purity and alignment.

Bulk synthesis of GaN nanostructures mostly involves two typical growth mechanisms, namely, VLS and VS processes.[2-5] The metal catalyst–assisted growth is widely known as VLS growth. It was initially proposed for the growth of whiskers by Wagner and Ellis.[6] The growth is driven by a catalyst without interfering with the reaction. In most cases, source materials such as liquid Ga are heated in the presence of NH_3 to vaporize the source material at elevated temperature as well as to cause dissociation of NH_3 to take part in nitridation reaction. At a fixed temperature, the vapor phase reactants dissolve in the liquid-phase of metal catalyst. When the liquid metal reaches its solubility limit during the continual addition of reactant species, it starts precipitating into a solid phase. As long as the reactant supply continues, the precipitation is continuous that leads to formation of NW. Transition metals such as Fe, Ni, Co and their oxides are also found to be efficient catalysts for the precipitation of GaN materials from a molten catalyst droplet supersaturated with the metal vapor. Au is a better choice of catalyst for synthesizing GaN nanostructures owing to its high defect formation energy (~4eV) in GaN as compared to Ni substitution (1.2 eV).[7] Hence, product purity is expected to be better while using Au catalyst even though it has poor solubility for N as compared to other transition metals, like Fe and Ni. However, the radial size distribution of target NWs is strongly influenced by the catalyst particle size. The orientation of the NW can also be controlled via epitaxial growth followed by VLS process.[1] The length of the 1D nanomaterials depends on the reaction time and reactant flux. The choice of catalysts and dopant concentrations also plays a pivotal role. A schematic representation of the VLS based growth process is shown in figure 3.1(a). Catalyst nanoparticulates are often observed in negligible amounts at the tip of the NW [Fig. 3.1(b)].

In contrast with above observations, the VS mechanism relies on direct crystallization of solid from a vapor or via self-catalytic process. VS process excludes inclusion of foreign atoms, which are ubiquitous in the catalytic VLS growth process. In the VLS process, the dominant morphology typically observed is NWs because the liquid catalyst droplet defines nucleation and growth. In contrast, the VS process often results in more varied morphologies, including NWs, NTs, nanotips, NPs, owing to the lack of constraints imposed by the catalyst. In addition, the growth is highly anisotropic in nature despite being relatively simple while compared to VLS process.

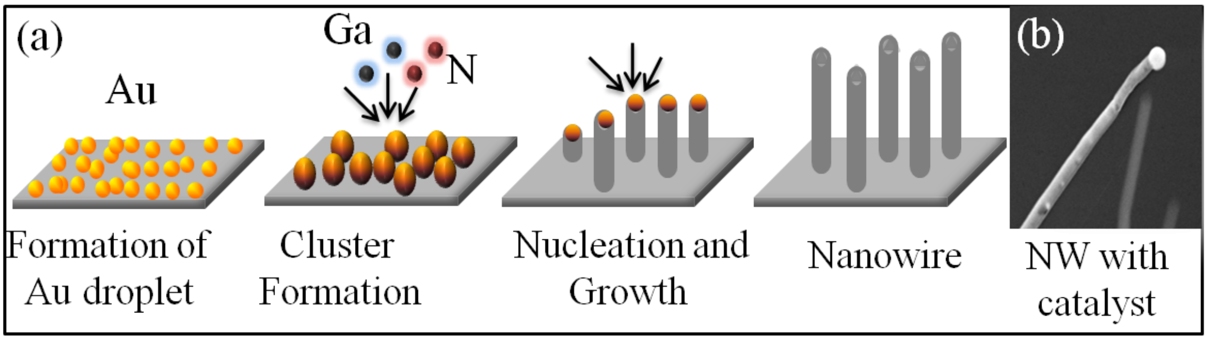

Fig. 3.1 (a) Schematic representation of the growth of GaN NWs via VLS process; (b) a typical FESEM image of an Au terminated NWs.

However, in all these cases a direct reaction of metallic Ga under flowing NH_3 at a temperature above 900 ^{o}C was used for the growth of various GaN nanostructures that follows the reaction:

$$2Ga\,(g) + 2NH_3\,(g) = 2GaN\,(s) + 3H_2\,(g) \qquad (1)$$

From this prospective, VLS process has been widely exploited in demonstrating controlled growth of 1-D nanostructures. However, the underlying mechanistic concepts involved in the VS growth process for large-scale realization of 1-D GaN nanostructures are still in infancy. In fact, reports on VS grown GaN nanostructures with controlled morphology are limited owing to the difficulties encountered in controlling important growth parameters such as Ga and N flux rates and subsequent switching between the fluxes. Understanding the variation of morphology and crystallographic orientation is very important while building devices out of these highly anisotropic GaN nanostructures.

3.2 Surface Polarity in GaN vs Morphology:

Generally, *WZ*-GaN contains polar and nonpolar low-index surfaces. When the number ratio between Ga and N of any cleaved surface is 1:1 (i.e. stoichiometric) then, this surface is termed as non-polar. On the other hand, any surface on which the number ratio is out of 1:1 is termed as polar. In principle, the number of polar surfaces available is infinity.[8]

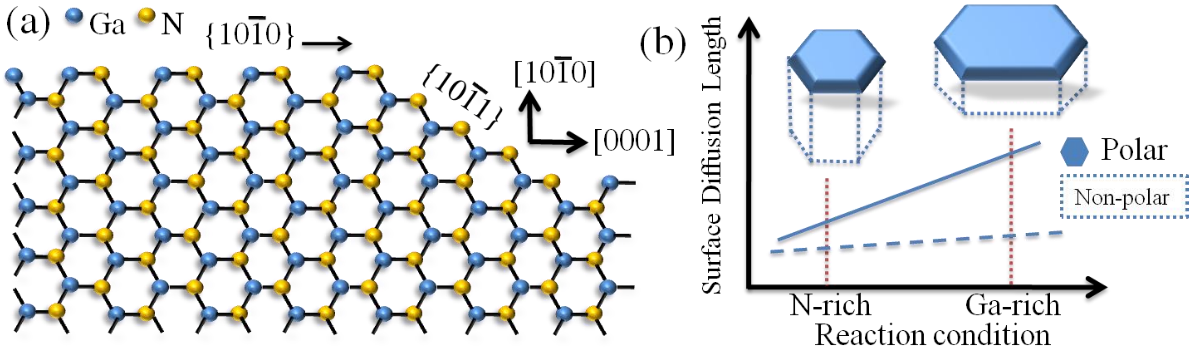

Fig. 3.2 (a) Atomic geometry of cleaved GaN plane constitutes of polar and non-polar surfaces; (b) Schematic diagram showing the dependence of Ga reactant surface diffusion length on the reaction condition.[8] Under the N-rich condition, the surface diffusion lengths of Ga on polar and non-polar surface are relatively same that results in a small length scale of polar surface, while Ga-rich condition favors a large length scale of polar surface.

However, in case of GaN, only energetically favorable polar surfaces are either Ga- or N-terminated low index surfaces. As shown in figure 3.2(a), {0001} (*c*-planes) and {10$\bar{1}$1} (slanted against the *c*-axis) are typical polar surfaces that consists of either Ga or N atoms, whereas, $\{10\bar{1}0\}$ and $\{\bar{1}2\bar{1}0\}$ are non-polar surfaces. The difference in growth rates of these aforementioned structurally distinct surfaces has a significant influence on the resulting nanostructure morphology and growth orientation. Interestingly, Polar surfaces in GaN are always favored to be Ga stabilized (one dangling bond per atom in $\{0001\}$ and three in $\{000\bar{1}\}$) irrespective of the chemical environment (Ga or N-rich), whereas the non-polar surfaces maintain their Ga-N stoichiometry.[8,9]

These Ga-stabilized polar surfaces play a significant role during growth of GaN nanostructures. As a matter of fact, the Ga adatoms/reactants have a significantly lower diffusion barrier on the polar surface [$\approx$ 0.4 eV along the (0001)] because the adsorbate-surface interaction is dominated by very weak delocalized metallic Ga–Ga bonds owing to the lower melting point of Ga (30 °C).[8] Notably, it is observed that, in case of GaN thin films grown in [0001] direction, Ga-rich condition results in a broad and smooth polar surface whereas N-rich condition induces formation of roughness or multiple facets that are composed of polar and nonpolar surfaces.[10] An important consequence is that the effective diffusion length of Ga reactant on the Ga stabilized surface is very sensitive to the chemical environment. If excess N adatoms/reactants are available (N-rich condition), it will frequently interrupt the free surface diffusion of Ga by forming Ga-N covalent bond and reduce the Ga diffusion length. Once the diffusion length becomes shorter than the mean distance between the binding sites, a statistical roughening and formation of facets is expected. Furthermore, in a Ga rich regime, Ga-adatoms are highly mobile and a step flow mode is expected. Consequently, a smoother surface morphology with a lower density of stacking faults is expected.

These reasonings are applied to understand the observed morphological variations in our GaN nanostructures. In this regards, various CVD process parameters like incoming

Ga/N flux rate and incubation time were varied for the optimization of particular GaN nanostructure synthesis such as NW, NT, nanotips and NPs.

3.3 Vapor-Liquid-Solid Growth: GaN Nanowires

3.3.1 Synthesis of GaN Nanowires:

In all the GaN nanostructure synthesis processes used in the present work, Ga was employed source and NH_3 as a reactant gas in a thermal CVD system. In detail, molten Ga (~0.5 mg) is placed on the up-stream of a high pure ceramic crucible, and at the same time, different substrates (for NWs and NTs) coated with 2-10 nm of Au are kept at a distance of 3-8 cm away from the Ga source. The substrates are often placed in both vertical and horizontal directions. The source and the substrates loaded in the ceramic crucible and kept at the centre of the quartz tube within a horizontal tube furnace (detailed in the experimental section). The system is pre-evacuated at a temperature of 300-400 °C down to a base pressure of one mbar [Fig. 3.3(a)]. Then, the temperature of the furnace is gradually increased at a rate of 10-50 °C/min from 400 °C to the reaction temperature of 800-1000 °C, and kept for 10 to 300 min under a constant flow of 10 sccm of NH_3. In all these cases, growth occurs at atmospheric

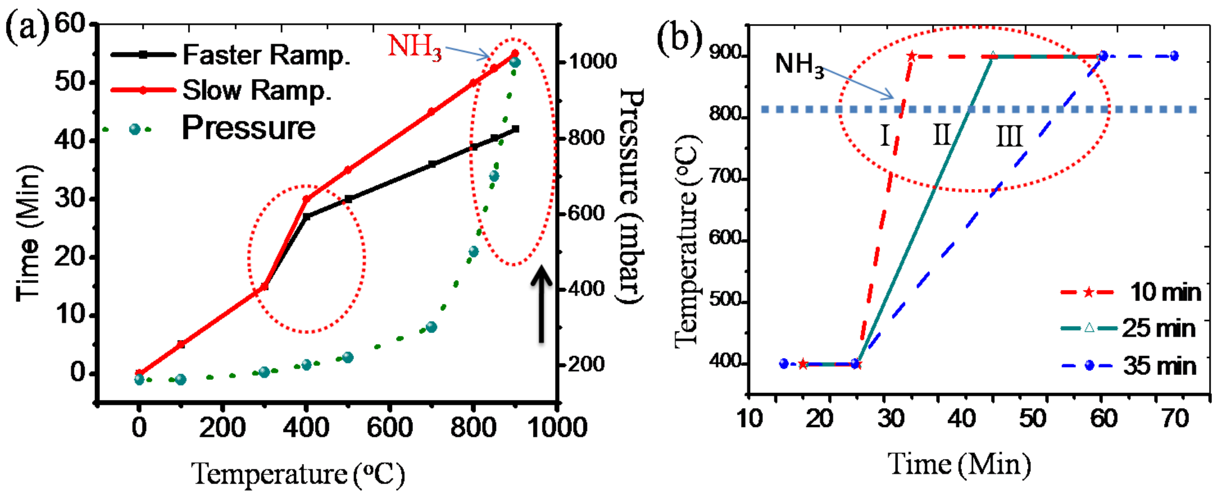

Fig. 3.3 (a) Temperature profile with respect to the growth time and partial pressure inside the chamber; (b) shows the different temperature ramping rate employed for the growth of NWs with varying morphology.

pressure. After the reaction gets over, the furnace is cooled down to room temperature and the resulting nanostructures are collected for further study. Typical temperature profile with respect to the base pressure and growth time in the CVD [Figs. 3.3(a,b)] system employed for growth of GaN NWs with varying morphology. Different NWs morphologies, namely, cylindrical, hexagonal, triangular, and square types could be realized by precisely controlling the ramping rate of temperature [Fig. 3.3(b)] from 400 to 900 ^{o}C and accurate inclusion of NH_3 gas flow. The optimum growth parameters used are as follows;

- ✓ Temperature of Substrate = 900 ^{o}C
- ✓ Base Pressure = 1 mbar
- ✓ Deposition pressure = 1000 mbar
- ✓ NH_3 Flow rate: 10 sccm
- ✓ Distance between substrate and source = 30 mm

3.3.2 Morphological and Structural Variation:

In an effort to optimize the growth morphology for a particular set of NW, several CVD parameters were considered. Apart from the aforementioned optimized CVD parameters, variation of incubation time was carried out, which in turn depended on the ramping rate of temperature between 400 to 900 ^{o}C, as a most decisive parameter. it is found that faster ramping rate [Region I, Fig. 3.3(b)] increases the roughness as well as causes diameter oscillation along the length of the NWs [Figs. 3.4(a-c)], whereas slow ramping rate [Region II and III, Fig. 3.3(b)] gives rise to relatively smooth and controlled NWs [Figs. 3.4(d-f)]. During the faster ramping rate, it is observed that an amorphous layer is formed initially in the base region of the NWs and further growth occurs over this layer irrespective of the growth duration. Figures 3.5(a,b) show a cross sectional view of NWs grown on Si substrate for 180 min and 30 min, respectively. In both of these samples, an amorphous layer of thickness ~ 0.5 to 2 μm is observed. It may be arising due to over supplied of Ga vapor species during the nucleation stage. On the other hand, samples grown with a slow ramping

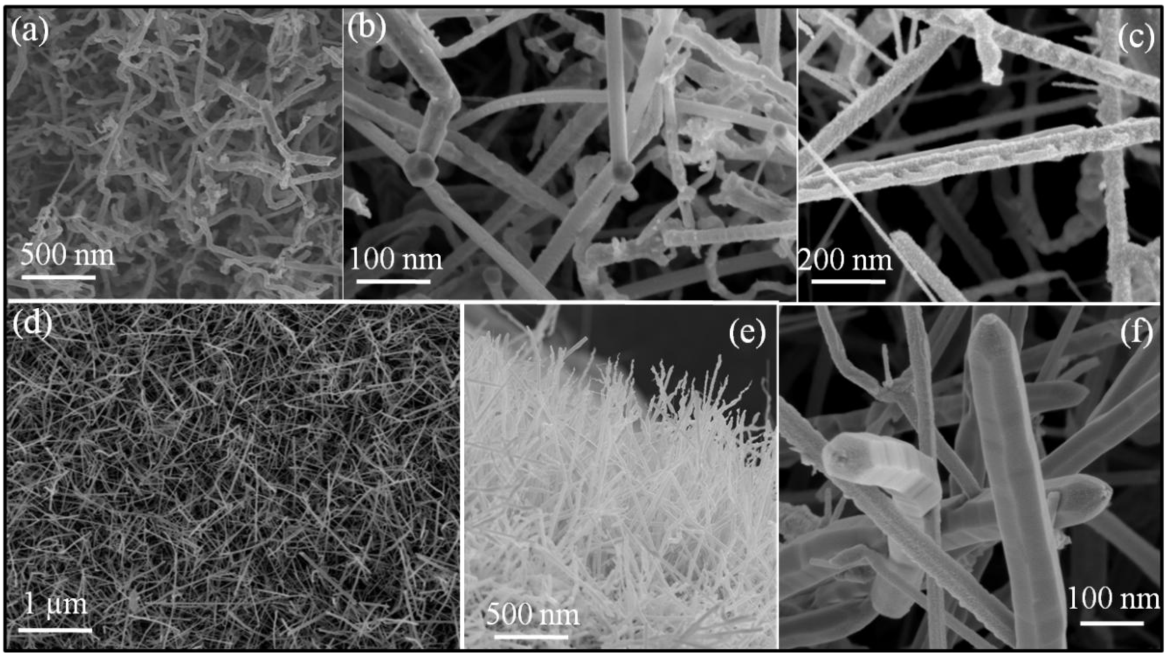

Fig. 3.4 FESEM micrographs of GaN NWs grown in (a-c) faster and (d-f) relatively slow ramping rate of temperature in the CVD system; Faster temperature ramping rate randomizes the growth whereas slow ramping rate gives smooth and well defined geometry of NWs.

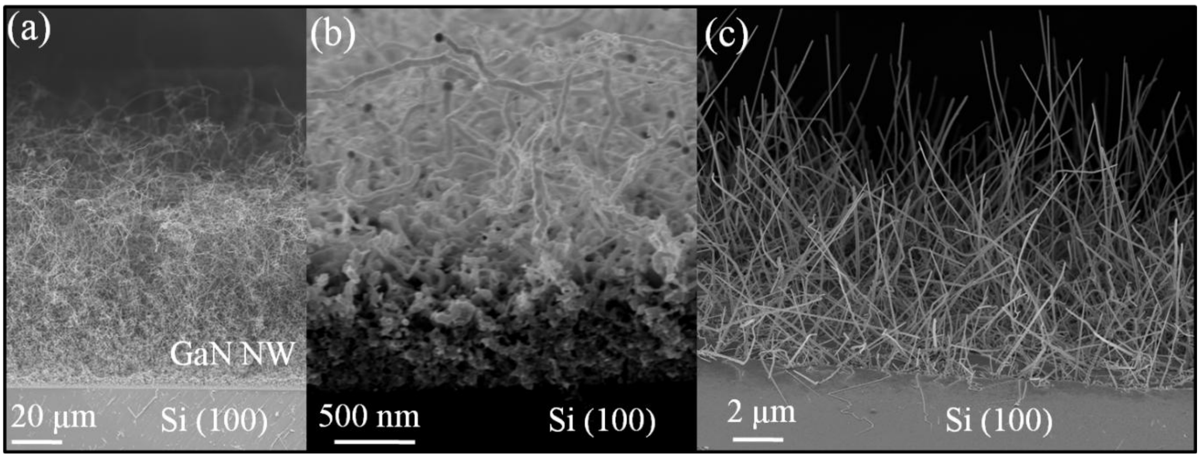

Fig. 3.5 Cross-sectional FESEM images of NWs grown under faster temperature ramping rate for (a) 180 min and (b) 30 min growth condition; (b) slow ramping rate of 30 min.

rate (more than 20 min) possess smooth and well defined geometry [Figs. 3.5(c)]. Notably, these NWs grow presumably over the Si substrate directed by the metal catalyst while maintaining a specific geometry.

Apart from the above optimized conditions used for the growth of well-directed NWs, it is noticed that catalyst particle size also influences the diameter of the resulting NWs.

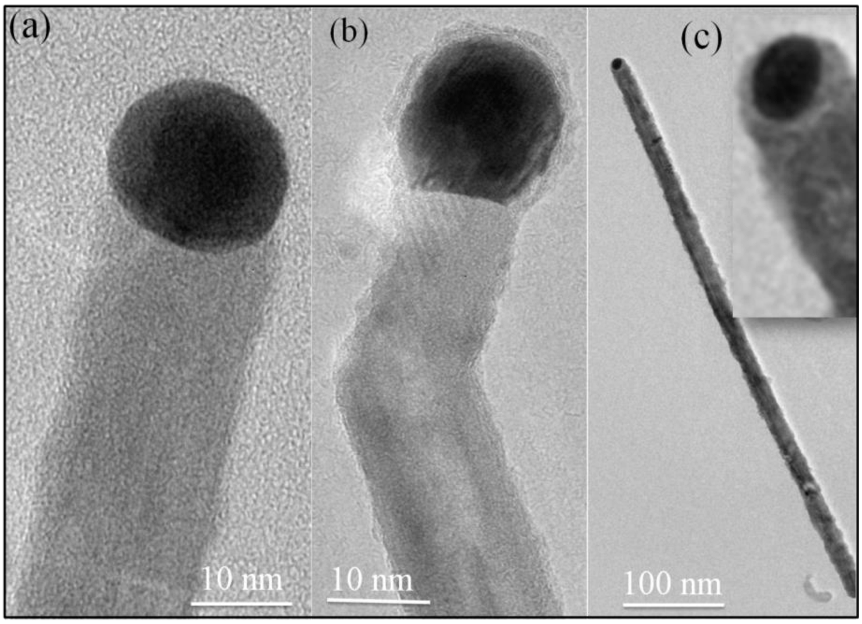

Fig. 3.6 TEM images of GaN NWs with catalyst particle (a) compared with NW diameter, (b) bigger than NW diameter, and (c) for a long NW with small catalyst particle compared to NW diameter.

Bigger catalyst particles compared to the NW diameter induces severe secondary effects such as diameter oscillation and roughness. Figure 3.6(a) shows an optimally sized catalyst particle in order to obtain NW of a regular size and atomically smooth sidewalls. Tapering and diameter modulation are observed when catalyst particle size exceeds the size of NW diameter [Fig. 3.6(b)]. In contrast, the smaller catalyst particles are able to maintain uniform cross-section of the NW over several micrometers in length without tapering [Fig. 3.6(c)]. Together, choosing a small catalyst particle (3 nm Au film) and slower ramping rate (20 to 35 min), it is possible to obtain wide control over NWs growth with particular geometry.

3.3.2.1 Hexagonal GaN Nanowires:

Figure 3.7(a) shows lattice resolved TEM image corresponding to the perfectly hexagonal GaN NW. A smaller catalyst particle of ~10 nm is observed at the tip of the NW as revealed by the FESEM images [as shown in the inset as well as in Fig. 3.4(f)]. The near-perfect lattice fringes with an inter-planar spacing of 2.76 Å, corresponds to $(10\bar{1}0)$ non-polar plane of *WZ*- GaN. The growth of NW is subtended along the c-axis. A relatively

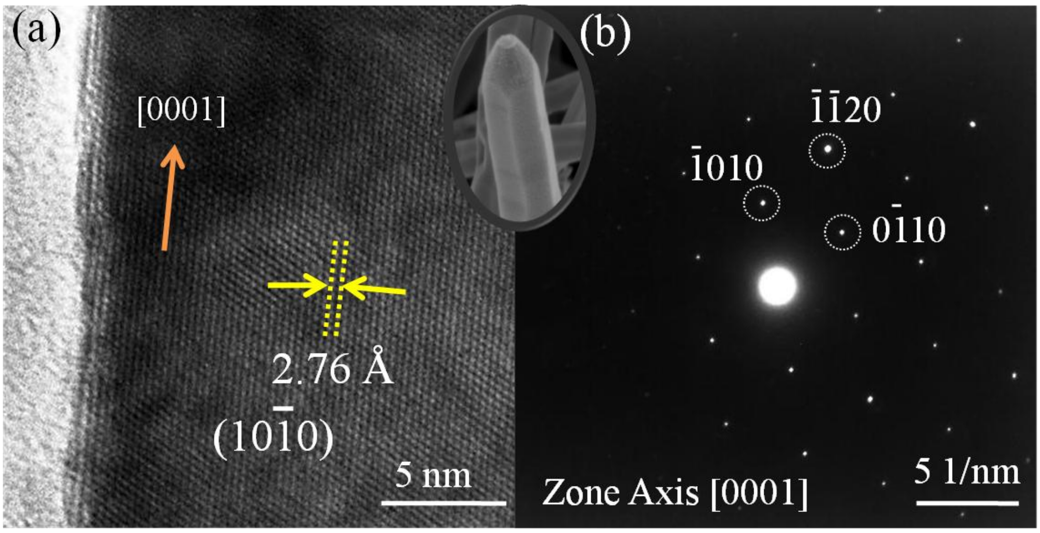

Figure 3.7 (a) HRTEM image of a NW grown along [0001] direction of *WZ*-GaN; inset shows a typical FESEM image of a perfectly hexagonal GaN NWs used for this analysis; (c) SAED pattern of a single GaN NW obtained along the *WZ* [0001] zone axis.

smooth surface termination with very small roughness amplitude extending up to 2-3 atomic layers is observed. The corresponding SAED pattern further demonstrates that the NWs are single crystalline in character, which can be indexed to [0001] zone axis of the *WZ*-GaN. The clear electron diffraction data reveal that the NW is crystalline and ideally possesses neither extended defects like dislocations nor stacking faults.

3.3.2.2 Triangular GaN Nanowires

Figure 3.8(a) shows an HRTEM image of a triangular NW with Au metal catalyst at the tip. These NWs are obtained in 1 h growth condition with temperature ramping rate of 25 min and keeping the substrate in a vertical position that is 30 mm away from the Ga source. While resolving the lattice image during the HRTEM analysis, only one face could be seen at a time and other inclined face becomes more obscure. This confirms that the NWs are of triangular type [Fig. 3.8(a)]. One of the exposed faces is composed of (0001) plane and the NW is subtended along [1$\bar{1}$00] direction. The NW grown in this direction are enclosed with$(11\bar{2}0)$, $(\bar{1}\bar{1}20)$ and (0001) side planes. Figure 3.8(b) is the fast Fourier transformed (FFT) image corresponding to the dotted square region from the figure 3.8(a). It reveals that

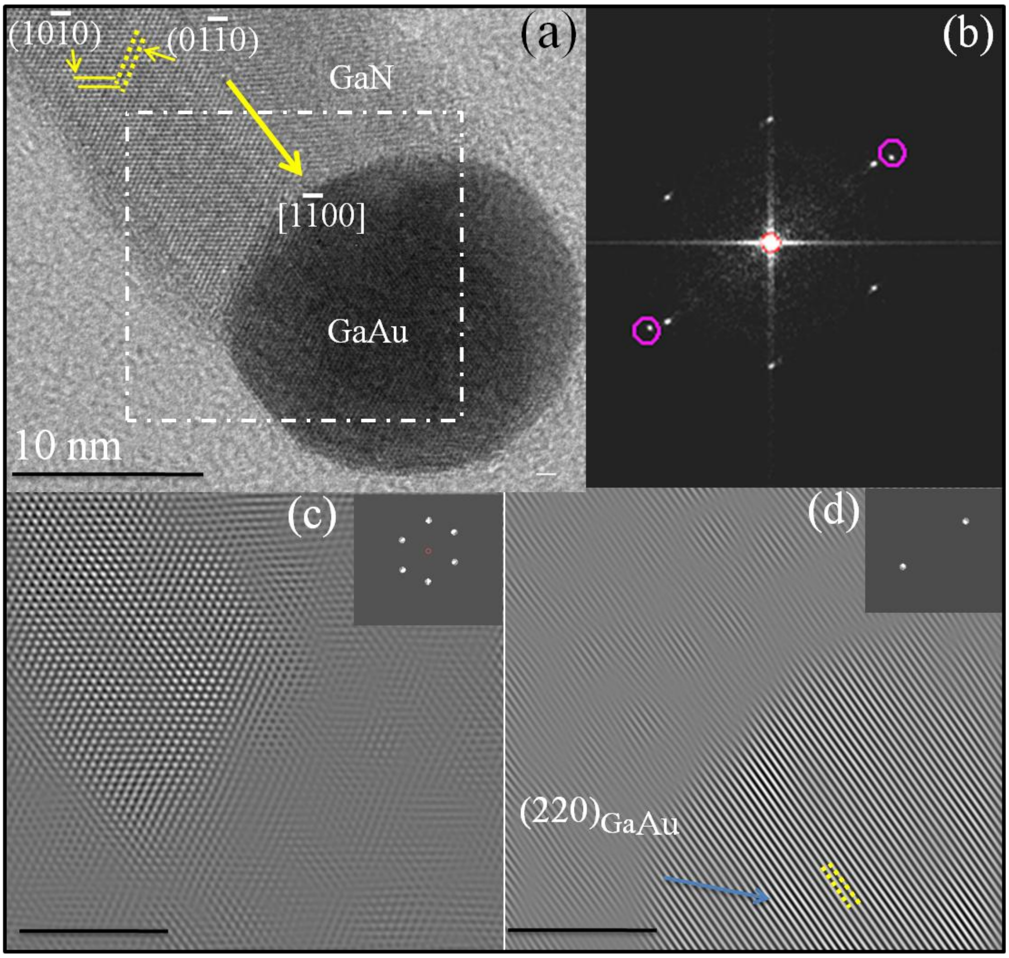

Figure 3.8 (a) HRTEM image of a triangular GaN NW with metal catalyst at the tip; (b) FFT corresponding to the square region of (a); inverse FT image belongs to (c) *WZ*-GaN Phase and (d) cubic Au phase as shown in the inset, respectively. The Scale bar in (c) and (d) is 5 nm.

the tip region is composed of two distinct phases which are mostly belongs to *WZ*-GaN with zone axes along [0001] and the encircled region corresponds to cubic Au phase. The inverse Fourier transformed (IFT) image reveals that well crystalline *WZ*-GaN phase is formed only beneath the Au droplet [Fig. 3.8(c) and inset], whereas the tip region is mostly dominated by cubic Au phase [Fig. 3.8(d) and inset]. The lattice spacing belonging to the catalyst droplet at the tip can be indexed to (200) plane of cubic Au. This infers that only Ga precipitates on the Au droplet and subsequent nitridation occurs around the neck region forming GaN phase because N_2 has poor solubility in Au. This result is consistent with the reported arguments made by many research groups towards elucidation of the underlying VLS mechanism of NW growth process.[7]

3.3.2.3 Wurtzite/Zinc-blende Biphase Homostructure in Triangular GaN Nanowires:

A unique *WZ* and zinc-blende homostructure of GaN was formed in a typical case of triangular NW. The HRTEM image of a triangular NW with alternating strips parallel to the NW longitudinal direction is shown in the figure 3.9 (a) and in the inset. It indicates a sharp transition of ~1-3 atomic layers between phases. An interplanar spacing of 2.68 Å is

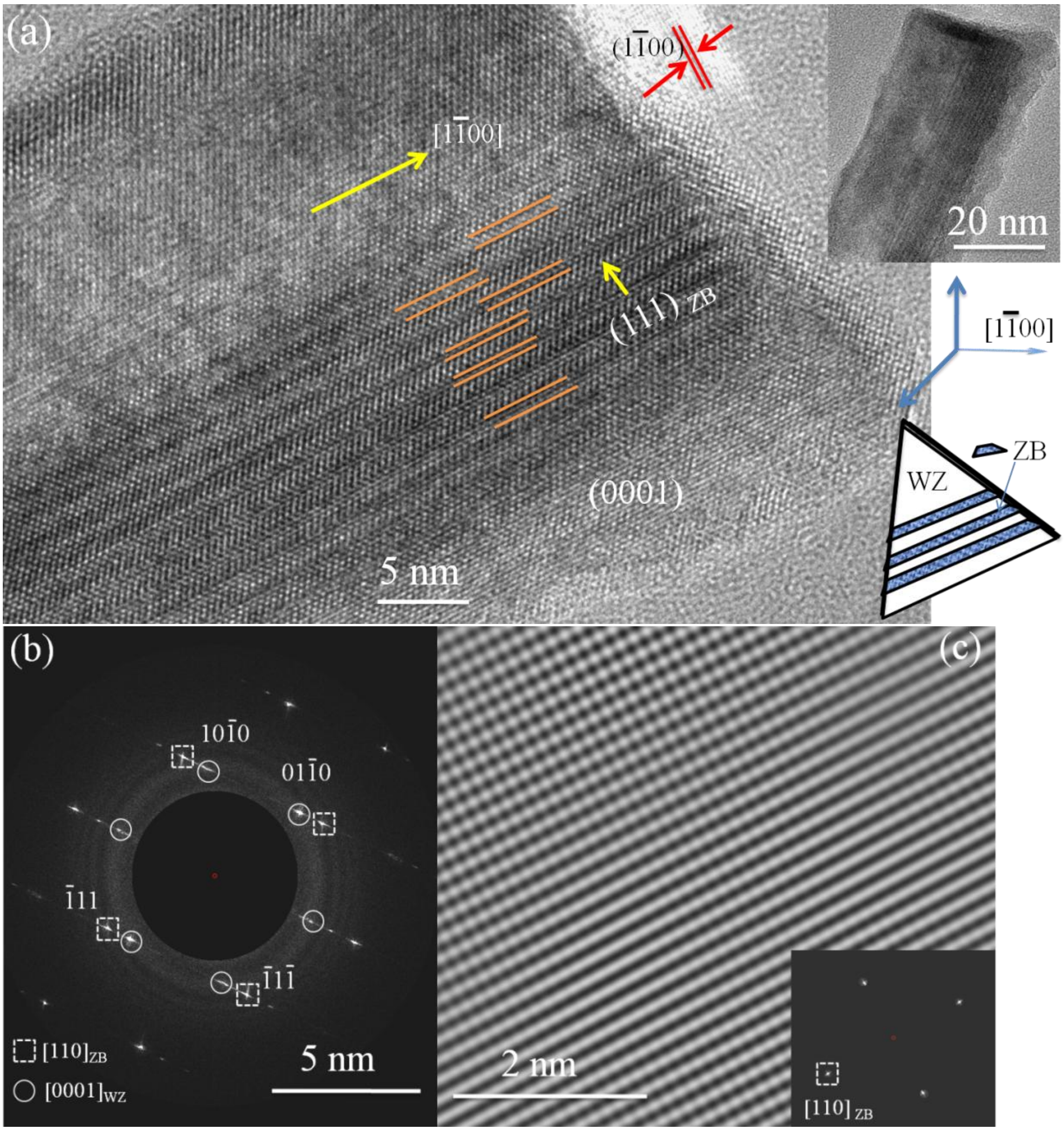

Fig. 3.9 (a) HRTEM image of a biphase GaN NW; inset shows the TEM image of a triangular shaped NW (upper right), and (bottom right) showing a schematic representation along with the growth direction of the NW; (b) SAED pattern from the biphase region showing the presence of *WZ* and zinc-blende (noted as ZB) phase of GaN; (d) IFT lattice imaging corresponding to the zinc-blende phase of GaN.

measured from the base region, which has been assigned to the d-spacing of $(10\bar{1}0)$ planes of *WZ*-GaN. The observed value is less than that of the bulk lattice spacing (2.76 Å). However, this is assigned as c-plane keeping in mind that these planes are inclined to the electron beam position during TEM measurements and hence a reduction of the bulk value is expected.

SAED patterns are used to substantiate the presence of biphasic structure inside the NW, as shown in figure 3.9(b). The diffraction pattern is composed of both WZ ([0001] zone axes) and zinc-blende ([110] zone axes) phase of GaN. It was further confirmed with FFT and IFT in the same area where SAED is taken. The IFT lattice images corresponding to the zinc-blende phase is shown in figure 3.9(c). By indexing appropriate diffraction spots it is concluded that the growth direction of the NW is in the $[1\bar{1}00]$ direction of the *WZ* phase, and in the [110] of zinc-blende phase. On the other hand it is found that triangular NW is grown along the $[1\bar{2}10]$ direction [Fig. 3.10(a)] exhibiting a large number of stacking faults [Figs. 3.10(a,b)] on the basal plane similar to that reported in the literature.[11] The formation of such structure may arise as a result of any small fluctuation in growth parameters or from strain accumulation and relaxation during growth process.[11,12]

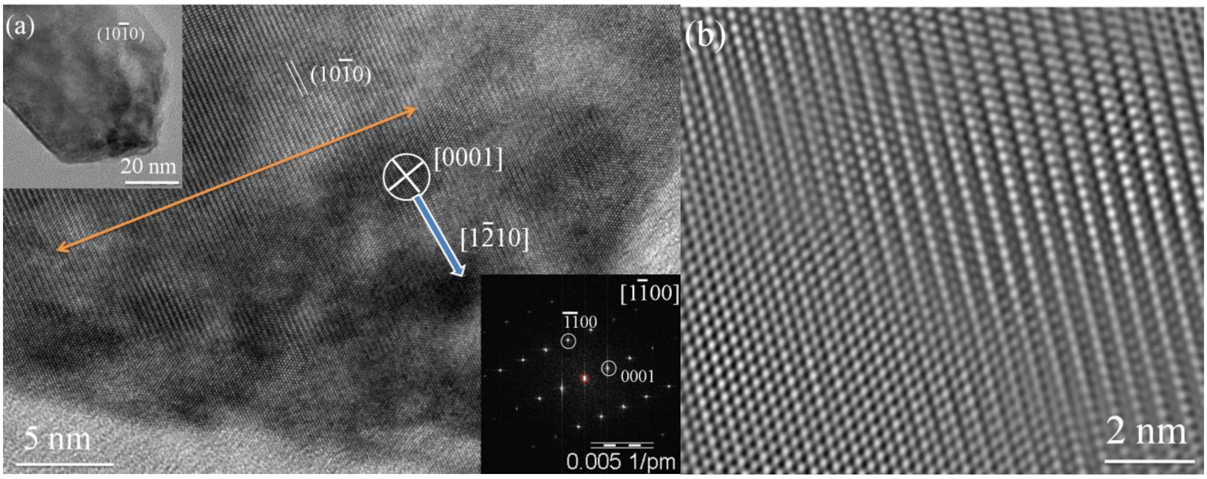

Fig. 3.10 (a) HRTEM image of a triangular NW grown along $[1\bar{2}10]$ direction of *WZ*-GaN phase; Inset showing the SAED pattern index to $[1\bar{1}00]$ zone axis; (b) a typical IFT lattice image of transition region which clearly showing the presence of stacking faults on the surface.

3.3.2.4 Square Shaped GaN Nanowires:

Figure 3.11(a) shows a HRTEM image of a square shaped NW with perfect lattice fringes. The corresponding FESEM image [Fig. 3.11(b)] clearly illustrates the presence of distinct edges of these NWs which are grown over 1 h duration with 35 min of temperature ramping rate where the substrate was kept in a vertical position 30 mm away from the Ga source. The observed bright patches over the NW surface emerge from Au nanoparticles deposited for the purpose of SEM analysis. Fig. 3.11(c) shows the SAED pattern corresponding to the figure 3.11(a), which can be indexed to [0001] zone axis of *WZ*-GaN. By indexing this diffraction pattern, it is found that these square shaped NWs are grown along $[11\bar{2}0]$ direction and these are enclosed with $\{0001\}$ and $\{1\bar{1}00\}$ side faces. These

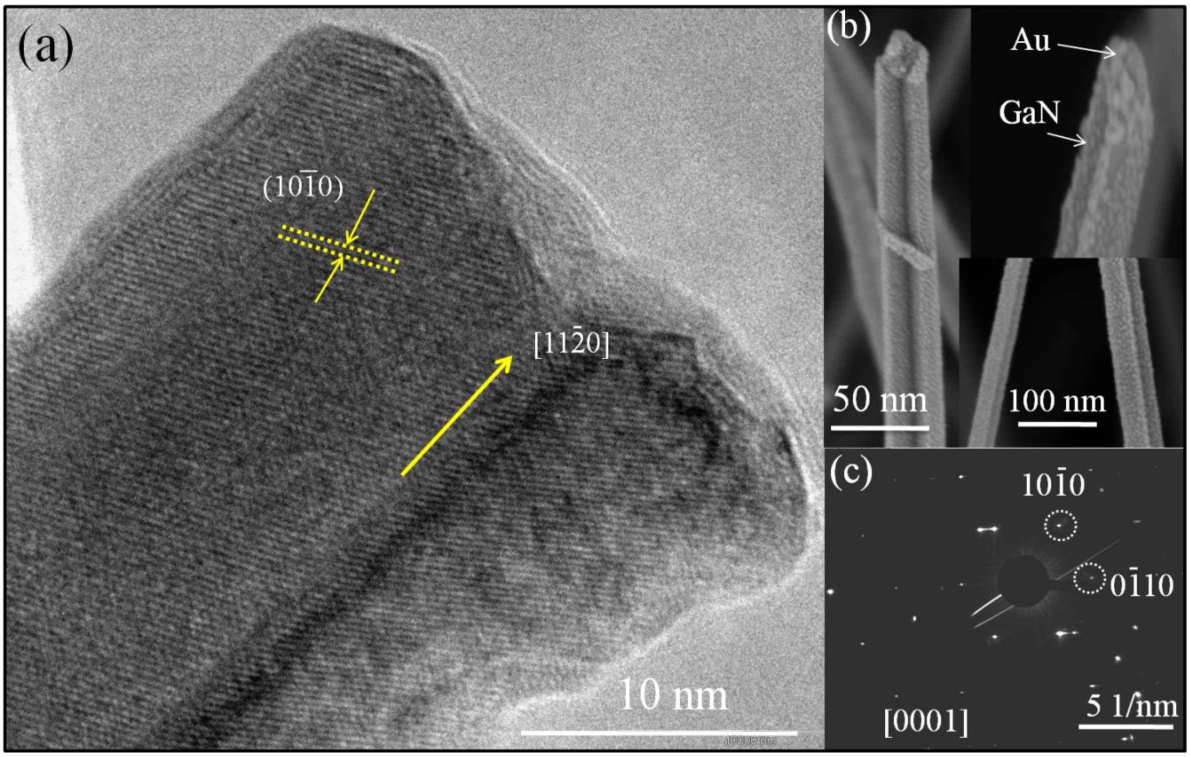

Fig 3.11 (a) HRTEM image of a square shaped GaN NW grown along $[11\bar{2}0]$ direction and enclosed with $\{0001\}$ and $\{1\bar{1}00\}$ side faces; (b) Typical cross-sectional FESEM images of the vertically aligned square shaped GaN NW, Inset-images are from different set of sample with Au nanoparticle at the tip; (c) SAED pattern of a NW, corresponding to the HRTEM image, indexed to [0001] zone axis of *WZ*-GaN phase.

NWs grow on the Si(100) substrate via VLS method and vertically aligned with aspect ratio reaching around ~350 [Fig. 3.5(c)]. In addition, stacking faults or dislocation lines are also not observed in this growth condition used for square shaped NWs. Such materials are ideal candidates for NW based optoelectronics.

3.3.3 Steady State Growth of Nanowires:

It is believed that the catalyst mediated VLS mechanism is very stable with the alloy droplets which generally do not get consumed even when the reaction conditions change. However, recent experiments differ, which suggest that even under cleanest growth conditions, VLS mechanism may not produce long, thin, uniform, single-crystal NWs of high purity (Fig. 3.12). The electrical, hydrodynamic, thermodynamic, and surface tension related properties have strong influence on NW growth. Furthermore, parameters accruing from mesoscopic effects like nanoparticle seeds, charge distribution in catalyst droplets, electronegativity difference between catalyst droplet and reactive NW vapor species, growth

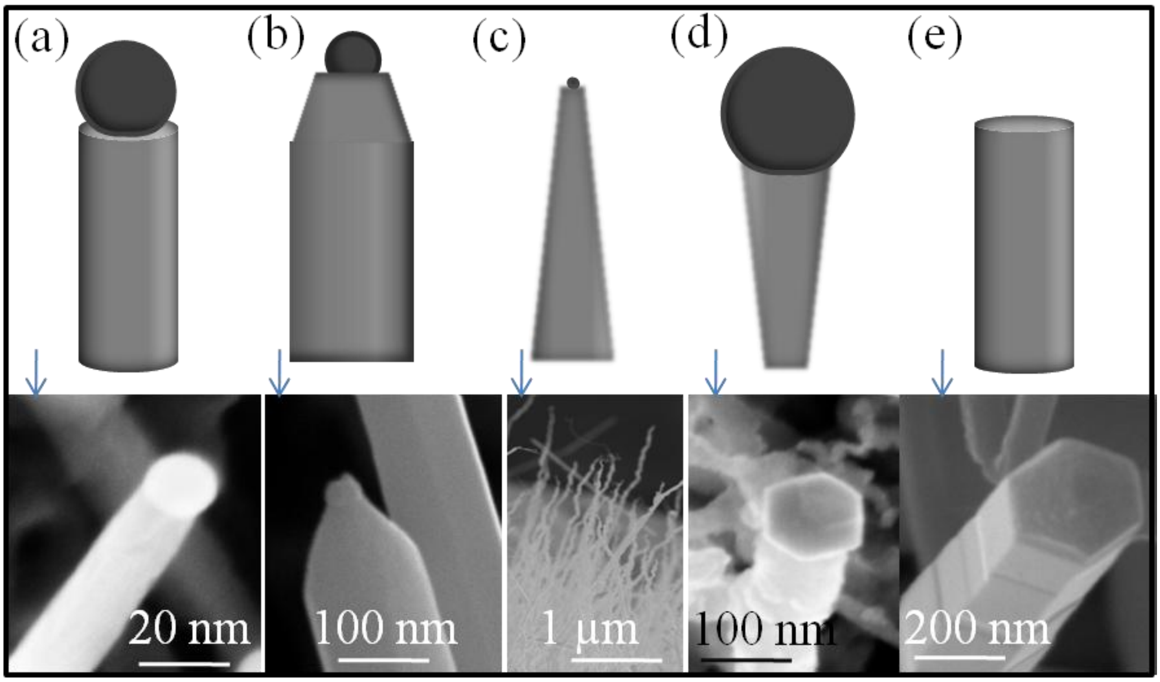

Figs. 3.12 (a-e) Schematic representation and the corresponding observed NWs (indicated by arrow) grown by VLS mechanism with metal catalyst at the tip.

temperature, and chamber pressure also play an important role in VLS based growth processes. Indepth analysis on various issues illustrate that the VLS process may generate NWs of various shapes and sizes with slight fluctuations in any intriguing parameters (Fig. 3.12). Most of the NWs exhibit metal droplets at the tip region in varying sizes that dictates the resulting morphology as well. The different shapes and morphologies of NWs observed include; 1) cylindrical [NW of uniform diameter with catalyst droplet of equal size; Fig. 3.12(a)], 2) conical at the tip [uniform morphology up to a certain extent but narrow down around the tip region with catalyst droplets of smaller size; Fig. 3.12(b)], 3) needle shape [the NW is gradually thinned as it grows, and is pointed at the droplet edge; Fig. 3.12(c)], 4) tapered NWs [the catalyst droplet is much bigger than the NW diameter; Fig 3.12(d)] and 5) diameter modulated NWs [Fig. 3.12(e)]. Keeping all this in mind, it is found that the variation in NW morphologies with growth condition is in close agreement with the simple steady state model propounded by Kuo et al.[7] It explains that the NW with a smaller catalyst droplet is ideal for obtaining regulatory growth than an NW with a larger size catalyst droplet. It is assumed that Ga is activated through the catalyst and the reaction takes place only at the AuGa/GaN interface, and, NH$_3$ does not dissolve into the catalyst, as shown in figure 3.13.

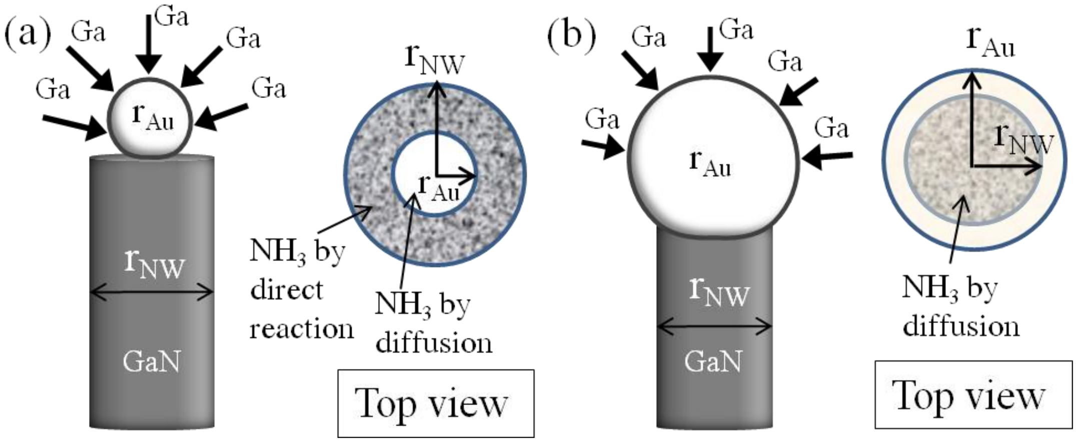

Fig. 3.13 Schematic representation showing steady state growth of NWs with (a) a smaller catalyst droplet and (b) a larger catalyst droplet; Assuming that Ga is activated through the catalyst and the reaction takes place only at the AuGa/GaN interface.

When the radius of catalyst particle (r_{Au}) is smaller than the radius of the NW (r_{NW}), as illustrated in figure 3.13(a), the conditions;[7]

$$R_{in} = \alpha . r_{Au}^2 \qquad 3.1$$

$$R_{GaN} = \beta . r_{NW}^2 \qquad 3.2$$

where R_{in} and R_{GaN} are incoming flux rates for Ga and formation rate of GaN, respectively; α and β are rate constants, would be applicable. Under these conditions, the growth of NW always converges to a certain critical radius meaning thereby that it does not depend much on the mean fluctuation of R_{in} [Figs 3.13(a) and Figs. 3.4(d-e)]. Whereas for $r_{\text{NW}} < r_{\text{Au}}$, as shown in figure 3.13(b), the growth rate of GaN becomes[7]

$$R_{GaN} = \delta . r_{NW} \qquad 3.3$$

where δ is rate constant. The diffusion of N takes place only in the circumferential region between Au and GaN. Here, the growth of the NW is likely to become unstable beyond a critical point. This situation often leads to occurrence of diameter oscillation and tapering in NWs [Fig. 3.13(d) and Figs. 3.4(a-c)].

This study finds that increase in diameter of the droplet with a time of tapered NWs results primarily from the gradual incorporation of oversupplied NW species into the catalyst mediated droplet. It also finds that optimum compositions of the droplet constituents are crucial for VLS NW growth. In general, smaller the size of the catalyst particle lower is the probability of formation of disorder and defects in the resulting NWs grown through VLS process.

3.3.4 Optical Properties:

The detailed studies of optical phonons and types of native defects present in the as-grown GaN samples are essential for their further uses as light emitters and detectors. In this regard, optoelectronic properties of NWs are studied using Raman and Photoluminescence spectroscopy.

3.3.4.1 Raman Scattering Study:

The phonon dispersion of hexagonal *WZ*-GaN has a close relation to that of zinc-blende GaN (cubic) phase. In the hexagonal structure, the primitive cell contains four atoms (two Ga-N pairs) while it contains only two atoms in the cubic phase (one Ga-N pair). Therefore, the number of phonon branches in the *WZ* structure is doubled than that of zinc-blende phase. Furthermore, as shown schematically in figure 3.14, the phonon dispersion along $\Gamma \rightarrow$ A [0001] direction in the *WZ* structure can be constructed by simply folding the phonon dispersion of the cubic structure along Γ → L [111] direction in half with respect to the *A* point.[14] Brillouin zone of the zinc-blende extends twice longer than that of *WZ* owing to

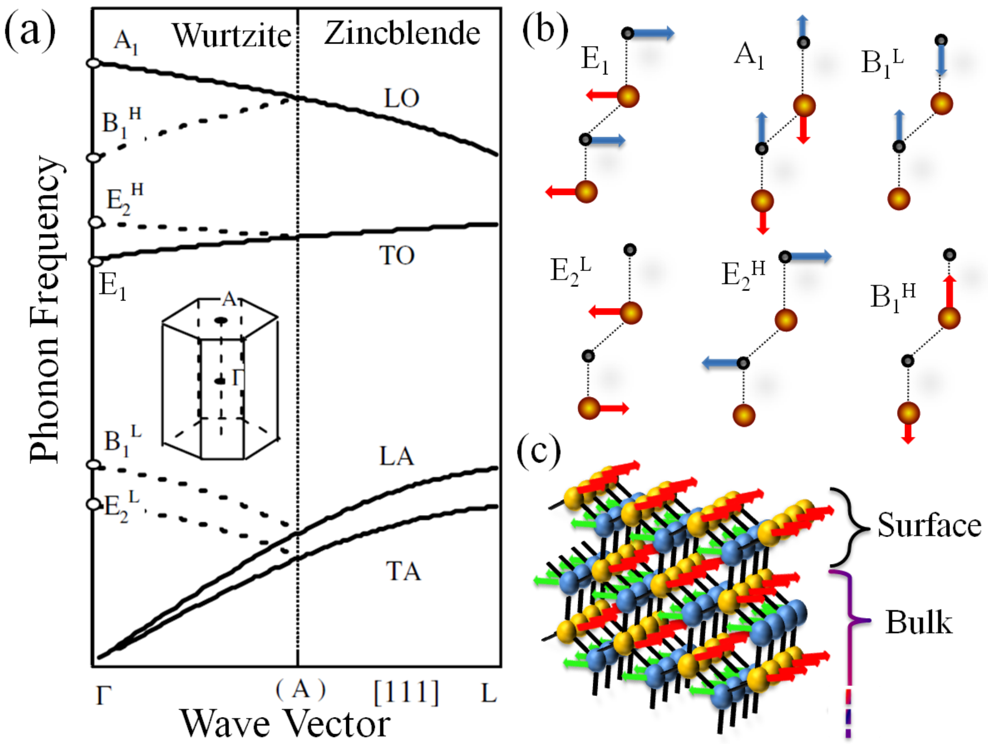

Fig. 3.14 (a) Schematic representation of the phonon dispersion in wurtzite and zinc-blende structure [with permission, Ref. 14]; Phonon branches along [111] in the zinc-blende structure is folded to approximate those of wurtzite structure along [0001] (b) Optical phonon modes in the wurtzite structures; (c) Schematic representation of surface phonon and bulk phonons.

the difference in the length of unit cells along the direction. In addition, in *WZ* structure, some phonon branches are split due to the electrostatic field created by the polar character of the phonons. From the group theory analysis, *WZ* structure has eight sets of phonon normal modes at the Γ point, $2A_1 + 2E_1 + 2B_1 + 2E_2$. These modes are classified into Raman ($2A_1 + 2E_1 + 2E_2$), silent ($2B_1$), and infrared active ($A_1 + E_1$). Although the GaN is noncentrosymmetric, the A_1 and E_1 modes are further split into LO (longitudinal optical) and TO (transverse optical) components. The atomic displacement schemes of these optical modes are depicted in figures 3.14(b,c).

The typical Raman spectrum of GaN NWs samples using Ar$^+$ ion (514.5 nm) laser excitation source is shown figure 3.15. The peaks at 533, 560, 569, 725 cm^{-1} agree with the phonon vibration frequencies of A_1(TO), E_1(TO), E_2 (high), A_1(LO), respectively, of the crystalline *WZ*-GaN.[2] The frequencies and assignments of the phonon modes corresponding to figure 3.15 are listed in Table 3.1. Within the experimental error, our results are agreed well with those of reported value for GaN bulk.[14,15] In polar semiconductor NWs, peaks in the Raman spectra are usually identified with the TO and LO phonon modes at zero wave vector ($q = 0$), because the wavelengths of light used as an excitation source were a small

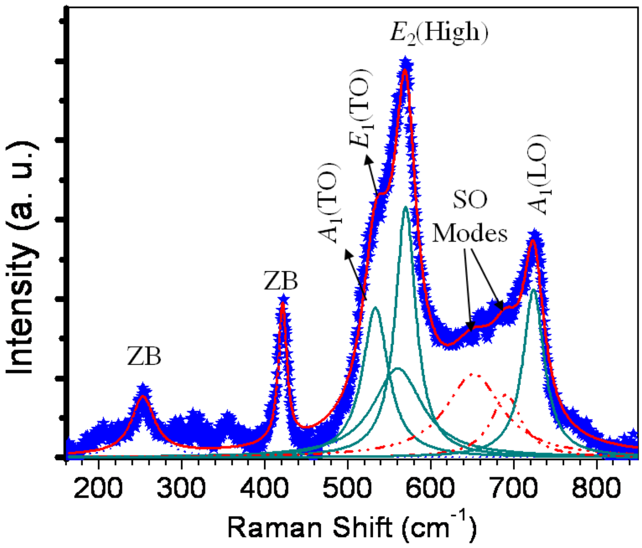

Fig. 3.15 Room-temperature Raman-scattering spectrum of GaN NWs showing the experimentally observed data and the Lorentzian fits for the individual peaks.

fraction of the Brillouin zone. The frequencies of these peaks are similar to that reported for the bulk. However, the long-range nature of the electromagnetic fields associated with the phonons has also derived from the “shape effect” for polar semiconducting NWs. The result of shape effect can induce new optic modes whose frequency may differ by 2-10 cm^{-1} from that of the q = 0 optic mode.[2] Influence on the intensity of LO mode in the presence of surface plasmon resonance of Au nanocluster is insignificant because the amount of Au in the catalyst droplet at the tip of the NW is very small.

Table 3.1 Raman modes in the bulk and various GaN nanostructures reported in this study at 300 K, and the corresponding phonon lifetime (for NWs) and symmetry assignments; ZB refer to the zone-boundary phonon. The Raman spectra of GaN nanotip, nanoparticles, and nanotubes are discussed subsequently.

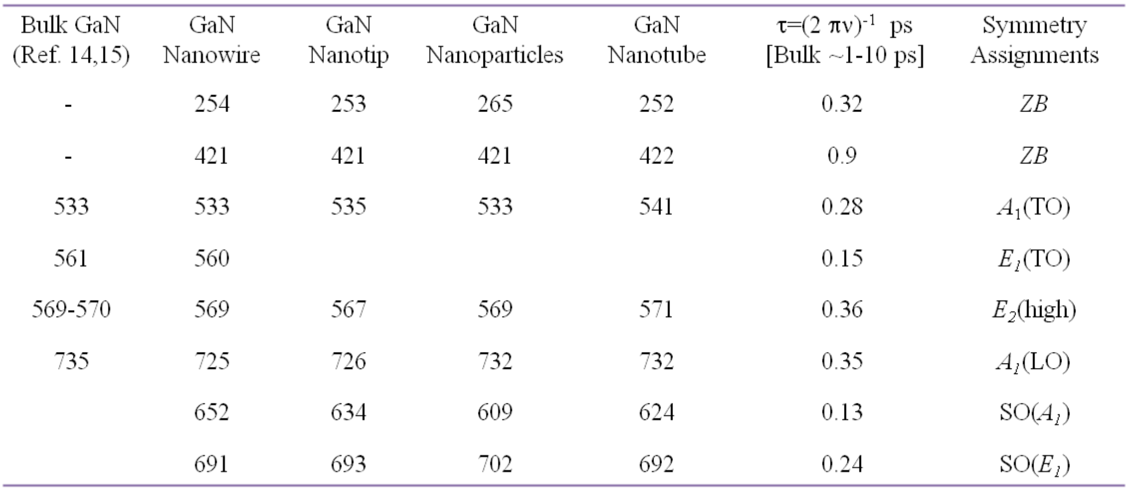

Bulk GaN (Ref. 14,15)	GaN Nanowire	GaN Nanotip	GaN Nanoparticles	GaN Nanotube	$\tau=(2\pi\nu)^{-1}$ ps [Bulk ~1-10 ps]	Symmetry Assignments
-	254	253	265	252	0.32	ZB
-	421	421	421	422	0.9	ZB
533	533	535	533	541	0.28	A_1(TO)
561	560				0.15	E_1(TO)
569-570	569	567	569	571	0.36	E_2(high)
735	725	726	732	732	0.35	A_1(LO)
	652	634	609	624	0.13	SO(A_1)
	691	693	702	692	0.24	SO(E_1)

The observed phonon peaks for the GaN NWs broaden substantially. The line width (FWHM) of these phonon peaks can be correlated with the phonon lifetime as $(2\pi\tau)^{-1}$. The FWHM increases roughly by a factor of 2 to 5, as compared to that for the bulk. The lifetime of optical phonons in these NWs is calculated and found to be a fraction of picoseconds (Table 3.1). This shorter lifetime in NWs than that of the bulk (1-10 ps) is due to the increased anharmonic interaction of the optical phonons in the former, resulting the possibility of the decay into acoustic branches.[2]

Four additional modes are also observed at ~ 254, 421, and 652, and 691 cm^{-1}, all of which are not allowed by the C_{4v}^{6} space group in first-order Raman scattering at the zone center. Possible mechanisms that could bring about these features are discussed as follows. In the reduced dimension for nanostructured materials, the relaxation of the q=0 selection rule due to the effect of finite crystallite size not only broadens the Raman-allowed modes, but also causes new modes to appear that correspond to $q \neq 0$ phonons. Two extra peaks seen at ~254 and 421 cm^{-1} in GaN NWs could possibly be attributed to the zone boundary (ZB) phonons.[16] It is worth mentioning that the 254 and 421 cm^{-1} features are consistently observed for all types of GaN NWs samples. Raman bands around 652 and 691 cm^{-1} may be identified with SO modes, as the larger surface-to-volume ratio along with surface corrugation and roughness inducing instability in surface potential (SP) along the diameter of the NW. The instability in SP may activate the SO phonon in the Raman scattering. This phenomenon were also reported extensively for II-VI, and other group III-nitrides.[17] In all these cases the broken translational symmetry of surface wave vector, induced by the surface disorder, cause the surface to absorb the phonon momentum in units of q=2π/λ, where λ is the length of the surface modulation. In case of a perfect surface, the SO modes cannot be observed optically due to momentum conservation constraints. However, optical detection of the surface modes is possible only if a source of wave vector is supplied through strong Fourier components of the surface potential.[17,2]

In order to understand the SO band quantitatively in our NWs, theoretical calculation was performed considering the cylindrical geometry of GaN NWs. The dispersion relation $\omega_{SO}(q)$ for an infinite long cylindrical wire, in the limit where the phonon wave vector $q >> \omega/c$, can be written as[18]

$$\omega^2{}_{so} = \omega^2{}_{TO} \frac{\varepsilon_0 - \rho_{nx}\varepsilon_m}{\varepsilon_\infty - \rho_{nx}\varepsilon_m} \tag{3.4}$$

where ω_{TO} is the frequency of the TO phonon, ε_0 and ε_∞ are the static and high frequency dielectric constant of the material, and ε_m is the dielectric constant of the medium. ρ_{nx} is given by

$$\rho_{nx} = \frac{K_1(x)I_0(x)}{I_1(x)K_0(x)} \tag{3.5}$$

Where I_j, and K_j are the modified Bessel functions and $x=qr$ (r being radius of the nanostructure). From the Lyddane-Sache-Teller relation, $\omega^2_{LO}/\ \omega^2_{TO}=\varepsilon_0/\varepsilon_\infty$, the LO-TO splitting of E_1 mode gives a static dielectric constant of ε_0=10.2 using ε_∞=5.8.[18] The SO phonons associated with A_1(TO) at 533 cm^{-1} and E_1(TO) at 560 cm^{-1} are calculated for GaN by taking the qr value of 1.07, which yields SO phonon frequencies (ω_{so}) pertaining to A_1 (654 cm^{-1}) and E_1 (688 cm^{-1}) characters [Fig. 3.15]. Hence, the observed peaks around 652 and 691 cm^{-1} may be assigned to SO modes in GaN.

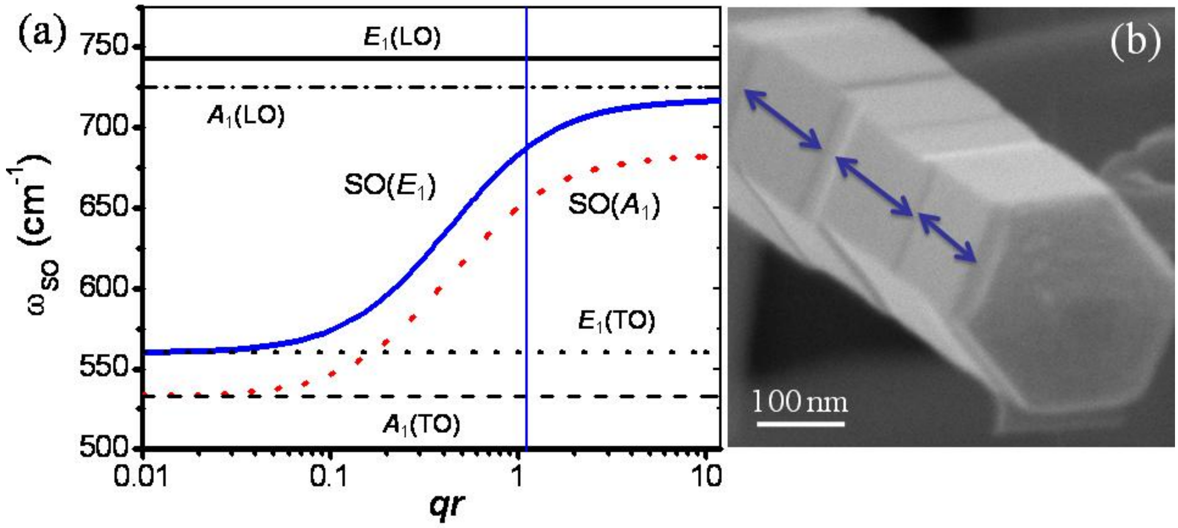

Fig. 3.16 (a) Calculated SO phonon frequencies as a function of qr, full curve: SO(E_1), dashed curve: SO(A_1), horizontal lines are the LO and TO frequencies of E_1 and A_1 modes, Vertical dotted line is marked for qr=1.07; (b) Morphological study at high resolution for the GaN nanowire with arrows showing the modulation of the surface in the range of 150-300 nm.

The magnitude of surface roughness determines the SO peak intensity owing to the breakdown of the translational symmetry of the SP. The wavelength $\lambda = 2\pi/q$ (qr=1.07; r

~250) corresponding to the perturbation of surface potential can be estimated as ~ 1500 nm for the GaN nanostructures (using the dispersion relations in Fig. 3.16(a) and for typical nanostructure of diameter of ~300 nm). Surface roughness with a modulation of ~150-300 nm is observed [indicated by the arrows in Fig. 3.16(b)] with any integral multiple equivalent to the λ (10x150 nm=5x300 nm=1500 nm) will be sufficient to initiate the breakdown of translational symmetry for the contribution of SP toward SO modes. This makes the intensity of the surface mode comparable to that of the other phonons. This surface modulation or self-oscillating nature of the NW cross section, stemming via VLS mechanism, is related to growth conditions such as temperature, impurities, and supersaturation. Moreover, the appearance of SO modes in the phonon spectra should be a general indicator of the presence of a corrugated surface along the wire cross section.

3.3.4.2 Photoluminescence Study:

Typical Low temperature micro-PL spectra of NWs grown under optimized condition (grown for 1 h) show strong emission in the region of photon energy 3.1 - 3.5 eV [Fig. 3.17(a)]. The PL emission line at 80 K is dominated by a strong peak at 3.394 eV which has been assigned to the near band-edge-emission (NBE) line of *WZ*-GaN.[3,19,20] As the temperature increases, its intensity gradually decreases, due to the thermal dissociation of carriers. It is interesting to note that the NBE is the only dominating emission process in the as-grown NWs even at 300 K. The NBE is blue shifted by 20 meV while decreasing the temperature from 300 to 80 K. In addition, the intensity of NBE at 80 K is increased by ~ 95% to that observed at 300 K. It is observed that as temperature decrease from 300 to 80 K, an additional shoulder appears at 3.43 eV and on the lower-lying side of NBE. The peak at 3.43 eV corresponds to the recombination of exciton bound to neutral donors (I_2).[20] The additional peaks observed at 3.31, 3.28 eV and 3.19 eV have been assigned to zero phonon line and their phonon replica of the free-to-bound (FB) emission, respectively.[20] The broad full-width-half-maximum (FWHM) of the PL spectra probably reflects to the wide size distribution of GaN NWs as well as to the small crystallite sizes.

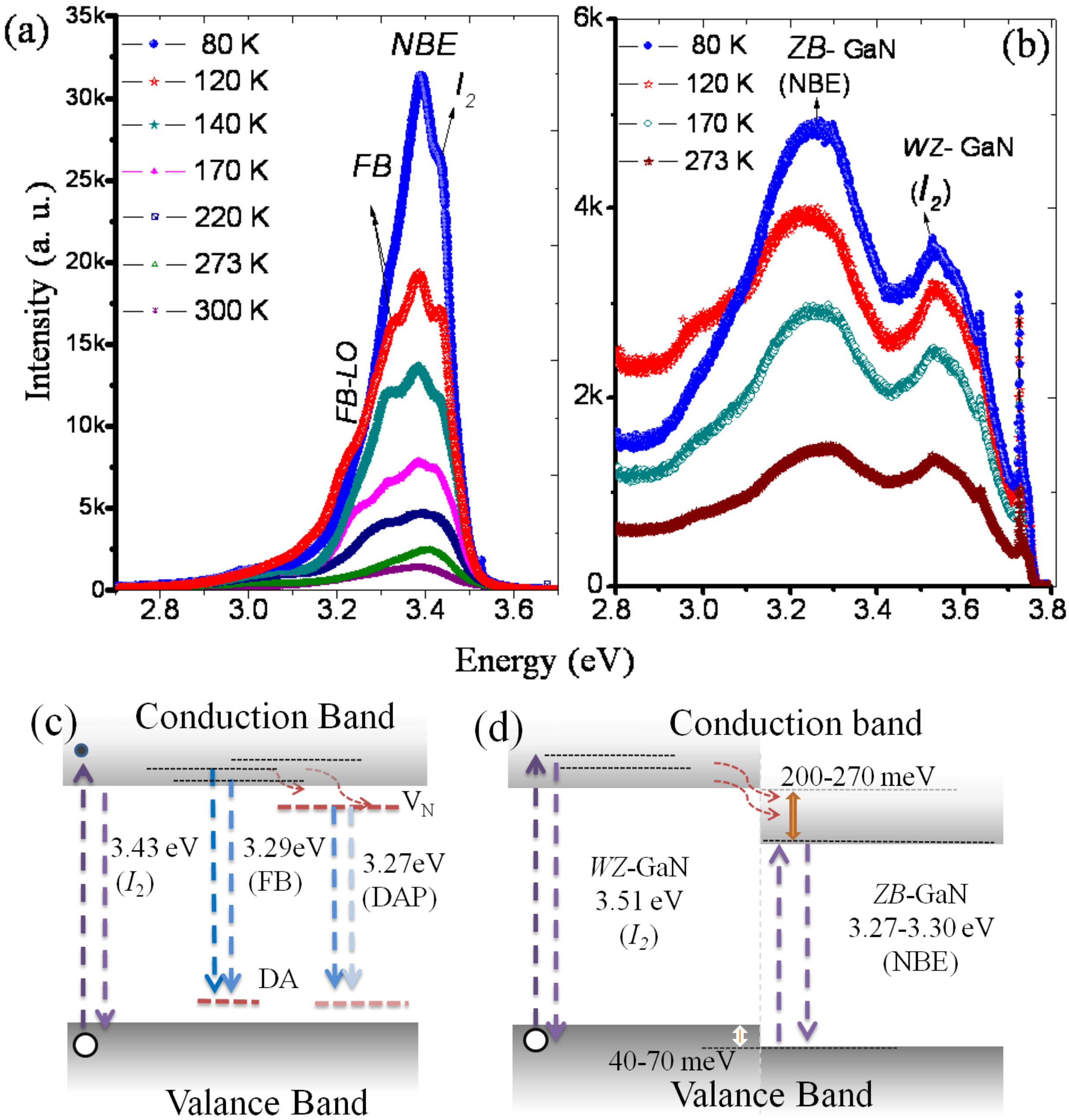

Fig. 3.17 Low temperature micro-PL spectra of (a) *WZ*-GaN NWs (b) *WZ/*zinc-blende (noted here as *ZB*) biphase homostructure in triangular GaN NWs using 325 nm laser excitation; the corresponding schematic representation of the emission mechanism in (c) *WZ*-GaN NWs and (d) *WZ/*zinc-blende (noted here as *ZB)* biphase GaN.

In the case of *WZ/*zinc-blende biphase homostructure in triangular GaN NWs, however, peculiar PL spectra are observed [Fig. 3.17(b)]. Two broad peaks at 3.51 and 3.27-3.3 eV are dominated in the room temperature PL spectrum. Interestingly, the relative intensity of the two leading peaks increases simultaneously while decreasing the temperature from 300 K to 80 K. The peak at 3.51 eV corresponds to I_2 line of *WZ*-GaN, which is blue shifted by ~70 meV. On the other hand, zinc-blende GaN phase usually shows near-band-edge emissions at 3.27–3.30 eV at low temperatures.[21,22] Therefore, the peak around 3.27-3.3 eV is assigned to the NBE emission of cubic GaN. It is in good agreement with the observed HRTEM results [Fig. 3.9], which indicates the existence of cubic GaN layers in the hexagonal GaN NW matrix. In contrary, a donor-acceptor pair (DAP) emission often appears at 3.28 eV in the low temperature PL spectra of *WZ*-GaN.[3] However, the uniform increase in the intensity of relevant bands does not support DAP as the origin of the observed 3.27-3.3 eV peaks.[22] In fact, the very thin zinc-blende layers embedded in the *WZ* matrix may be regarded as stacking faults in which electrons can be confined in zinc-blende layers that further attract holes via Coulomb interactions to form excitons.[22] All these process are responsible for the observed blue shift of I_2 line as well the broadening of all the relevant emission bands. The schematic representation of the various emission processes in the *WZ*-GaN and the *WZ/*zinc-blende biphase homostructure of GaN NWs are shown in figures 3.17(c) and (d), respectively.

3.4 Vapor-Solid (VS) Growth: GaN Nanotips and GaN Nanoparticles

VS process excludes inclusion of foreign atoms, which are ubiquitous in the catalytic VLS process. In this context, efforts are being made worldwide to grow uniformly distributed 1-D GaN nanostructures in a self catalyzed process via molecular beam epitaxy using a template approach along with controlling the Ga and N flux rates.[23-26] It is based on the fact that large anisotropy with respect to Ga and N adatom diffusion along the polar and non-polar surfaces leads to formation of 1D NWs and NRs. However, the underlying mechanistic concept involved in uniaxial self-catalyzed growth of 1D GaN nanostructures is still in infancy. As a matter of fact, reports on self-catalyzed CVD grown GaN nanostructures with controlled morphology are limited owing to the difficulties encountered in controlling important parameters such as Ga and N flux rates and subsequent switching between the fluxes. Growth modes significantly influence the properties of resulting nanostructures, which include shape, size, and crystal structure. Apart from NWs, there are considerable interests in exploring various other forms of GaN nanostructures.[1] Here, an effort has been made to cast light on the evolutionary stages of the nucleation mediated morphology of nanotips, NPs and NTs.

Wide band gap nitride based nanotips with low work function are known to be hard and chemically stable. These qualities make it potentially useful for applications in the field emission devices and scanning near field optical microscopy.[1,27] Until now, electron beam or focused-ion-beam (FIB) lithography and dry etching techniques, employing SiO_2 nanomask and subsequent reactive ion etching, are widely used for large area growth of aligned nanotips.[28,29] The processes are limited to specific substrates only. Syntheses of well-aligned GaN nanotips in self-catalytic process have raised sufficient scientific excitement.

3.4.1 Materials and Methodology:

Nanotips and NPs, were synthesized employing same CVD reactor used for the growth of NW.[3] The only difference employed here is the choice of substrate without catalyst. In this case, the Alumina boat itself act as substrate for the growth of nanotips and NPs by playing with the incubation time alone in the optimum growth conditions used for NW growth. For the growth of ultra-long nanotips, a slow temperature ramping rate of ~15 ^{o}C per min was maintained, whereas a faster rate of ~ 40 ^{o}C per min was maintained for the growth of NPs. In both the cases, 10 sccm of NH_3 was bleeding after the temperature reached around 850 ^{o}C, and the growth was carried out at atmospheric pressure. Reaction times and temperatures were varied from 1-3 h to obtain substantial amounts of nanotips/NPs. After the reaction was over, large quantity of nanotips/NPs were collected from the alumina boat around the source material. The reaction parameters, namely, growth rate, temperature, growth time, and NH_3 partial pressure were varied independently to identify the growth mechanism of nanotips. Growth temperature dependent evolution of NPs morphology was studied by varying growth temperature between 880-950 ^{o}C. Moreover, the optimized values for the growth of nanotips/NPs were found only at the temperature of 900 ^{o}C and NH_3 flow rate of 10 sccm.

3.4.2 Characterization

3.4.2.1 Morphological and Structural Properties:

The high-yield, free standing nanotips grow over a large area around the Ga source kept inside alumina boat as substrate [Figs. 3.18(a,b) for 1 h and (c) for 3 h]. The magnified optical micrograph of 1 h grown nanotips is shown in figures 3.18(d). Figure 3.18(e) shows typical FESEM images of a 3 h grown single nanotip and a magnified image of the base

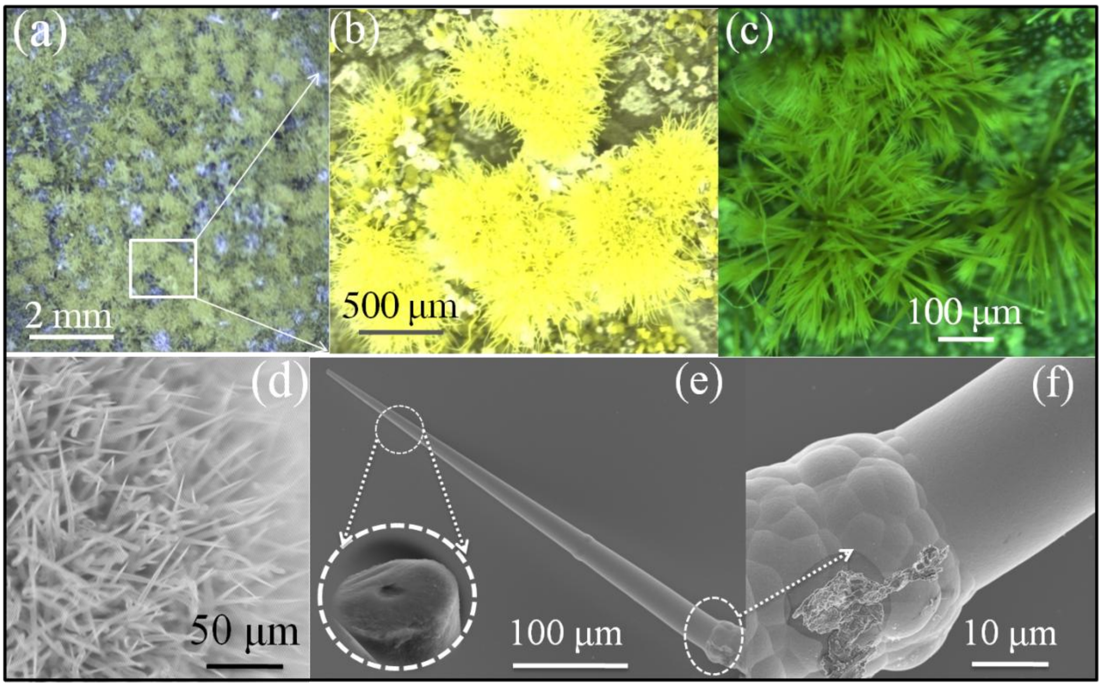

Fig. 3.18 (a) Large scale growth of nanotips over an area of 10 mm; (b) a set of nanotips grown in 1 hour and (c) in 3 h; (d) Magnified optical microscopic image of nanotips grown for 1 h, FESEM image (d) of a 3 h grown nanotips; inset shows the broken part of the tip region; (f) the transition of the Ga-rich base region of the N-rich smooth conical region.

region that depicts smooth transition from columnar to conical morphology [Fig 3.18(f)]. Most of the conical nanotips are solid and homogeneous [inset of Fig. 3.18(e)].The samples grown over 1 h duration possess a base diameter of ~20 µm, tip diameter having a value less than 200 nm and lengths extending up to hundreds of micrometers. The aspect ratio (length/base diameter) is of the order of 20 which is one order of magnitude less than the sample grown over 3 h duration. At the same time, the base diameter of 1 h grown nanotips is nearly half that of 3 h grown nanotips. Nanotips are grown with varying time to observe the evolution of the tip structure over a period of 10 to 180 min [Fig. 3.19(a-f)]. The formation of Ga droplet of size ~5-20 µm from the Ga nodule and further growth of nanotips are shown with increasing growth period.

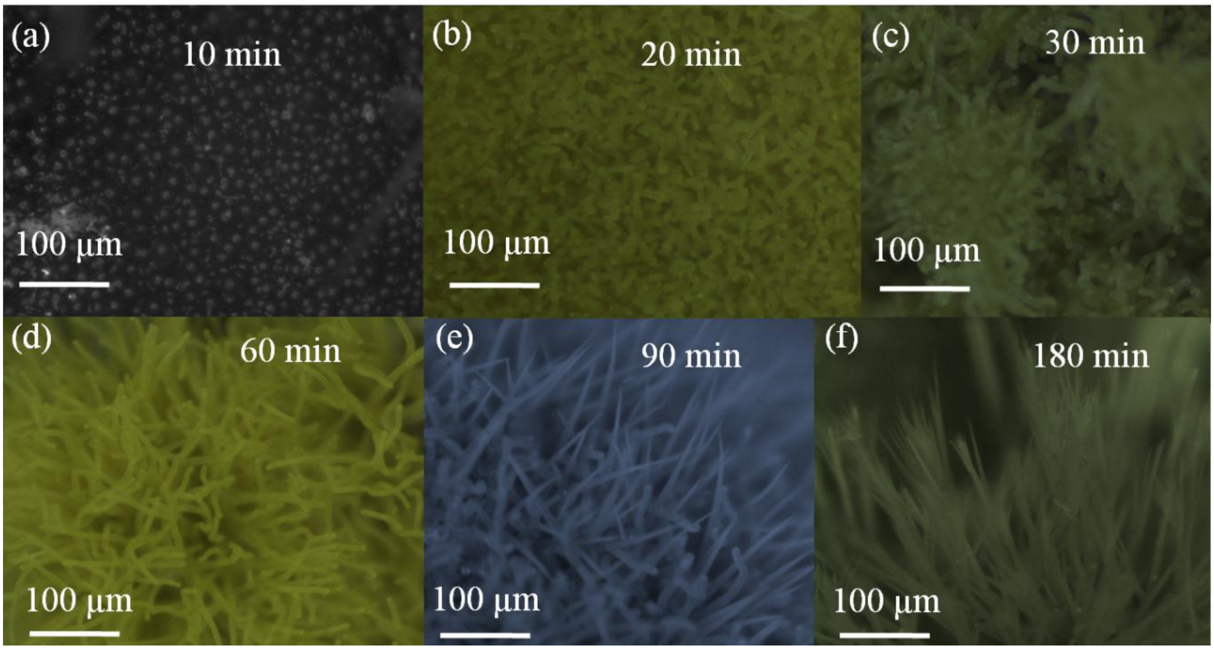

Fig. 3.19 Optical microscopy images of the formation of (a) Ga droplet by annealing Ga nodule in 10 min; Nucleation of GaN by self agglomeration followed by growth of nanotips after (b) 20 min, (c) 30 min, (d) 60 min, (e) 90 min and (f) 180 min. The nanotip grown above 1 h possesses sharp tip type morphology.

Morphological features for GaN NPs are shown in figures 3.20(a-c). The FESEM image [Fig. 3.20(a)] of the sample grown at 900 ^{o}C and the corresponding TEM image [Fig.

3.20(b)] show that the as-grown samples have platelet type surface morphology with average particle size of ~ 50 nm and thickness less than 15 nm whereas the sample grown at 950 ^{o}C mostly exhibit elongated morphology. All the samples are crystalline in nature.

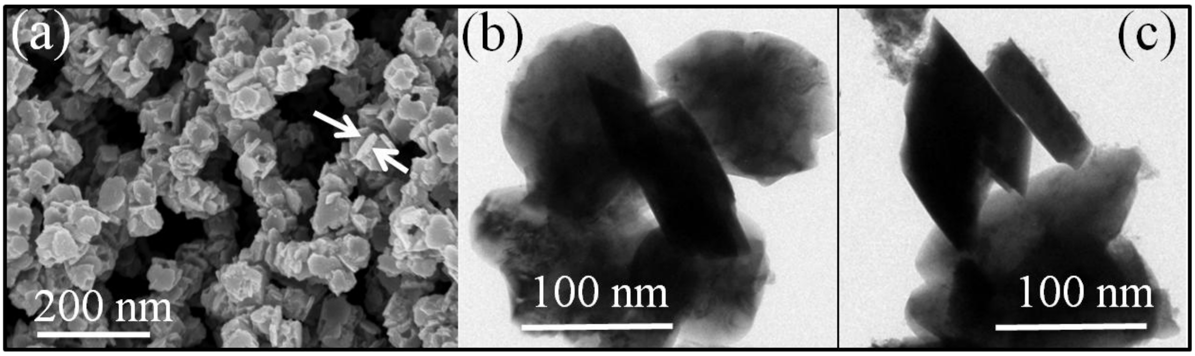

Fig. 3.20 (a) FESEM image of the NPs grown at 900^{o}C, the corresponding TEM image of NPs grown at (b) 900 ^{o}C and (c) 950 ^{o}C.

From EDX analysis, along the longitudinal direction of nanotip, it is found that the Ga/N ratio decreases from 4.8 to 0.64 in atomic percentage (data not shown).[3] It indicates that the growth that occurs in the Ga rich condition eventually ends up with N rich condition. HRTEM image along the basal plane shows that the surface is relatively smooth and consists of lattice fringes [Fig. 3.21(a)]. The near-perfect lattice spacing, with an inter-planar spacing of 2.598 Å, corresponds to (0002) plane of *WZ*-GaN. Growth occurs along [0001] direction with relatively smooth surface termination having a minimal amount of extended defects like dislocations and stacking faults along the surface. However, two distinct interfaces are observed around the tip region of the nanotips [Figs. 3.21(b,c)]. It is found that the surface layer is consisting of mostly $(10\bar{1}0)$ non-polar, and few polar $(10\bar{1}1)$ planes. These planes are presumably grown over (0002) polar surface belonging to *WZ*-GaN phase. The transition from polar to non-polar surface results in accumulating large amounts of stacking faults at the interface [inset of Fig. 3.21(c)]. The Formation of these stacking faults may have been favored by the N rich condition.[10] The lattice images became obscured towards the core region as the thickness increases. Figure 3.22(a) shows the typical lattice images of NPs

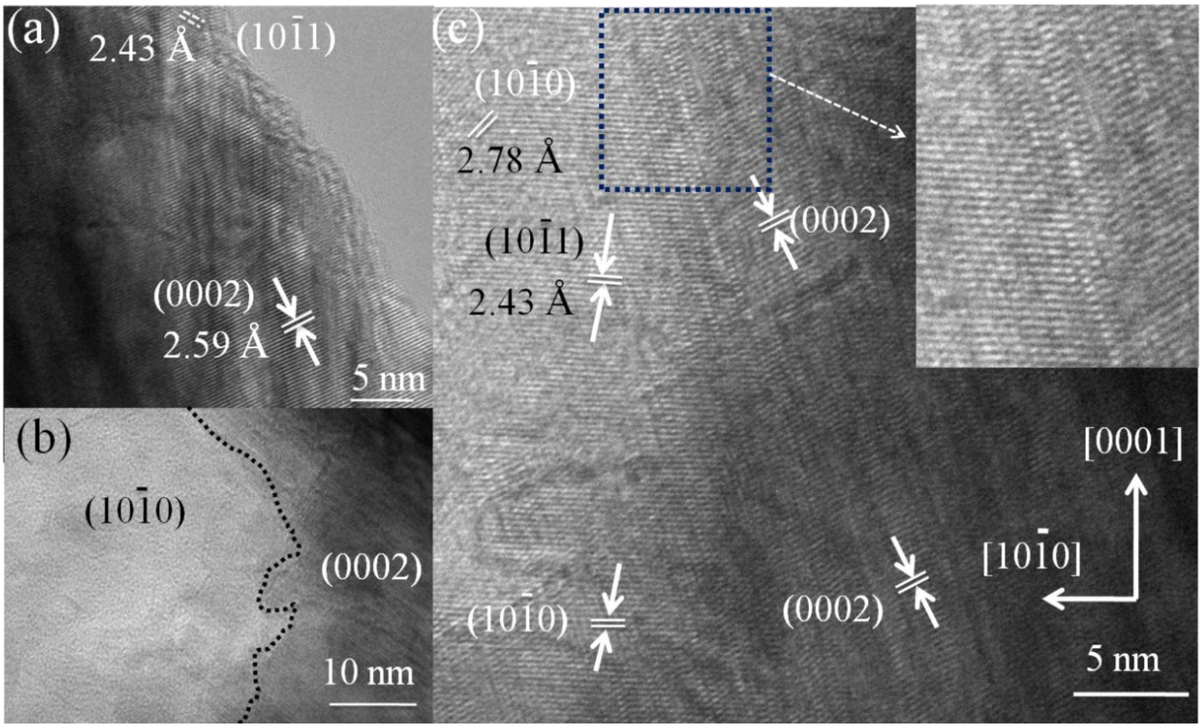

Fig. 3.21 HRTEM image of a single nanotips around (a) base region, (b) tip region and (c) high resolution image of the transition region between polar (0001) and non-polar $(10\bar{1}0)$ surface, around the tip region of the nanotips. Inset in (c) shows the magnified region of the transition region with large stacking faults.

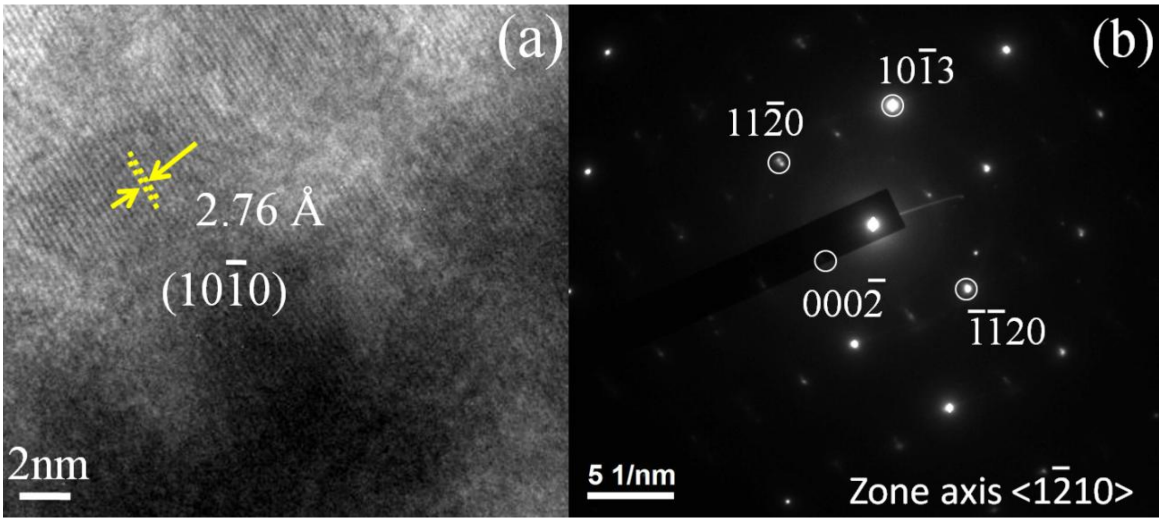

Fig. 3.22 (a) HRTEM image of the NPs grown at 900 ^{o}C, (b) SAED pattern of single NPs obtained along the *WZ* <1$\bar{2}$10> zone axis.

grown at 900 ^{o}C. Inter-planar spacing of 2.76 Å corresponds to the $(10\bar{1}0)$ polar surface of *WZ*-GaN. The corresponding SAED pattern is taken from a NP [Fig. 3.22(b)] which is indexed to <1$\bar{2}$10> zone axis of the *WZ*-GaN.

3.4.2.2 Raman Scattering Study:

Typical micro-Raman spectrum [Fig. 3.23(a)] for nanotip shows mode frequencies around 535, 567 and 726 cm^{-1}. Raman spectrum for NPs shows [Fig. 3.23(b)] modes around 533, 569 and 732 cm^{-1}. All these peaks correspond to A_1(TO), E_2(high) and A_1(LO) phonon modes of *WZ*-GaN phase.[2] All the spectra exhibit strong E_2(high) mode. A relatively smaller line width of 8 cm^{-1} of the nanotips than that of NPs (11.9 cm^{-1}) proves the superior crystalline quality of nanotips. Broad line width of NPs may arise due to the small grain size. LO modes are blue shifted to 9 cm^{-1} (line width ~ 17 cm^{-1}) and 3 cm^{-1} (line width ~18 cm^{-1}) for nanotips and NPs, respectively. Additional peaks at 253-265 cm^{-1}, 421 cm^{-1} are primarily attributed to ZB phonons arising from the finite size effect. The peaks at 96, 609 and 702 cm^{-}

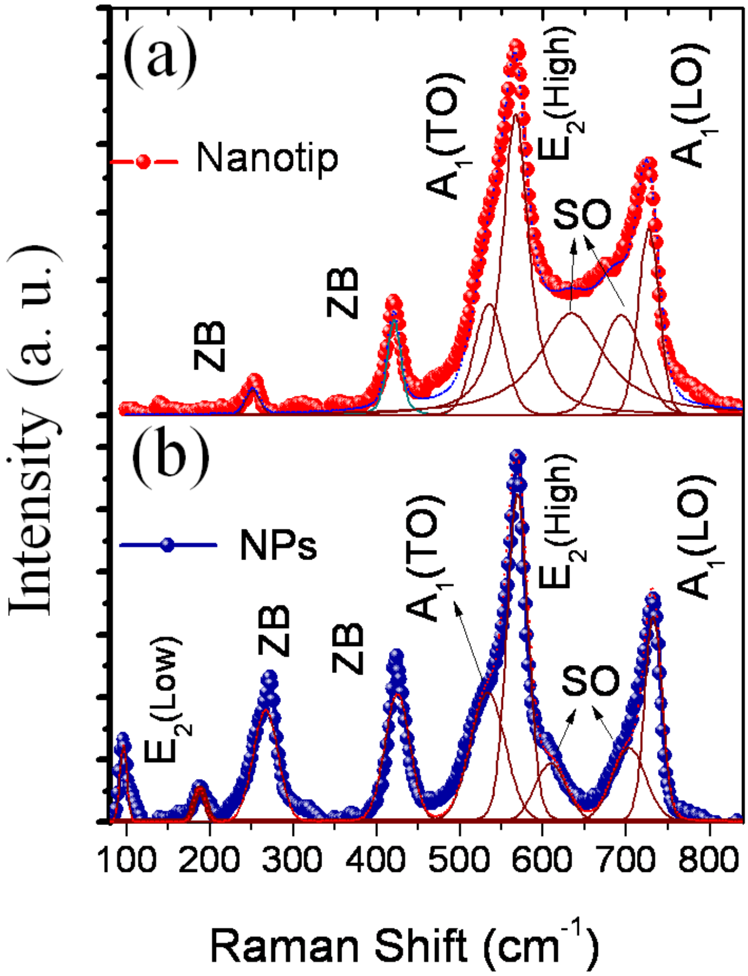

Fig. 3.23 Raman spectra for (a) nanotips and (b) nanoparticles showing wurtzite GaN phase.

^{1} in NPs may be related to acoustic phonon overtones. The broad peaks around 634 and 693 cm^{-1} in NTs are surface disorder induced SO modes.[2]

3.4.2.3 Stress Analysis:

Typical phonon modes along the lateral cross-section are shown in figure 3.24(a). Similar phonon spectra, as recorded in the surface region of nanotips [Fig. 3.23(a)], are observed around the shell region. However, a blue shift of 18 cm^{-1} for the E_2(High) mode is estimated at the core region of the nanotips. It shows the presence of a compressive strain developed along the core direction during the radial growth. The relation between the frequency shift $\Delta\omega$ (cm^{-1}) of E_2 (high) mode and biaxial stress σ(GPa) is estimated to be $\Delta\omega=(4.2\pm0.3)\sigma$.[30] Thus, the compressive stress developed inside the nanotip core is nearly equal to 4.29 GPa. Furthermore, the alternation of LO mode from A_1 to E_1 symmetry in the

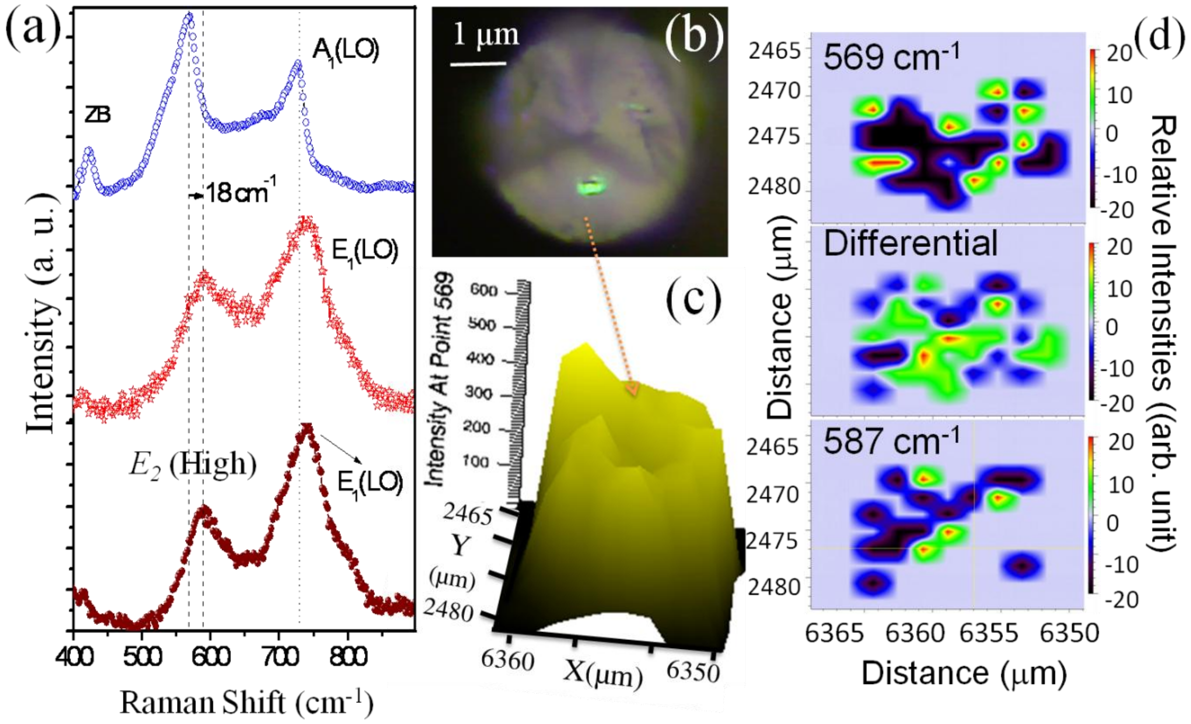

Fig. 3.24 (a) Typical Raman spectra along the diameter of a GaN nanotip at three different locations, surface, middle and core region; Cross-sectional Raman area mapping of a nanotip (b) along the diameter and (c) intensity distribution at 569 cm^{-1}; (d) differential stress mapping image corresponding to peak intensity observed at 569 cm^{-1} and the shifted peak at 587 cm^{-1}.

core region may be of geometric origin. The asymmetric behavior of optical phonons along the lateral cross section [Fig. 3.24(b)] of the nanotips is further analyzed by 3D mapping over an area of 20×20 μm. The map of the intense band of GaN phase with 568 cm^{-1}, E_2(high) mode frequency for the bulk GaN, illustrates [Fig. 3.24(c)] that strain free GaN phase is intensely distributed along the surface region with a contrast in the core region due to strain accumulation. A differential image [Fig. 3.24(d)], obtained by comparing the 2D mapping of peak intensity corresponding to observed E_2(high) mode at 569 cm^{-1} and the shifted peak at 587 cm^{-1} depicting the strained region in the core, is also shown as further evidence.

3.4.2.4 Photoluminescence Study:

RT micro-PL spectra of a single nanotip and NPs show strong emission in the photon energy in the range of 3.0 - 3.6 eV [Figs. 25(a,b)]. All the observed emission lines possess a broad and asymmetric line shape with weak band-edge-emissions.

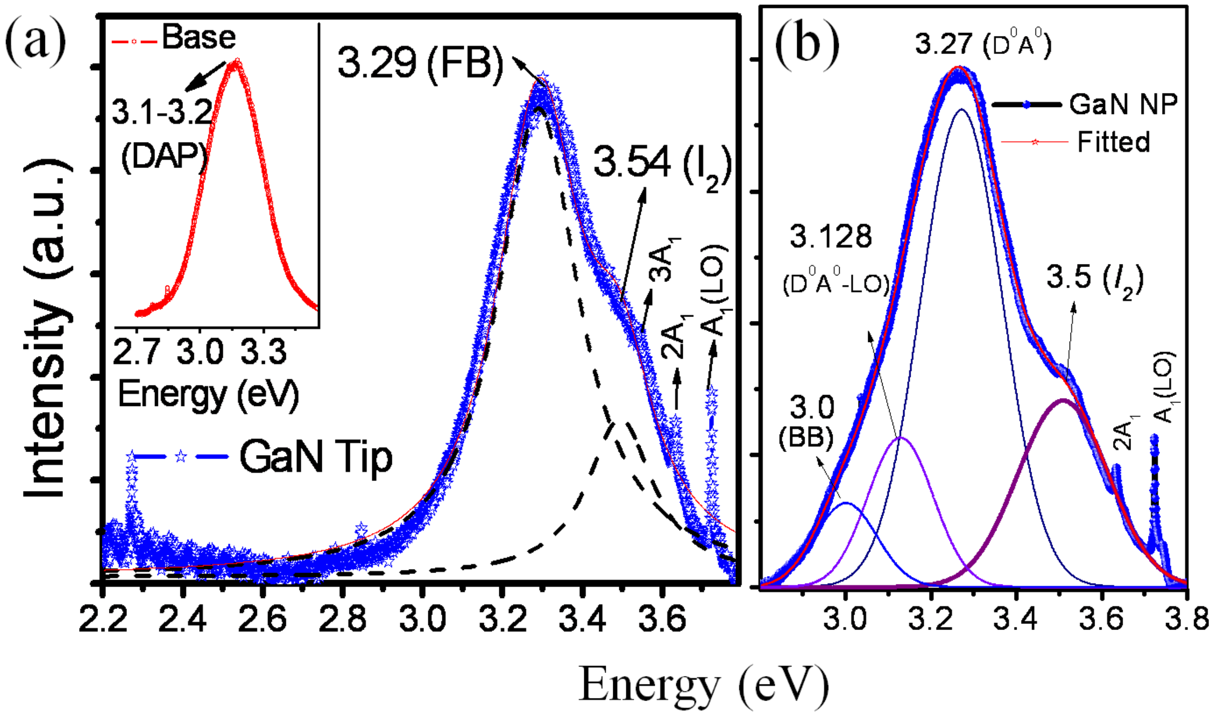

Fig. 3.25 Typical micro-PL spectrum shows for (a) nanotips and (b) NPs; Inset in a) shows the PL spectrum at the base region of nanotips.

The peak at 3.54 eV for the nanotip corresponds to I_2 emission line of *WZ*-GaN which is blue shifted by 80 meV with a broad line shape of ~105 meV [Fig. 3.25(a)]. Such a shift in this system is not expected due to quantum confinement effect. However, PL line shift and additional broadening possibly arises due to strain in the system.[30] The relation between the change in the excitonic PL, δE (meV) and biaxial stress σ(GPa) is estimated to be $\delta E=(20\pm3)\sigma$.[30] Thus, a compressive stress of 4 GPa in the nanotip is estimated. This is in close agreement with the previously calculated value of compressive stress using a Raman shift of E_2(high) mode. The I_2 line in the PL spectrum of GaN NPs shows a broad line shape (~124 meV) with a blue shift of 30 meV. Since the NPs are grown in the vapor phase without using any substrate, the effect of stress is ruled out. The ambiguity of the observed blue shift, broad line width and the asymmetric line shape of the I_2 line of the NPs may be attributed to small sized crystallites. In addition, strong broad bands centered at 3.29 and 3.27 eV are observed for the nanotip and NPs, respectively, with similar line widths of ~134 MeV. The peak at 3.29 EV of the nanotip has been assigned to the FB emission line. The FB transition is mediated by the free to a deep acceptor (DA) state. This possibly stems from Ga vacancy (V_{Ga}) formed under N-rich condition and will be discussed later. However, additional peaks appearing in the spectra of NPs belong to various electronic origins. The peaks centered at 3.27 eV and 3.128 eV are due to recombination of neutral donor acceptor pairs (D^0A^0) and their LO phonon replica (D^0A^0-LO), respectively.[3,19] Additional peak at 3 eV may be assigned to a blue band (BB). The well-known yellow band centered at 2.2 eV is not noticeable in both these samples, indicating high purity and crystallinity. Overtones of LO phonon modes upto 3rd-order are also observed in the right arm of the PL spectra [Figs. 3.25(a,b)]. Higher order phonon modes arise due to strong electron-phonon coupling mediated Frolich interaction with excitations above the band gap (325 nm, ~3.81 eV). This supports the above argument of higher crystalline quality in the nanostructures. On the other hand, PL spectrum [inset in Fig. 3.25(a)] from the base region of the nanotip shows a broadband emission around 3.1 eV. It is observed from EDX and Raman study (data not shown)[3] that the base region of the nanotip is Ga rich and contains oxide phases. Significant amount of nitrogen vacancies (V_N) is present in the base region, which act as shallow donors. The transition from a shallow donor state (V_N) to a deep acceptor state is expected to occur around 3.26 eV in case of GaN epilayers.[19,31] Nevertheless, it is assigned to DAP recombination lines after taking into account the transition from a shallow donor state V_N to a deep acceptor state, such as, $V_{Ga}O_N$ type defect complex present in the nucleating region. The broad DAP line is red shifted by 100 MeV indicating presence of significant amounts of defect in the base region. Nevertheless, oxide related native defects might have supported the foundation of strong nucleation sites for nanotips as incubation time with low N_2 concentration is found to be high in the initial stage for a low ramping rate. The issue will be further elaborated in the subsequent paragraph.

3.4.3 Polarity Driven Growth Mechanism:

It is observed that the Ga/N ratio in the vapor phase plays an important role in determining the resulting morphology of nanotips and NPs.[23-26] During the vacuum annealing of Ga precursor and subsequent increase in temperature from 800 to 900 ^{o}C at 200 mbar pressure, nano-sized Ga liquid droplets might have formed around the source material. This is supported by the recent reports, where small uniform sized Ga droplets have been used as an effective catalyst for the growth of the aligned SiO_2 NW.[32] Weak Ga-Ga bond, the longest liquid range and high vapor pressure of Ga might have helped the nucleation process. In the present study, different ramping rates of temperature of the reactor have been used in order to control incubation time of incoming adatom species. These are detrimental in controlling the size for forming nano-sized Ga droplets. These nano-droplets of Ga are likely to be used as nucleating center for formation of nanotips and NPs.[25] In case of nanotips, the slow ramping rate of temperature of the reactor (~15 ^{o}C/min) leads to formation of large Ga droplets of size ~1-20 μm as a result of self-agglomeration process. Energy stored in the defects and dangling bonds on the surface of Ga droplets might act as possible nucleating centers for the growth of GaN phase. In addition, it is observed that the formation of a dilute amount of oxide phase at the nucleation site is also occurring during slow ramping rate that cannot be avoided as nitride formation temperature at ~900 ^{o}C is delayed. During this process the residual and the adsorbed O_2 species from the alumina surface reacted simultaneously and helped in the nucleation process with a formation of complex oxy-nitride phase.[33] There are several reports exits based on oxide assisted nucleation process for the growth of GaN nanostructures.[33,34] Reduction or conversion of Ga_2O_3 phase to GaN phase at moderator temperature between 900-950 ^{o}C, is also reported during ammoniation process.[35] Being a low symmetric crystal oxide phase, Ga_2O_3 accelerates the nucleation process. Upon increasing the local ambient from Ga rich to N_2 rich condition, the oxygen contents reduced subsequently. It can be stated alternatively, that the N_2 overpressure may have helped in the nucleation of GaN inhibiting the further formation of oxide phase. The sub-micron sized GaN column grows from the GaN seeds in a diffusion limited self-agglomeration process promoted possibly by high vapor pressure of Ga and slow ramping rate towards reaction temperature.[36] Furthermore, the conically shaped nanotips grow smoothly over the GaN column up to several millimeters. The growth is favored in the longitudinal direction due to the fact that vapor pressure at the conical-shape convex surface of the nanotips is much higher than that on the top-edge.[36] The growth, can possibly, be explained by VS mechanism which is very sensitive to gas phase kinetics during the growth process.

The observed conical shape of nanotip morphology can further be elucidated by considering the characteristic length scale of polar surface with respect to different reaction conditions (either Ga-rich or N-rich). It is observed that Ga-rich condition results in a broad polar faces while in N-rich condition, morphology mainly contains rough surfaces and facets.[23-26] Ga-stabilized polar surfaces play an important role during GaN growth because Ga atoms have a significantly lower diffusion barrier on this polar surface.[8] The effective diffusion length of Ga reactant on the Ga-stabilized polar surface is sensitive to the chemical environment. If an excess N reactant is available, as in N-rich condition, the free surface diffusion of Ga is disrupted owing to the formation of Ga-N covalent bonds which ultimately inhibits Ga diffusion length.

However, a rapid ramping rate (about 3 times more than that used in case of nanotip growth) of the temperature of the reactor is employed in the formation of NPs. The rapid ramping rate of the temperature on the substrate reduces the effective adatom migration period. This hinders self-agglomeration, and limits the size of Ga droplets to a smaller size than what is encountered during nanotip growth. Meanwhile, NH_3 is introduced before the small Ga droplet ripens into big cluster and helps in the nucleation process at the vapor phase itself. This occurs before the onset of incubation time. Thus, small Ga droplets react with NH_3 in forming a large number of GaN islands and subsequent formation of NPs in the N-rich condition.

Interestingly, we can notice a unique relationship among the Ga and N flux rates, growth orientation and the resulting morphologies of nanotips and NPs. HRTEM data reveal that the nanotips growth occurs along [0001] polar direction (Fig. 3.21). The characteristic length of the polar surface of the base region is ~20 μm. However, after a typical distance from the base region (≥ 1μm) the surface layers of the nanotips are mostly non-polar. It is basically dominated by $(10\bar{1}0)$ planes [Fig. 3.21(c)]. The polar surface is found to shrink gradually towards the tip region. This variation of growth orientation is strongly supported by our growth conditions in which Ga and N flux rates have been altered after a typical incubation time of ~ 10 min during the growth. In case of nanotip growth, the reaction condition is initially Ga-rich which favors growth of polar surfaces. This can be explained by the fact that the interaction between adsorbate and surface is predominately realized by very weak delocalized metallic Ga-Ga bonds, which are isotropic with low diffusion barriers ≈ 0.4 eV along the (0001) polar surface.[23-26] However, anisotropic and differential growth orientations with the shrunken polar surface is expected when the reaction condition becomes relatively N-rich upon NH_3 flow. It is known that N-rich condition increases the nucleation rate of GaN due to the higher strength of the Ga - N bond and shorter diffusion length of Ga than that of Ga-Ga bond. Therefore, the Ga atoms will be bonded to N atoms before they complete their migration to step edges, to promote 3D growth and introduce roughness.[10,25] Apart from this, recently first principle calculation by Lymperakis et al.[37] have revealed that N-rich condition promotes island nucleation and the Ga adatom incorporation is more probable on the (0001) polar surface than that of other non-polar surface (*a*- and *m*-planes). Thus, the diffusion-induced mechanism of adatom migration on the polar surface promotes faster material transport occurring from the side facets (non-polar surface) towards the top. Thus, the higher nucleation rate towards the top is expected to stimulate and favors the axial growth over radial growth for the nanotips.[38] In other words, the observed nanotip morphology can be thought of driving by the strain, as indicated from the Raman [Fig. 3.24(a)] peak positions shift, in the system appearing due to the differential growth rate among competitive facets.

To summarize our model, three important consequences can be listed. These are 1) incubation time, 2) anisotropy of diffusion and 3) rate limiting factor of Ga and N adatoms in polar (0001) and non-polar ($10\bar{1}0$) surfaces of GaN facets play significant roles in deciding the final morphology of nanotips [schematic in Figs. 3.26(a,b)] and NPs [schematic in Figs. 3.26(c,d)]. Molecular N flux is found to have a stronger influence on the growth rate than nucleation.[3] It is also found that few nanotips have branches at the end of the tip during longer (3 h) growth period. These branches may be due to the formation of facets that occurs during N-rich condition [schematic in Fig. 3.26(a)]. On the other hand, NPs grown initially in N-rich condition, show appearance of nanometric seeds with a multitude of facets as shown in figure 3.26(c). These facets are made up of non-polar surfaces of $(10\bar{1}0), (11\bar{2}0)$ and $(1\bar{1}00)$ [Fig. 3.26(d)]. Such phenomena limit isotropic growth that invariably results in platelet morphology.

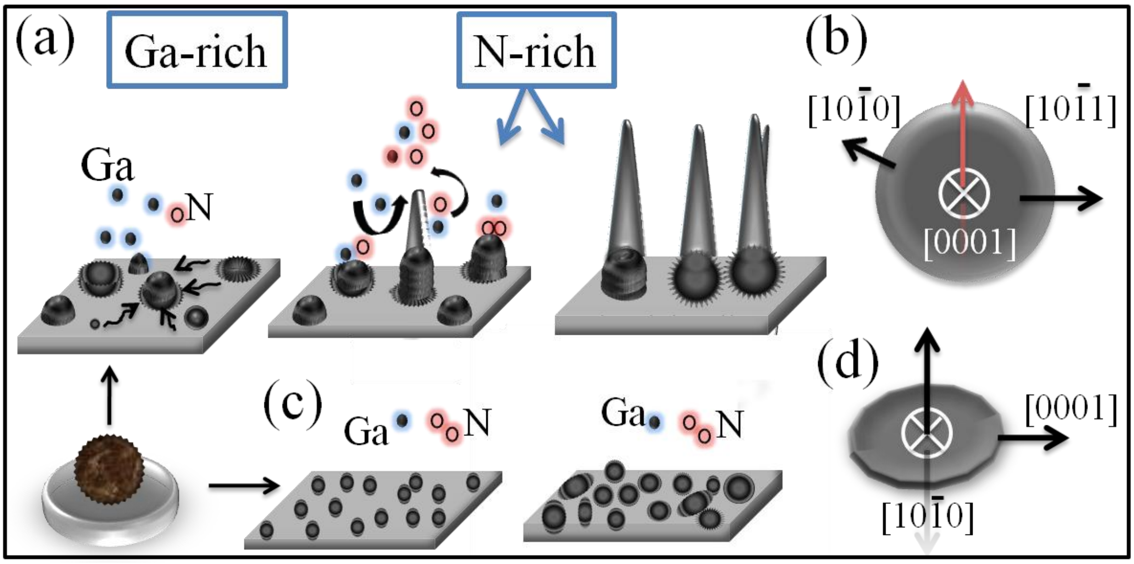

Fig. 3.26 Schematic showing the possible growth mechanism of (a) GaN nanotips in different Ga-rich and N-rich growth conditions, b) growth on polar surface; (c) GaN NPs in N rich condition; (d) growth on non-polar surface.

Apart from NWs, nanotips and NPs, other forms of GaN nanostructures, namely, core-shell Ga_2O_3@ GaN microbelts and GaN nanotubes are described in the subsequent chapters.

3.5. Summary:

High yield single crystalline GaN NWs of varying morphology are synthesized employing standard VLS mechanism in the CVD system. Various process parameters are optimized to realize NWs of particular morphology, including hexagonal, triangular, wurtzite/zinc-blende biphase, and square shaped forms. A simple steady state model has been used to correlate the nanowire growth morphology with the catalyst droplet size. The detailed morphological and structural studies are performed by FESEM and HRTEM. Phonon spectra of GaN NWs reveal the presence of dominating *WZ* phase in all the as-grown samples. Surface optical modes associated with the surface modulation in GaN NWs are identified and validated with the theoretical calculation. The as-grown NWs show strong band edge luminescence and hence can be used as ideal materials for optoelectronics and sensor applications.

On the other hand, catalyst free vapor-solid process is employed for the growth of single crystalline GaN nanotips and nanoparticles. The nanotips nucleate in the Ga-rich condition and get converted to N-rich condition as the reaction moves forward. N_2 overpressure is proposed to play an important role in the nucleation of GaN phase inhibiting the further formation of oxide phase nucleated during long incubation time with the slow ramp rate for nanotips. The conical shape of the nanotips is explained in terms of reduced surface diffusion length in the N-rich condition than that of Ga-rich core region. Unidirectional growth of the nanotips is proposed to be driven by the strain developed due to the differential growth rate among different competitive facets. On the other hand, nanoparticles are nucleated initially in N-rich condition with the relatively smaller incubation time that does not favor formation of facets, and consequently limits the growth. The ability to control growth of nanotips and nanoparticles stemming via self-catalyzed process is expected to be advantageous in realization further complex structures.

3.6 Reference:

1. Sahoo, P.; Dhara, S.; Dash, S.; Tyagi, A. K. *Nanoscience & Nanotechnology-Asia* **2011**, 1, 140.
2. Sahoo, P.; Dhara, S.; Das, C.R.; Das, S.; Tyagi, A. K.; Raj, B. *Int. J. Notechnology.* **2010,** 7, 823.
3. Sahoo, P.; Dhara, S.; Amirthapandian, S.; Kamruddin, M.; Dash, S.; Tyagi, A. K. *Cryst. Growth Des.* **2012**, 12, 2375.

4. Wagner, R. S.; Ellis, W. C. *Appl. Phys. Lett.* **1964**, 4, 89.
5. Mohammad, S. N. *Nano Lett.* **2008,** 8, 1532.
6. Mohammad, S. N. *J. Chem. Phys.* **2007,** 127, 244702.
7. Kuo, C-K.; Hsu, C-W.; Wu, C-T.; Lan, Z-H.; Mou, C-Y.; Chen, C-C.; Yang, Y-J.; Chen, L-C.; Chen K-H. *Nanotech.* **2006**, 17, S332.
8. Nam, C. Y.; Tham D.; Fischer, J. E. *Appl. Phys. Lett.* **2004**, 85, 5677.
9. Zywietz, T.; Neugebauer, J.; Scheffler, M. *Appl. Phys. Lett.* **1998,** 73, 487.
10. Myoung, J. M.; Gluschenkov, O.; Kim, K.; Kim, S. *J. Vac. Sci. Technol. A* **1999,** 17, 3019.
11. Huang, J. Y.; Zheng, H.; Mao, S. X.; Li, Q.; Wang, G. T. *Nano Lett.* **2011,** 11, 1618.
12. Xu, H. Y.; Liu, Z.; Liang, Y.; Rao, Y. Y.; Zhang, X. T.; Hark, S. K. *Appl. Phys. Lett.* **2009,** 95, 133108.
13. Stamplecoskie, K. G.; Ju, L.; Farvid, S. S.; Radovanovic, P. V. *Nano Lett.* **2008,** 8, 2674.
14. Harima. H. *J. Phys.:Condens. Matter.* **2002**, 14, R967.
15. Davydov, V. Y.; Kitaev, Y. E.; Goncharuk, I. N.; Smirnov, A. N. *Phys. Rev. B* **1998**, 58, 12899.
16. Siegle, H.; Kaczmarczyk, G.; Filippidis, L.; Litvinchuk, A. P.; Hoffmann, A.; Thomsen, C. *Phys. Rev. B* **1997**, 55, 7000.
17. Dhara, S.; Sahoo, P.; Tyagi, A. K.; Raj, B. "Surface Optical Modes in Semiconductor Nanowires, Nanowires - Implementations and Applications, Intech- Open Access Book, **2011**, *ISBN 978-953-307-318-7.*
18. Ruppin, R.; Englman, R. *Rep. Prog. Phys.* **1970**, 33, 149.
19. M. A. Reshchikova, H. Morkoç, *J. Appl. Phys.* **2005**, 97, 061301.
20. Bae, S. Y.; Seo, H. W.; Park, J.; Yang, H.; Kim, H.; Kim, S. *Appl. Phys. Lett.* **2003,** 82, 4564.
21. Vurgaftman, I.; Meyer, J. R.; Ram-Mohan, L. R. *J. Appl. Phys.* **2001,** 89,5815.
22. Xu, H. Y.; Liu, Z.; Liang, Y.; Rao, Y. Y.; Zhang, X. T.; Hark, S. K. *Appl. Phys. Lett.* **2009,** 95, 133108.
23. Cheze, C.; Geelhaar, L.; Jenichen, B.; Riechert, H. *Appl. Phys. Lett.* **2010**, 97, 153105.
24. Gotschke, T.; Schumann, T.; Limbach, F.; Stoica, T.; Calarco, R. *Appl. Phys. Lett.* **2011**, 98, 103102.
25. Consonni, V.; Trampert, A.; Geelhaar, L.; Riechert, H. *Appl. Phys. Lett.* **2011**, 99, 033102.
26. Lefebvre, P.; Garrido, S. F.; Grandal, J.; Ristić, J.; García, M-A. S.; Calleja, E. *Appl. Phys. Lett.* **2011**, 98, 083104.
27. Chattopadhyay, S; Chen, L.C.; Chen, K.H. *Critical Reviews in Solid State and Materials Sciences.* **2006**, 31, 15.
28. Yoshida, H.; Urushido, T.; Miyake, H.; Hiramatsu, K. *Jpn. J. Appl. Phys.* **2001**, 40, L1301.
29. Lin, C.; Yu, G.; Wang, X.; Cao, M.; Lu, H.; Gong, H.; Qi, M.; Li, A. *J. Phys. Chem.*, C **2008,** 112, 18821.
30. Kisielowski, C.; Kruger, J.; Ruvimov, S.; Suski, T.; Ager, J. W.; Jones, E.; Weber, Z. L.; Rubin, M.; Weber, E. R.; Bremser, M. D.; Davis, R. F. *Phys. Rev. B* **1996**, *54*, 17745.

31. Sahoo, P.; Oliveira, D. S.; Cotta, M. A.; Dhara, S.; Dash, S.; Tyagi, A. K.; Raj, B. *J. Phys. Chem. C* **2011**, *115*, 5863.
32. Zheng, B.; Wu, Y.; Yang, P.; Liu, J. *Adv. Mater.* **2002**, 14, 122.
33. Xue, S.; Zhang, X.; Huang, R. Zhuang, H.; Xue, C. *Dalton Trans.* **2008**, 32, 4296.
34. Shi. W. S.; Zheng, Y. F.; Wang, N.; Lee, C. S.; Lee, S.T. *Chem. Phys. Lett.* **2001,** 345, 377.
35. Lan, Z.H.; Liang, H.; Hsu, C.W.; Wu, C.T.; Lin, H.M.; Dhara, S.; Chen, K.H.; Chen, C.; Chen, C.C. *Adv. Func. Mater.* **2004,** 14, 233.
36. Choi, H. J.; Kim, D. H.; Kim, T. G.; Lee, J. C.; Sung, Y. M. *J. Electroceram.* **2006**, 17, 221.
37. Lymperakis, L.; Neugebauer, J. *Phys. Rev. B* **2009,** 79, 241308.
38. Bertness, K. A.; Roshko, A.; Mansfield, L. M.; Harvey, T. E.; Sanford, N. A. *J. Cryst. Growth* **2007**, 300, 94.

CHAPTER 4

SINGLE-STEP GROWTH DYNAMICS AND PHYSICOCHEMICAL PROPERTIES OF CORE–SHELL Ga_2O_3@GaN MICROBELTS

4.1 Introduction:

Over the past several years, technological and scientific excitement has stimulated the synthesis of various forms of 1D GaN nanostructures such as core-shell, radial and axial heterostructurs.[1] 1D core–shell heterostructures of group III-V compound semiconductor with compositional tunability provide unique functionality leading to various applications, which include single photon detector, solar cell, LEDs, one-dimensional electron waveguides, laser, and metal-oxide-semiconductor devices.[2-5] Limited reports on GaN and Ga_2O_3 core shell nanostructures are available in the literatures; including 1D coaxial metal-oxide−semiconductor (Au−Ga_2O_3−GaN) heterostructures grown by VLS method,[5] GaN-Ga_2O_3 core shell nanocable[6] and nanoparticles by thermal oxidation methods.[7,8] The widespread use of it, however, has been limited because of the difficulties encountered in synthesizing well aligned structures. In most of the cases materials are grown in the form of percolated networks. Many methods have been used in synthesizing GaN belts in the catalyst assisted reaction of Ga in NH_3 ambience.[9-10] Mostly, all these methods are based on vapor–liquid–solid (VLS) growth mechanism or assisted with template, which would introduce impurities unavoidably. Catalyst-free synthesis may exclude the possibility of metallic impurities providing better control of chemistry towards building functional devices.[11] Moreover, micron sized belts have the advantage of getting integrated into practical devices more easily over nanobelts which require sophisticated techniques to be used.[12]

Direct single step syntheses of GaN over Ga_2O_3 with well define interfaces and geometry, employing VS process, is limited. A single step technique to grow large quantities of uniformly distributed, high purity freestanding GaN microbelts with nanoprotrusions on distinctively shaped Ga_2O_3 as core is demonstrated.[13] The growth mechanism of the core-shell formation is elucidated using morphological and structural studies. The self-affine nanoprotrusions on the microbelt surface can be used as an ideal surface for sensing, nanodelivery and for nanofluidic applications.

4.2 Growth of Core-Shell Ga_2O_3@GaN Microbelts:

4.2.1 Materials and Methodology:

Free standing, ultralong belt like core-shell microstructures of GaN on Ga_2O_3 were synthesized using CVD technique at atmospheric pressure. Ga (99.999%, Aldrich) nodule, placed inside a high purity alumina boat was annealed above 850 ^{o}C for 10 minutes with a base pressure of 1×10^{-2} mbar. Then, the temperature of the Ga source was set at 900 ^{o}C with the subsequent introduction of high pure NH_3 at a flow rate of 10 sccm for 3-5 hours. The system was allowed to cool down up to room temperature in the same NH_3 ambient. A large quantity of free standing ultra-long belt like microstructure was found on the alumina boat around the source material without the use of any catalyst. Reaction time varied from 3 to 5 h to obtain substantial amounts of micrometer sized belts, keeping all other parameters same.

Morphological features of the belts were examined with visible-light microscope and FESEM. Two thin cross sections (from longitudinal and transverse direction) of the belt were lifted off for structural characterization by a dual beam focused ion beam (FIB). HRTEM (JEOL 2010 at 200 KV) was used for microstructural characterization and structure determination. Micro-Raman (514.5 nm excitation) and Raman phase mapping studies were performed for structural characterization. A single microbelt was kept like a microcantilever in order to study its wetting behavior.

4.2.2 Morphological and Structural Studies:

Typical visible-light micrographs of free standing microbelts corresponding to 3 h and 5 h deposition periods are shown [Figs. 4.1(a) and 4.1(b)]. The high-yield, free standing microbelts grew over a large area around the Ga source. Figure 4.1(c) shows a typical FESEM image of a single microbelt grown on the walls of the alumina boat at 5 h. These belts are uniform in width (10-100 μm), thickness (1-10 μm) and possess a length up to a few

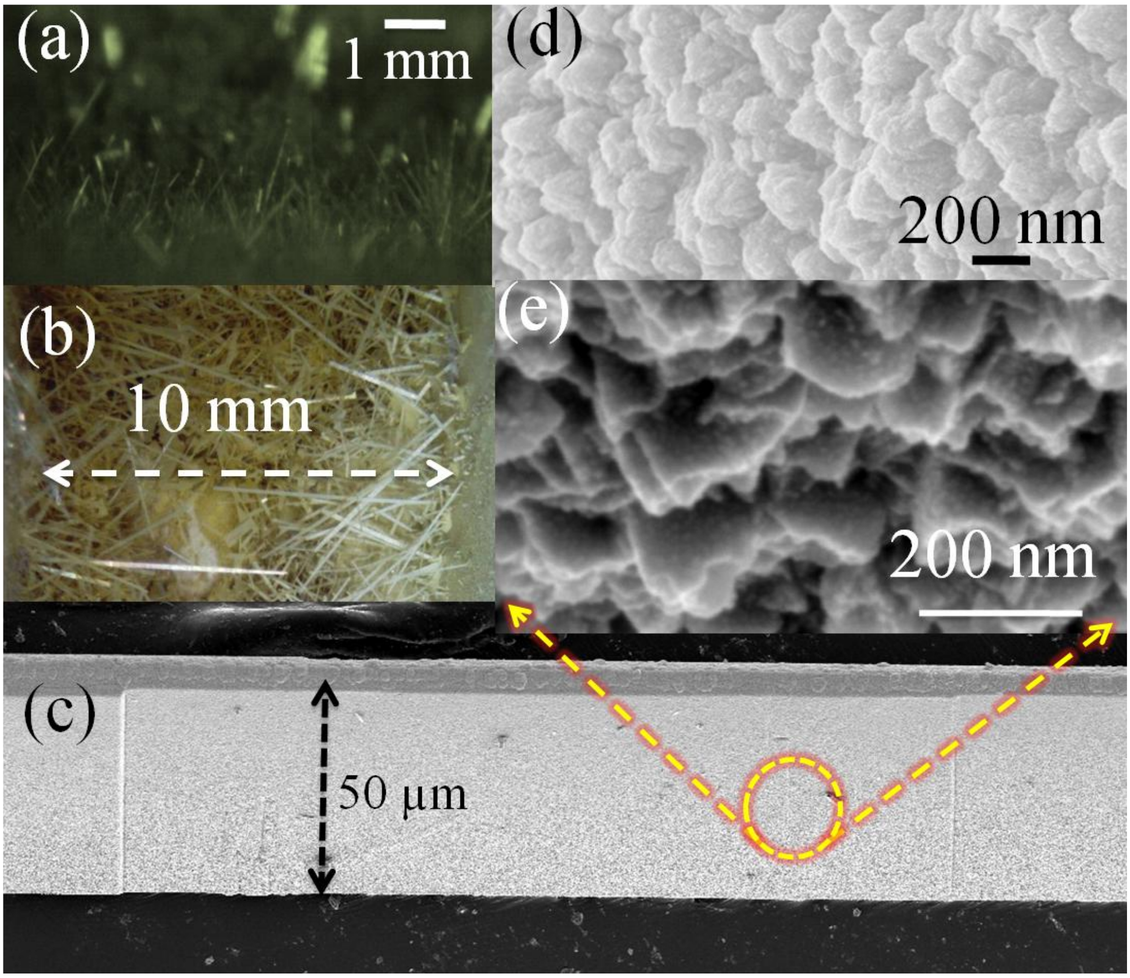

Fig. 4.1 Visible-light image of the large scale growth of microbelts with growth time of (a) 3 h, and (b) 5 h; (c) low high magnification FESEM image of the 5 h grown microbelt; high magnification FESEM image of the microbelt surface features with the presence of nanoprotrusions for (d) 3 h and (e) 5 h grown samples.

millimeters (1-7 mm). The thickness is nearly same but the width varies for a fixed growth time with other growth parameters remaining constant. However, a distinct surface morphology for 3 h grown samples is observed on the belt surface revealing nanoprotrusions with *rms* roughness of 30 nm and average inter island separation ~125 nm [Fig. 4.1(d)]. The similar surface structure was observed for samples grown for 5 h with *rms* roughness of 50 nm [Fig. 4.1(e)]. Further structural analysis, discussed later, confirms that these belts are indeed composed of wurtzite GaN crystal with Ga_2O_3 core. Two FIB sections in the longitudinal and vertical direction are taken from the microbelt. The cross section of the core-shell structure was prepared by a lift-up technique using FIB as shown in the schematic representation [Figs. 4.2(a-c)]. The high-resolution images of the Ga_2O_3 phase from both the sections are reconstructed to obtain a 3D picture of the microbelt.

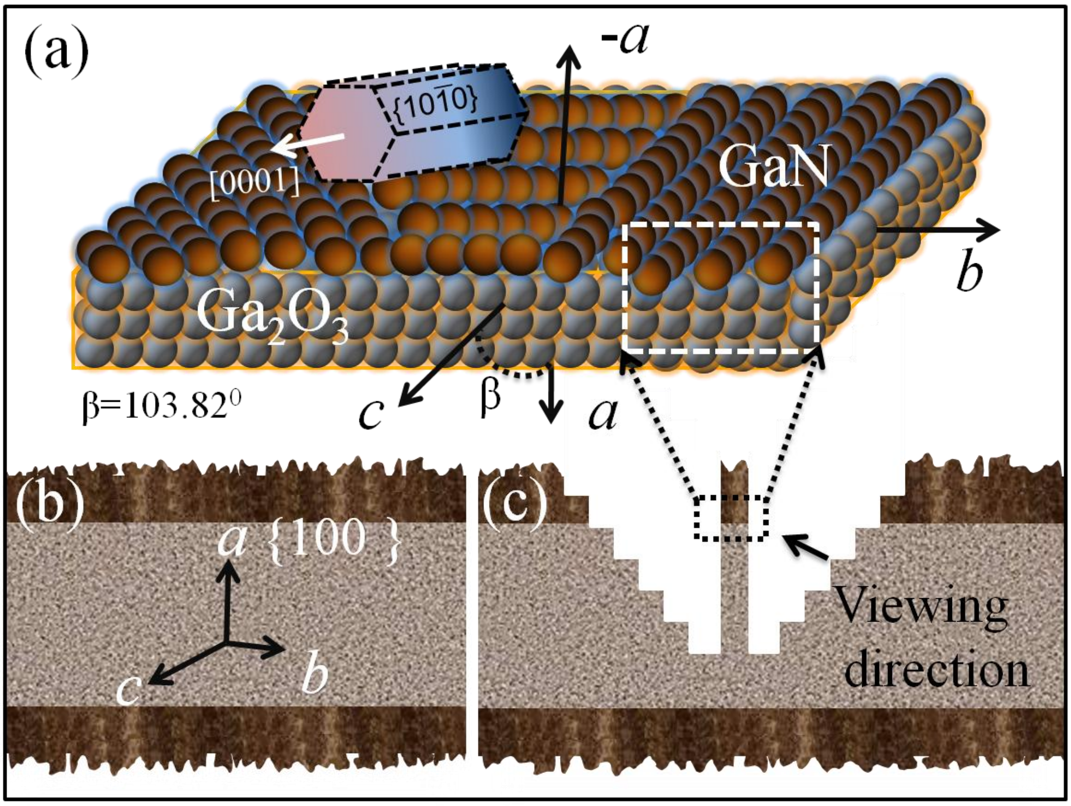

Fig. 4.2 Schematic representation shows (a) the formation of wurtzite GaN structure over monoclinic Ga_2O_3 core; (b) cross-sectional view of a single Ga_2O_3@GaN microbelt; (c) the viewing direction after FIB sectioning.

A typical TEM micrograph of the FIB section of the belt is shown in figure 4.3(a). It is observed that GaN layer is ~1000 nm in thickness. The top surface of the GaN layer is undulated and the interface between GaN and Ga_2O_3 is fairly sharp and distinct. The GaN grains are columnar with a width of ~100 nm. The diffraction pattern of the GaN layer close to the interface layer [inset in Fig. 4.3(a)] consists of a number of Debye rings with uniform intensity distribution indicating poly-crystallinity in the sample having randomly oriented crystallite with no preferred orientation. The d-spacing calculated from the diffraction pattern matches closely with the hP4 *WZ*-GaN with a= 3.18 Å and c= 5.18 Å. A high magnification image of the Ga_2O_3 layer is given with the hP4 *WZ*-GaN with a= 3.18 Å and c= 5.18 Å. A high magnification image of the Ga_2O_3 layer is given in the figure 4.3(b) with the electron diffraction pattern from the Ga_2O_3 layer having sharp and distinct spots in the inset of figure 4.3(b). This necessarily proves that Ga_2O_3 layer is either single-crystalline or the grain size is so large that at one time only one grain can be captured for diffraction pattern. The diffraction

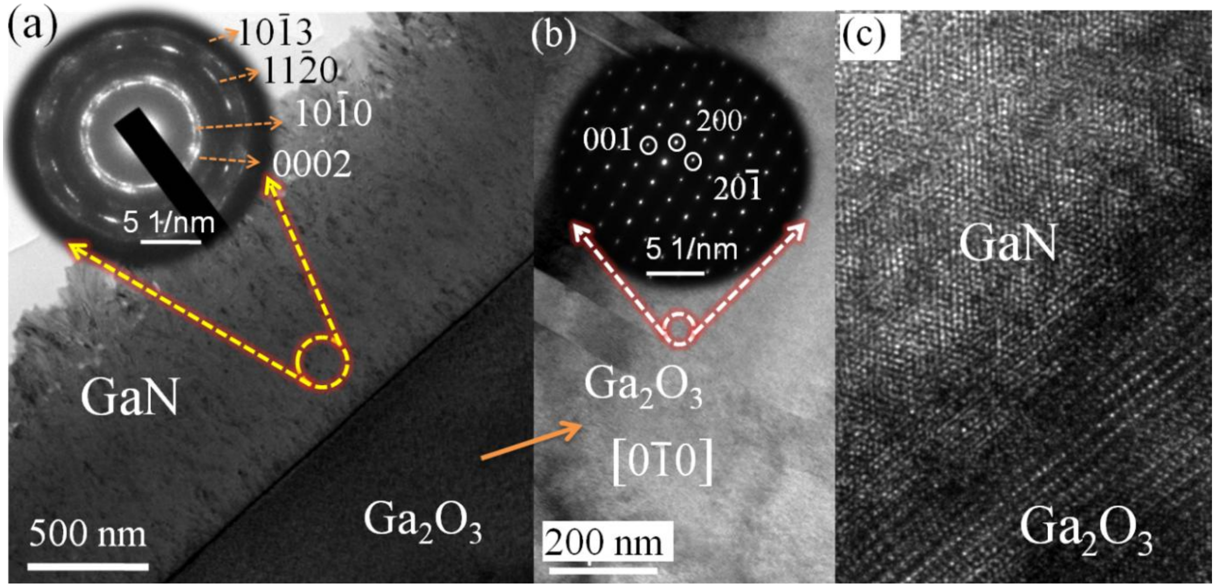

Fig. 4.3 (a) Cross-sectional image of the belts showing GaN and Ga_2O_3 interface. The inset shows the diffraction pattern of the GaN layers; (b) High magnification image of the Ga_2O_3 layer showing the presence of alternating bright and dark contrast representing planar defects; The inset shows the diffraction pattern of the GaN and Ga_2O_3 layers; (c) High-resolution image of the GaN-Ga_2O_3 interface.

pattern closely matches with monoclinic mC20 Ga_2O_3 phase with a= 12.27 Å, b= 3.03 Å, c= 5.80 Å and β= 103.82^0. Analysis of the diffraction pattern indicates that the grains are oriented along the zone axis $[0\bar{1}0]$. A number of bands with alternating bright and dark contrast are present in the grain body [Fig. 4.3(b)] indicating presence of planar faults in the Ga_2O_3 phase. The planar faults are inclined to the viewing direction of the microscope and due to the local changes in thickness over which the faults appear, alternating bright and dark bands are observed. A high-resolution image with a further magnified view of the GaN-Ga_2O_3 interface is shown [Fig. 4.3(c)]. In Ga_2O_3 side of the micrograph 1D lattice fringe is observed with spacing of 5.94 Å, which is close to the reported 200 spacing of mC20 Ga_2O_3. A high-resolution micrograph and the corresponding electron diffraction pattern from the top of a columnar GaN grain is given in figure 4.4. In the high resolution image multiple lattice planes are observed together [Fig. 4.4(b)]. The spacing between the fringes is 2.78 Å and 2.51 Å, which corresponds to the $(10\bar{1}1)$ and $(10\bar{1}0)$ lattice spacing of hexagonal GaN. As observed, the GaN crystal is defect free and the top surface is faceted. The facets are mostly parallel to the $(10\bar{1}1)$ and the $(10\bar{1}0)$ planes of GaN. The analysis of the diffraction pattern indicates that grain is oriented along $<1\bar{2}13>$ zone axis where $10\bar{1}1$ and $10\bar{1}0$ reciprocal lattice spots are visible [Fig. 4.4(c)]. Apart from that a few faint spots very close to the original spots are also visible. Analysis of the spots indicates that they are also from the $(10\bar{1}0)$ and $(10\bar{1}1)$ planes of GaN. It is concluded from this observation that these extra spots come from another GaN grain which is lying below the original grain which is rotated by ~12^o. As the original and the faint spots are having some rotational relationship, it can be concluded that the two grains are having a rotational relationship along the $1\bar{2}13$ axis.

From the detailed structural analysis, it can be concluded that GaN grows on the *bc*-plane of the monoclinic Ga_2O_3. The GaN-Ga_2O_3 interface can easily be recognized, as the change in orientation on the GaN planes can be observed at the interface. The Ga_2O_3 to GaN

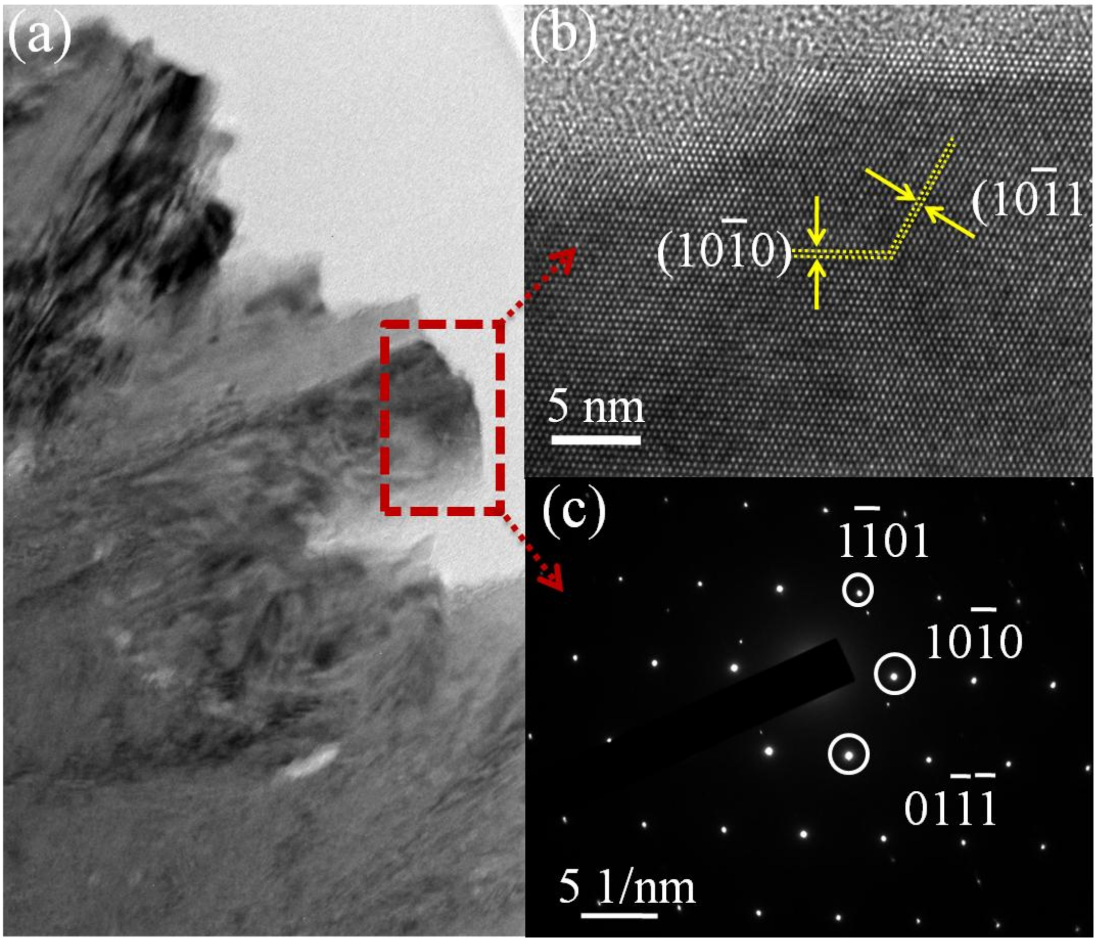

Fig. 4.4 (a) A TEM image the top columnar GaN grain and (b) the corresponding HRTEM lattice image; (c) Diffraction pattern shows the wurtzite phase of GaN layer with $[1\bar{2}13]$ zone axis.

transition takes place rather smoothly at the interface. It is assumed from this observation and also discussed later that a sharp transition in chemistry might have taken place at the interface. This observation further substantiates that GaN independently nucleates on the Ga_2O_3 surface and it is not a nitridation of Ga_2O_3 surfaces. In case of nitridation the GaN-Ga_2O_3 interface would have been non-uniform and undulated. Protrusions on the GaN surface may also originate from the local change in polarity of GaN due to the presence of surface steps on Ga_2O_3 core. These structural features are explained in terms of inversion domain boundaries (IDB) or stacking mismatch boundaries (SMB). None of these boundaries were observed in the present study. This clearly indicates that independent nucleation processes lead to the observed core-shell structure formation.

4.2.3 Optical Properties

4.2.3.1 Raman Scattering Study:

Typical micro-Raman spectra of a single GaN belt are shown in figure 4.5(a) at different spots across the belt [Fig. 4.5(b)], as well as on epitaxial GaN thin film (Lumilog, Germany, grown by metal-organic CVD technique) used for comparison. The Raman peaks appear at about 530 [A_1(TO)], 553 [E_1(TO)], 568 [E_2 (high)], and 729 [A_1(LO)] cm^{-1} correspond to the *WZ*-GaN [top spectra in Fig. 4.5(a)].[14] The peaks at 252 and 422 cm^{-1}, assigned to the ZB phonons, are observed due to the presence of crystalline imperfections including finite size effect. Finally two broad peaks belonging to SO modes are observed around 653 and 690 cm^{-1}. The SO modes arise due to the breakdown of translational symmetry of surface potential as a result of corrugations and disorders along the surface. Significantly broadened Raman peaks for the GaN microbelts, as compared to that observed

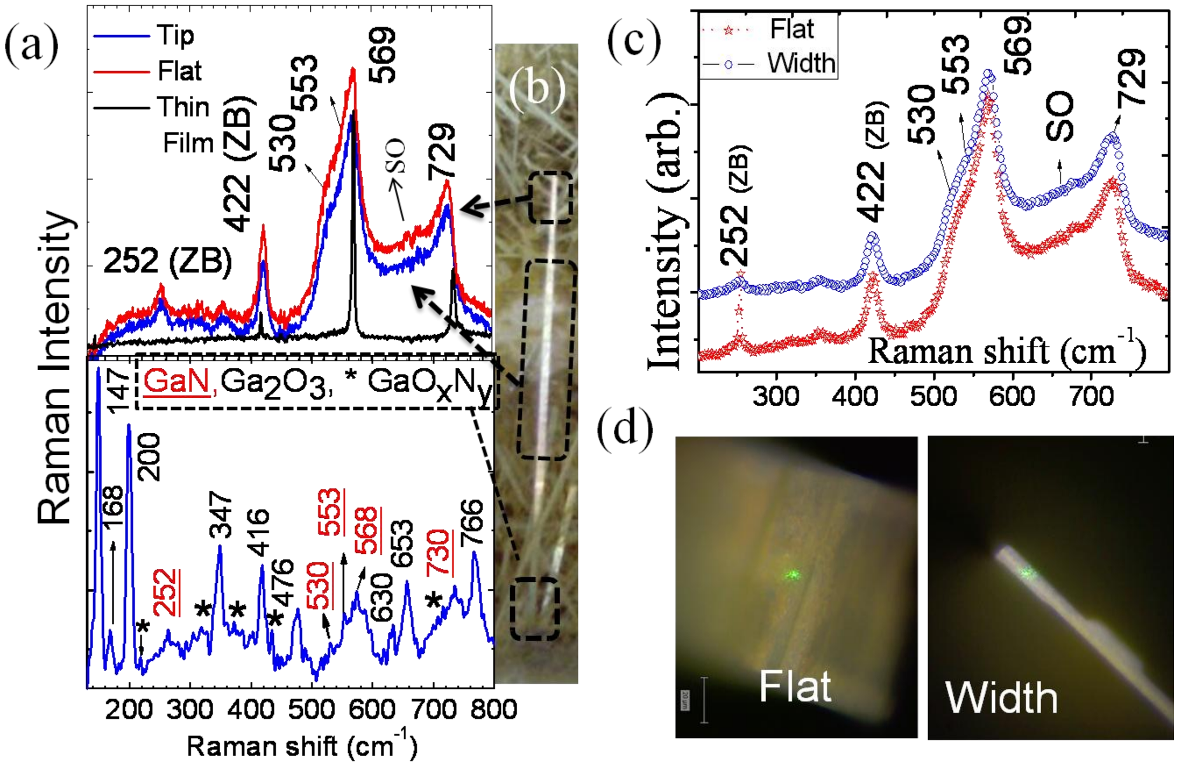

Fig. 4.5 Raman spectra (a) at different locations of the belt as shown in (b) the outset indicating crystalline phases present; (c) flat and tip side of the belt as shown by the (d) optical micrograph images with a laser spot of < 1 µm.

for GaN thin film [top spectra in Fig. 4.5(a)], are attributed to the nano-features along the belt surface. However, a complex Raman spectrum is captured from the base of the belts [bottom spectra in Fig. 4.5(a). The peaks originated in 147, 168, 200, 347, 416, 630, 653, 766 cm^{-1} are attributed to β-Ga_2O_3 phase,[15] essentially found at the base of the belt along with peaks of *WZ*-GaN phase. Furthermore, the feasible peaks pointed out by star mark (*) in the bottom spectra of Fig. 4.5(a) may originate from the complex phases of Ga oxy-nitrides (GaO_xN_y).[16] Raman study provides information on the surface states (up to few microns) of the belts. There is no change in the Raman spectra [Fig. 4.5(c)] of a microbelt recorded from the flat and the width side [Fig. 4.5(d)]. Therefore, it is clearly evidenced that the nucleated oxide phase is predominantly observed only in the base region of the microbelt while GaN phase is uniformly distributed.

4.2.3.2 Raman Phase Mapping:

The core-shell structure of the microbelt is further explored by Raman phase mapping. Figure 4.6(a) shows the FESEM image of a core-shell Ga_2O_3@GaN microbelt and

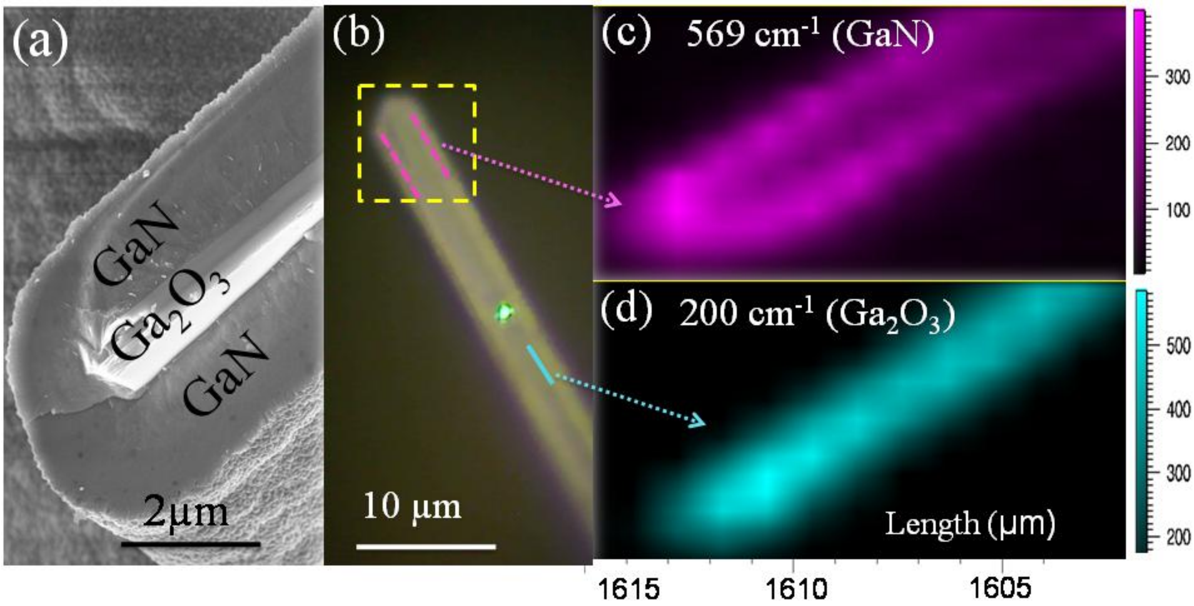

Fig. 4.6 (a) FESEM image of a core-shell Ga_2O_3@GaN microbelt; (b) Cross-sectional view of a microbelt showing the area of Raman mapping for (c) GaN shell and (d) Ga_2O_3 core in the same scale.

the corresponding optical image of the cross section of a vertically kept microbelt used for Raman mapping is shown in figure 4.6(b). The Raman phase mapping is performed over an area of 15x18 μm [Figs. 4.6(c,d)] with 1 μm steps. Raman area mapping of the shell structure using 569 cm^{-1} is shown in figure 4.6(c) which reveals that GaN phase is distributed in the shell region only. Whereas, Ga_2O_3 phase is found from the core region of the belt by Raman area mapping with 200 cm^{-1} [Fig. 4.6(d)] mode of monoclinic-Ga_2O_3 phase.[15] The Raman maps illustrate that the GaN phase is uniformly distributed over the Ga_2O_3 core.

4.2.3.3 Photoluminescence Study:

In order to understand the GaN defect states in this core-shell structure micro-PL spectra are taken at different locations of a single belt using a He-Cd laser (~325 nm) excitation. The spectra exhibit emission in the ultraviolet range at 3.47 eV [Fig. 4.7(a)] which is attributed to the direct band-to-band transition peak of GaN. The second dominant emission peak has been observed around 3.1~3.25 eV from different parts of the microbelt; base region corresponds to spot 1 and spot 2, 3 are referred to middle and tip region [inset in Fig. 4.7(a)] of the belts, respectively. This emission has been assigned to DAP lines.[17,18] The strong red shift in the emission (3.1~3.25 eV) band may be attributed to the rough surfaces of belts, having a high level of defects on the surface. We have observed a quenching of the direct band-to-band transition peak intensity than that of DAP originated peaks. The undesirable broad emission band, centered on 2.2 eV, is so-called yellow luminescence (YL) [Fig. 4.7(b)]. The key factor responsible for YL band results from the native defects. The V_{Ga} is the most likely candidate from an energetic point of view.[19] The atomic geometry of the V_{Ga} is characterized by a strong outward relaxation of the surrounding N atoms. The V_{Ga} corresponds to a transition of 3^- to the 2^- charge state, ~ $E^{2^-/3^-}$≈1.1 eV above the valence band, and thus indicative of a deep acceptor level.[17] A schematic of the V_{Ga} formation is shown in figure 4.7(c). However, an alternative defect configuration of V_{Ga} and oxygen

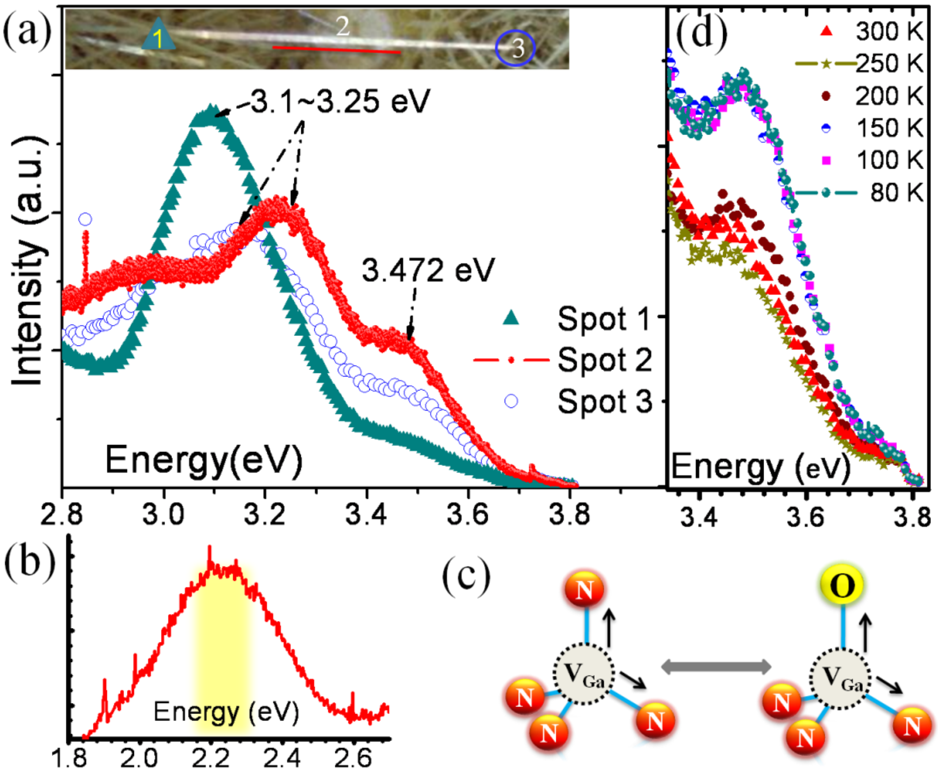

Fig. 4.7 (a) Micro-PL spectra of GaN belt at different locations; The insets show a single belt with spots 1, 2 and 3 marked; (b) typical YL band at ~ 2.2 eV corresponding to spot 2 in the low energy region of the spectra and schematic representation of the atomic geometry of V_{Ga}-O_N complex defects; (c) Temperature dependent PL spectra of the microbelt show blueshift with decreasing temperature.

antisite (O_N) complex corresponding to the similar energy transition $E^{1^-/2^-}$~1.1 eV is also reported as the origin of YL band. Presence of oxygen related defects in the GaN microbelts can be correlated to the quenching of intensity for band edge transition with respect to that for the DAP originated peaks. Native oxide may lead to non-radiative recombination process in GaN,[20] and may cause the Fermi level to be pinned at a slightly deeper position. Thus, the YL band in the microbelt may be accounted due the formation of V_{Ga}-O_N complex [Fig. 4.7(c)]. Temperature dependent PL studies of a single GaN microbelt have been carried out and show an expected blue shift with decreasing temperature corresponding to the band edge transition [Fig. 4.7(d). The band edge emission peak at 300 K is ~60% of that at 80K. However, electro-optical applications of radiative processes will require careful control of the type and number density of such defects.

4.2.4 Single Step Growth Mechanism:

Hence, it is possible to elucidate a growth mechanism of the core-shell microbelts from the above observations. Ga, evaporated above 850 ^{o}C, reacts with the residual and adsorbed O_2 available in the chamber and on the boat surface to nucleate Ga_2O_3. Monoclinic Ga_2O_3 being a low symmetry crystal, further atomic attachments on all exposed surfaces is not equally probable. This leads to anisotropic growth of Ga_2O_3 in the longitudinal direction leading to belt morphology. Subsequently, GaN nucleates on the belt surface leading to the formation of GaN layer onto Ga_2O_3. Thus, formation of both core oxide and surface nitride phases occur simultaneously in a progressive manner during the growth period to form the Ga_2O_3@GaN microbelts. The sharp interface structure between GaN and Ga_2O_3 and the absence of IDB or SMB in GaN indicates that GaN nucleates on Ga_2O_3. At the interface of GaN and Ga_2O_3, incorporation of O_2 into the GaN lattice might take place to a certain extent.

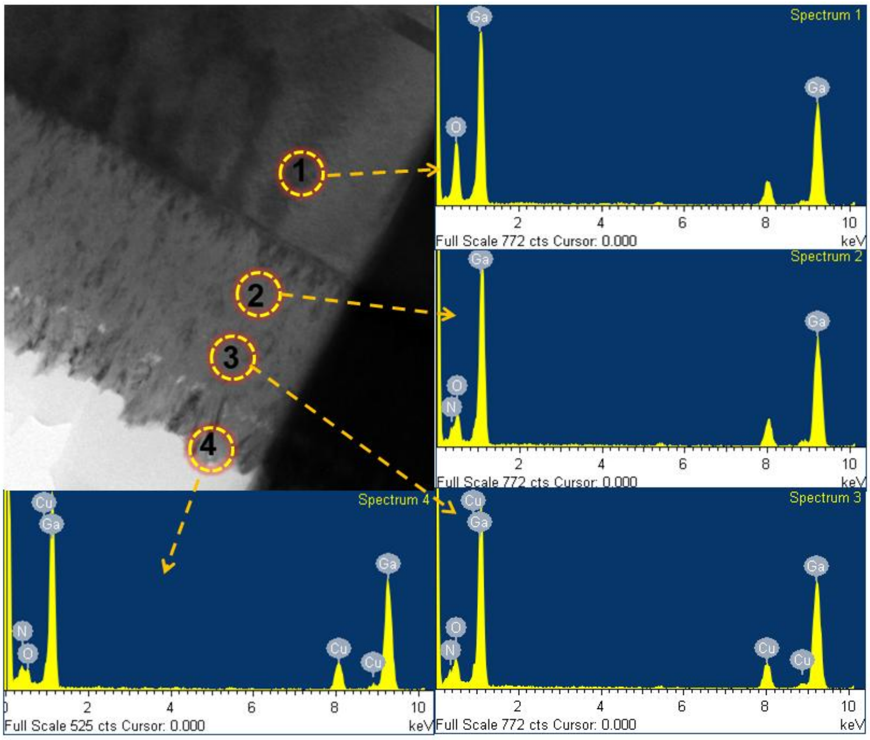

Fig. 4.8 Energy dispersive X-Ray spectra shown across the GaN-Ga_2O_3 interface. Spot 1 corresponds to Ga_2O_3 phase of the core-shell Ga_2O_3@GaN microbelts. The percentage of O_2 was reduced and N_2 concentration increases significantly while moving towards the surface of the GaN phase (spots 2 to 4).

As evidenced from EDX [Fig. 4.8], O_2^- concentration drop off gradually from the interface and N_2 concentration goes up. So the interface region compositionally may be an oxy-nitride phase of Ga. The GaN phase grows on the {100} face of Ga_2O_3. It has been reported that the growth of micrometer sized belts and ribbons (size in the micrometer to millimeter) could be achieved via metal-catalyzed VLS method or by a twin-plane growth mechanism.[9-11,21-23] Catalyst free growth of microbelts excludes the necessity of the above mentioned mechanisms. Instead, a conventional VS mechanism following the principle of self-catalysis is best suited to explain the growth of Ga_2O_3@GaN microbelts reported in the study. Figure 4.9 shows the schematic representation of the growth of the core-shell Ga_2O_3@GaN microbelts in the CVD technique.

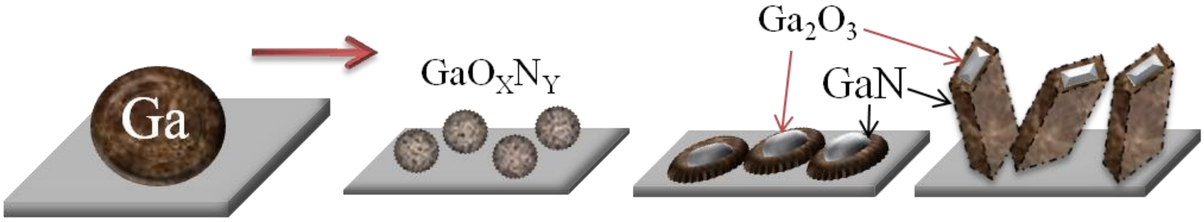

Fig. 4.9 Schematic representation of the growth mechanism of the core-shell Ga_2O_3@GaN GaN microbelts.

4.3 Physicochemical Properties of Core–Shell Ga_2O_3@GaN microbelts

Along with other applications, GaN and its alloys with other group III metal are of great interest for sensors because of their surface sensitivity, high mobility, low drift current, optical transparency, and high thermal breakdown temperature. Its implementation in high performance electronic and photonic devices, gas, bio-chemical sensors, and other surface sensitive devices requires a thorough understanding of the surface and interfacial properties for their optimal performances. In this contest, the detailed physical properties associated with the nanoprotruded GaN microbelts surface are studied for possible application in the field of sensor.[18]

4.3.1 Study of Surface Potential on Single GaN Microbelt by Kelvin probe force microscope (KPFM)

4.3.1.1 Importance of the Study:

To date, mats of GaN NWs and AlGaN/GaN high electron mobility transistor structure are particularly used for hydrogen and other gas sensing.[24,25] In most of the cases sensing studies have been conducted with dry nitrogen. A few experiments were performed in dry air conditions. However, in real applications for detecting gas, humidity may play a significant role because water vapor in the air sometimes perturbs the response of the other sensing components. Therefore, intensive investigation on the effect of humidity of GaN based nanostructure is required. Here, we report the response of nanoprotruded GaN microbelts for the detection of humidity using KPFM. We found, SP is strongly dependent on the humidity, suggesting that attention to control moisture is essential for sensing applications of chemical species other than water vapor.

4.3.1.2 Methodology:

In KPFM mode, the contact potential between sample and tip is compensated by applying external bias voltages and thus facilitating the simultaneous acquisition of topography and surface potential (SP) images, $SP = \Delta\varphi/e$. Here, $\Delta\varphi$ is the difference between tip and sample work functions and e is the electron charge. For the SP measurement, the GaN belts were transferred to clean Cu substrates, which were electrically grounded. Commercially available metallorganic chemical vapor-deposited GaN films (6-7 µm thick) on sapphire were electrically contacted through the top layer to avoid capacitance effects. Topography and SP images were acquired simultaneously using an Agilent 5500 with a three-lock-in amplifier in the amplitude modulation KPFM.[26,27] For the measurements, V_{AC} bias at frequencies in the range 10-15 kHz plus a DC bias, V_{DC}, were applied between tip and sample. The detector signal amplitude at the V_{AC} frequency should be proportional to (V_{DC}-

$\Delta\phi)V_{AC}\ \partial C/\partial z$, where C and z are the capacitance and distance between tip and sample, respectively.[28] The SP images thus show the values of the DC bias which minimize this amplitude at each measured point. These images show only SP variations along the image, since the lock-in adjustments are made so that the initial SP value is close to zero. The KPFM measurements were carried out in an environmental chamber where humidity levels in the atmosphere could be controlled by injecting pure N_2 flow. Dry atmosphere refers to humidity levels below 15%.

4.3.1.3 Surface Potential Variation:

Topography and KPFM potential fluctuation maps of the nanoprotruded microbelts are shown in figures 4.10(a,b). The *rms* roughness of these surfaces is in the range 30-40 nm. A clear evidence for the presence of nanoprotrusion along the surface of the microbelts is shown in the FESEM image [inset of Fig. 4.10(a)]. Moreover, large steps (between 0.1 and 0.4 µm in height) can also be observed [marked as dotted lines in Fig. 4.10(a) and corresponding KPFM image Fig. 4.10(a)] along the belt surface with enhanced roughness due to larger crystallites exposed at the edges. Topographic and the corresponding SP value of an isolated surface feature are marked with dotted circle. The electrical images acquired

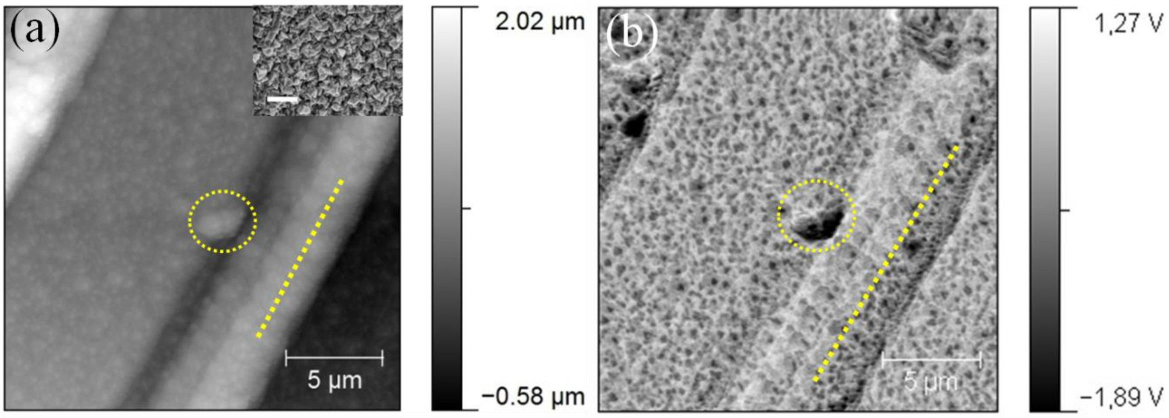

Fig. 4.10 (a) Topography (left) and (b) SP (right) images of the GaN microbelt with nanoprotrusions (inset, scale bar 300 nm), both under a dry atmosphere. Dotted lines and circles are guided to surface features mentioned in the text. Solid circle and box represent surface features related to extended defects discussed in the text.

simultaneously on dry atmospheres show a more uniform background with smaller SP values associated with the larger grains and to the step edges present in the image. The decrease in SP values at these regions reaches over 1 V. In this context, it is worth mentioning that the SP images show minimal artifacts or signal crosstalk due to the large roughness variation in the images,[29] as indicated by the presence of steps in figure 4.10(a,b).

We compare our result with commercially available GaN films. The topography [Fig. 4.11(a)] and SP images [Fig. 4.11(b)] of the GaN film under dry atmosphere. The film is completely different from the belts, showing very smooth morphologies where mono or bilayer step edges [along the dotted line drawn in Fig. 4.11(a)] are observed. The SP image [Fig. 4.11(b)] shows that the potential values are lower (~50 mV) in some regions closer to step edge. A lower SP value means it is lower in electron potential, i.e. excess negative fixed charges as indicated by the dark spot in the squared region [Fig. 4.11(b)]. The most likely origin of these extended defects is clustering of Ga vacancies [V_{Ga}; inset in Fig. 4.11(b) showing a possible configuration for a single vacancy], which is discussed later in details. Some small depressions, or pits, which can be associated to threading dislocations [marked with a circle in Fig. 4.11(a)], are also observed in the GaN film. The total dislocation density

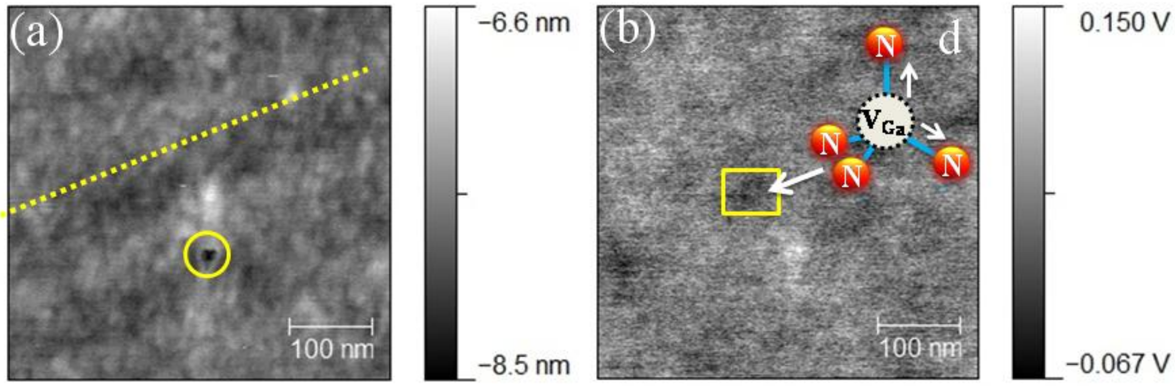

Fig. 4.11 (a) Topography (left) and (b) SP (right) images of the GaN thin film both under a dry atmosphere. The regular variations of height in (a) are steps on the surface of the GaN film. The inset in (b) shows the atomic configuration of the V_{Ga} in the 3^- and 2^- charge states; Dotted lines and circles are guided to surface features mentioned in the text. Solid circle and box represent surface features related to extended defects discussed in the text.

in the film is estimated as 2×10^8 cm^{-2}. The SP value increases at the pit [Fig. 4.11(b)], indicating a carrier depleted region - a higher SP signal corresponds to regions with higher value in an electron energy diagram i.e., the presence of positive charges or depletion of electrons.[30] Our result is in agreement with earlier observations of Hansen et al.[31] of similar surface structures, where a smaller capacitance consistent with a larger depletion depth was observed near the dislocations relative to the regions between dislocations. The variation in SP values in nanoprotruded microbelts, however, is at least one order of magnitude larger than those from the GaN film. This indicates a variation of Fermi level energy, which generally speaking may arise from different crystallographic phases, dopant levels or defect densities present in these regions towards the mid gap of the semiconductor.

High magnification AFM images of topography, phase, and SP [Figs. 4.12(a, b, c)] provide significant input in order to understand this material issue. Large variations of phase [Fig. 4.12(b)] are observed at the nanoprotrusions, indicating a drastic change in the viscoelastic properties of the surface. The corresponding electrical image [Fig. 4.12(c)] shows that the larger SP variation is localized in these same regions and not necessarily correlated to the height variation along the surface. When a large number of such regions are present in the images, the SP profile around them is also minimized with regard to the surrounding surface. These features altogether indicate the presence of a different material within the microbelt. The differences in SP value larger than 500 mV can be attributed to the presence of Ga_2O_3

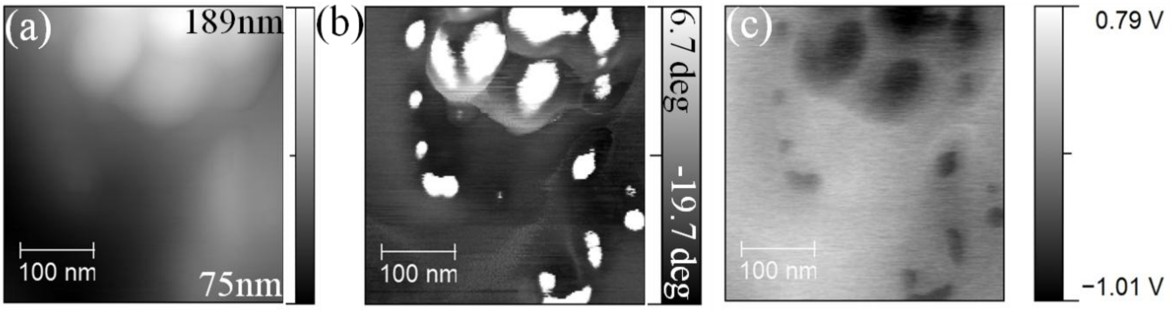

Fig. 4.12 (a) Topography, (b) Phase and (c) SP images attributed to the oxide and oxynitride phases of the nanoprotruded region on GaN microbelts.

phases on the surface.[32] However, both the resulting strain at the interface with GaN as well as the compositional variation (e.g., formation of intermediate GaO_xN_y phase) can originate the gradual increase in SP as one move away from the oxide core.[32] As observed from the PL spectra of the GaN microbelts [Fig. 4.7(a)], the native V_{Ga}-O_N complex certainly alters the electron shielding containing a negative fixed or interface charge and hence may be consistent with the observed enhanced SP variation along the sample surface.

4.3.1.4 Enhanced Variation of Surface Potential with Humidity Levels:

The scenario changes when SP images are acquired under larger humidity levels. In that case, the average SP variation on the surface drops, and the localized regions attributed to the oxide cores can no longer be clearly observed. Even a small humidity variation [Figs. 4.13(a, b)] can alter the electrostatic profile of the sample as compared to the dry image. The

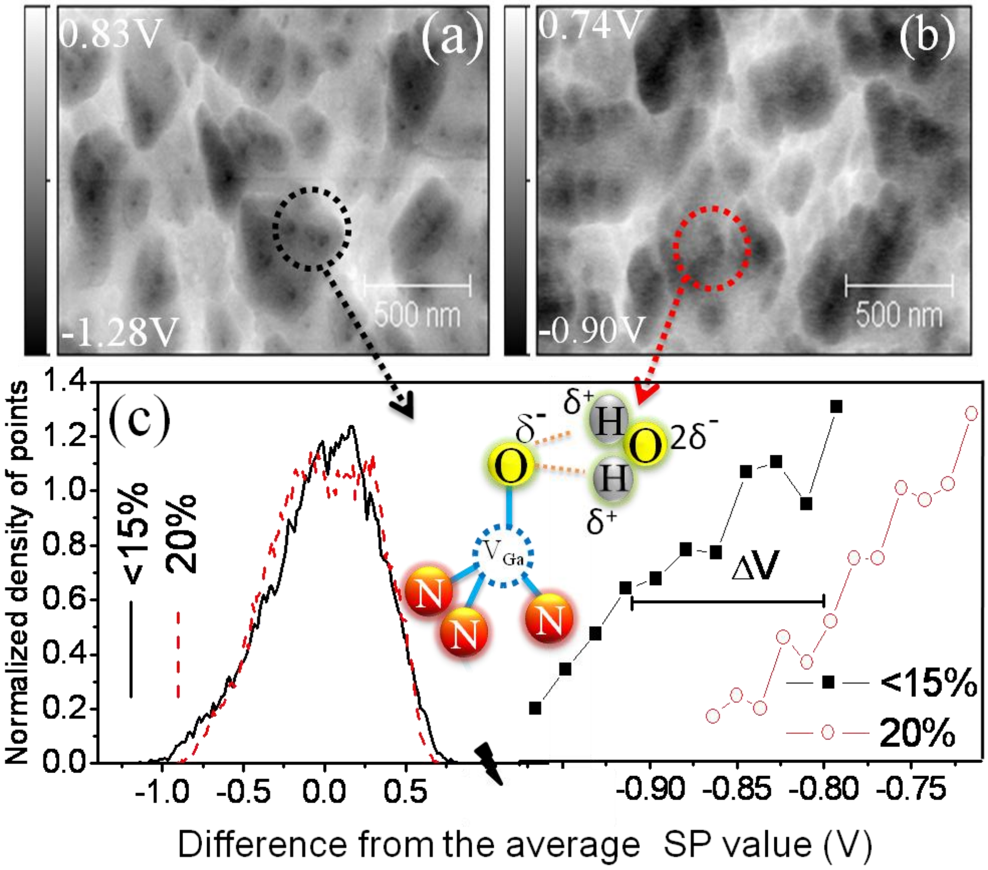

Fig. 4.13 SP surface profiles at (a) dry atmosphere and (b) 20% humidity level. The normalized density of SP points in each image is shown at (c); outset shows variation with a 5% increase in moisture condition over a small SP range (> 100 mV). The inset in (c) shows the schematic of water adsorption on GaN screening the electrical features of the original surface.

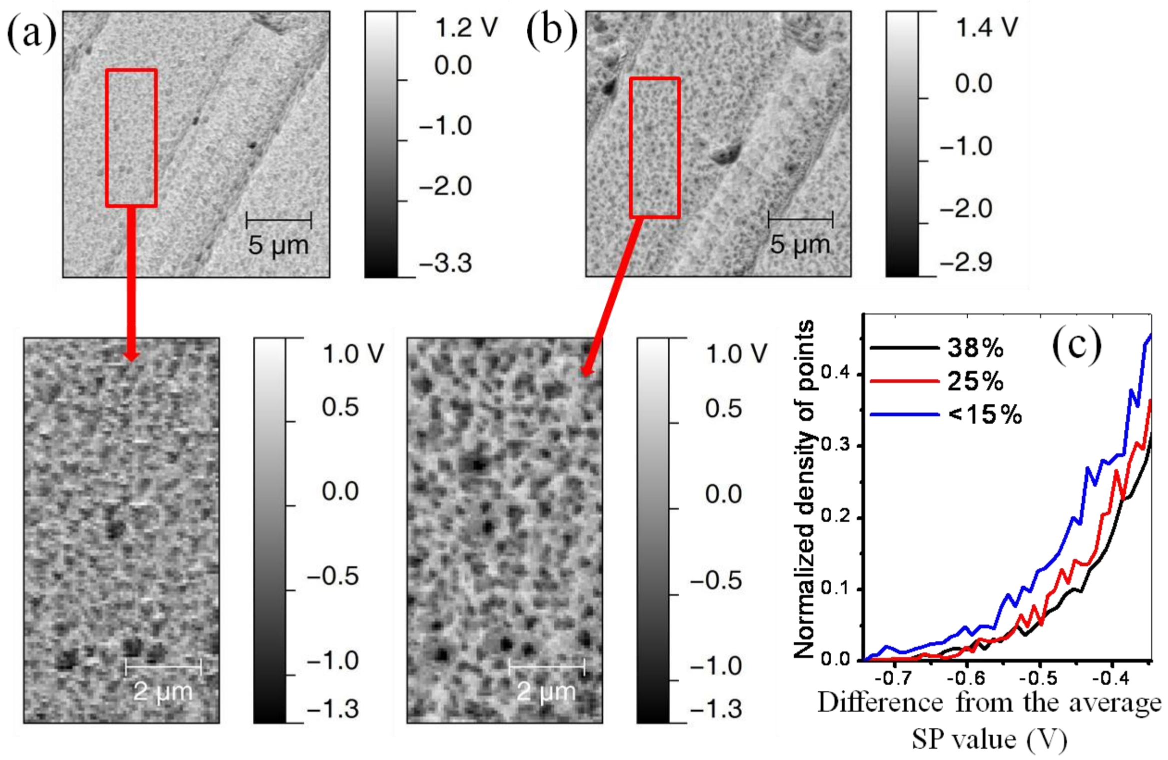

Fig. 4.14 SP images of the same region with different (a) 46%, (b) <15% humidity levels and the corresponding normalized density of points as indicated by the arrow; (c) The normalized density of SP points for three different humidity levels showing the decrease in SP values with increasing humidity in the AFM chamber.

normalized density of points in each image [Fig. 4.13(c)] provides statistical average SP value on exposure of moisture over an extended region. A variation in density of SP value is readily deconvoluted with even a 5% increase in the moisture condition shown over a small SP range >100 mV [outset of Fig. 4.13(c)]. This behavior indicates a screening of the original surface electrical features due to water adsorption. It is also observed for GaN films, but the enhanced SP variation along the nanoprotruded belt surface provides a distinct phenomenological evidence for the screening process. The prominent presence of V_{Ga}-O_N complexes [inset in Fig. 4.13(c)] in the belt may be assumed to be responsible for the accumulation of negative charges on the surface and the subsequent increase in the band bending leading to an enhanced response of humidity in the microbelt. Moreover, the diminished contrast in SP images with larger moisture levels, shown generally and specially in the encircled region, is also a clear indication of screening by surface charges.[30] We have also studied the normalized density of SP points corresponding to the humidity levels of 46% as compared to that <15% [Figs. 4.14(a,b)] and for other three different humidity levels [Fig. 4.14(c)] showing the decrease in SP values with increasing humidity in the AFM chamber.

4.3.1.5 Molecular Mechanism of Surface Potential Variation in the GaN Microbelts:

It often occurs that the adsorption pathway (associative versus dissociative) depends on surface morphology, with atomically rough surfaces being more active for H_2O dissociation than atomically smooth surfaces. The rough surface of the microbelt offers an effective strong interaction with H_2O molecule, as these molecules on a stepped or corrugated surface probably occupy positions at the top of the ridges or steps.[33] A comprehensive experimental investigation of the reaction of molecular water on GaN surfaces has been reported and shows that water adsorbs in a dissociative way on the GaN surface, even at low coverage.[34,35] However, it may be understood that the enhanced SP variation on the microbelts occurs from the dissociation of H_2O, dominated by the reaction at defect sites and facet edges of the protruded region associated to the presence of an oxide phase. With an increase in humidity, the lack of saturation of adsorbed H_2O at various locations/coordinates on the belts suppresses the charge accumulation (electron deficient). A typical schematic for the interaction of H_2O with native defect is shown in the inset of figure 4.13(c). Furthermore, the influence of defect lattice sites and "nonlattice" oxygen atoms at surfaces appears to be quite important. Like native defects, chemisorbed oxygen makes surfaces more reactive toward water decomposition and subsequent hydroxylation. The presence of different phases and crystalline orientations will also influence a quantitative spatial correlation. The surface, saturated with H_2O, is anticipated to end up in flatband conditions or even in a slight downward band bending.[36] However, pronounced dislocation densities, surface strain, other contaminant surface states, surface relaxation, and/or dipole layer from the charge leakage could contribute to the band bending. All these physical properties are significantly observed in belts, and hence, it provides a pragmatic sensitivity of SP to moisture ambience.

4.3.2 Superhydrophobicity in Single GaN Microbelt

4.3.2.1 Introduction:

Nature has learnt to control liquid in a myriad of ways with regard to design of biosurface having special wetting characteristics.[37] Recently, self-cleaning or water-repellent properties emanating from superhydrophobicity have become significant for several applications in biotechnology and micro-/nano-fluidics. It is believed that the excellent water repellent properties of lotus leaf are attributed to a unique combination of micro- and nano-hierarchical surface morphology. Surface protrusions create an energetically unfavorable situation for a liquid to be sucked or 'imbibed' into the surface texture of the superhydrophobic surfaces leading to an increased beading-up tendency. The effectiveness of this process for any given textured surface depends on both the roughness amplitude and the wetting property of the liquid. On the other hand, the liquid should penetrate into the bed in case of hydrophilic surfaces, having a tendency to spread the liquid. In this process the additional surface area from the sides of the nails causes a force that sucks the liquid into the texture. So, in turn roughness should amplify the hydrophilicity.

However, some recent reports demonstrate that roughness can also lead to formation of a superhydrophobic contact angle on a hydrophilic substrate.[38] For example, the leaves of Lady's Mantle show superhydrophobic properties owing to the elasticity of the hydrophilic hairs on the leaves.[39] Some report had shown a transition from hydrophilicity domain to superhydrophobicity region by decorating the substrate with organic polymer surfaces.[40] Mostly, the above results have been explained by the Cassie–Baxter model by assuming a small value of φ_s, which denotes the fraction of the wetted solid area to the total area under the droplet. In all these cases, the salient feature to promote a favorable non-wetting thermodynamic state is to form a composite state having entrapment of air within the trenches of rough surface. The phenomenon of entrapment of air indicates that the geometrical parameters of a nanostructure have an influence on the wetting behavior and contribute to the reversible switching between hydrophilicity to superhydrophobicity. [38] The challenge here is to demonstrate a superhydrophobic surface irrespective of the nature of the surface by merely controlling the geometry of the microstructure.

In this regard, a superhydrophobicity state in a single microbelt of GaN is demonstrated, which is otherwise hydrophilic in nature. [41] The changeover from hydrophilicity to superhydrophobicity on GaN microbelts are examined from the viewpoint of the geometry of the surface, and surface energy.

4.3.2.2 Materials and Methodology:

Free standing, ultralong GaN microbelt used for this study is taken from the 5 h grown set of sample. Each belt is ~ 100 µm in breadth, 10 µm in width and several millimeter ~3-7 mm in length [Figs. 4.15(a,b)]. Figure 4.15(c) shows the presence of nano-metric surface protrusions on the surface of GaN microbelts as revealed by the FESEM image analysis. The root mean square value of roughness was measured using an AFM microscope (Agilent 5500 with 3 lockin module, Pt-coated Si tips). A single microbelt was kept like a microcantilever with one end fixed and the other end hanging in the air [Fig. 4.15(b)]. A drop of water about few nanoliter amount, was delivered smoothly on to the microbelts using a micro-syringe. The shape of water droplet on the belt was recorded using optical microscopy in both vertical and glazing view. The effect of droplet size, and evaporation rate was taken into consideration. The contact angle measurements of GaN thin film were evaluated at room temperature using a First Ten Angstroms contact angle goniometer and a water drop of volume ~8 µL.

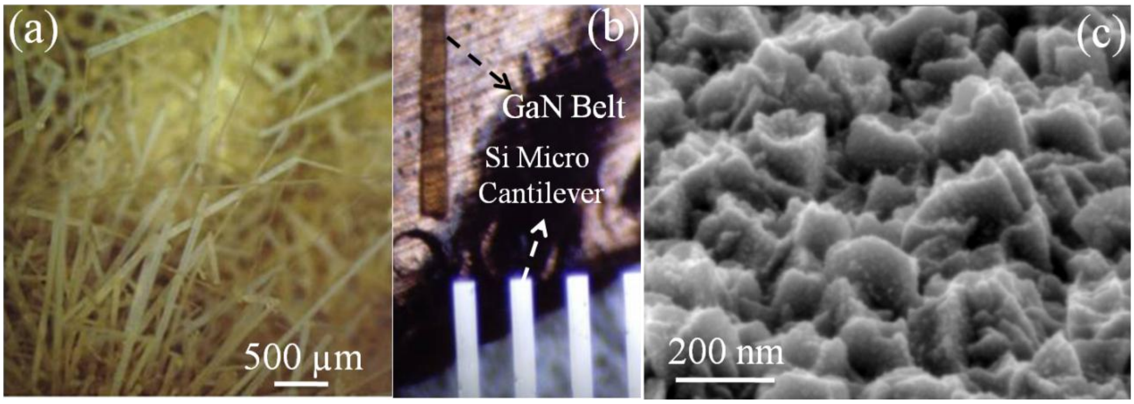

Fig. 4.15 Optical image of the microbelts (a) Optical microscopic image of free standing GaN microbelts; (b) show a comparative size of the microbelt to that of the silicon micro cantilever (width ≈100 µm); (c) FESEM image (tilted view) shows the presence of nanometer-sizes surface protrusions on the microbelts.

4.3.2.3 Wetting Properties of a Single Microbelt:

In-situ optical microscopic images show the liquid droplets delivered onto the commercially grown epitaxial GaN film [Fig. 4.16(a)] and microbelt [Figs. 4.16(b,c)]. As discussed earlier, roughness contributing to wetting properties, the area of the solid-liquid interface in the water drop is influenced by a factor of roughness parameter *r*, as described by the Wenzel model,[37]

$$Cos\ \theta^{*} = r\ Cos\ \theta \tag{1}$$

Where, θ^* is the resulting contact angle for a rough surface, θ corresponds to the contact angle on the equivalent flat surface. The roughness parameter *r* is the ratio of the real surface area to the projected flat surface area, thus always $r > 1$. This condition holds if there is no air entrained in the cavities of the roughness below the liquid. It can easily be understood from a Wenzel model that roughness drives the original contact angle, *i.e.*, a hydrophilic surface ($\theta < 90°$) that becomes more hydrophilic when the surface is rough ($\theta^* < \theta$). Conversely, a hydrophobic solid ($\theta > 90°$) shows increased hydrophobicity ($\theta^* > \theta$). In the case of a composite surface, however, a reduced contact area, φ_s between solid and liquid is introduced. At equilibrium, the apparent contact angle is given by the Cassie – Baxter model,

$$Cos\ \Theta = -1 + \varphi_s\ (Cos\ \theta + 1) \qquad (2)$$

Contact angle for the GaN epitaxial film (rms roughness 5 nm) is found to be θ =83° [Fig. 4.16(a)]. However, a contact angle $\Theta \approx 150°$ (±5°) is obtained for microbelts [Fig. 4.16(c)]. It still needs to be explained why a large contact angle ~ 150°, is found if the water droplet is deposited onto the microbelt at ambient condition. This discrepancy may reflect the inadequacy of the Wenzel's and Cassi-Baxer model. However, a sinusoidal model with special air entrapped cavity microstructure was being used to describe this discrepancy along with the actual shape of the meniscus present at the opening of the cavity.[38] A hint can be gained by looking at grazing incidence through the drop onto its lower interface [Figs. 4.16(b,c)]. One observes a shiny layer which is due to reflection of light at some air trapped in the surface structure. In this case, Wenzel's and Cassi-Baxer models are not anymore valid, and it has been shown that the contact angle can be increased if the air pockets underneath the liquid are allowed.[42] There are multiple equilibrium states for a drop on a rough surface. A particular shape of a drop, and therefore, the corresponding energy minima, strongly depend on the process by which the drop is formed as well as the special air-proof microstructure.

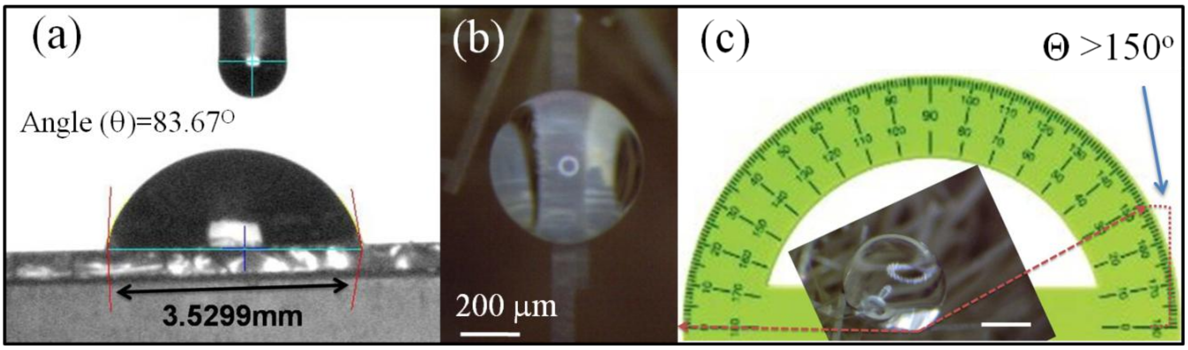

Fig. 4.16 Contact angle measurements a) GaN epitaxial thin film, b) Top view of a water drop on a single belt, c) contact angle of the liquid drop on the single micro belt. Scale bars are 200 μm.

4.3.3.4 Mechanism of Superhydrophobicity:

Nanoprotruded surface is processed by the ImageJ software analysis and correlated with the AFM data. The 3D interacting volume plot of the microstructure, analyzed using ImageJ software, reveals a sinusoidal [Figs. 4.17(a)] surface topography in all directions.[43]

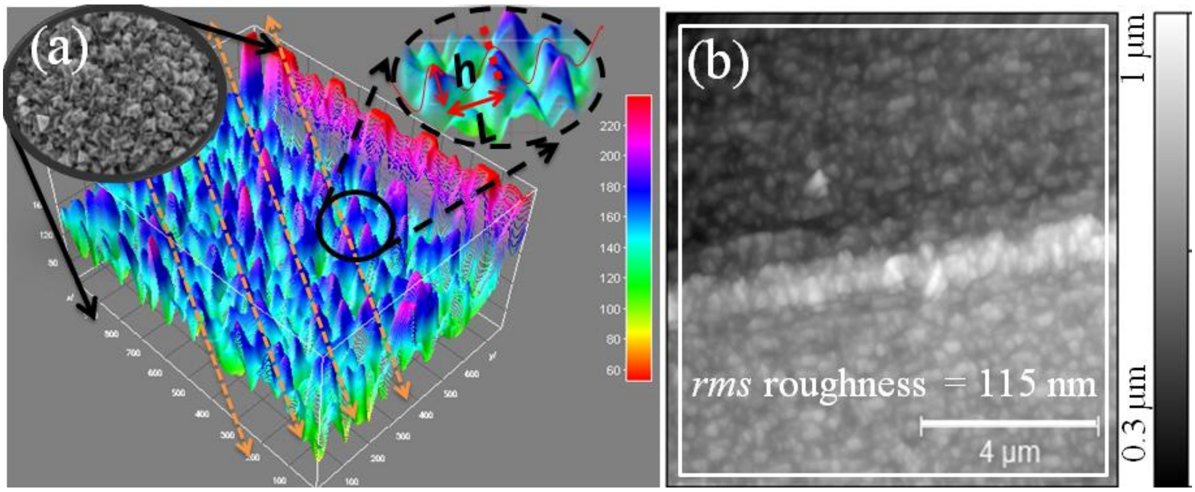

Fig. 4.17 (a) 3D interracting volum plot of the GaN microbelt surface by microscopic image analysis (ImageJ software) corresponding to the FESEM surface topography (inset, left corner); Inset (right corner) shows the magnified view as an indication of sinusoidal surface pattern, *L* (≈ 200 nm) is the length between each post and *h* (≈ 115 nm) being the height, (b) AFM microscopic image of GaN microbelt.

The sinusoidal pattern surface has an average amplitude of ~50 nm and the separations between two post is nearly ~200 nm with microstructure open to air. In analogous to AFM data, the rms value of roughness on the surface of the mcrobelts is found to be 115 nm [Figs. 4.17(b)]. This value is nearly equal to the calculated value of rms from the 3D interacting volume plot with a difference of ± 10 nm. The half of the rms value of roughness (~ 50 nm) is taken as the amplitude of each post which holds up the liquid for further calculation purpose. A careful observation from the from the 3D interacting volume plot reveals that there are formation of nanocavities in the vicinity of sinusoidal posts as shown in the figure 4.18(a).

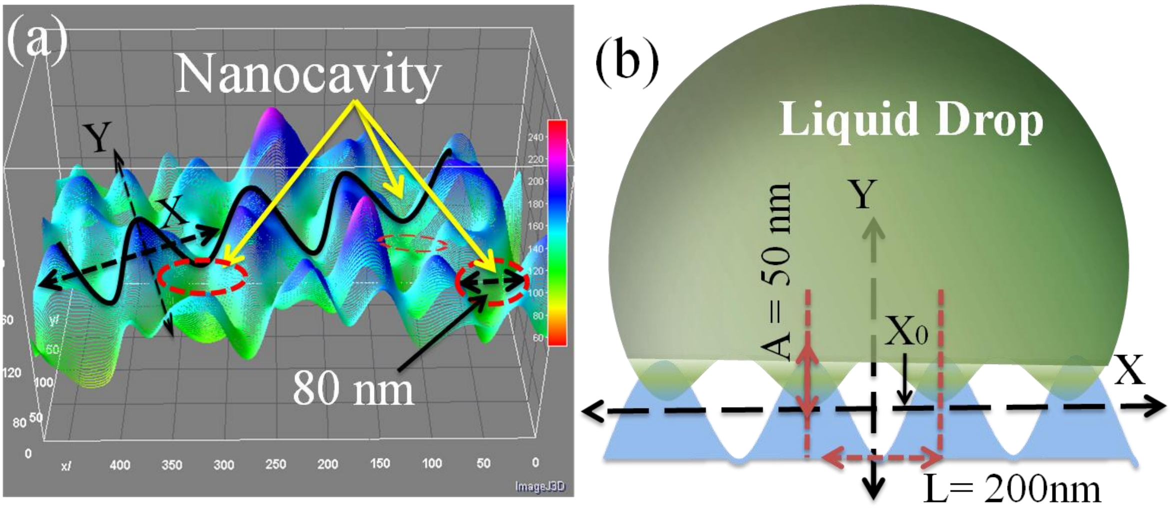

Fig. 4.18 Image analysis of microbelt surface (a) 3D surface plot of the typical microbelt, indicating the presence of nanocavities and (b) The shape of the meniscus at the triple contact point (x_0) within the sinusoidal surface.

The wettability could be better explained by considering a sinusoidal surface with a shape function of the form,[8] where the characteristic sizes are much smaller than that of the liquid droplet on it;

$$Y(x) = -A\cos(kx) \tag{3}$$

Here, A is the roughness amplitude (~50 nm), $k = 2\pi/L$ the wavenumber, and L the wavelength (~200 nm). The local contact state of the solid/liquid/vapor interface is schematically shown in figure 4.18(b), where the air between the liquid and the substrate is open to the atmosphere via the interconnecting microstructure. Such a state is governed by Cassie–Baxter model (or composite model). Young's equation is satisfied at the triple contact point x_0 [Fig. 4.18(b)].

Across the liquid/vapor interface, there is an over-pressure (Laplace pressure difference) in the liquid with respect to the exterior pressure, which is related to the surface curvature by,[44] $\Delta P = p_{in} - p_{out} = \frac{2\gamma}{R}$, where, p_{in} and p_{out} are the pressures in the liquid drop and the vapor phase, respectively, γ is the surface tension of liquid/vapor interfaces and R is the radius of curvature. The validation of the Cassie–Baxter model as well as the Wenzel model on a sinusoidal substrate requires $\Delta P > 0$ and should satisfy Young's equation, which predicts an invariably downward-concave meniscus to the hydrophobic surface. From the viewpoints of geometry and energy, in other words, a downward-concave vapor–liquid interface cannot exist within the period of the hydrophilic sinusoidal substrate, and the liquid must wet the whole substrate region beneath the droplet. As a result of the above geometrical restrictions, the Cassie–Baxter model cannot hold good for such a hydrophilic substrate with a sinusoidal surface microstructure. On the other hand, the Wenzel model can be always valid. So in case of a sinusoidal surface, open to air, the existence of Cassie–Baxter state of a hydrophilic substrate tends to be invalid.

Considering a special air proofed sinusoidal surface, Liu et al,[38] predicted a model to get a complete understanding of superhydrophobic states, no matter whether the substrate is hydrophobic or hydrophilic. The shape function of the meniscus formed within the airproofed sinusoidal microstructures can be written as;

$$Y = -A \cos (kx_0) - \sqrt{{R_c}^2 - x_0^2} + \sqrt{{R_c}^2 - x^2} \tag{4}$$

where R_c is the radius of the arc and x_0 is the triple contact point. For several specified values of the triple-point locations $\tilde{x}_0 = \frac{x_0}{L} = 0.4, 0.3, 0.2$ and 0.1 beneath the liquid droplet in a single valley, the corresponding meniscus shapes [Fig. 4.19(a)], where we set $\theta = 83^0$. It is seen that different contact positions of the triple line can be achieved with the variation of the Laplace pressure difference induced by the trapped air. This shows a convex meniscus shape of the liquid drop at the interface and reasonable validation of the Cassie–Baxter model. Besides geometrical limitation, the macroscopic Cassie-Baxter contact angle (Θ) is expressed considering the surface energy,[38]

$$\cos \Theta = 2 \cos \theta \int_{\tilde{x}_0}^{1/2} \sqrt{1 + (2\pi\tilde{A})^2}\, sin^2(2\pi\tilde{x}) d\tilde{x} \; - 2\tilde{R}\, arcsin \frac{\tilde{x}_o}{\tilde{R}}, \tag{5}$$

where $\tilde{x}$=x/L, $\tilde{A} = A/L$ and $\tilde{R}_c = R_c/L$. Accordingly, different triple-point positions produce different macroscopic contact angles. The underlying principle of the model describes the trapped air within the microstructure may generate a negative Laplace pressure difference across the interface. These isolated trapped air pockets by the liquid drop keep the balance at the interface, and cause to induce the superhydrophobic properties on a hydrophilic surface. The macroscopic contact angle is predictable from the Cassie–Baxter model, as shown in the plot [Fig. 4.19(b)] and in the schematic [Fig. 4.18(b)]. It is found that with increase in the absolute value of the negative Laplace pressure difference, $\tilde{x}_0$ increases along with the value of *Θ*. When $\tilde{x}_0$ is sufficiently large, a high contact angle of *Θ* = 150° is achieved on a hydrophilic belt.

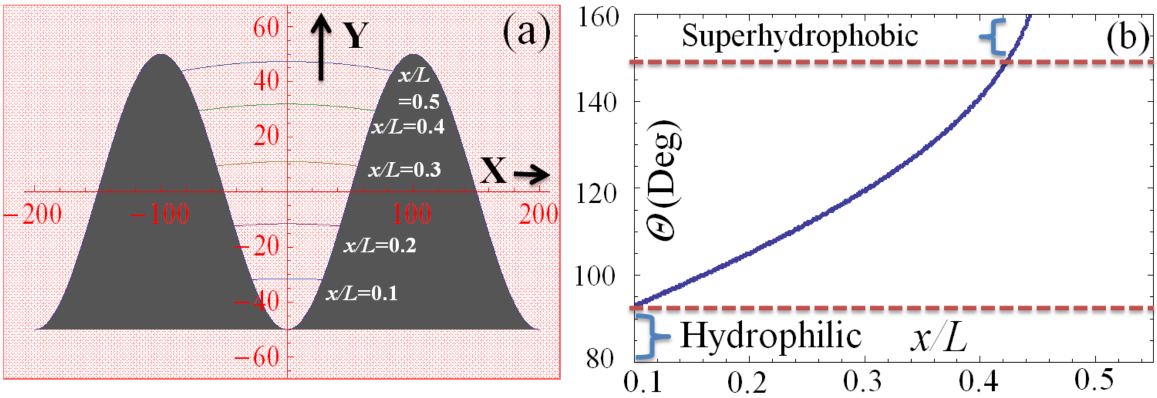

Fig. 4.19 (a) Shape of the meniscus formed in the vicinity of nanocavity at different *x/L* ratios, (b) The macroscopic contact angle (*Θ*) predicted by the Cassie–Baxter model as a function of the triple-point locations (*x/L*), calculated for a local contact angle *θ* = 83°.

From energy consideration, wetting surfaces are high energy ~ 0.5 – 5 Nm^{-1} (0.3-3 $eVÅ^{-2}$) surfaces where chemical binding energy is in the range of a few electron volts. The surface tension between GaN epitaxial thin film to air ($\gamma_{GaN/Air}$=1.89 Nm^{-1})[45] is 27 times higher than that of water to air ($\gamma_{water/Air}$= 0.0719 Nm^{-1}), and thus it should show a hydrophilic behavior. In contrary, superhydrophobic behavior is observed with a contact angle of nearly 150° on the microbelts. The dynamics of switching between hydrophilic to superhydrophobic is due to the presence of special air trapped cavity within the surface protrusions. In this case, by approximating the average cavity size of 80 nm [Fig. 4.18(a)], the pressure is calculated to be around 36 atm for water/air interface using Laplace pressure imbalance formula.[44] This extra pressure inside the bubble may lead to the transition from hydrophilicity to hydrophobicity.

4.3 Summary:

We have synthesized high-yield ultra-long single-crystalline and catalyst-free core–shell Ga_2O_3@GaN microbelts by a self-catalyzed vapor–solid growth process using chemical vapor deposition technique. FESEM, FIB, HRTEM, Raman and Photoluminoscence techniques are employed to characterize the detailed structural and optoelectronic properties of the as-grown core-shell Ga_2O_3@GaN microbelts. Most of these microbelts are well-ordered, and have a distinct shape with nanoprotrusions on their surface that are likely to be a model material over many compound semiconductor belts.

The existence of nanoprotrusion on the surface of the microbelt is shown to be very sensitive to humidity level in the atmosphere as compared to GaN thin films. We have demonstrated the variation of surface potential as a function of humidity level using Kelvin probe force microscopy. Oxide and oxinitride phases, as well as native defect complexes comprising of Ga vacancies and oxygen antisite, are assumed to be responsible for the surface charge accumulation leading to enhanced response to the surface potential variation as a measure of humidity. Furthermore, this study is particularly useful for calibration purpose for GaN based field-effect transistor sensors, where the sensor active area (GaN) is exposed to the electrochemical sensing of an environment. The outcome of this work shows that the electrical properties of GaN microbelts are sensitive to changes in compositional homogeneity as well as humidity. Therefore, a special attention should be given to humidity levels in the air to achieve the optimal value of GaN-based optoelectronic devices.

The self-affine topography and presence of air-trapped region within the vicinity of the nanoprotrusions of the microbelts are shown to be an ideal surface to generate superhydrophobic state. Surface microstructures have a significant influence on the wetting properties of solid surfaces. The mechanisms of superhydrophobic state stemming from a hydrophilic substrate is well explained after taking into account the presence of trapped air bubble presence in nanometer-sized cavities of GaN microbelts. The nanotextured surface described here shows a high degree of hydrophobicity and may find applications, e.g., in nanofluidics and will be useful in developing biocompatible nanobiosensor.

4.4 References:

1. Sahoo, P.; Dhara, S.; Dash, S.; Tyagi, A. K. *Nanoscience and Nanotechnology-Asia* **2011**, 1, 140.
2. Dong, Y.; Tian, B.; Kempa, T. J.; Lieber, C. M. *Nano Lett.* **2009,** 9, 2183.
3. Guo, W.; Zhang, M.; Banerjee, A.; Bhattacharya, P. *Nano Lett.* **2010,** 10, 3355.
4. Carnevale, S. D.; Yang, J.; Phillips, P. J.; Mills, M. J.; Myers, R. C. *Nano Lett.* **2011**, 11, 866.
5. Hsieh, C. H.; Chang, M. T.; Chien, Y. J.; Chou, L. J.; Chen, L. J.; Che, C. D. *Nano Lett.* **2008**, 8, 3288.
6. Lee, S.; Ham, M. H.; Myoung J M.; Lee, W. *Acta Materialia*. **2010**, 58, 4714.
7. Miao, J.; Chen, C-C.; Song, C.; Nishino,Y.; Kohmura, Y.; Ishikawa, T.; Johnson, D. R.; Lee, T-K.; Risbud, S. H. *Phys. Rev. Lett.* **2006**, 97, 215503.
8. Tong, J.; Risbud, S. H. *J. Solid State Chem.* **2004**, 177, 3568.
9. Xue, S.; Zhang, X.; Huang, R.; Zhuang, H.; Xue, C. *Dalton Trans*. **2008**, 32, 4296.
10. Bae, S. Y.; Seo, H. W.; Park, J.; Yang, H.; Park, J. C.; Lee, S. Y. *Appl. Phys. Lett.* **2002**, 81, 126.
11. Perea, D. E.; Hemesath, E. R.; Schwalbach, E. J.; Lensch-Falk, J. L.; Voorhees, P. W. *Nat Nanotech.* **2009**, 4, 315.
12. Sysoev, V. V.; Strelcov, E.; Sommer, M.; Bruns, M.; Kiselev, I.; Habicht, W.; Kar, S.; Gregoratti, L.; Kiskinova, M.; Kolmakov, A. *ACS Nano* **2010**, 4, 4487.
13. Sahoo, P.; Basu, J.; Dhara, S.; Fang, H.C.; Liu, C-P.; Ravindran, T. R.; Dash, S.; Tyagi, A.K. *J. Mater. Sci.* **2012**, 47, 3447.

14. Sahoo, P.; Dhara, S.; Dash, S.; Tyagi, A. K.; Das, C. R.; Chandramohan, P.; Srinivasan, M. P. *Int. J. Nanotechnol.* **2010**, 7, 823.
15. Lan, Z. H.; Liang, C. H.; Hsu, C. W.; Wu, C. T.; Lin, H. M.; Dhara, S.; Chen, K. H.; Chen, L. C.; Chen, C. C. *Adv. Funct. Mater.* **2004**, 14, 233.
16. Soignard, E.; Machon, D.; McMillan, P. F.; Dong, J.; Xu, B.; Leinenweber, K. *Chem. Mater.* **2005**, 17, 5465.
17. Reshchikov, M. A.; Morkoç, H. *J. Appl. Phys.* **2005**, 97, 061301.
18. Sahoo, P.; Oliveira, D. S.; Cotta, M. A.; Dhara, S.; Dash, S.; Tyagi, A. K.; Raj, B. *J. Phys. Chem. C* **2011**, 115, 5863.
19. Neugebauer, J.; Van de Walle, C. G. *Appl. Phys. Lett.* **1996**, 69, 503.
20. Garcia, M. A.; Wolter, S.D., Kim, T. -H.; Choi, S.; Baier, J.; Brown, A.; Losurdo M.; Bruno G. *Appl. Phys. Lett.* **2006**, 88, 013506.
21. Wagner, R. G.; Treuting, R. G. *J. Appl. Phys*. **1961**, 32, 2490.
22. Li, L.; Yu, K.; Wu, J.; Wang, Y.; Zhu, Z. *Cryst. Res. Technol*. **2010**, *45*, 539.
23. Pan, Z. W.; Dai, Z. R.; Wang, Z. L. *Science* **2001**, *291*, 1947.
24. Berven, C. A.; Dobrokhotov, V.; McIlroy, D. N.; Chava, S.; Abdelrahaman, R.; Heieren, A.; Dick, J.; Barredo, W. *IEEE Sen. J.* **2008,** 8, 930.
25. Lo, C. F.; Chang, C. Y.; Chu, B. H.; Pearton, S. J.; Dabiran, A.; Chow, P. P.; Ren, F. *Appl. Phys. Lett.* **2010**, 96, 232106.
26. Weaver, J. M. R.; Abraham, D. W. *J. Vac. Sci. Technol. B* **1991**, 9, 1559.
27. Narvaez, C.; Chiaramonte, T.; Vicaro, K. O.; Clerici, J. H.; Cotta, M. A. *Nanotechnol.* **2009**, 20, 465705.
28. Vicaro, K. O.; Cotta, M. A.; Gutiérrez H. R.; Bortoleto, J. R. R. *Nanotechnol.* **2003**, 14, 509.
29. Sadewasser, S.; Leendertz, C.; Streicher. F.; Lux-Steiner, M. C. *Nanotechnol*. **2009**, 20, 505503.
30. Hsu, J. W. P.; Ng, H. M.; Sergent A. M.; Chu, S. N. G. *Appl. Phys. Lett.* **2002**, 81, 3579.
31. Hansen, P. J.; Strausser, Y. E.; Erickson, A. N.; Tarsa, E. J.; Kozodoy, P.; Brazel, E. G.; Ibbetson, J. P.; Mishra, U.; Narayanamurti, V.; DenBaars, S. P.; Speck, J. S. *Appl. Phys. Lett.* **1998,** 72, 2247.
32. Lin L. M.; Lai, P. T. *J. of the Electrochem. Soc.* **2007**, 154, G58.
33. Thiel, P. A.; Madey, T. E. *Surf. Sci. Rep.* **1987**, 7, 211.
34. Shen, X.; Allen, P. B.; Hybertsen, M. S.; Muckerman, J. T. *J. Phys. Chem. C* **2009**, 113, 3365.
35. Bermudez, V. M.; Long, J. P. *Surf. Sci.* **2000**, 450, 98.
36. Lorenz, P.; Gutt, R.; Haensel, T.; Himmerlich, M.; Schaefer, J. A.; Krischok, S. *phys. status solidi C* **2010**, 7, 169.
37. Quere, D. *Annu. Rev. Mater. Res.* **2008**, 38, 71.
38. Liu, J. L.; Feng, X.-Q.; Wang, G.; Yu, S. W. *J. Phys.: Cond. Matter*, **2007**, 19, 356002.
39. A. G. Bhuiyan, A. Hashimoto and A. Yamamoto, *J. Appl. Phys.* **2003**, 94, 2779.

40. Feng, L.; Song, Y. L.; Zhai, J.; Liu, B. Q.; Xu, J.; Jiang L.; Zhu, D. B. *Angew. Chem. Int. Edn.* **2003**, 42**,** 800.
41. Sahoo, P.; Dhara, S.; Dash, S.; Raj, B.; Manna, I.; Tyagi, A.K. *Appl. Phys. Lett.* **2011**, 98, 043103.
42. Yang, J. T.; Yang, J. H.; Chen, C. Y.; Yao, D. J. *Langumir* **2008**, **24**, 9889.
43. Rasband, W. S. *ImageJ, U. S. National Institutes of Health, Bethesda*, *Maryland*, *USA*, http://rsb.info.nih.gov/ij/, 1997-2005.
44. Adamson, A. W. *Physical Chemistry of Surfaces* (Wiley-VCH, New York, 1990).
45. Dhara, S.; Magudapathy, P.; Nair K. G. M.; Raj, B. *J. Raman Spectrosc.* **2010**, 41, 628.

CHAPTER 5

GROWTH AND FUNCTIONALIZATION OF GaN NANOTUBES FOR CATALYTIC AND GAS SENSING APPLICATION

5.1 Introduction:

Hollow nanostructures with tailored structural, optical, and surface properties, has received considerable interest in a wide range of applications pertaining to catalysis, chemical sensing, nanocapillary electrophoresis, nanofluidics, drug delivery, fillers, and nano-optoelectronics.[1-4] Among different nanostructures, nanotubes (NTs) exhibit unique properties because of the unidirectional curvature and large surface areas. There is only a few published work on the growth of amorphous, polycrystalline, and single-crystalline GaN NTs, which are mostly realized by employing template, or using metal catalysts.[5-8] However, incomplete removal of template material, partial inclusion of catalyst into the tube annulus and high porosity in as-grown samples were major blocks in the fabrication process of high pure GaN NTs. To date, contamination-free direct fabrication of a GaN tubular structure has been a technical challenge. In the present work, an effort has been made to synthesize catalyst-free growth of GaN NTs via a quasi-VS process elucidating the underlying growth mechanism.

While looking towards the device performance using NTs, the role played by various functional groups in interface with zero-dimensional nanocrystallities assumes enormous importance.[9] Decoration of compound semiconductors with novel metal nanoclusters like Pd or Pt are of specific interest since these metals act as catalysts for numerous surface chemical reactions. An oxidation step is usually employed to specifically impart photocatalytic H_2 generation capability,[10] and to produce continuous hot electron flow in nanodiodes.[11-12] In addition, such a step usually enhances electrochemical activity[13] and H_2 sensing response across wide range of temperatures.[14,15] For example, there were several reports from Somorjai's group on the generation of steady state chemicurrent using a novel planar nanodiode device which employs 5-8 nm sputtered thin film of Pt over thick GaN film, and also often using metal-oxide bases.[11,12] They have achieved hot electron generation induced chemicurrent yield of $(3.5 \pm 0.8) \times 10^{-3}$ under catalytic reaction of O_2 or CO gas. Above value is found to be one order of magnitude higher than that for Pt/Pd-TiO_2.[11] There are several reports on Pt catalyzed carbon materials, metal oxides and metal-oxynitrides used in large scale solar energy assisted H_2 production from water.[16] Pt-loaded metal nitride nanoclusters depict superior quantum yield than oxide counterpart with respect to solar energy assisted H_2 production. However, studies on the metal-semiconductor interface structures, focusing morphology, crystallinity, and roughness and the local environments are important from several viewpoints as these aspects will ultimately control the efficiency of the end product generation process.

For some applications involving noble metals Pt or Au like hadron therapy,[17] radiotherapy, photo-thermolysis of cancer[18] and photocatalysis, it is often necessary to expose the materials to high levels of ionizing radiation such as laser light. This process is likely to induce secondary effects like phase transformation, melting or cleavage of materials. It is therefore, essential to know the thermal stability of the nanostructured materials in a catalytic environment. Recently, photo-assisted localized oxidation of group III- nitride thin films has been reported by Hwang et al. employing laser light onto water bridge between GaN thin film and Pt-coated atomic force microscopic (AFM) tip.[19] Several groups have also reported oxidation of GaN thin film using AFM, UV light assisted photo-induced wet chemical oxidation, anodic treatment, and often by high power laser irradiation.[20] Breakdown in single GaN NWs were reported by in-situ TEM characterizations.[21,22] These studies revealed that the semiconductor NWs break at the mid-point by means of thermal heating under the influence of high electric bias voltage (~35 V).[21] Individual NW breaks at a maximum temperature of ~ 1000 K via thermal decomposition.[22] However, the influences of catalysts on heat dissipation of GaN upon scaling down to lower dimensions and the effect on morphological evolution by laser power irradiation are not studied in detail.

5.2 Quasi Vapor-Solid Growth of GaN Nanotube:

5.2.1 Materials and Methodology:

NTs were synthesized using same CVD reactor used for the growth of GaN NWs.[23,24] The only difference maintained here is that the 3 nm Au coated Si substrate was kept horizontally at a height of 10 mm from the Ga source, whereas, the substrates were usually kept vertically from the Ga source for the growth of NWs. In addition, a faster temperature ramping rate of ~ 40 ^{o}C per min was maintained while increasing the temperature from 500 ^{o}C to 900 ^{o}C at a base pressure of 1 mbar. After the chamber temperature reached at 900 ^{o}C, the base pressure was slowly increased to 1 atm pressure in 10 minutes by bleeding high purity NH_3 gas at a flow rate of 10 sccm. The reaction was terminated after duration of 2 h. The system was allowed to cool down slowly to room temperature in the same NH_3 ambient. A large quantity of light yellowish material was found to be uniformly coated throughout the Si substrate. To identify the growth mechanism of NTs, the role of the most decisive growth parameters, namely, growth rate, temperature, and NH_3 partial pressure was taken into consideration.

5.2.2 Morphological and Structural Properties:

Figures 5.1(a-c) show typical FESEM images of the NTs on Si substrate. A highly dense GaN layer of thickness ~40 µm is seen over the Si substrate, as revealed from the cross-sectional image [Fig. 5.1(a)]. A close view of the magnified image at middle region [Fig. 5.1(b)] reveals that NTs are homoepitaxially grown over a layer of GaN nanoclusters with overall thickness ~5 µm [Fig. 5.1(c)]. The underlying GaN nanoclusters layer may have

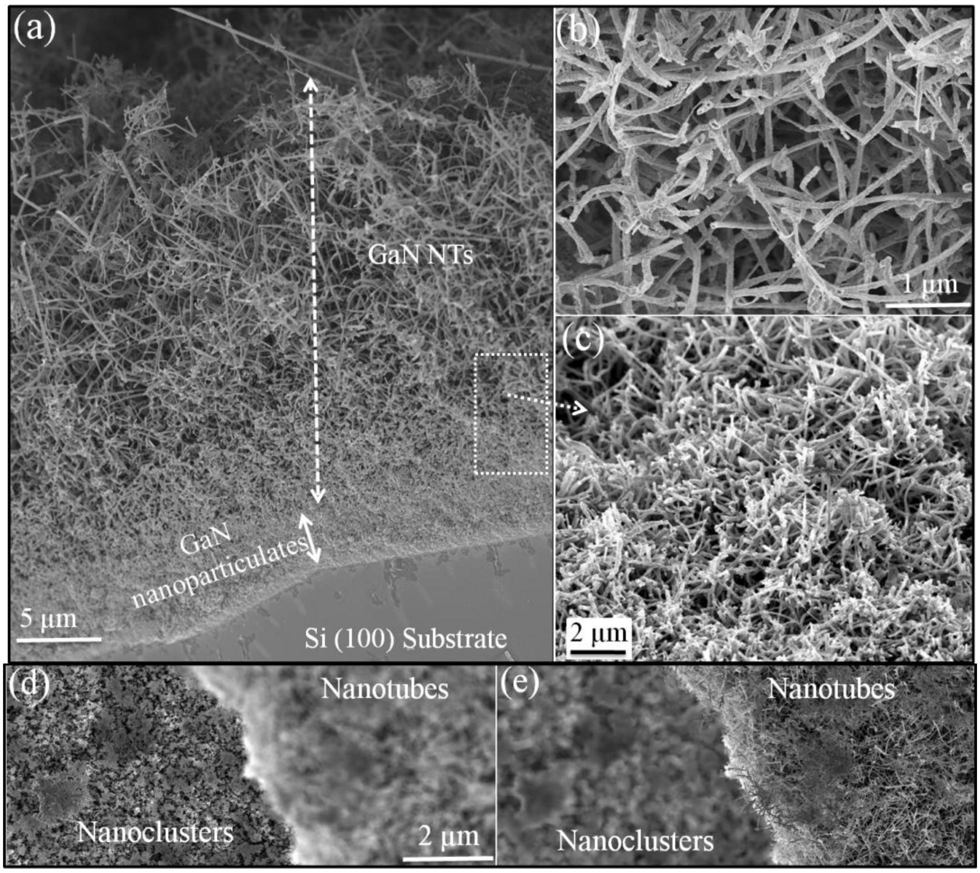

Fig. 5.1 FESEM image of GaN NTs grown on Si substrates; (a) cross-sectional view and (b) top view, (c) magnified view of the transition region from nanoclusters to NTs; Top view of GaN NTs grown over a thin layer of GaN nanoclusters by focusing on (d) GaN nanoclusters, (e) top surface of NTs.

acted like a buffer layer, which has initiated the NT formation. On mechanical scratching, it is found that the as-grown GaN NT layer can be smoothly removed from the nanocluster interface region. This is observed while focusing the of top and bottom part of as-grown GaN NT sample through FESEM [Figs. 5.1(d,e)]. It is worthwhile mentioning that NTs can be isolated without being contaminated with nanocluster impurity. The surface layer, as observed from the side [Fig. 5.1(b)] reveals that the GaN NTs are homogeneously distributed throughout the surface. Most of the NTs exhibit nearly square shaped cross-section [Fig. 5.2(a)] with wall thickness of about ~10-15 nm and average lateral dimensions of nearly ~ 50 nm [Fig. 5.2(b)]. A typical length extends to several micrometers. These images are recorded from the Pt nanocluster functionalized GaN NT samples (detailed in subsequent sections).

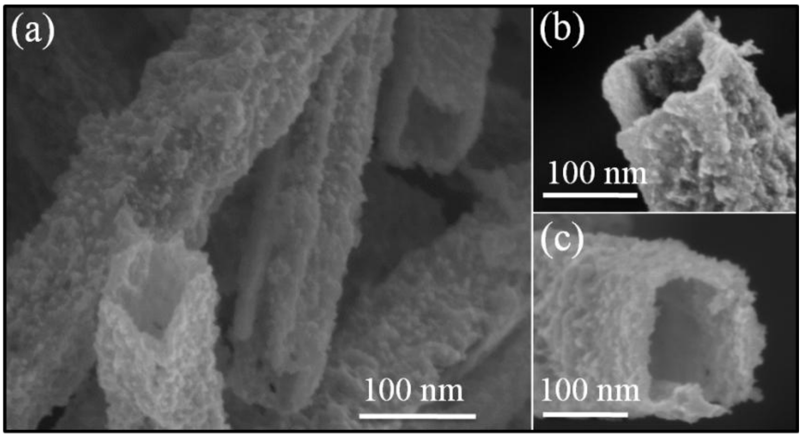

Fig. 5.2 FESEM images of the NTs with (a) and (b) square shaped (c) nearly square shaped facets.

Figure 5.3 shows the X-ray diffraction (GIXRD; Bruker D8 Discover) pattern of the as-synthesized GaN NTs. The peaks correspond to (100), (002), (101), (102), (110), (103) and (112) planes of hexagonal *WZ*-GaN phase with lattice parameter of a = 0.318 nm and c = 0.518 nm (JCPDS: 50-0792), while no cubic phase is found. All the peaks of the as-grown GaN NTs are relatively sharp and the value of the full width at half maximum (FWHM) has narrow peak width. The GIXRD analyses show that the GaN NTs possess well developed crystalline character. The structures of the individual GaN NT are further investigated by HRTEM analysis. The typical tube like contrast is observed [Fig. 5.4(a)]. The areas close to the edge are appearing darker than the central zone. The NTs exhibit uniform cross-section

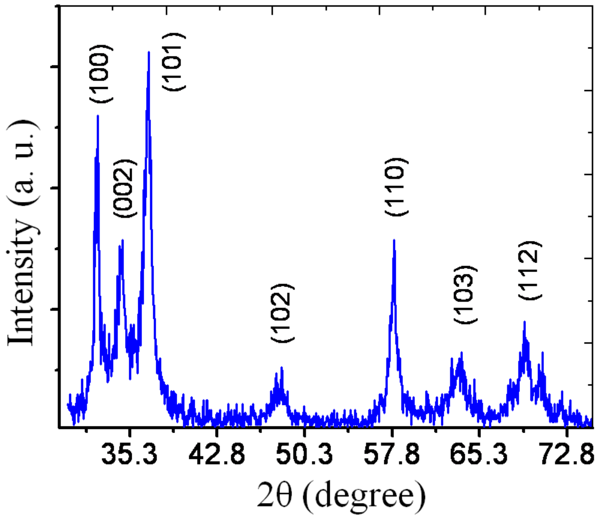

Fig. 5.3 GIXRD pattern of the as synthesized GaN NTs. The corresponding peaks are indexed to *WZ*-GaN phase.

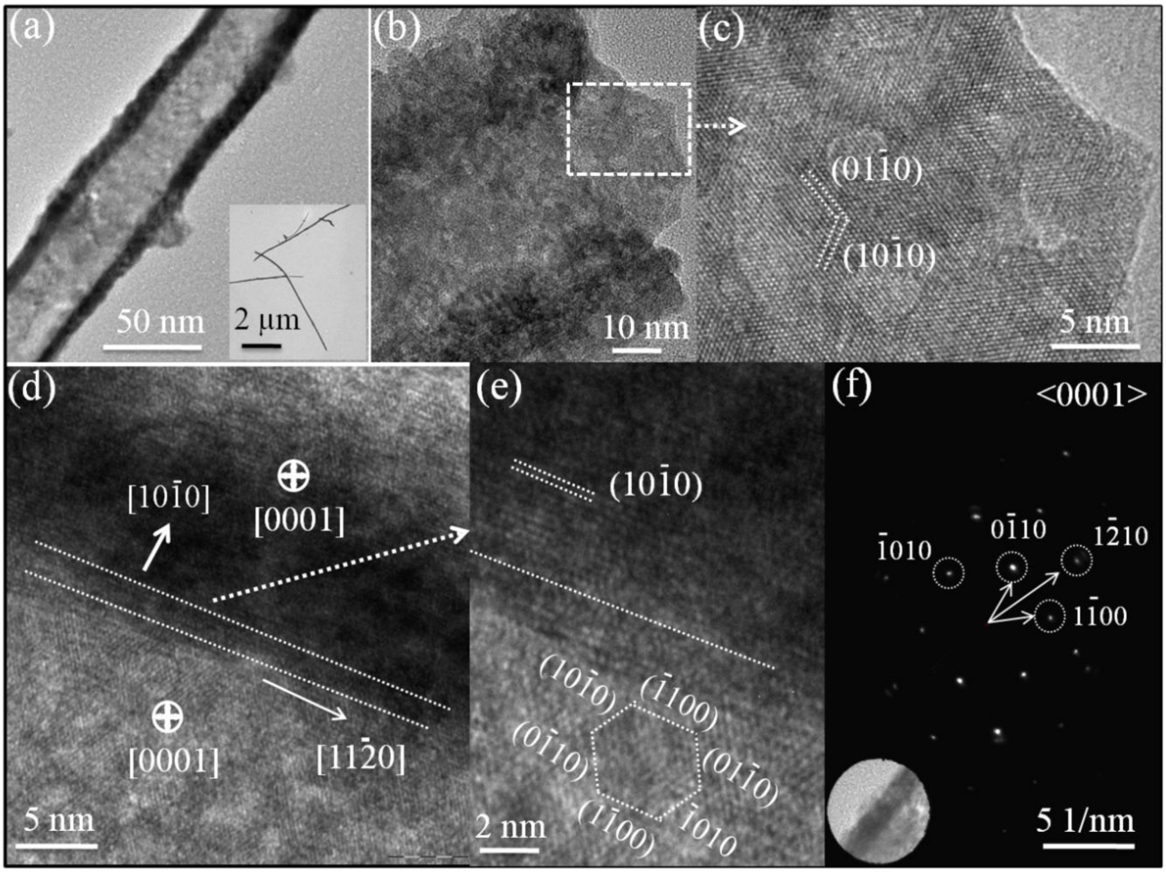

Fig. 5.4 (a) TEM images of a NT with visible side facets, (b) tube with open end, (c) lattice images of the NT shows presence of family of *m*-planes and growth direction along $[11\bar{2}0]$, (d) smooth transition between side facets and (e) corresponding lattice image; (f) SAED pattern of NTs shows *WZ*-GaN phase; Inset shows the region from which the pattern is generated.

and extend to several micrometers in length [inset Fig. 5.4(a)]. The external surface is relatively rough as seen from the HRTEM image [Fig. 5.4(b)]. The typical segment of the open end of a NT is shown in figure 5.4(c). Lattice pattern shows a family of *m*-planes with growth direction along$[11\bar{2}0]$. A smooth transition takes place between the side faces of the NT as indicated by the HRTEM image [Fig. 5.4(d)]. Further studies suggest that the tube surfaces are composed of (0001) planes and the tube axis is subtended along $[11\bar{2}0]$ direction, which is normal to *a* plane. The high resolution lattice image of the transition region, with the interface region at the corner over ~2 nm, is shown in figure 5.4(e). The *m* planes, orthogonal to *c* plane are indicated in the high resolution image. A typical SAED pattern along one of the facets shows zone axes along [0001] of *WZ*-GaN phase [Fig. 5.4(f)].

Faint spots close to the indexed diffraction spots in the SAED pattern indicate twin like features, which are essentially from the opposite facet of the NT having same crystalline orientation ([0001]) with a small tilt. The tilt is likely as the facets are not exactly parallel to each other. The observation, however, establishes the fact that all the facets are oriented along [0001] direction.

5.2.3 Growth Mechanism:

The growth mechanism of GaN NTs proceeds via a quasi-VS process. As depicted schematically in figure 5.5, it is postulated that the nucleation and further growth of the NTs might occur in following stages: 1) generation of ultra-small, nanosized GaN clusters on the substrate surface, 2) self-agglomeration and coalescence induced formation of facets, and 3) further oriented attachment of incoming vapor phase clusters to specific crystallographic facets.[8,24-26] In the present study, experiments are conducted with faster ramping rates, initially, to provide enough population density of Ga followed by the atomic nitrogen flux to start the nucleation process aided by Au catalyst. Under this condition, unlike the VLS process the reaction occurs faster than the effective incubation time, stimulating the formation of agglomerated nanoclusters. A longer incubation time is anticipated in the VLS process and Au-Ga interfacial energy drives a directional growth. Upon increasing the

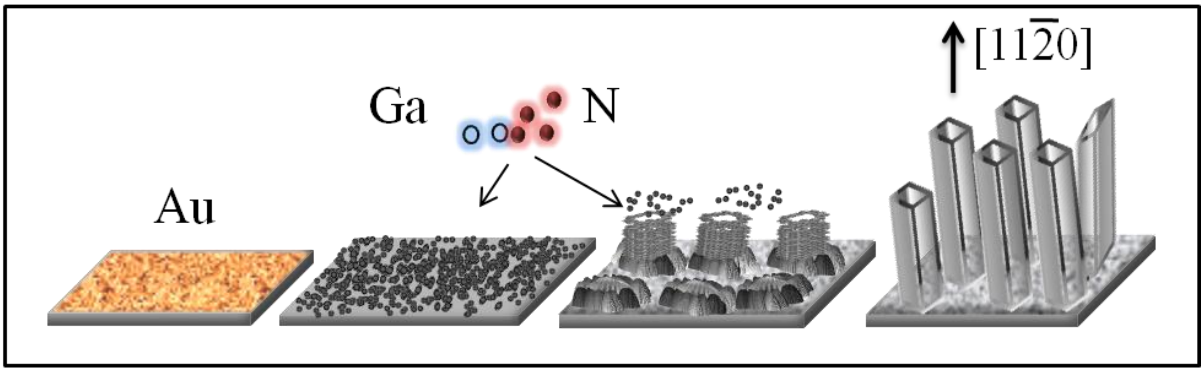

Fig. 5.5 Schematic representation of NT growth mechanism via quasi vapor-solid process in the CVD technique.

incoming Ga and N flux rate, the nanoclustes undergo further self-agglomeration process. The nucleation of facets leading to NT formation possibly stems from agglomeration of GaN clusters leading to coalescence process, which might form ring shaped nucleation front. Further, reactant species from the vapor phase is exposed continually over these nucleated facets leading to the formation of GaN NTs. The observed square or rectangular shape of NTs possibly results due to the differential adatom migration behavior among different crystallographic faces.[24] Faceting of nucleated grains stems from the fact that certain crystal faces are energetically disfavored for co-ordination with adatoms thereby restricting growth directions. The calculated surface energy for polar (0001) and non-polar $(11\bar{2}0)$ surfaces of GaN are 100 and 123 meV/Å, respectively.[27] Although, the difference of surface energy between the non-polar and polar surface is relatively small, nevertheless, they do behave differently to incoming adatom species. As a matter of fact, polar surfaces prefer systematic adsorptions, whereas non-polar surfaces maintain their stoichiometry by systematic atomic diffusions. The interaction between adsorbate and surface is strongly dependent on the most decisive parameter such as incoming Ga or N flux ratio. In Ga rich condition, a nonstoichiometric surface having Ga-Ga dimers is stable.[24,28] N-rich condition increases the nucleation rate of GaN due to the higher strength of the Ga-N bond and shorter diffusion length of Ga than that of Ga-Ga bond. It is thus apparent that, N-rich condition promotes stoichiometric growth of non-polar surface. The higher nucleation rate in the $(11\bar{2}0)$ surface over (0001) surface is expected to stimulate the axial growth of the NTs along $[11\bar{2}0]$. On the other hand, relatively lower surface energy along (0001) planes than that of the $(11\bar{2}0)$ plane promote formation of (0001) facets in the square symmetry, while the GaN system is in the hexagonal symmetry.

5.3 Functionalization of GaN Nanotube with Platinum Nanoclusters:

5.3.1 Materials and Methodology

For catalytic and sensor application, the as-grown NTs were functionalized with Pt nanoclusters using lysine [$HO_2CCH(NH_2)(CH_2)_4NH_2$] as a capping agent. Initially, GaN NTs were treated with 50% aqueous solution that contained a mixture of H_2SO_4: H_2O_2 (ratio 3:1) for a period of 5 min, and then washed with double distilled water followed by drying using N_2 gas. This process was often used for cleaning nitride surfaces as well as to activate hydroxyl groups on the surface. The hydroxylated samples were further dipped inside 3 ml of H_2O solution containing 1mM of lysine followed by addition of another 3ml of H_2O containing 1mM of $HPtCl_4$. The suspension was gently stirred for a period of 30 min, and then 3 ml of 0.1 M fresh $NaBH_4$ (slightly in excess) solution was added to reduce $HPtCl_4$ to metallic Pt. After stirring for further 30 min, the samples were washed with water and dried with flowing N_2 gas. This reduction invariably results in nanocrystallites of Pt.

5.3.2 Morphological and Structural Properties:

Figures 5.6(a,b) shows the FESEM image of Pt nanocluster functionalized GaN NTs (Pt-GaN) from top view and side view, respectively. The typical high-resolution image reveals that the Pt nanoclusters are uniformly spread over the GaN NT with different

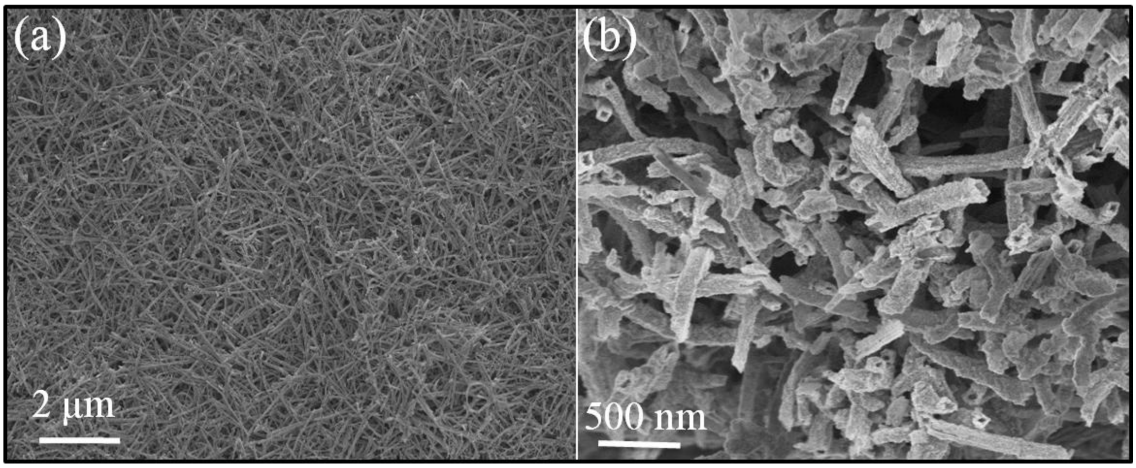

Fig. 5.6 FESEM image of Pt nanocluster functionalized GaN NTs (a) from top and (b) side view.

crystalline orientations [Fig. 5.7(a)]. The corresponding *d*-spacings are indexed to cubic Pt along with the presence of *WZ*-GaN calculated from the SAED pattern [Fig. 5.7(b)]. Figure 5.7(c) shows the bright field image of Pt decorated NTs and the corresponding dark field image is depicted in figure 5.7(d). These images are recorded by taking <111> diffraction spot of the Pt nanoclusters. The Pt-GaN NT exhibit relatively rough external surface as compared to that for the pristine NTs, as shown in the inset of figure 5.7(c). By analyzing a number of samples, the average size distribution of Pt nanoclusters is found to be ~1.6 nm (Fig. 5.8). It is further inferred from EDX analysis that along with the depth of the bulk sample, the present method of Pt functionalization provides an excellent spatial distribution of Pt (~ 1.5 atomic percentage) across a depth extending to well over 10 µm from the surface layer [Figs. 5.9(a-c)].

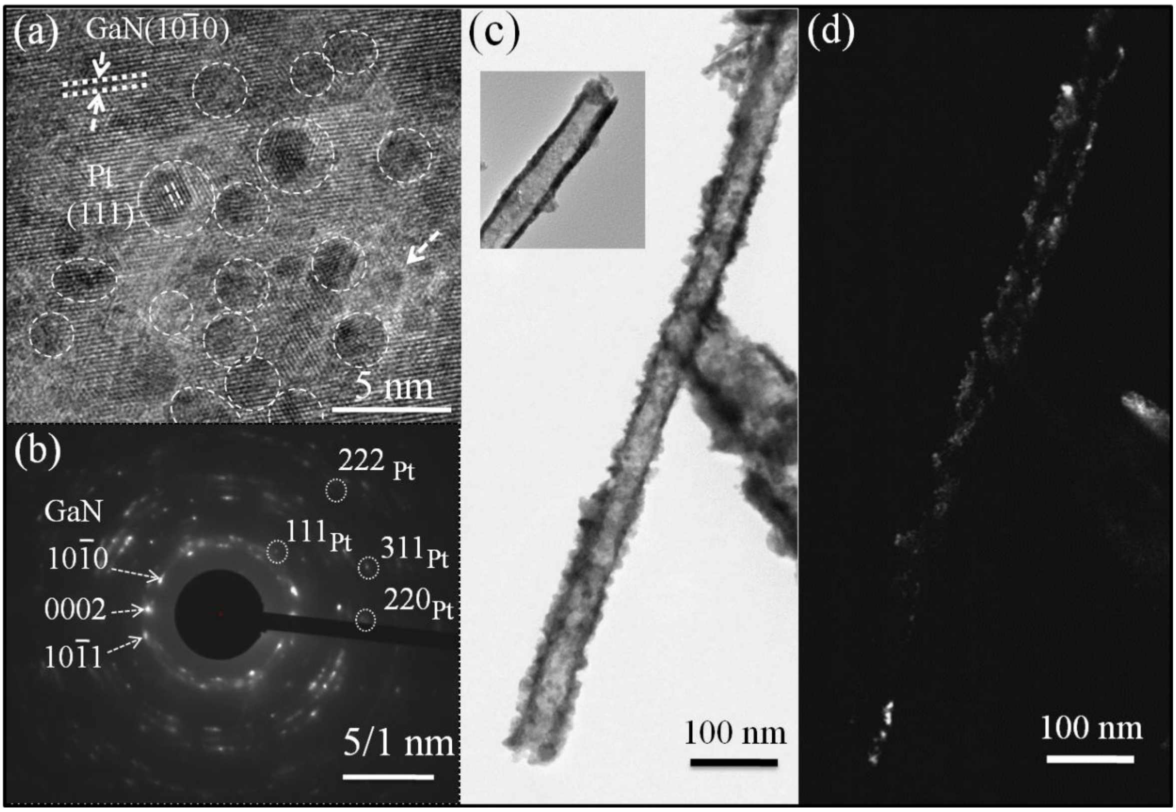

Fig. 5.7 (a) HRTEM images of Pt nanoclusters functionalized NT decorated on NT walls with different crystalline planes; (b) SAED pattern showing the presence of both the phases of *WZ*-GaN nanotube and cubic Pt nanoclusters; Corresponding bright (e) and (f) dark field image of Pt-decorated GaN NTs recorded by taking <111> diffraction spot of Pt; Inset shows a pristine NT.

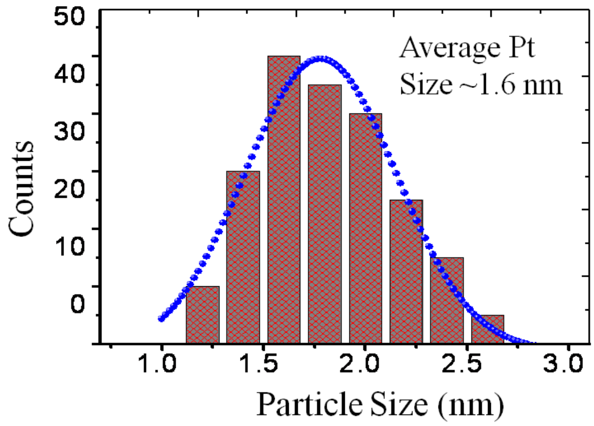

Fig. 5.8 shows the average size distribution of Pt cluster decorated on the NTs wall.

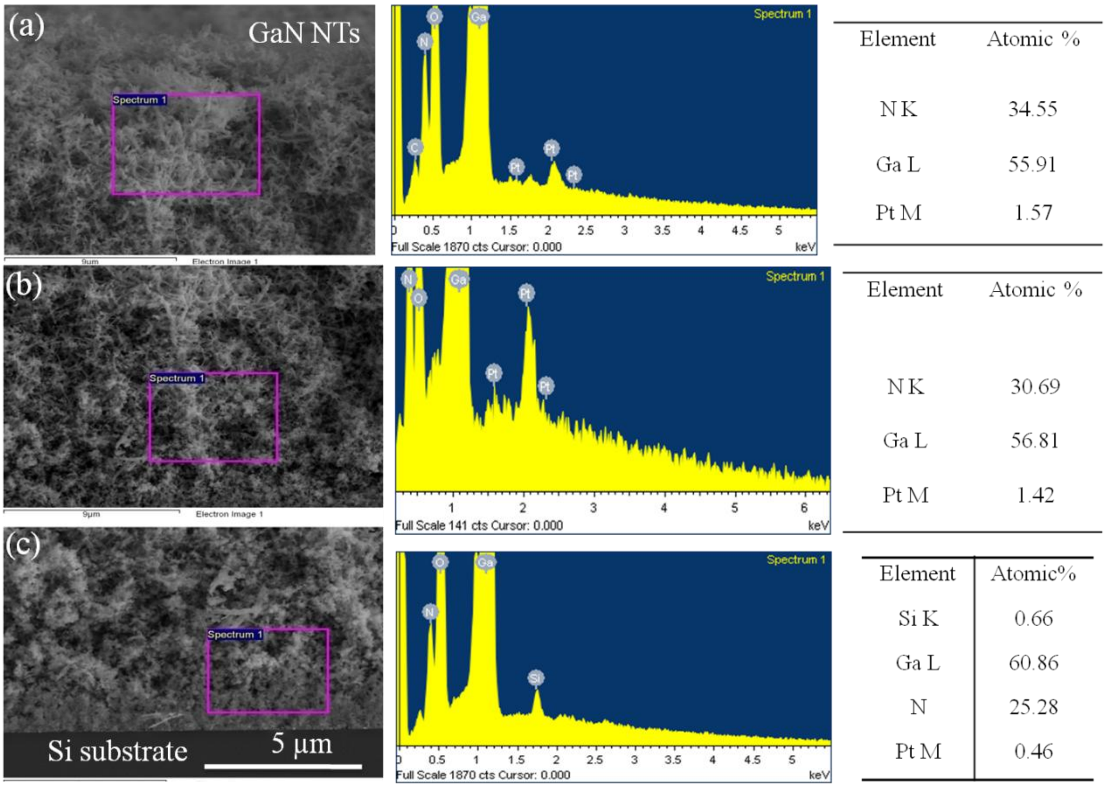

Element	Atomic %
N K	34.55
Ga L	55.91
Pt M	1.57

Element	Atomic %
N K	30.69
Ga L	56.81
Pt M	1.42

Element	Atomic%
Si K	0.66
Ga L	60.86
N	25.28
Pt M	0.46

Fig. 5.9 Cross-sectional FESEM images and the corresponding EDX analysis showing the distribution of Pt nanocluster in the (a) surface, (b) middle and (c) close to the substrate region of the GaN NTs.

5.4 Optical Properties:

Figure 5.10(a) shows the typical micro-Raman spectra of control NTs at incident laser power of 2 mW using 514.5 nm laser line. The Raman spectra reveal three fundamental modes with frequencies around 541, 571 and 732 cm^{-1}, which correspond to A_1(TO), E_2(high) and A_1(LO) phonon modes of *WZ*-GaN phase, respectively.[29] The spectra exhibit strong E_2(high) mode, blue shifted by 2 cm^{-1} with a broad line width of ~10 cm^{-1}. This may be attributed to small crystallite size. Similarly, LO mode is also blue shifted by 8 cm^{-1} with line width ~ 14 cm^{-1}. Additional peaks are attributed to ZB and SO phonons as described earlier. Low temperature micro-PL spectra of NTs show strong emission in the region of photon energy 3.0-3.6 eV [Fig. 5.10(b)]. The PL emission lines at 300 K (RT) possesses a broad and asymmetric line shape with weak band-edge-emission. Pt functionalization leads to a decrease of emission line by two orders of magnitude compared to the emission spectra of control NTs because of the quenching effect due to carrier transfer taking place between GaN and Pt nanoclusters. As temperature decreases to 80 K, the emission is dominated by a peak at 3.47 eV with a series of emission peaks centered at 3.24 and 3.30 eV. The peak at 3.47 eV corresponds to I_2 emission.[24] The I_2 emission possesses broad line shape of ~ 65 meV, which is blue shifted by 18 meV. This is attributed to the size effect in the NTs. The prominent

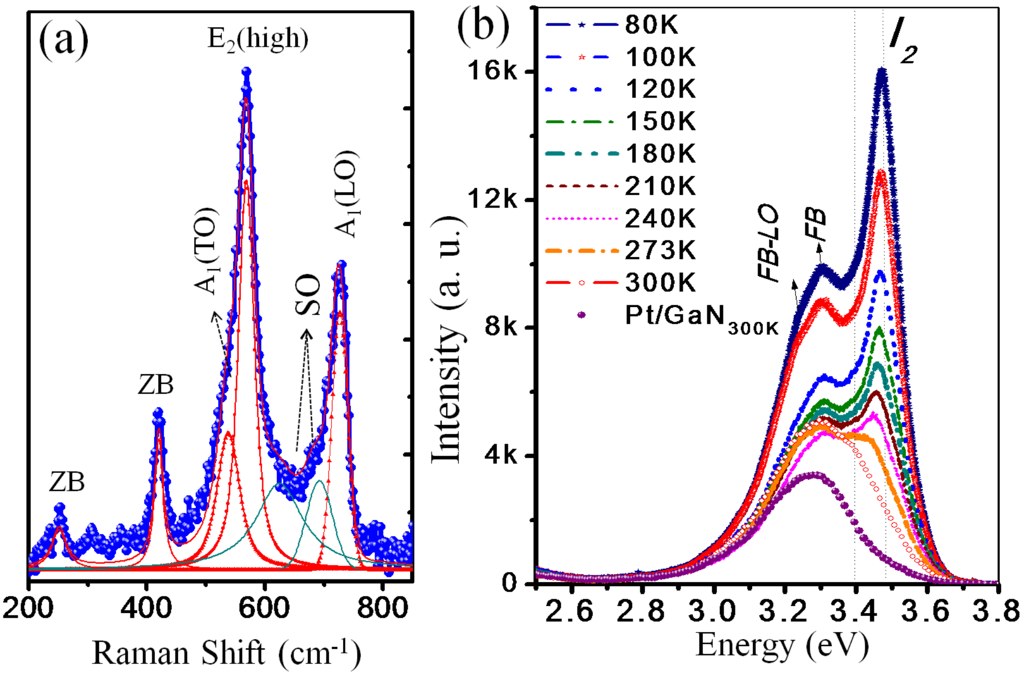

Fig. 5.10 (a) Raman spectra of GaN NTs at room temperature corresponding to *WZ*-GaN phase; (b) Low temperature micro-PL spectra of GaN NTs using 325 nm laser excitation. The spectra possess a strong I_2 line at low temperatures.

peaks observed at 3.3 and 3.24 eV have been assigned to zero phonon line and their phonon replica of the FB emission line, respectively.[30]

5.5 Laser Assisted Catalysis

The Pt nanoparticles are known to act as catalyst for numerous applications. Here, the catalytic activities of Pt nanoclusters functionalized over GaN NTs are demonstrated by coupling with high laser power and appropriate local ambience. Understanding the mode of catalytic action induced by the laser power is important from many technical points of view and for advanced optoelectronic applications.

5.5.1 Laser Induced Localized Oxidation and Photofragmentation of GaN Nanotube:

Figure 5.11(a) shows the typical micro-Raman spectra of control NTs at different incident laser power (2 - 40 mW) using 514.5 nm laser line. At low laser power (2 mW), all the Raman modes are corresponding to *WZ*-GaN phase. Upon increasing the laser power from 2 to 40 mW, while maintaining the same exposure time, it is observed that all primary modes are red shifted and asymmetrically broadened on the low frequency side, as plotted in figure 5.11(b). The E_2(high) mode, recorded at 40 mW laser power, is red shifted by ~4 cm^{-1} and the corresponding intensity increases by a factor of 12. The observed red shift can be attributed to the laser heating effect of the NTs and that the asymmetric line shape is apparently originated from Fano resonance, which arises as a result of interference between scattering from the k = 0 optical phonon and electronic continuum scattering from photo-generated carriers in the conduction bands.[31] However, there is no observation of structural evolution during the laser exposure. Notably, a peculiar scenario is observed on Pt-decorated NTs upon exposure with different laser power [Fig. 5.11(b)]. A structural change from *WZ*-GaN phase to monoclinic (β-) Ga_2O_3 phase occurs after irradiation with a threshold of laser power exposure above 4 mW [Figs. 5.11(c,d)]. The new peaks those evolveed, upon 20-40 mW of laser power exposure, correspond to mode frequencies of 147, 168, 200, 347, 416, 476, 630, 653, 766 cm^{-1} of β-Ga_2O_3 phase.[32] The origin of such chemical-structural evolution is deliberated in forthcoming sections.

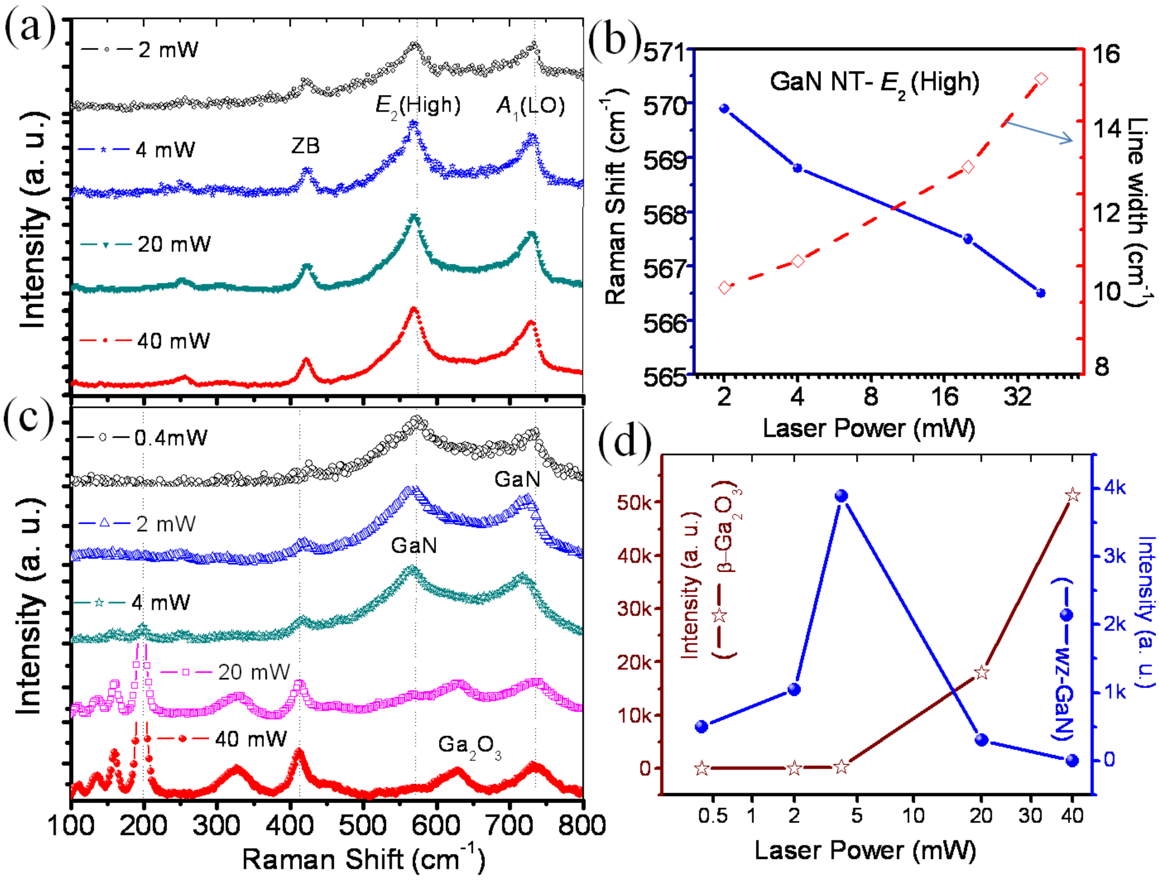

Fig. 5.11 Raman spectra recorded by varying the laser power from 2 to 40 mW of (a) control GaN NTs, (b) Pt decorated NTs; (c) laser power dependent change in the line width and Raman peak shift corresponding to E_2(high) mode of as-grown samples; (d) Raman intensity plots corresponding to β-Ga_2O_3 and *WZ*-GaN phases showing the evolution of the latter over the former.

Laser induced morphological transformation of NTs is clearly elucidated by analyzing the laser treated zone by FESEM [Fig. 5.12(a)] analysis. Pt-decorated GaN NTs, exposed to 20-40 mW laser irradiations, undergo immediate melting and fragmentation in ambient conditions. Hole burnt into the specimen is depicted in figure 5.12(a). A hole of diameter ~ 2 μm, which is nearly equal to the size of the laser beam gets engraved [Figs. 5.12(b,c)]. However, there was no noticeable mark of melting or damage corresponding to the exposure

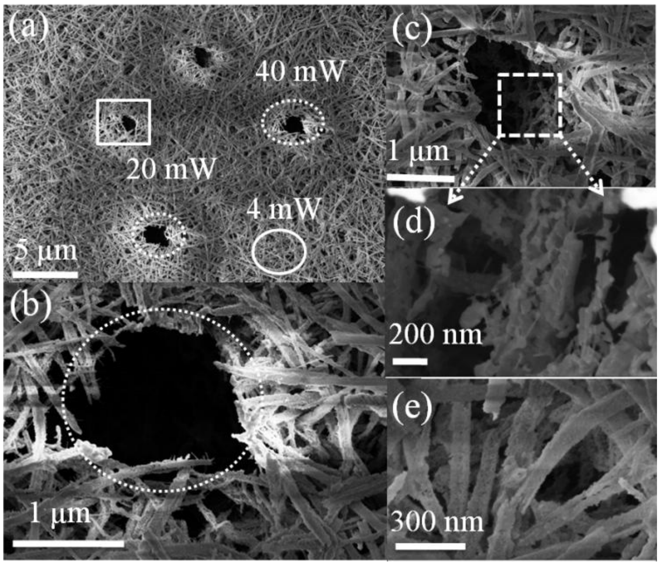

Fig. 5.12 (a) Laser induced photo-fragmentation of NTs with different laser power (4-40 mW), magnified image of the hole region at (b) 40 mW and (c) 20 mW laser power irradiation; (d) high resolution image of the photo-fragmented NTs and (e) along the close proximity of laser heated

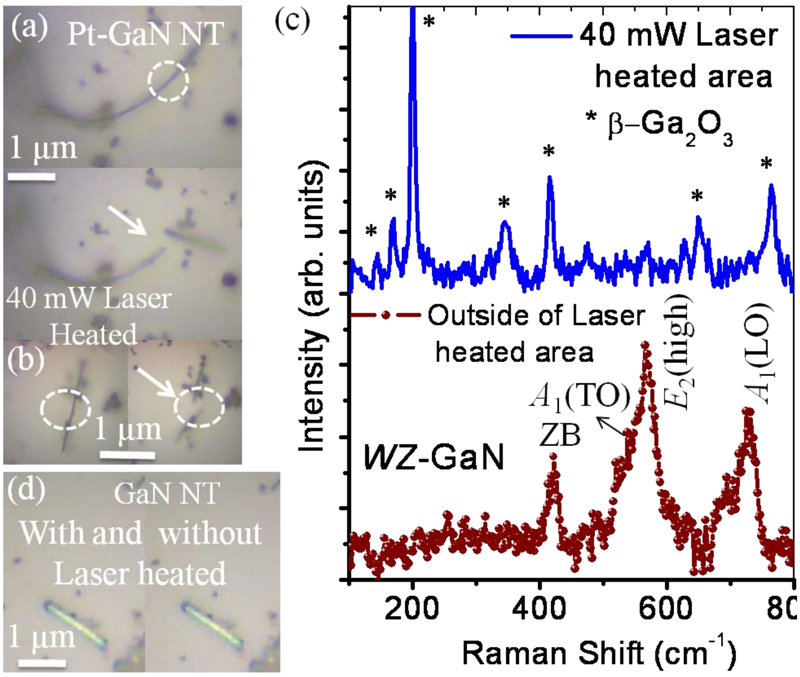

Fig. 5.13 Single Pt-decorated GaN NT before and after (a) 40 mW, (b) 20 mW laser irradiation; (c) Raman spectra of single Pt-decorated GaN NT within and outside of the laser heated area; (d) single control GaN NT before and after laser irradiation with 40 mW laser power.

below 4 mW laser power. Magnified image within the hole regions [Fig. 5.12(b) at 40 mW, and Fig. 5.12(c) at 20 mW] reveal that the NTs cleave into fragments. These fragments are constituted by Ga_2O_3 phase. Interestingly, a similar effect has been observed in case of a single Pt-decorated GaN NT dispersed over HOPG substrate [Fig. 5.13(a)]. Pt-decorated NT melts down in the vicinity of the laser exposed (40 mW) zone in less than 1 second duration, as indicated by the arrow in the microscopic images, recorded in a confocal mode [Figs. 5.13(a,b)]. Typical Raman spectra [Fig. 5.13(c)] of a single Pt-decorated GaN NT shows oxide phase formation within laser heated area. However, increase in laser power does not bring about any morphological changes for NTs [Fig. 5.13(d)]. As usual, no structural transformation was also observed (not shown in figure) without Pt decoration. From the aforementioned observations, a photocatalytically motivated local oxidation seems to have caused the crystallo-chemical transformation.

A photo-thermal process causing the enhanced rate of oxidation of the Pt-decorated surface is quite feasible. In order to further understand the synergistic effect of Pt catalyst and laser power dependent local oxidation, as well as melting of GaN NTs, the measurement temperature is varied from RT to 773 K while keeping the laser power below the threshold limit (4 mW) in air ambient (Fig. 5.14). The thermal heating process neither affects the oxidation nor induces any structural changes, as it is observed in the Raman spectra [Fig. 5.11(c)] for the case of RT laser exposure with power ≥ 20 mW. Hence, the observed

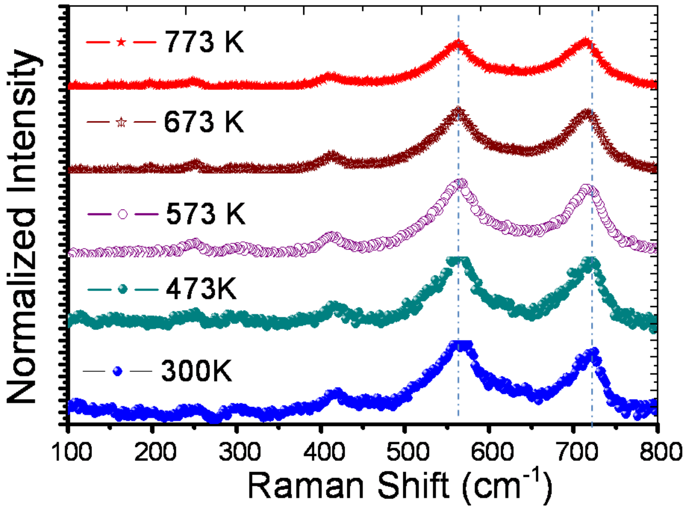

Fig. 5.14 Raman spectra of Pt-GaN NTs with increasing substrate temperature from RT to 773 K with 4 mW laser irradiation in air ambient. All the spectra correspond to *WZ*-GaN.

oxidation and melting of GaN NTs is definitively not as a result of localized thermal heating effect.[33] However, it is believed to be photocatalytic in origin. Figure 5.15(a) shows the low temperature Raman spectrum of Pt-decorated GaN NTs using 40 mW of 514.5 nm excitation acquired over 80- 473 K span under N_2 flow condition [Fig. 5.15(a)]. Remarkably, the oxidative process of transformation, presumably aided by catalytic process, is apparent even at 80 K. The spectra show two distinct phases, namely, β-Ga_2O_3 and *WZ*-GaN [Fig. 5.15(a)]. The relative intensities of the Ga_2O_3 phases are nearly similar over the full range of temperature [Fig. 5.15(b)]. It is to be noted that GaN phase is still observed in the N_2 ambient even after exposure with 40 mW laser power in the presence of Pt catalyst. Interestingly, any surface structural damage like melting and fragmentation of NTs is not noticed under aforementioned condition despite local oxidation. Hence, by suitably choosing the local ambience, catalyst and laser power, it is possible to oxidize localized pockets. This novel methodology, although simple, can find potential applications in nanoelectronics, namely, in CMOS devices and in-situ gate dielectrics.

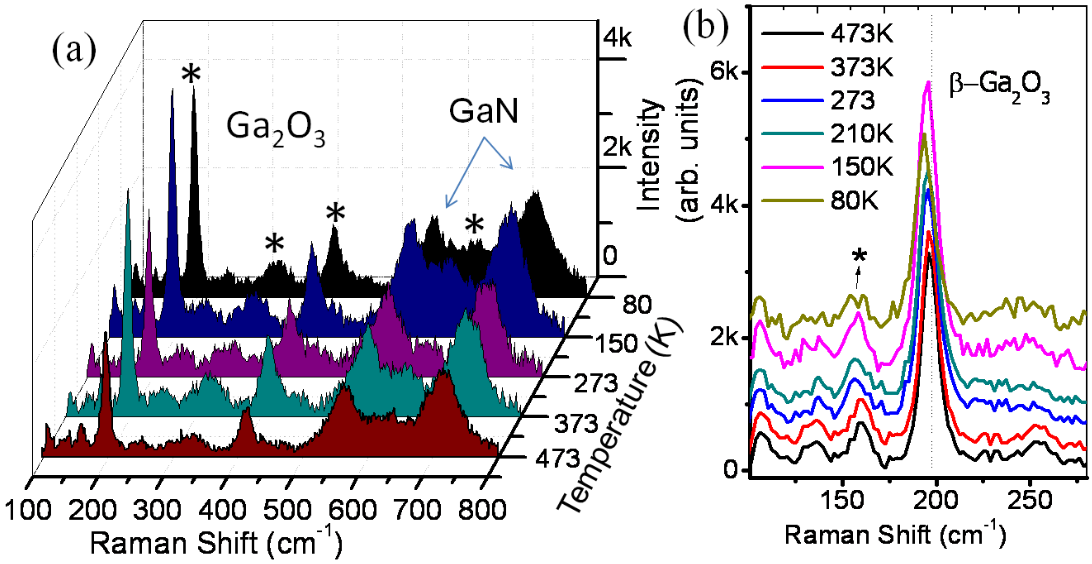

Fig. 5.15 (a) Raman spectra of Pt-decorated GaN NTs recorded from 80 K to 473 K with 40 mW laser irradiation in N_2 flow condition. All the spectra are indexed to two distinct phases, *WZ*-GaN and β-Ga_2O_3 (*); (b) The Raman intensity of 200 cm^{-1} peak corresponds to β-Ga_2O_3 phase with varying temperature.

5.5.2 Mechanism of Photocatalyzed Oxidation in Pt-GaN Nanotube:

The quantitative data obtained here is used to gain further insight into the mechanism of photocatalyzed oxidation of GaN NTs. There is a change in mode of catalytic action induced by the laser power in the presence of different local ambient; O_2 or N_2. It was shown by Baker et al.[34] that Pt nanocluster with diameter less than 25 nm could catalytically oxidize graphite in dry O_2 at temperature above 600 ^{o}C. It was found that Pt nanoclusters initiated formation of pits followed by channel propagation, usually along $< 11\bar{2}0 >$ direction, making 60 or 120 degree angle between them. Photo-thermal-catalytic processes initiated by laser incidence appear to preponderate over thermally activated process. Since the coverage of Pt nanocluster is uniform over the NTs, and the NTs possess a large number of dangling bonds and relatively small wall thickness (~10 nm), it is expected that the rate of oxidation is more appreciable. The process may form pits and channels, which may have initiated the rapid breakdown of specimens. The rate of channel propagation indeed depends on catalyst particle size. Smaller the particle size higher is the rate of channel formation due to an additional increase in the mobility, as observed in our case for Pt nanoclusters with diameter ~1.6 nm. The mode of action of the Pt nanocluster is further enlightened from the phenomenological view point of laser matter interaction. A photo-catalytic oxidative pathway appears mechanistically feasible. Recent studies reveal that high power laser irradiation raises local temperature of the metal nanocluster surface above the melting point leading to shape deformation.[18,35] In addition, there is a high probability of generation of multiple ionization states in noble metal nanoclusters as a result of high plasmon resonance absorption, during laser irradiation. For ultra short laser pulse, the high production of multiphoton ionization state leads to the Coulomb explosion and subsequent photo-fragmentation of the material.[18] Generation of multiple ionization states, mediated wide thermionic emission during laser irradiation, raises the temperature of metal nanoclusters higher than that of the surrounding medium. Meanwhile, the available native O_2 species may be oxidized and emits the hot electron that flows at the interface between nanocluster and NTs. The catalytically activated exothermic process can cause partial melting of GaN NT surface, which ballistically combines with ionized/radical O_2 to result in topographic transformation of a surface containing channels and pits.

Two distinct mechanisms are involved in bringing about the photo-fragmentation process. The exothermic step generates thermal energy that fails to get dissipated quickly in the GaN NT matrix due to poor thermal conduction. This eventually causes surface cracks and fragmentation which reveal a multitude of surface dangling bonds. These bonds ballistically combine with available photo-generated O_2 ionic / radical species, represented schematically in figure 5.16, to yield chemisorbed oxide layer of Ga_2O_3. Control of local ambience (flow of N_2 gas) by reducing the number of reactive O_2 species can reduce the rate of photocatalytic activity, which can modulate the photo-fragmentation process. Only a few literature are available on melting behavior of GaN NTs using molecular dynamic simulation.[36,37] The results reveal that NTs begin to melt at the surface, and then the melting rapidly extends to the interior of the NTs with increase in temperature. The anomalies in the melting behavior were reported by Wang et al., which showed that NT with $[10\bar{1}0]$ oriented lateral facets was having higher propensity towards melting than that for $[11\bar{2}0]$ oriented

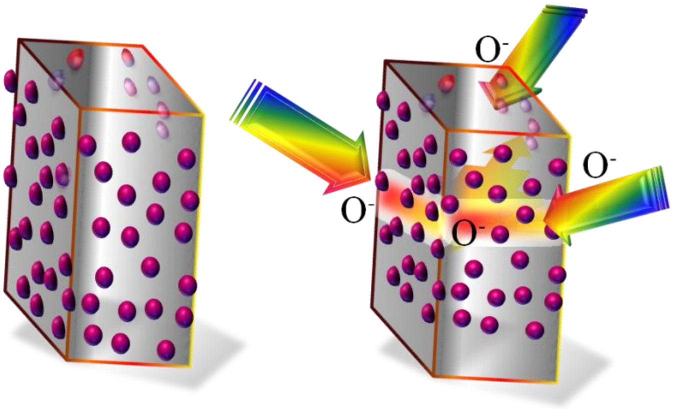

Fig. 5.16 Schematic representation of laser induced catalytic oxidation and photo-fragmentation region of Pt-decorated GaN NTs.

lateral facets for a given wall thickness.[36] Furthermore, surface roughness and phonon confinement can also contribute significantly to the reduction of the lattice thermal conduction, and the latter is more prominent at low temperatures. All the above phenomena significantly cause energy imbalance, which results in photo-fragmentation as a consequent dissipative pathway.

5.6 Hydrogen Sensing Properties of GaN Nanotube

There has been significant recent interest in the development of nanomaterial based gas and chemical sensor for the benefits of health, safety, and environments. In particular, H_2 sensors are of increasing importance in connection with its uses in fuel cells, nuclear reactor and in industrial applications.[42] Performance of any sensor is based on few important parameters, such as measuring range, sensitivity, selectivity, and response time. Apart from this, sensor operation at room temperature is of considerable interest in many areas of sensor technology. Comparative H_2 sensing performance of widely used materials with GaN NTs functionalized with Pt nanocluster is enlisted in table 5.1.

5.6.1 Materials and Methodology:

Mats of Pt functionalized GaN NTs were used for H_2 sensor. Prior to sensor application, the Pt coated samples were heated at 300 ^{o}C for 30 minutes to remove any unwanted lysine, used as a linker molecule between GaN NT and Pt nanocluster. H_2 sensor contact probes were made by sputtering a 5 nm Cr followed by 80 nm Au films on interdigitated electrodes with 1 mm spacing.

5.6.2 Pt Catalysed Hydrogen Sensing Properties of GaN Nanotube:

The H_2 oxidation on the Pt-decorated GaN NTs is investigated as a function of time over a wide range of H_2 concentration (25 - 200 ppm) in N_2 background, and temperature (RT to 473 K) as shown in figures 5.17(a,b). The material shows good sensitivity to H_2 with

Table 5.1 Comparative H_2 sensing properties of selected promising nanomaterials to that of values reported in this work.

No	List of Material	T (ºC)	**H_2 Sensor**				Remarks
			Detection Level (ppm)	Sensitivity $\lvert\Delta R\rvert/R$ - ppm	Response time	Reaction time	
1	Multiple GaN NWs + Pt coated	RT	200-2000	~1.7% at 200ppm ~1.9% at 2000ppm	600s	120	7.3 kcal mol^{-1} 2000ppm [14]
2.	Multiple GaN NWs + Pd	RT	200-2000	7.4% at 200 ppm 9.1% at 1500 ppm	~600s expo.	120	Schlocky diode [15]
3.	Multiple GaN NWs / Ga_2Pd_5 Nanodot	RT	100 to 2000	~ bare samples: 0.58% ~34.1% at 100 ppm	600s at 200 ppm	300 1000 ppm	[39]
4.	Pd-single walled CNT ~10KΩ	RT	100-3000	0.42%	480s~ 300ppm	≥20min 100ppm	~Recovery Faster in Humid air [40]
5.	ZnO Nanorods + Pd	RT	10-500	2.6% at 10, 4.2% at 500	600s exposure	20s by Air	[41]
6.	SnO2 Nanowire Pd	200	10 to 1000	0.2	0.4	---	[42]
7.	Pd nanocrystaline NWs (5nm, 15nm)	RT	---	1.0%	1-5 s		-High sensitivity -Unstable [43]
8.	Pt- Graphene/SiC	175	1%	--	700s	700s	[44]
9.	GaN Nanotube + Pt nanocluster	RT	25	0.4% 3.8% at 100 ºC	120 sec	300 s	In this work

response time of 120 sec and recovery time of about 5 min at RT. At RT, Pt-decorated GaN NTs show relative sensitivities of 0.4 at 25 ppm, and 0.95 at 100 ppm level for H_2, which are factors of 10 as compared to that shown by control NTs. However, the relative sensitivities of H_2 increased to 3.8 at 25 ppm and 10.8 at 100 ppm at 373 K [Fig. 5.17(c)]. The reported value of 25 ppm of H_2 at RT using the NTs, in the present study, is the lowest ever reported in the GaN system. Wright et al.[14] reported the previous lowest value with a relative response of 1.7 at 200 ppm of H_2 for 7 nm Pt sputter-coated GaN NWs with longer exposure time ~10 min at RT and 0.1 V bias condition. By comparison, Pt functionalized GaN NTs are found to be more sensitive than Pt sputter-coated on GaN NWs. Thus the uniform distribution of Pt

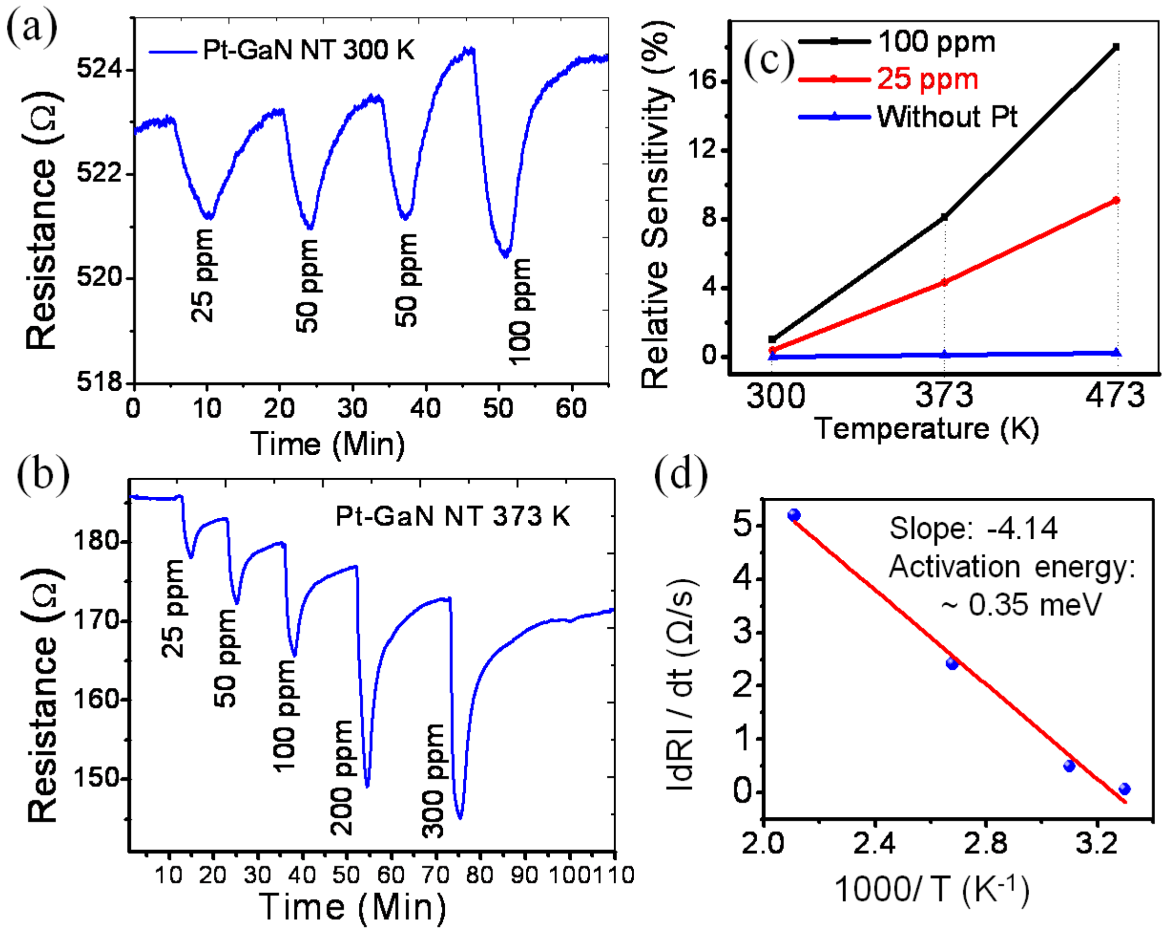

Fig. 5.17 Time dependent changes in resistance of Pt decorated GaN NTs at (a) RT and (b) 373 K with different H_2 concentration; (c) relative sensitivity to H_2 at different temperatures for Pt coated and control NTs; (d) Arrhenius plot of the rate of change in resistances for the highest change in resistance (10-30 sec) with temperature.

nanoclusters over NTs, using green chemistry methodology in the present study, is advantageous over sputter-coated film, and found to be more effective in catalytic dissociation of molecular H_2 at RT. An Arrhenius plot of the rate of change of resistance in Pt-decorated NTs with temperature is used to calculate the adsorption activation energy of 0.35 meV [Fig. 5.17(d)]. The value obtained here is found to be the lowest ever reported, as compared to other GaN systems. The calculated activation energy is well below the reported value of ~ 300 meV for Pt and Pd sputtered GaN NWs,[14,15] which confirms the superiority in sensitivity and responsivity of our GaN NT based H_2 sensor.

5.6.3 Mechanism of Hydrogen Sensing in GaN Nanotube:

There is growing evidence which indicates that Schottky barrier formed between the metal and semiconductor surface gets altered as a result of a chemical reaction at the interface.[45] Upon interaction with H_2 the excess electrons, generated as a result of catalytic oxidation of H_2 on Pt active sites, can easily exceed the Schottky barrier, and travel ballistically through the metal conduction band. These electrons possibly reach at the semiconductor surface where it would contribute to the conduction process resulting in the decrease of resistance at Pt-decorated GaN NTs interface. The low activation energy of Pt-decorated GaN NTs interface and small Pt nanocluster size distribution enhance the catalytic dissociation of H_2 through a non-adiabatic energy transfer route leading to a high value of sensitivity. Such H_2 sensor has also an important advantage over others in terms of the fact that the sensing elements can be effectively integrated with GaN based electronics leading to further miniaturization.

5.7 Summary:

Single crystalline GaN NTs with regular square facets are synthesized using the CVD technique. The NTs nucleate via a quasi VS process followed by self-agglomeration induced facet formation limited by the differential growth rate along crystallographic faces. Green way of functionalizing NTs with well dispersed Pt nanoclusters exhibit noble catalytic properties. Catastrophic sensitization of Pt nanoclusters in GaN NTs matrix, leading to the rapid oxidation and photo-fragmentation process, can be controlled by modulating the gas phase kinetics as well as tuning the laser power irradiation. It is, thus, apparent that the sensitization of Pt nanoclusters is enhanced due to auto-amplified electronic cascades inside the nanoclusters, which reinforces the energy deposition in the close vicinity of the metal and semiconductor interface during gas phase kinetics as well as on high power laser irradiation. The process can be termed as laser-assisted catalysis.

H_2 induced decrease in resistance has been measured to the lowest value of 25 ppm level at RT with activation energy of 0.35 meV for Pt-decorated GaN NT surfaces, as compared to other GaN systems. These ideal surfaces can be used for multiple applications in realizing high throughput optoelectronic devices and sensors. The integration of nanoelectronic components with inbuilt sensing potential in a single microchip can go hand in hand.

5.8 References:

1. Goldberger, J.; Fan, R.; Yang, P. *Acc. Chem. Res.* **2006**, 39, 239.
2. Fan, H. J.; Gcsele, U.; Zacharias, M. *Small* **2007**, 3, 1660.
3. Lu, W.; Lieber, C. M. *Nat. Mater* **2007** 6, 841.
4. Sahoo, P.; Dhara S.; Dash. S.; Tyagi, A.K. *Nanoscience & Nanotechnology-Asia* **2011**, 1, 140.
5. Goldberger, J.; He, R.; Zhang, Y.; Lee, S.; Yan, H.; Choi, H.J.; Yang, P. *Nature* **2003**, 422, 599.
6. Hu, J.Q.; Bando, Y.; Golberg, D.; Liu, Q.L. *Angew. Chem. Int. Ed.* **2003,** 42, 3493.
7. Ding, S.; Lu, P.; Zheng, J.G.; Yang, X.; Zhao, F.; Chen, J.; Wu, H.; Wu, M. *Adv. Funct. Mater*. **2007**, 17, 1879.
8. Mohammad, S. N. *J. Chem. Physics.* **2007**, 127, 244702.
9. Yamada, Y.; Tsung, C-K.; Huang, W.; Huo, Z.; Habas, S.E.; Soejima, T.; Aliaga, C.E.; Somorjai, G. A.; Yang, P. *Nat. Chemistry* **2011**, 3, 372.

10. Chen, X.; Shen, S.; Guo, L.; Mao, S. S. *Chem. Rev.* **2010**, 110, 6503.
11. Park, J. Y.; Renzas, J.R.; Hsu, B.B.; Somorjai, G. A. *J. Phys. Chem. C* **2007**, 111, 15331.
12. Ji, X.; Zuppero, A.; Gidwani, J. M.; Somorjai, G. A. *J. Am. Chem. Soc.* **2005**, 127, 5792.
13. Chen, J.; Lim, B.; Lee, Eric P.; Xia, Y. *Nano Today* **2009**, 4, 81.
14. Wright, J. S.; Lim, W.; Gila, B. P.; Pearton, S. J.; Johnson, J. L.; Ural, A.; Ren, F. *Sens. Actus. B* **2009**, 140, 196.
15. Lim, W.; Wright, J. S.; Gila, B. P.; Johnson, J. L.; Ural, A.; Anderson, T.; Ren, F.; Pearton, S. J. *Appl. Phys. Lett.* **2008**, 93, 072109.
16. Maeda, K.; Higashi, M.; Lu, D.; Abe, R.; Domen, K. *J. Am. Chem. Soc.* **2010**, 132, 5858.
17. Porcel, E.; Liehn, S.; Remita H.; Usami, N.; Kobayashi, K.; Furusawa, Y.; Sech, C.L.; Lacombe, S. *Nanotechnology* **2010**, 21, 085103.
18. Letfullin, R. R.; Joenathan, C.; George, F. T.; Zharov, P. V. *Nanomedicine* **2006**, 1, 473.
19. Hwang, J. S.; Hu, Z. S.; You. Z.Y.; Lin, T. Y.; Hsiao, C-L.; Tu, L.W. *Nanotechnology* **2006,** 17, 859.
20. Hwang, J. S.; Hu, Z. S.; Lu, T. Y.; Chen, L. W.; Chen, S. W.; Lin, T. Y.; Hsiao, C-L.; Chen, K-H.; Chen, L-C. *Nanotechnology* **2006**, 17, 3299.
21. Westover, T.; Jones, R.; Huang, J.Y.; Wang, G.; Lai, E.; Alec, Talin, A. *Nano Lett.* **2009**, 9, 257.
22. Zhao, J.; Sun, H.; Dai, S.; Wang, Y.; Zhu, J. *Nano Lett.* **2011**, 11, 4647.
23. Sahoo, P.; Dhara, S.; Dash, S.; Amirthapandian, S.; Tyagi, A. K. *J. Nanopart. Res.* (Under Review)
24. Sahoo, P.; Dhara, S.; Amirthapandian, S.; Kamruddin, M.; Dash, S.; Tyagi, A. K. *Cryst. Growth Des.* **2012**, 12, 2375.
25. Cheze, C.; Geelhaar, L.; Jenichen, B.; Riechert, H. *Appl. Phys. Lett.* **2010**, 97, 153105.
26. Consonni, V.; Hanke, M.; Knelangen, M.; Geelhaar, L.; Trampert, A.; Riechert, H. *Phys. Rev. B* **2011,** 83, 035310.
27. Northrup, J. E.; Neugebauer, J. *Phys. Rev. B* **1996**, 53, R10 477; Northrup, J. E.; Neugebauer, J.; Feenstra, R. M.; Smith, A. R. *Phys. Rev. B* **2000,** 61, 9932.
28. Lymperakisand L.; Neugebauer, J. *Phys. Rev. B* **2009**, **79**, 241308.
29. Sahoo, P.; Dhara, S.; Das, C.R.; Das, S.; Tyagi, A. K.; Raj, B. *Int. J. Nanotechnology*. **2010**, 7, 823.
30. Reshchikova, M. A.; Morkoç, H. *J. Appl. Phys.* **2005**, 97, 061301.
31. Gupta, R.; Xiong, Q.; Adu, C. K.; Kim, U. J.; Eklund, P. C. *Nano Lett*. **2003**, 3, 627.
32. Sahoo, P.; Basu, J.; Dhara, S.; Fang, H.C.; Liu, C-P.; Ravindran, T. R.; Dash, S.; Tyagi, A.K. *J. Mater. Sci.* **2012,** 47, 3447.

33. Schwede, J. W.; Bargatin, I.; Riley, D. C.; Hardin, B. E.; Rosentha, S. J.; Sun, Y.; Schmitt, F.; Pianetta, P.; Howe, R.T.; Shen, Z-X.; Melosh, N. A. *Nature Mater*. **2010**, 9, 762.
34. Baker, R. T. K.; France, J. A.; Rouse, L.Waite, R. J. *Journal of Catalysis* **1976**, 29, 22.
35. Hartland, G. V. *Chem. Rev*. **2011**, 111, 3858.
36. Wang, Z.; Gao, F.; Crocombette, J-P.; Zu, X.T.; Yang, L.; Weber, W.J. *Phys. Rev. B* **2007,** 75, 153303.
37. Sar, D. K.; Nanda K. K. *Nanotechnology* **2010**, 21, 205701.
38. Huberta, T.; Brettb, L. B.; Blackb, G.; Banacha, U. *Sens. Actuators B* **2011**, 157, 329.
39. Kim, S. S.; Park, J. Y.; Choi, S-W.; Kim, H. S.; Na, H. g.; Yang, J. C.; Lee, C.; Kim, H. W. *Int. J. Hydr. Energy* **2011**, 36, 2313.
40. Mubeen, S.; Zhang, T.; Yoo, B.; Deshusses, M. a.; Myung, N. *J. Phys. Chem. C* **2007**, 111, 6321.
41. Wang, H. T.; Kang, B. S.; Ren, F.; Tien, L. C.; Sadik, P. W.; Norton, D. P.; Pearton, D. J.; Lin, L. *Appl. Phys. Lett.* **2005**, 86, 243502.
42. Wang, B.; Zhu, L. F. Yang, Y. H. Xu, N. S.; Yang, G. W. *J. Phys. Chem. C* **2008**, 112, 6643.
43. Yang, F.; Taggart, D. K.; Penner, R. M. *Nano Lett.* **2009**, 9, 2177.
44. Chua, B. H.; Loa, C. F.; Nicolosia, J.; Changb, C.Y.; Chena, V.; Strupinskic, W.; Peartonb, S.J.; Ren, F. *Sen. Actuators B* **2011,** 157, 500.
45. Dobrokhotov, V.; McIlroy, D. N.; Norton, M. G.; Abuzir, A.; Yeh, W. J.; Stevenson, I.; Pouy, R.; Bochenek, J.; Cartwright, M.; Wang, L.; Dawson, J.; Beaux, M.; Berven, C. *J. Appl. Phys.* **2006**, 99, 104302.

CHAPTER 6

IN-SITU LABEL FREE IMPEDIMETRIC NANOWIRE BASED DNA BIOSENSOR

6.1 Introduction

6.1.1 Impedimetric Biosensor:

A biosensor is an analytical device that detects or quantifies a biological molecule of interest such as a particular DNA sequence or particular virus.[1,2] It consists of two important components, namely a biochemical molecule that serves as a receptor and a transducer for selective recognition of the bio-event at the readout system. Most of the biosensors are affinity-based, in which a probe molecule is used to capture a target or analyte. It leaves several challenges to selectively detect a target in solution thereby detecting a specific change at a localized surface that can be measured in a variety of ways. In a long run, electrical biosensors appears to be promising that depends only on the change in currents and/or voltages to detect a bioevent.[2-4] This method is relatively simpler than sensors that require light (e.g., surface plasmon resonance, fluorescence or absorption), mechanical motion (e.g., quartz crystal microbalance, piezoelectric or resonant cantilever), magnetic particles, and so on. In addition, electrical biosensor provides several advantages, including, low cost, low power, small instrument size and speed of analysis that hold great promise for applications pertaining to point-of-care diagnostics at bedside, screening of various cancer cells and diseases, bio-warfare agent detection, bioprocess monitoring, and water quality testing.

Depending on the mode of electrical measurement, electrical biosensors are subdivided into many forms, namely Voltametric, Amperometric, Coulometric, potentiometric, conductometric, impedimetric and field-effect transistor based biosensor. In

Voltametric and Amperometric measurement processes, a DC or pseudo-DC voltage is generally applied to measure the current that intentionally changes the electrode condition. On the other hand, impedimetric biosensor measures the impedance at the interface in the AC steady state at a constant DC bias condition by imposing a small sinusoidal voltage at a particular frequency.[3] By suitable choosing the frequency range and peak potential, any irreversible change in the electrode surface can be avoided. This will allow the device to be reproducibility used for several times.

6.1.2 Electrochemical Impedance Spectroscopic (EIS) Technique for Label-free DNA Biosensor:

EIS is an effective and simple technique both for understanding the nature of surface-modified electrodes and for analytical applications. This technique has the inherent potential for label-free and real time detection capability without the use of any fluorescence dyes, enzymes, redox, or radioactivelabels. Impedance biosensors can detect a variety of target analytes, including DNA, nucleic acids, proteins, whole cells, microorganisms, antibodies, and antigens.

However, in the real-world application various issues related to sensitivity, stability and reliability of a biosensor are of technical importance because the actual samples typically contain uncontrolled as well as non-target molecules. Apart from this, the nature and sensitivity of the transducer/electrode plays a critical role while looking towards the ultimate limits of detection down to single molecular level. In this regards, various efforts have been directed towards realization of a highly efficient and stable electrode surface to read out the appropriate bioevent. These electrodes are classified according to the electrode material (metals/metal oxides, glassy carbon, semiconductors, nanomaterials, organic and inorganic layers), geometry of the electrode (conventional electrode arrangement, interdigitated electrodes or array system), the analyte (proteins, antibodies, nucleic acids, etc.), or the amplification protocol used (label-free, enzyme labels, florescent dyes, conducting polymer films, nanoparticles, etc.). The choice of semiconductor as electrode is advantageous over metal based electrode in terms of surface band bending and reduced electron transfer rate across the interface between analyte and electrode.[5,6] Moreover, the interfacial charge transfer resistance and capacitance change significantly when any bio-recognition event takes place at the electrode surface. The effect is used as the fundamental basis for EIS based DNA biosensor.

6.1.3 Progress and Prospects of Nanowire Based DNA Biosensor:

NWs have emerged as one of the promising class of functional materials for their versatile roles, not only in high throughput optoelectronic device but also in ultrasensitive, direct electrical detection of biological and chemical species.[7-11] Compared to thin film counterpart, NWs possess large surface-to-volume ratio, unidirectional conduction channels and diameters comparable to the sizes of molecules being sensed. These aspects have generated considerable interest to use NWs as an effective bio-electrochemical transducer. Remarkably, the conductance in NWs is very sensitive to small surface perturbations.[5] The NW based field-effect-transistor (FET) is most widely used for biosensing purposes, such as the detection of particular DNA sequence, pH, protein, viral and cancer markers.[7-10] However, progress in successful implementation of FET based NW biosensing devices is hindered by several challenges, including precise and reproducible placement of NWs during the large-scale miniaturization processes, specificity in the surface modification processes for selective recognition of a biological species or chemicals of interest, and precise transduction of the signal from the bio-event to the readout system. Without the requirement of expensive instruments and reagents, NW based electrochemical sensing techniques can allow in-situ, real-time, non-destructive, and label-free detection of specific biomolecule of interest by exercising appropriate control over the physical properties and surface functionality.[1,3,12,13]

The current approach towards biosensor is focused on single nanowire based devices. The cost and difficulties involved in the integration of individual NWs into thin-film-based sensor-chips can be simplified by using as-synthesized NWs directly after appropriate surface modification. However, most of the reports on GaN based applications in biosensing are limited to the thin film configuration; for example GaN based planar transistor has been reported to detect specific DNA sequence, changes in pH, glucose, and even detecting proteins associated with breast cancer.[14,15] Nonetheless, GaN NWs based DNA sensor has been recently demonstrated by Chen et al. employing electrochemical impedance spectroscopy (EIS) technique.[16,17] It is found that selective detection of a particular DNA sequence can be achieved by suitable functionalization of GaN NWs with 3-merkapto-tri-methoxy-silane (MPTS). Moreover, the sensitivity and stability of DNA biosensor can be enriched by modulating the surface chemistry and choosing appropriate tether molecule in order to generate multiple docking sites to immobilize significant amount of probe (p-) DNA molecules. In this context, dendrimer can serve as a tether for surface confinement of the large amount of probe DNA.[18,19] Zhu's et al. demonstrated that fourth generation poly(amidoamine)dendrimer (G4-PAMAM) modified Au electrode increases the sensitivity and also lower the detection limit of the electrochemical based DNA biosensor as compared to the similar kind of biosensors where oligonucleotides are directly immobilized on Au electrodes.[18] Similar behavior is observed for (PAMAM) modified carbon nanotubes (CNT) dip coated onto a glassy carbon electrode.[19] The use of G4-PAMAM monolayer on Au electrode for covalent DNA immobilization and further signal amplification by Au NPs is also reported.[20] However, in most of the cases, the maximum achievable detection of target (t-)DNA is traced down to few fM levels. Several factors limit the ultra low detection capability as well as further development of the above mentioned report, which includes the difficulties involved in (1) separating metallic and semiconducting CNTs because metallic components do not function like semiconductor counterpart, (2) selective surface modification of CNT for binding a wide range of analytes, and (3) appropriate interface with the readout system for both CNT and Au nanoparticle based sensor probe. Thus, it is expected that the integration of dendrimer based surface chemistry onto NW based electrodes will lower the detection limit for the electrochemical DNA biosensing.

We have demonstrated a very simple and generic protocol for ultrasensitive in-situ label-free detection of DNA hybridization with a high degree of selectivity and specificity spanning over a wide range of DNA detection. A case study using EIS method is performed to explore the possibility for detecting and to quantify the extent of cellular damage in complementary target (ct-)DNA molecules upon irradiation with ionized radiation such as γ-rays. Finally, a realistic picture of DNA sensing methodology at the semiconductor/electrolyte interface is discussed.

6.2 Experimental Protocols and Methodology:

For this study, a correlated DNA sequence of influenza A (H1N1) Swine flu virus (24 base pair) was employed as a model. The human influenza A (H1N1) virus corresponds to the orthomyxoviridae family, which is still creating pandemic concern as of now.[21,22] One of the maximum used laboratory tests for confirmation of novel influenza A (H1N1) cases are based on real-time reverse transcription-polymer chain reaction.[23] Other methodologies, based on antigen, immune-fluorescence or viral culture, are also often used.[24] However, impedance based detection can also provide a parallel and consistent response.[24]

6.2.1 Chemicals and Reagents:

The following chemicals and reagents were used in the experiments: sulfuric acid (98%), and hydrogen peroxide (H_2O_2) from Merck; 1,10-decanedicarboxylic acid [$HOOC(CH_2)_{10}$ COOH; 99.9%] from Lancaster UK; 1-Ethyl-3-(3-dimethylaminopropyl) carbodimide (EDC), G3-PAMAM dendrimer (99.9%) with an ethylenediamine core containing 32 surface primary amine groups, phosphate buffered saline (PBS) buffer (0.30M NaCl, 10mM sodium phosphate buffer; pH 7.4; 99.9%) and TE buffer (10mM Tris–HCl and 1mM ethylenediaminetetraacetate (EDTA); pH 8.0; 99.9%) from Sigma-Aldrich, USA; Duplex buffer (30 mM 4-(2-hydroxyethyl)-1-piperazineethanesulfonic acid (HEPES) + 100 mM potassium acetate; pH 7.5; 99:99.5%) from SRL, India. All other chemicals were of at least analytical reagent grade and used without further purification. Aqueous solutions were prepared with deionized water (resistivity ≈ 16.8 MΩ cm^{-1}) from Millipore.

H1N1 Swain-flu Gene Sequences:

The probe DNA (p-DNA) and complementary target DNA (ct-DNA) used for this experiment were adopted from the H1N1 swine flu gene. The details are enlisted in table 1 along with single and triple base mismatch target (t-)DNA. All the oligonucleotides were high-performance liquid chromatography (HPLC) purified for accuracy in the measurement system, and purchased from Metabion International Matrinsried Deutschland, Germany. DNA stock solutions were prepared with TE Buffer solution with pH 8.0 and stored in freezer below 0 ^{o}C while not in use.

Table 6.1 : DNA protocols used in this study

DNA type	**Sequence**
PO_4- DNA : (p-DNA)	PO_4-5`-TGC AGT CCT CGC TCA CTG GGCACG-3`
Complementary t-DNA: (ct-DNA)	3`-ACG TCA GGA GCG AGT GAC CCG TGC-5`
Single mismatch t-DNA : (sm-DNA)	3`-**G**CG TCA GGA GCG AGT GAC CCG TGC-5`
Triple mismatch t-DNA : (tm-DNA)	3`-**TA**G TCA GGA GCG AGT GAC CCG TG**A**-5`

6.2.2 Surface Functionalization of Nanowires:

Prior to DNA sensing, a series of functionalization steps were employed over NWs. Initially, GaN NWs were treated with Piranha solution (H_2SO_4: H_2O_2 :: 3:1) for a period of 10 min, and then washed with double distilled water followed by drying with N_2 gas. This process was often used for cleaning nitride surfaces, removing native oxides, as well as to activate hydroxyl group on the surface of NW. The hydroxylated samples were further treated with 5 ml of H_2O solution containing 1mM of 1,10-decanedicarboxylic acid for 6 h under gently stirring condition. Then the samples were washed three times with deionized water to remove all residual acids and dried with N_2 gas. This process generates –COOH functional group on the GaN surface.[25] For dendrimer functionalization, COOH terminated NWs were mixed with 2mg/ml G3-PAMAM solution containing 1mM EDC for 8 h at room temperature under gentle stirring which leaves the surface with NH_2 groups. Then, the samples were washed three times with deionized water as a linker to p-DNA.

6.2.3 DNA Probe Immobilization:

The p-DNA immobilized surface is a necessary step to selectively detect ct-DNA during the hybridization process. The G3-PAMAM-modified GaN NWs were incubated in 10 nM of p-DNA (diluted in 1 mM TE buffer) solution containing 1 mM EDC for 12 h at room temperature (RT) to immobilize the p-DNA on the GaN surface. The p-DNA modified substrates were finally rinsed with 1mM phosphate buffer solution followed by double distilled water to remove non-specific adsorbed molecules. These p-DNA/PAMAM/GaN NWs modified electrode were used for in-situ sensing of different t-DNA molecules.

6.2.4 In-Situ Detection of DNA Hybridization:

The in-situ impedance study of DNA hybridization was performed using the p-DNA/PAMAM/GaN NWs electrode within 10 mL of duplex buffer solution medium as the background electrolyte without any use of redox marker. Duplex buffer was used to maintain a constant pH (7.5) and the ion concentrations of these solutions generally match those of the human body. For in-situ measurement, ct-DNA of various concentrations ranging from 10^{-9} to 10^{-19} M levels were added slowly and allowed to hybridize for 2 h at RT. The selectivity of the sensor probe was performed in the same procedure by adding single and triple base-pare miss matched t-DNA of various concentrations. The specificity of the sensor probe, subjected to any radiation induced damage, was studied by monitoring the hybridization response from the γ-irradiated ct-DNA sequence. The γ-rays dose of 1Gy and 10 Gy were carried out over the ct-DNA from a Co-60 Gamma Chamber-900 source.

6.2.5 Methodologies:

Micro-Raman scattering with the 514.5 nm line of Ar^+ laser excitation and micro-PL with the 325 nm line of He-Cd excitation was used for identification of different surface functional groups on the modified NWs sample. During Raman and PL measurement, the incident laser power was kept below a threshold limit of 1 mW with the faster scan rate in order to avoid any unwanted damage to DNA. AC impedance measurements were carried out with Eco Chemie Autolab PG STAT 30 in a conventional three-electrode mode where a platinum foil was used as a counter electrode and a saturated calomel electrode through a luggin capillary as a reference electrode. GaN NWs of 6x8 mm area grown over n^+-Si substrate were used as a working electrode (WE). All the impedance spectra were recorded at a stable open circuit potential and applying a sinusoidal voltage of amplitude ± 10 mV in the frequency range of 100 - 0.005 Hz.

6.3 Characterization

GaN NWs grown directly over the Si substrate with an average diameter of 20 nm are used as a transducer for the DNA biosensor. The detailed surface modification steps and subsequent DNA hybridization process are schematically illustrated in figure 6.1.

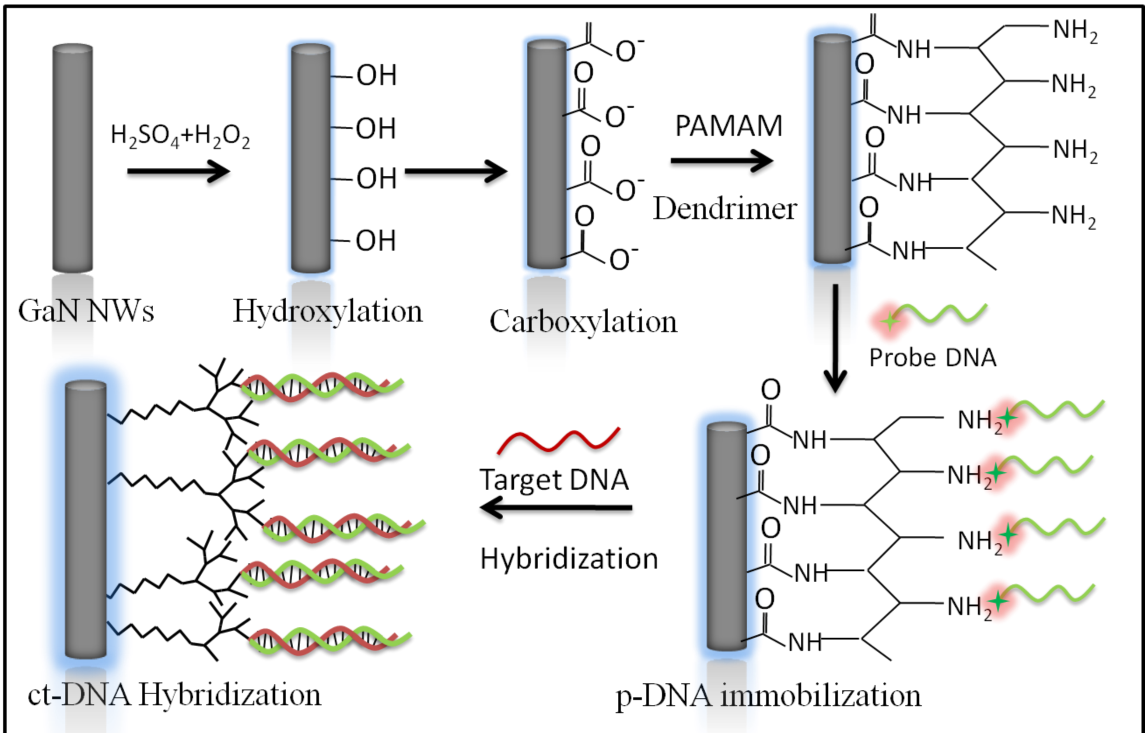

Probe: 5`-PO_4-$(CH_2)_6$-TGC AGT CCT CGC TCA CTG GGC ACG-3'
Target: 5'-CGT GCC CAG TGA GCG AGG ACT GCA-3'

Fig. 6.1 Schematic representation showing all the series of functionalization steps involved for immobilization and hybridization of specific DNA on the PAMAM dendrimer modified GaN nanowire.

Luminescence quenching/enhancement in semiconductor nanostructures is a useful signal of binding (or adsorption) of molecular species to surface. PL and Raman spectroscopic studies are performed to ensure the covalent bonding of the functional groups with the NW surface molecules. Figure 6.2(a) shows the typical PL spectra of NWs with subsequent surface modification. Room temperature PL spectrum of pristine GaN NWs is composed of two broad peaks around 3.46 and 3.29 eV. The peak at 3.46 eV corresponds to I_2 line. The broad peak at 3.25 eV corresponds to a recombination of carriers from a shallow donor state [N_2 vacancy (V_N)] to a deep accepter state (DAP) line. These two peaks are consistent with the PL figure print of GaN.[26,27] The quenching of I_2 line is attributed to the presence of native defects, which takes part in the nonradiative recombination process in GaN by trapping carriers at the defect states. The defects which can directly serve as radiative centers

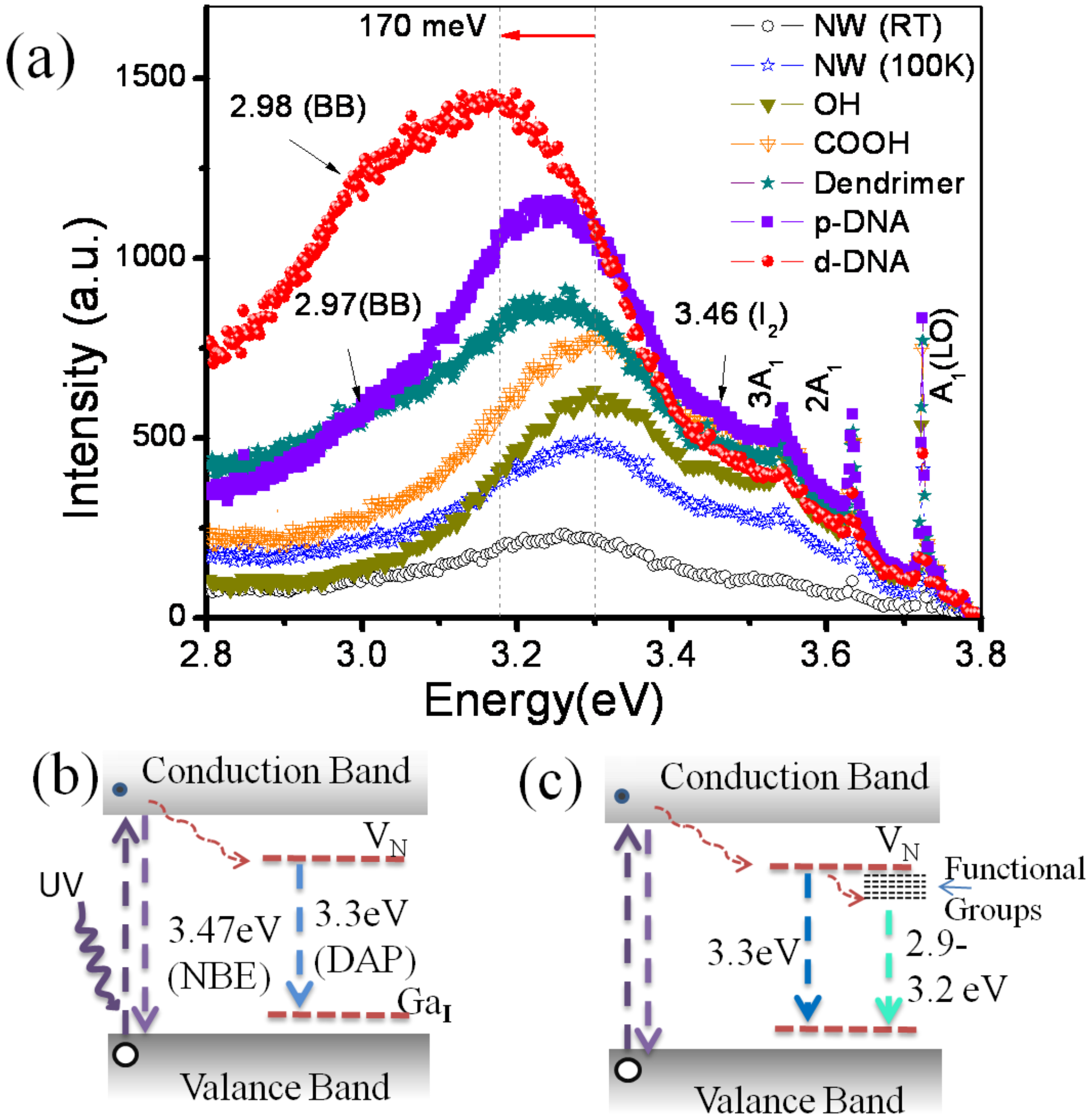

Fig. 6.2 (a) Low temperature micro-PL spectra of GaN NWs functionalized with different bioorganic molecules and DNA using 325 nm laser excitation; (b) Schematic PL band diagram of the various transition processes involved before and (c) after surface functionalization of NWs.

correspond to 3.25 eV. PL spectra of NWs recorded at 100 K show an expected blue shift with an increase in the intensities of the corresponding bands. The observed blue shift, broad and asymmetric line shape in the half width at half-maximum at the lower energy side of the PL peaks of NWs are accredited to the largest concentration of carriers.[27] Notably, CVD grown GaN NWs usually possess higher carrier density, as compared to that of MBE grown NWs. These inherent properties of CVD grown GaN NWs confer it to be used as an effective transducer for biosensing applications.[17] In order to confirm the presence of functional groups on the NW surface, all the PL spectra are recorded at 100 K. Low temperature measurements have been performed to avoid the secondary effect on functional groups induced by local heating by incident laser light. It is observed that the band edge emission has not been significantly affected by the chemical modification. However, the DAP emission band has shown spectacular variation with every stage of the chemical functionalization process. The DAP line is blue shifted and intensity gets enhanced after the hydroxylation process carried out on NW samples. It may arise as a result of surface state passivation during the acidic treatment, which helps in removing the absorbed oxygen and surface defects from NW surface. A subsequent enhancement in the intensity of DAP line is also observed during carboxylic acid treatment followed by the dendrimer modification of the hydroxylated surface. Notably, the DAP peaks are red shifted compared to hydroxylated sample. The red shift may be attributed to the creation of sallow donor states in the hydroxylation process playing its role in the DAP recombination process. With subsequent p-DNA modification, the DAP line is enhanced by three times of magnitude, and further red-shifted by 170 meV as compared to the pristine NWs at 100 K. A new shoulder at 2.9 eV appears only in the case of DNA modified sample. The formation of DNA molecular layer on the functional NW surface would have helped in activating the blue band at 2.9 eV, and amplified further after the hybridization process. Moreover, the observed enhancement in PL intensity and band shift in GaN NWs substantiates the covalent attachment of the functional molecules on the NW surface. A schematic representation of the detailed transition state in functional GaN NWs, before and after DNA modification steps has been depicted in figures 6. 2(b,c), respectively. As indicated in the figures 6.2(c), the molecular orbitals of organic layers may have generated multiple radiative states in the proximity of DAP transition level, which result in the enhancement of emission from DAP states. Immobilization, as well as hybridization of DNA molecules may be responsible in creating alternative nonradiative states for the observed blue band at 2.9 eV. The systematic changes in the PL spectra that occure with surface functionalization using DNA molecules require further investigation for confirmation. The DNA modification on the NW surface is also confirmed by Raman spectroscopy. Along with characteristic Raman features of GaN, the typical Raman spectrum of p-DNA modified GaN NW (Fig. 6.3) shows additional phonon modes at 745 cm^{-1} (Adenine), 751 cm^{-1} (nucleic acid), 784 cm^{-1} (cytosine) and 890 cm^{-1} [ν C-C starching, ν (C-O-C) 1,4 glycosidic link].[28] These additional peaks correspond to various vibrational modes of DNA base pairs. Thus, it provides necessary proof for the immobilization of p-DNA on GaN NW surface.

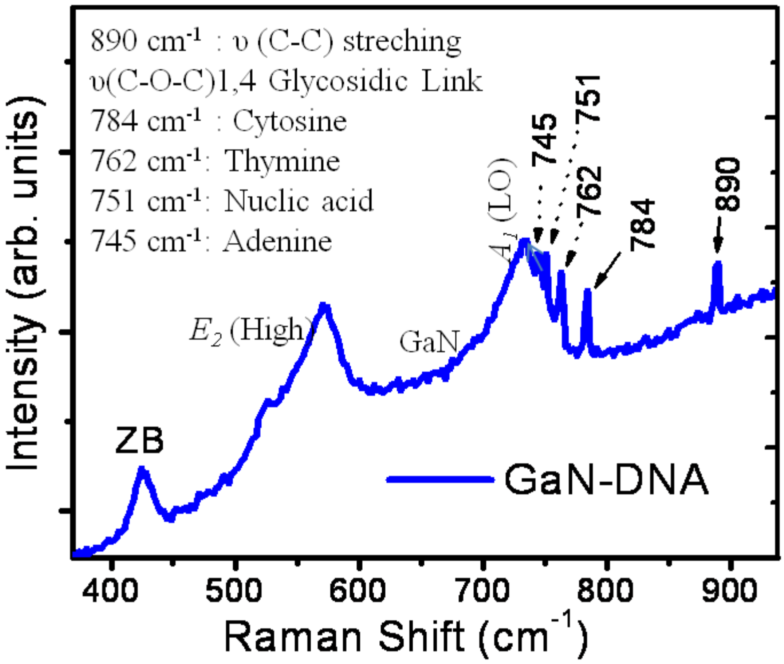

Fig. 6.3 Raman spectra of p-DNA immobilized GaN NWs. The sharp peaks in the range of 740 to 890 are corresponding to different vibrational modes of the DNA molecule.

6.4 GaN Nanowire Based Impedimetric DNA Biosensor

6.4.1 In-Situ Detection of H1N1 DNA Hybridization:

In-situ detection of the DNA-hybridization process is carried out by employing the p-DNA/PAMAM/GaN NWs as working electrode in the EIS technique and using the duplex buffer as a support medium without using any redox marker. The Nyquist plots, imaginary impedance $Z''(\omega)$ vs real impedance $Z'(\omega)$, of pristine GaN NWs and p-DNA modified NWs are shown in figure 6.4(a).[3,4] The impedance spectra are constituted by semicircle at low frequency side (electron-transfer-dominated process) and a 45° inclined line at the higher frequency side (diffusion-limited process). It shows the typical *Faradaic* type behavior. For this situation, a Randles equivalent circuit is used as shown in the inset of figure 6.4(a). It comprises of the solution resistance R_s, polarization resistance R_p, a constant phase element Q for better fitting for some of the elements instead of true capacitance (generally used due to the electrode surface non-idealities) and Warburg impedance W. Impedance due to Q is expressed as $Z_Q = 1/Y_o(j\omega)^{-n}$ where Y_o is the magnitude of the Q, ω is the angular frequency and n the exponential term of the Q. The value of R_p has been used as the parameter of interest for the present impedimetric DNA sensor. Figure 6.4(a) reveals that the R_p value increases after p-DNA immobilization over PAMAM/GaN NWs tether. Remarkably, the interfacial diffusion related process is suppressed in case of pristine GaN NWs. The increase in the value of R_p and appearance of strong tail in the impedance spectra of p-DNA/PAMAM/GaN NWs electrode reveals that there is an efficient charge transfer process

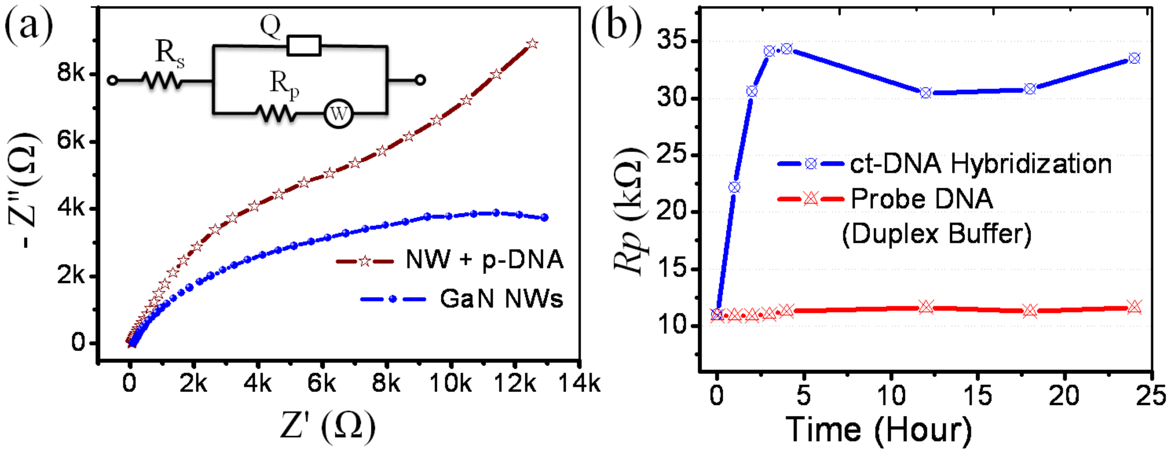

Fig. 6.4 (a) Nyquist plots, imaginary impedance $Z''(\omega)$ vs real impedance $Z'(\omega)$, of pristine GaN NWs and p-DNA modified NWs. Inset shows the Randles equivalent circuit comprised of R_s, R_p, Q and Warburg resistance W; (b) Optimum change in the R_p value of the p-DNA/PAMAM/GaN NWs sensor probe in the Duplex buffer medium over a time period of 24 h without and with the presence of ct-DNA.

occurs owing to the strong covalent bio-binding on the NW surface. These signatures are reflected as fingerprint for DNA modification occurring on GaN NWs.

Prior to the in-situ hybridization process, the stability of p-DNA/PAMAM/GaN NWs electrode in the duplex buffer environment has examined over 24 h without any addition of t-DNA solution to observe any noticeable change occurring over the R_p value [Fig. 6.4(b)]. It is found that this sensor probe provides a stable R_p value over a substantial time without any damage or leaching out of functional materials from the surface of the electrode. Further, addition of ct-DNA (1 pM concentration) onto the solution containing p-DNA probe, a significant change in the impedance spectra is observed within a period of 2 to 3 h and saturates over a substantial time [Fig. 6.4(b)]. On this basis, the optimum saturation time for the DNA hybridization has been taken as 2 h for carrying out further in-situ detection of t-DNA over a wide range of concentration. The in-situ DNA hybridization is performed by monitoring impedance spectra of the p-DNA/PAMAM/GaN NWs electrodes thereby adding the ct-DNA solution subsequently in the hybridization buffer over a range of 0.1×10^{-18} to 10×10^{-9} M concentration after each 2.30 h followed by mild purging with Ar gas. The impedance spectra are recorded after a period of 2 h from the addition of fresh ct-DNA solution into the hybridization buffer. Figure 6.5 displays the in-situ Nyquist plots for the DNA hybridized process over 0.1 aM to 10 nM of ct-DNA concentration at a constant OCP value. It is observed that the R_p value increases with an increase in the concentration of ct-DNA because of hybridization process. Remarkably, the detection of ct-DNA sequence is more pronounced and linear at low concentration level (aM to pM) while the change in the R_p value is low at high concentration. At higher concentration, secondary processes such as steric hindrance, coulomb repulsion, over population of ct-DNA, or reduction of DNA binding sites might have affected the in-situ hybridization process.

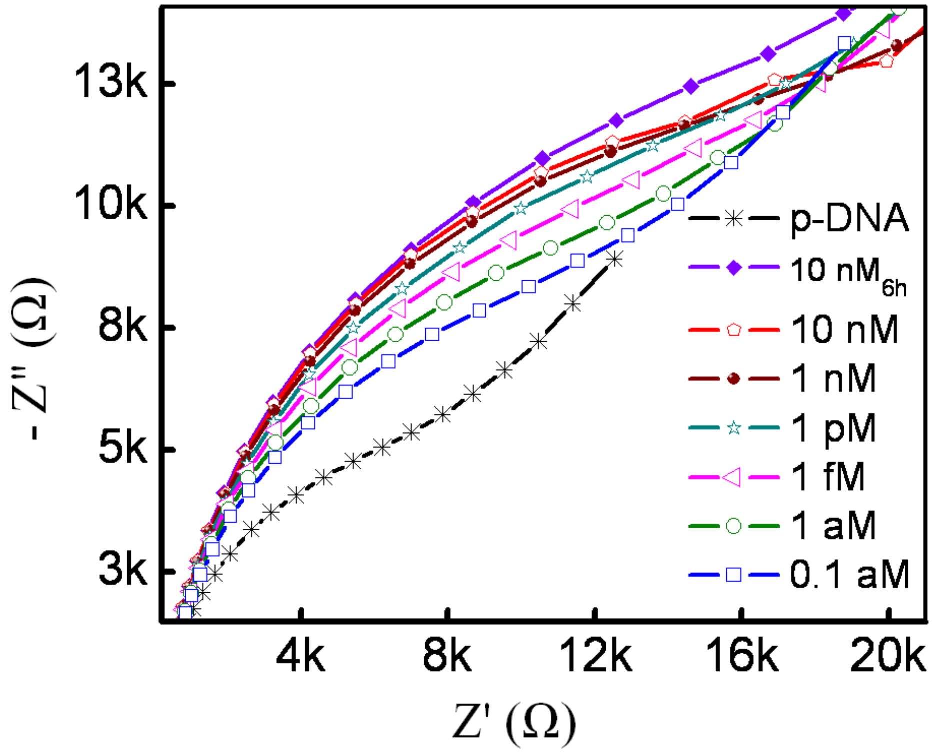

Fig. 6.5 In-situ impedance spectra of the p-DNA/PAMAM/GaN NWs sensor probe during the hybridization process by varying the ct-DNA concentration over a range of 0.1 X 10^{-18} to 10 X 10^{-9} M level at a constant OCP value.

6.4.2 Selectivity and Specificity:

To evaluate the selectivity of the impedimetric DNA biosensor, the p-DNA/PAMAM/ GaN NWs electrodes are incubated in the hybridization buffer containing different kinds of t-DNA molecules including single base mismatched (sm-DNA) and triple base mismatch (tm-DNA). An insignificant change in R_p value is observed when the p-DNA/PAMAM/GaN NWs electrode is subjected to incubate in the hybridization buffer containing the sm-DNA (Fig. 6.6) and no change in case of tm-DNA (data not shown). It shows that any nonspecific adsorption of non-complementary DNA has negligible effect on DNA hybridization. Thus, it endorses the excellent selective nature of the p-DNA/PAMAM/ GaN NWs sensor probe. This has been clearly elucidated in the bar diagram shown in figure 6.6, plotted by taking into account of the relative change in R_p value of the sensor probe against various concentrations of ct-DNA and sm-DNA. On the other hand, the specificity of the probe sensor has been

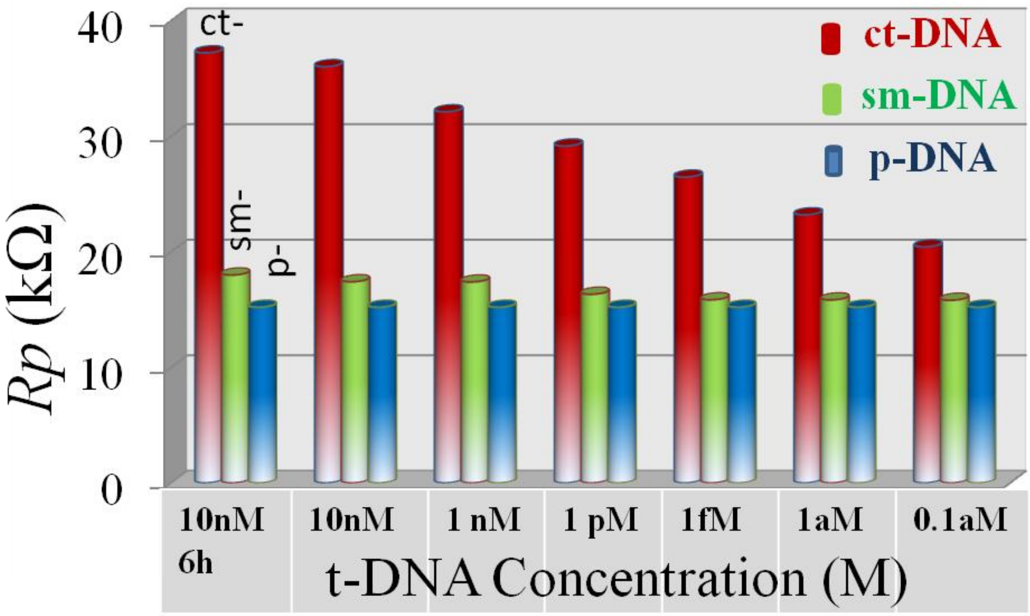

Fig. 6.6 Comparative bar diagram showing the relative change in R_p value of the p-DNA/PAMAM/GaN NWs sensor probe against various concentrations of ct-DNA and sm-DNA.

examined from the viewpoint of hybridization process getting affected by damaged ct-DNA. Figure 6.7(a) shows the impedance spectra acquired over a period of 5 h for 1 Gray γ-irradiated ct-DNA and figure 6.7(b) corresponds to 10 Gray γ-irradiated sample. The ct-DNA base-pair, upon irradiated with high ionized γ-rays, does not participate in the hybridization process. As a matter of fact, highly ionized irradiation would induce secondary effects on the DNA sequence, such as, alteration of the bases, rupture of the strand, destruction of the sugars, cross links and formation of dimers.[28] Hence, it is expected that ct-DNA undergoes significant change in its physiological properties after high ionized irradiation and hence does not take part in the hybridization process. Figure 6.7(c) shows the comparative bar diagram of the hybridization response as a measure of change in R_p values subjected to various t-DNA sequences. These results demonstrate that the changes of the R_p value of the electrochemical DNA biosensors are induced by the specific hybridization process between the p-DNA/PAMAM/GaN NWs sensor probe and the t-DNA in the duplex buffer medium. In addition, the impedance response of the sensor probe remains unchanged after measuring the impedance parameter of the same sensor probe after more than 1 week while stored in PBS buffer. This indicates that the present methodology for realizing a label-free DNA biosensor has good reproducibility, and stability characteristics.[29]

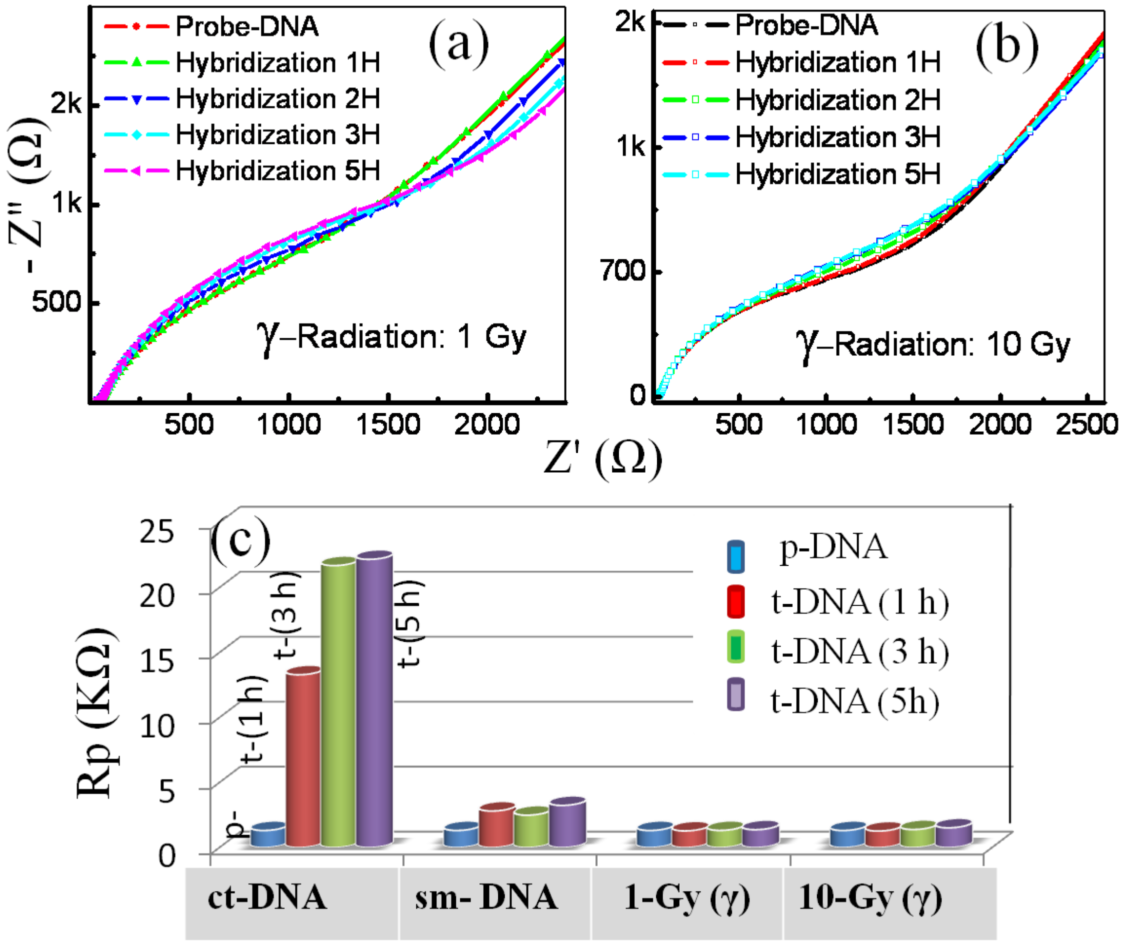

Fig. 6.7 In-situ impedance spectra of the p-DNA/PAMAM/GaN NWs sensor probe during hybridization process using (a) 1 Gray γ-irradiated and (b) 10 Gray γ-irradiated ct-DNA over a period of 5 h in the duplex buffer solution; (c) Comparative bar diagram showing the relative change in R_p value of the p-DNA/PAMAM/GaN NWs sensor probe against various concentrations of ct-DNA, sm-DNA and γ-irradiated ct-DNA molecules.

6.5 Mechanism of DNA Sensing using EIS:

The DNA sensing mechanism can be well understood from the viewpoint of band offset at the hetero-interfaces formed at the semiconductor/bioorganic layer as depicted schematically in figure 6.8(a). In this present study, the DNA molecules are covalently immobilized on the atomically smooth surface of GaN NW through the PAMAM linker. The

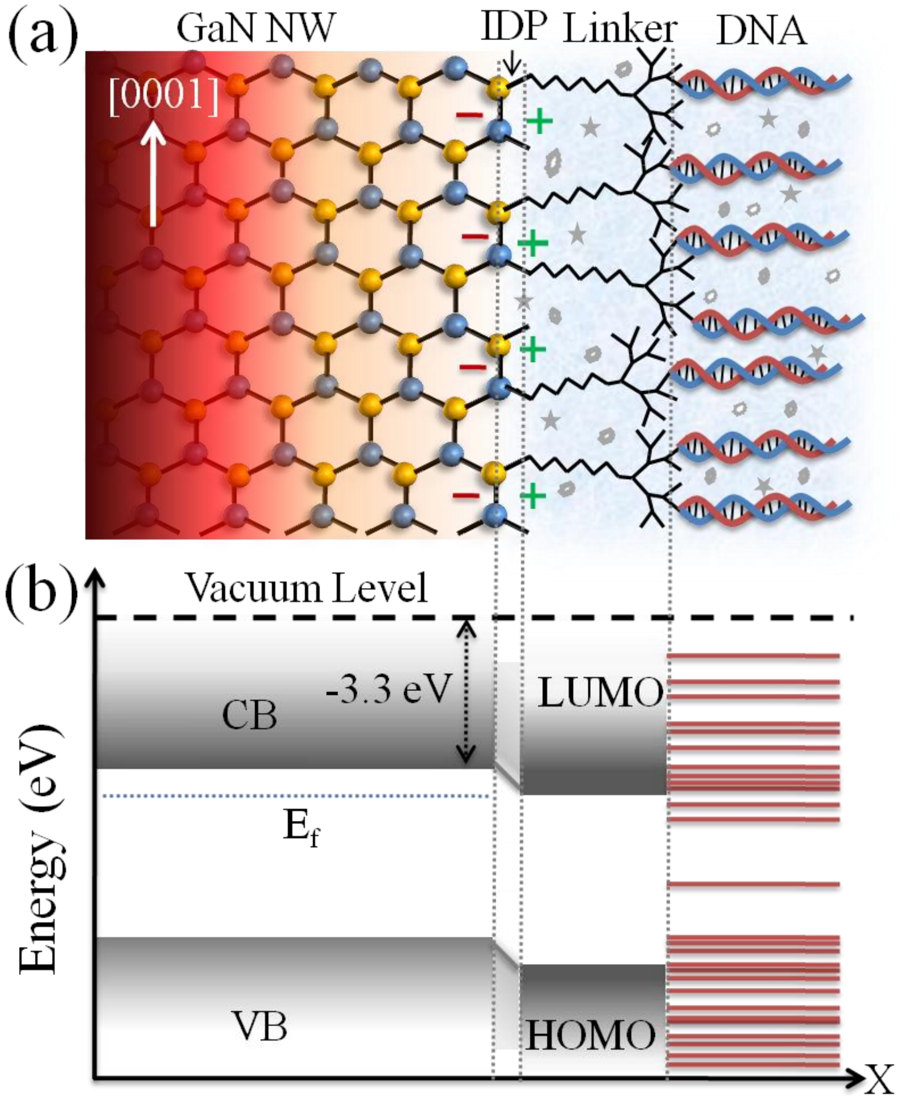

Fig. 6.8 (a) Schematic illustration of the hetero-interfaces formed at the interface between GaN NWs and bioorganic layer; (b) the corresponding band diagram of GaN NWs and the molecular orbitals, namely HOMO and LUMO levels of the organic linker and the DNA molecules. At the hetero-interface an IDP layer develops as a result of relevant molecular band offset. The substantial change in the IDP layer during the hybridization process forms the basis of the present impedimetric DNA biosensor.

characteristics of the linker molecule are likely to provide high density of docking sites for p-DNA and to maintain sufficiently low density of electronic defects at the semiconductor surface. The electronic properties of any semiconductor at the hetero-interface can be influenced by the valance and conduction band position with respect to vacuum level, and position of the Fermi level at any surface/interface. Generally, an interface dipole layer (IDP) develops owing to the formation of heteronuclear bonds at the interface when the semiconductor surface meets electrolyte/bioorganic layers.[30] The formation of IDP layer is responsible for hopping of the localized carriers along the gradient of electrostatic potential across the interface. On the other hand, the electronic properties of the linker molecules depend on the respective molecular electronic states, namely highest occupied molecular orbital (HOMO) and the lowest unoccupied molecular orbital (LUMO). Whereas, for the case of DNA considered as a prototypical biomolecule, there are reports on large variation in the position of molecular orbitals, ranging from metallic to insulating characteristics as indicated by the line in the right hand side of the figure 6.8(b).[30-32] The exact position of these aforementioned molecular levels can vary depending on the dynamical screening properties of the buffer medium. Electrostatic screening and thermal broadening of the molecular levels can also play a critical role.

Moreover, efficient and direct transfer of charge carriers between semiconductor substrates and bioorganic layers are pivotal conditions towards systematic detection of specific bio-events by means of band alignment of the relevant electronic levels of the hybrid interface. An IDP layer develops at the interface when NW electrode meets bioorganic layer [Fig. 6.8(b)] because of relevant molecular band offset leading to the formation of a space charge region beneath the semiconductor surface. In thermodynamic equilibrium, this process results in band bending in an upward direction for an intrinsically *n*-type GaN NW used in this present study. The subsequent chemical modifications and DNA immobilization on the NW surface increase the number of carriers that influence the widening of IDP layer followed by band bending at the interfacial region. During the hybridization process, there is a substantial change in ct-DNA concentration dependent IDP layer as well as upward band bending at the NW surface. These properties at the interface of semiconductor/bioorganic layers act as a characteristic basis for DNA sensing in the EIS spectroscopic technique.

A comparative data on difference in absolute position of valance and conduction band edges for most used semiconductor to that of LUMO and HOMO levels of some organic materials (polymers and DNA) reveal that wide band gap semiconductors (GaN and other group III alloys, ZnO, SiC and diamond) can be ideal to make better electronic contacts than that of classical semiconductors such as Si and GaAs.[30,33] It was found that GaN and its alloys with Al can cover a wide range of HOMO or LUMO positions in several bioorganic systems whereas most acclaimed and popular materials like Si or GaAs exhibit a considerable offset in the position of their band gaps with respect to the HOMO-LUMO gap of most of the organic systems. In this context, GaN NWs, being a direct wide band gap semiconductor with narrow conduction channels, are expected to be advantageous as a transducer element to read out the bio-event effectively by choosing appropriate physiological conditions and linker molecules characteristics.

6.6 Summary:

In summary, PAMAM dendrimer modified GaN NWs provide an unprecedented opportunity in realizing ultra sensitive label-free electrochemical DNA biosensor. By taking the advantage of PAMAM dendrimer comprising of high density of docking sites for p-DNA immobilization and narrow conduction channel of GaN NWs as transducer for the readout system, we have achieved an ultra low detection limit down to 0.1 aM target DNA solution. Comparative in-situ studies on single and triplet base pair mismatched, γ-irradiated and complementary target DNA in the hybridization process reveal selectivity and specificity of the p-DNA/PAMAM/GAN NWs sensor probe. During the hybridization process, there is a substantial change in ct-DNA concentration dependent interfacial polarization resistance, which forms the basis of the present DNA biosensor. Moreover, this novel methodology for specific DNA sequence detection, as compared to other existing methodologies is very robust, simple and highly sensitive, and thus could be reasonably anticipated for its potential applications in high performance DNA biosensors and bioelectronics.

6.7 References:

1. Wang, J. *Biosensors and Bioelectronics* **2006**, 21, 1887.
2. T. G. Drummond, M. G. Hill, J. K. Barton, *Nat. Biotechnol*. **2003**, 21, 1192.
3. Daniels, J. S.; Pourmand, N. *Electroanalysis* **2007**, 12, 1239.
4. Lisdat, F.; Schafer, D. *Anal. Bioanal. Chem.* **2008**, 391, 1555.
5. Grieshaber, D.; MacKenzie, R.; Voros, J.; Reimhult, E. *Sensors* **2008**, 8, 1400.
6. Wanekaya, A. K.; Chen, W.; Myung, N.V.; Mulchandani, A. *Electroanalysis* 2006. 18, 533.
7. Cui, Y.; Wei, Q.; Park, H.; Lieber, C. M. *Science* **2001**, 293, 1289.
8. Patolsky, F.; Lieber, C. M.; *Materialstoday* **2005**, 8, 20.
9. Wang, W. U.; Chen, C.; Lin, K-H.; Fang, Y.; Lieber, C. M. *Proc. Natl. Acad. Sci.* **2005**, 102, 3208.
10. F. N. Ishikawa, H.-K. Chang, M. Curreli, H.-I Liao, C. A. Olson, P.-C. Chen, R. Zhang, R. W. Roberts, R. Sun, R. J. Cote, M. E. Thompson, C. Zhou, *ACS Nano* **2009**, 3, 1219.
11. Sahoo, P.; Dhara, S.; Dash. S.; Tyagi, A. K. *Nanoscience & Nanotechnology-Asia* **2011**, 1, 140.
12. Feigel, I. M.; Vedala, H.; Star, A. *J. Mater. Chem*. **2011**, 21, 8940.
13. Pérez, E. M.; Arya, S. K.; Bhansali, S. *Analyst* **2011,** 136, 1686.
14. Ren, F.; Pearton, S. J.; Kang, B. S.; Chu, B. H. *AlGaN/GaN High Electron Mobility Transistor Based Sensors for Bio-Applications, Intech open access book Biosensors for Health, Environment and Biosecurity* **2011,** ISBN: 978-953-307-443-6.
15. Kang, B. S.; Pearton, S. J.; Chen, J. J.; Ren, F.; Johnson, J. W.; Therrien, R. J.; Rajagopal, P.; Roberts, J. C.; Piner, E. L.; Linthicum, K. J. *Appl. Phys. Lett.* **2006,** 89, 122102.
16. Chen, C.P.; Ganguly, A.; Wang, C.-H.; Hsu, C.-W.; Chattopadhyay, S.; Hsu, Y.-K.; Chang, Y.-C.; Chen, K.-H.; Chen, L.C. *Anal. Chem.* **2009,** 81, 36.
17. Chen, C. P.; Ganguly, A.; Lu, C.Y.; Chen, T. Y.; Kuo, C. C.; Chen, R.S.; Tu, W. H.; Fischer, W. B.; Chen, K. H.; Chen, L.C. *Anal. Chem.* **2011**, 83, 1938.
18. Zhu, N.; Gao, H.; Xu, Q.; Lin, Y.; Su, L.; Moa, L. *Biosensor and Bioelectronics* **2010,** 25, 1498.
19. Zhu, N.; Gu, Y.; Chang, Z.; He, P.; Fang, Y. *Electroanalysis* **2006**, 18, 2107.
20. Li, G.; Li, X.; Wan, J.; Zhang, S. *Biosensors and Bioelectronics* **2009**, 24, 3281.
21. World Health Organization, Swine influenza, *Wkly. Epidemiol. Rec.* **2009**, 84, 149.
22. Yang, Y.; Sugimoto, J. D.; Halloran, M. E.; Basta, N. E.; Chao, D. L.; Matrajt, L.; Potter, G.; Kenah, E.; Longini Jr, I. M. *Science* **2009**, 326, 729.
23. Wang, R.; Sheng, Z-M.; Taubenberger, J. K. *J. Clinical Microbiology* **2009**, 47, 2675.

24. Bonanni, A.; Pividori, M. I.; Valle, M. D. *Analyst* **2010**, 135, 1765.
25. Lao, C.; Li, Y.; Wong, C. P.; Wang, Z. L. *Nano Lett.* **2007,** 7, 1323.
26. Sahoo, P.; Dhara, S.; Amirthapandian, S.; Kamruddin, M.; Dash, S.; Tyagi, A. K. *Cryst. Growth Des.* **2012**, 12, 2375.
27. Bae, S. Y.; Seo, H. W.; Park, J.; Yang, H.; Kim, H.; Kim, S. *Appl. Phys. Lett.* **2003**, *82*, 4564.
28. Synytsya, A.; Alexa, P.; Boer, J. d.; Loewe, M.; Moosburger, M.; Wurkner, M.; Volka, K. *J. Raman Spectrosc* **2007**, 38, 1406.
29. Sahoo, P.; Sumathi, S.; Dhara, S.; Saini, G.; Rangarajan, S., Tyagi, A. K. (*Under Review*)
30. Stutzmann, M.; Garrido, J. A.; Eickhoff, M.; Brandt, M. S. *Phys. Stat. Sol. (a)* **2006**, 203, 3424.
31. Sugiyama, H.; Saito, I. *J. Am. Chem. Soc.* **1996**, 118, 7063.
32. Markus, T. Z.; Daube, S. S.; Naaman, R.; Fleming, A. M.; Muller, J. G.; Burrows, C. J. *J. Am. Chem. Soc.* **2009,** 131, 89.
33. Van de Walle, C. G.; Neugebauer, J. *Nature* **2003,** 423, 627.

CHAPTER 7

PROBING DYNAMICS OF BIOPHYSICOCHEMICAL PROCESSES AT THE NANO-BIO INTERFACE

7.1 Introduction:

Assessing the mechanism of nanoparticle (NP) induced toxicity to microbes is of immense importance in the area of nano-biotechnology.[1] A challenging task for analysts is to develop a rapid, highly sensitive, chemically specific, non-invasive method for obtaining useful information for NP induced toxicology. Until recently, electron microscopy has been the most sought after tool in elucidating the mode of action of NPs at the nanobio-interface for ecotoxicological and biomedical applications. However, Raman based techniques can provide label free, on-site, in-vivo analysis of chemical and structural information.[2] In the past decade, there was significant progress in the development of Raman based techniques for bacterial cell analysis,[3] chemotaxonomic identification of bacteria,[4] clinical diagnosis,[5] biomass processing,[6] detection of bacterial EPS[7] and biofilms.[8] With the advancements and success in chemical analysis of bacterial cells using Raman spectroscopy, it is now possible to interpolate this information to assess antibacterial effects of NPs down to single cellular level.

Biofilms are consortia of micro-organisms attached to biotic or abiotic surfaces.[9] Biofilm formation is a major concern in industrial, environmental, public health, clinical, medical implants and food processing units.[9-11] It is now believed that 60-80% of all these infections are caused by bacteria living in biofilms.[10] It has been established that persistence of infection in *Staphylococcus aureus* (*S. aureus*; skin, surgical wound, blood stream and lung infections); *Pseudomonas aeuriginosa* (*P. aeuriginosa*; cystic fibrosis); *Escherichia coli*

(*E. coli*; urinary tract infections) is due to biofilm forming mucoid strains.[12] Hence, prevention of bacterial adhesion and subsequent biofilm formation is of prime importance. Research into molecules inhibiting biofilm formation is of immense interest, as subinhibitory concentration of many antibiotics may actually promote biofilm growth as a consequence of stress-induced behaviour.

Prevention of biofilm formation or breaking down of biofilms seems to be a new therapeutic challenge.[13] Metal NPs seem to be promising alternative for antibacterial applications. Extensive studies have been carried out to assess the antibacterial effects of metal oxide and polymeric NPs.[14] Most of these studies have focused on killing or growth inhibition of planktonic cells.[15,16] Investigations are limited in assessing the toxicity of NPs to bacterial cells. Only very few studies deal with the involved mechanism due to limitations in analytical techniques, namely, lack of sensitivity, and complex sample processing.

In the search for alternatives, GaN seems to be a potential candidate material. GaN (E_g = 3.4 eV) is one of the most promising direct wide band gap semiconductors with potential applications in high performance optoelectronic devices and bio-chemical sensing.[17] Notably, Ga has already been approved by US FDA for treatment of malignancy and is now increasingly being recognized as an antibacterial agent.[18,19] Ga has also been known to treat tuberculosis[20] and malarial[21] infections. To the best of our knowledge, there are no reports studying the toxic effect of GaN NPs.

In this context, the present study has been carried out to trace the toxic effect as well as to assess the antibacterial and antibiofilm effects of GaN NPs against Gram positive and Gram negative bacterial strains. Further, an attempt has been made to explore the mode of action of GaN NPs on bacterial cells using confocal micro-Raman spectroscopy (CLRS), with single cell level resolution.

7.2 Materials and Methods

7.2.1 Synthesis, Functionalization and Characterization of GaN Nanoparticles:

The growth process and characterization of GaN NPs are detailed in chapter 3 as represented schematically in figure 7.1(a).[22] The NP used for this study are taken from sample grown for 1 h at 900 °C. The resulting diameter of NPs is close to ~ 50 nm. The NPs surface are further functionalized with dodecanodioic acid [$HOOC(CH_2)_{10}COOH$] as a surface passivating agent [Fig. 7.1(b)]. Initially, NPs were treated with 50% aqueous solution containing a mixture of H_2SO_4: H_2O_2 (ratio 3:1) for a period of 10 min, and then washed with double distilled water, followed by drying with N_2 gas. This process was often used for cleaning nitride surfaces as well as to activate hydroxyl groups on the surface. The hydroxylated samples were further mixed with 5 ml of H_2O solution containing 1mM of dodecanodioic acid. The suspension was kept under gentle stirring overnight. Finally, the samples were collected by centrifugation process carried out at 5000 rpm, and subsequently dried with flowing N_2 gas.

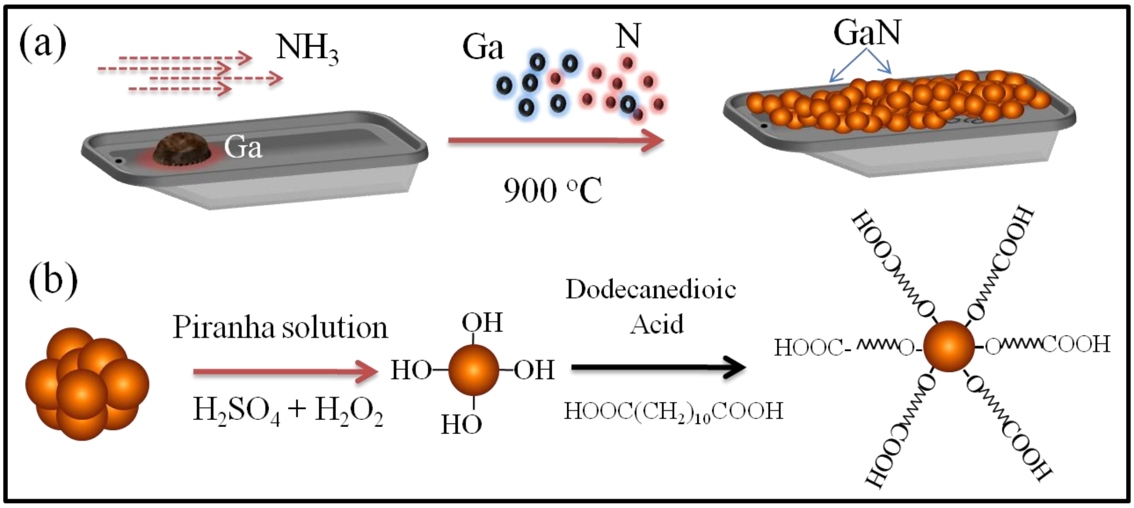

Fig. 7.1 Schematic representation of (a) the growth of GaN nanoparticles at 900 °C in the CVD technique, and (b) the steps for COOH surface functionalization of GaN NPs.

The appropriate covalent bonding formation of -COOH functional group on the NW surface is confirmed by Raman spectroscopic analysis. Typical micro-Raman spectrum [Fig. 7.2] of the as-grown NPs shows mode frequencies at 535, 567 and 729 cm^{-1} corresponding to A_1(TO), E_2(high) and A_1(LO) phonon modes of *WZ*-GaN phase, respectively.[23] Additional peaks appearing at 253 and 420 cm^{-1} are assigned to ZB arising from finite size effects of NPs. However, COOH functionalized NPs show similar characteristic features of *WZ*-GaN along with new phonon modes exhibited at higher wave numbers. The new peaks appearing at 1330, 1420, 1585 and 1784 cm^{-1} are tentatively assigned to the O-H deformation mode in –COOH monomer, comprising of C-O stretch and O-H deformation, COO$^-$ stretching anti-symmetry and C=O stretching, respectively.[24]

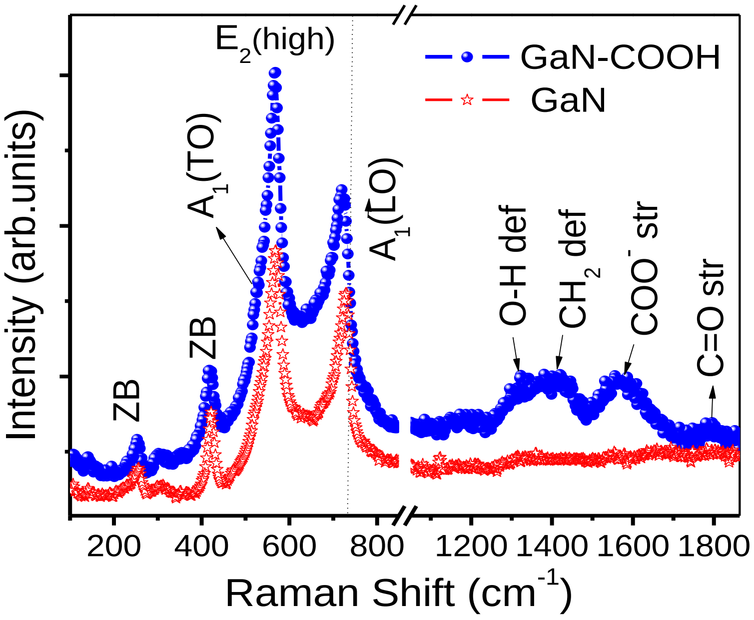

Fig. 7.2 Typical Raman spectra of pristine and COOH functionalized GaN NPs using 514.5 nm laser lines. The Raman spectra reveal wurtzite phase of GaN along with the appearance of new peaks after surface modification. These new peaks correspond to the vibration of surface functional groups in the range of 1200 to 1800 cm^{-1}.

7.2.2 Bacterial Strains and Culture Conditions:

A gram positive strain *S. aureus* and gram negative strains viz: *E. coli*, *Pseudomonas aeuriginosa* and *Pseudomonas putida* were used as the model test organisms because these species are widely distributed and known to form prolific biofilms. Pure cultures were grown in Luria Bertini (LB) medium and incubated overnight at 37 ^{o}C with shaking. From this, 1.0 ml of bacteria was sub-cultured in 15 ml of LB broth to reach a mid log phase observed by OD_{570} value of 0.12 to 0.16 having a cell density of 1.5 x 10^{7} CFU mL^{-1}.

7.2.3 Planktonic and Biofilm Inhibition Assays:

Assays were conducted in a 96 well microtitre plate.[25] Working concentration of NPs was prepared as following. NPs were dissolved in autoclaved sterile ultra pure water (Sartorius) and sonicated for 30 min to ensure uniform dispersion of the NP. The aliquot was serially diluted to get double the concentrations in 100 µl of sterile ultrapure water. Then 80 µl of sterile LB medium was added such that the final concentration of NPs in 200 µl corresponds to 0.25, 1.25, 2.5, 12.5 and 25 µg mL^{-1}. The plates were kept in a rotary orbital shaker (120 rpm – Scigenics Inc.) and incubated at 30 ^{o}C for 24 h. Growth of planktonic cells was measured as increase in OD_{570} after 1, 2, 3, 4, 19, 21 and 24 h of incubation using a UV-visible microplate reader (Thermo Scientific- Multiskan). OD values after 24 h of incubation were taken for making comparison between strains.

After 24 h of incubation multiwell plates were used for quantification of biofilm formation. Culture medium was removed from the wells. The wells were rinsed five times with sterile distilled water to remove loosely attached bacteria. Plates were air dried for 45 min and each well was stained with 150 µl of 1% crystal violet solution in water for 45 min. After staining the plates were rinsed with sterile distilled water five times. Biofilms were visible as purple rings that formed on the side of each well. The quantitative analysis of biofilm production was performed by adding 200 µl of 95% ethanol to destain the wells. 100 µl from each well was transferred to a new microtitre plate and the level (OD) of the crystal violet present in the destaining solution was measured at 570 nm. Each concentration of NPs was tested in triplicate. Parallel controls with plain LB medium without bacteria were also carried out. The data were statistically analyzed and represented as mean and standard deviation.

7.2.4. Methodology for the Study of Nanoparticle-Bacterial Cell Interaction:

7.2.4.1 Sample Preparation for FESEM Analysis:

Assessment of NP bacterial interactions was carried out in sterile 45 mm polystyrene petri dishes (Tarsons) at the lowest concentration of 0.25 µg mL^{-1}. A 15 mL of suspension containing NPs and 50% diluted LB broth was added to the petri dishes. Sterile 10 mm glass coupons were introduced into the petri dishes. A 1.0 mL of mid log phase culture (1.5 x 10^7 cells) was introduced into the petri dishes and incubated at 37 ^{o}C in a rotary orbital shaker (40 rpm) for 24 h. After incubation the glass slides were removed and fixed with 2% glutraldehyde for 15 min. After carrying out air drying for 30 min, the slides were passed through alcohol gradient series (90 to 50%) and then stored in sterile containers for FESEM analysis.

7.2.4.2 Confocal Laser micro-Raman Spectroscopic (CLRS) Analysis:

Interactions involving microbes and NPs were carried out in 2.0 ml micro-centrifuge tubes. The microbes and NPs interaction were studied using the inVia micro-Raman spectrometer equipped with a Leica confocal microscope having 100X objective lens, and 1800 gr·mm^{-1} grating. A thermoelectric cooled CCD detector is used in the backscattering configuration. An excitation of Ar$^+$ laser (514.5 nm) with a spectral resolution of 1.6 cm^{-1} power was used. The laser power at the sample surface was maintained below 1 mW in order to avoid laser induced damage to bacterial cells. The samples were loaded on an XYZ movable stage with a minimal possible step size of 0.1 µm capability. The spectra of planktonic cells were acquired in the extended scanning mode, with an integration time of 60 second, where the grating moves to cover a larger range of wave numbers resulting in longer acquisition times. Whereas the static mode was used for Raman mapping, in which the number of spectra in one image can be acquired in less time without the movement of the grating. The spectrometer provides true confocal capability by adjusting the detector slit and pinhole aperture. According to Abbe formula $0.63\lambda/NA$ where λ is the wavelength and NA is the numerical aperture of the objective (0.85 used for this study), the theoretical lateral resolution turns out to be about 381 nm. However, depending on the resolution of XY stage motion (100 nm), the actual lateral resolution could be approximately below 300 nm with the 100X objective on the XY plane. For comparison, all the spectra were recorded in the spectral range of 1000 to 2000 cm^{-1} to obtain the entire region of interest for detecting protein and nucleic acid molecules. Raman mapping of planktonic cells was performed in raster scan mode with a step size of 0.5 μm and spectral integration time of 1 s at 1 mW laser power. These parameters were chosen to increase the spatial resolution of the Raman mapping.

7.3 Tracing the Toxic Effect of GaN Nanoparticles

7.3.1 Effect of GaN Nanoparticles on Inhibition of Biofilm Formation:

Significant inhibition in biofilm formation is observed in all bacterial strains when treated with GaN NP. Maximum inhibition is observed in the case of Gram negative bacterium *E. coli* (71-84%) followed by *P. putida* (66-77%) and *P. aeruginosa* (38-74%), as shown in figure 7.3. Comparatively lower percentage of biofilm inhibition is observed with the Gram positive strain *S. aureus* (48-64%). In addition, COOH functionalized GaN NPs show greater inhibition for the Gram negatives (*E. coli* - 63-78%; *P. putida* – 68-76%; *P. aeuriginosa* - 48-75%). Whereas, Gram positive strain, *S. aureus* (43-66%) further lower the percentage of biofilm inhibition after COOH functionalization. On the other hand, the different surface functionalizations in Ga_2O_3 NPs show opposite results (for comparision purpose, data not shown).[26] A comparision among percentages of biofilm inhibition that occurred with GaN NPs and their functional derivatives to that of Ga_2O_3 NPs is listed in the table 7.1.

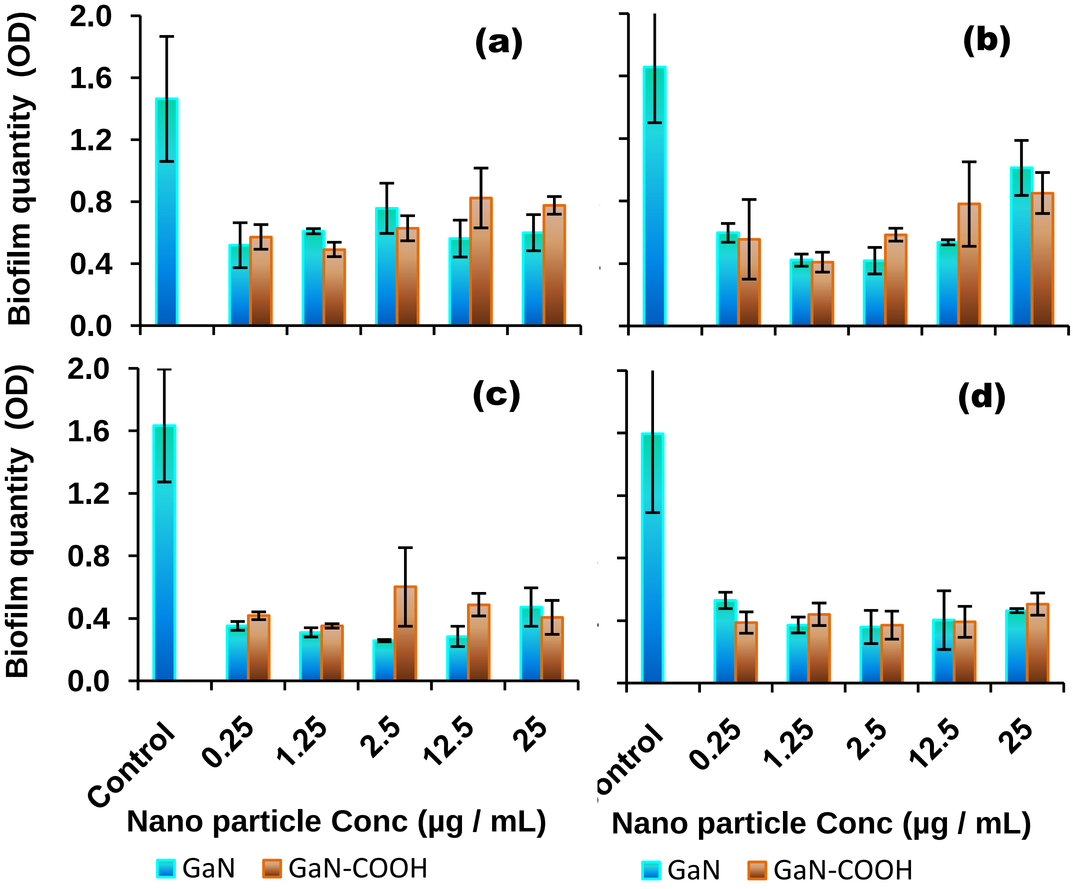

Fig. 7.3 Inhibition of biofilm formation by GaN NPs and -COOH functionalized nanoparticles in different bacterial species a) *S. aureus*, b) *P. aeruginosa*, c) *E. coli* and d) *P. putida*

Table 7.1: Comparatively percentage of biofilm inhibition between GaN NPs and their functional derivatives to that of Ga_2O_3 NPs.

Treatments	**S. aureus**	**PAO1**	**E. coli**	**P. putida**
GaN	64.4	64	78.4	66.8
GaN COOH Mod	60.9	66.5	74.5	75.7
Ga_2O_3	46.1	56.2	74.4	75.9
Ga_2O_3 COOH Mod	59.9	55.1	71.6	71.5
Ga_2O_3 Amino Mod	59.9	55.1	71.6	71.5

7.3.2 Destruction of Bacterial Membrane:

Results obtained from our antibiofilm activity evoked two intriguing questions relating to (1) reason for NPs showing significant inhibition for biofilm formation and (2) the underlying mechanism involved.

7.3.2.1 Morphological Study:

In this regards, we first investigated the morphological changes in bacterial cells exposed to different concentrations of NPs by employing FESEM technique [Fig. 7.4]. It is observed that membrane integrity of untreated planktonic cells - *E. coli, P. putida* and *P. aeruginosa* remain intact [Figs. 7.4(a,d,g)]. On the other hand, cellular integrity is

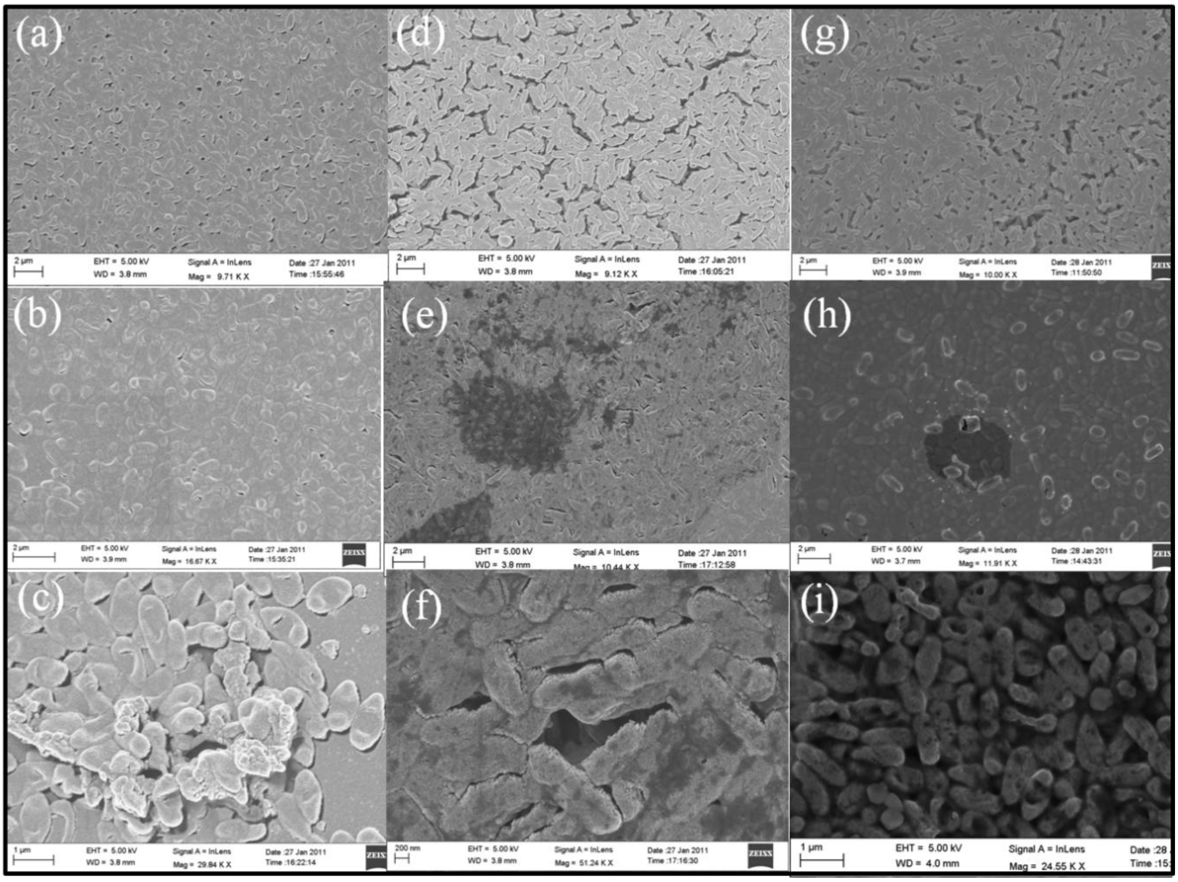

Fig. 7.4 FESEM images of the planktonic cells; (a) *Escherichia coli* -EC, (b) *Pseudomonas putida* –PP and (c) *Pseudomonas aeruginosa*- PA01 grown in the LB medium without NPs; (d) to (e) the morphology of the corresponding planktonic cells grown in the presence of 1µg of NPs, and (g) to (i) the corresponding high magnified image of the damage cells.

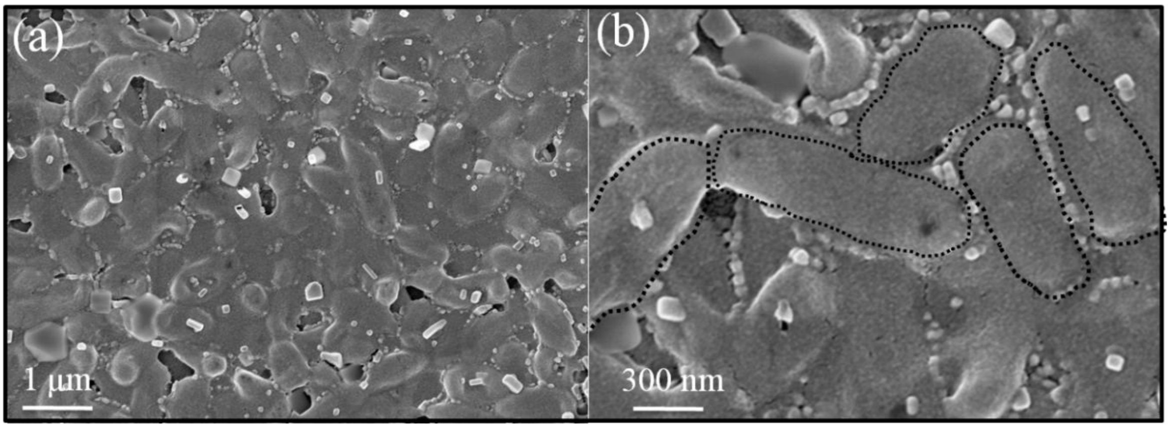

Fig. 7.5 (a) Morphology of *Pseudomonas aeruginosa- PA01* cultured under higher concentration of NPs (25 µg), and (b) FESEM image showing the agglomeration of NPs around the cell wall leading to the death.

compromised when the cells are incubated in the presence of NPs in the same LB medium [Figs. 7.4(b,e,h)]. Interestingly, there is a significant reduction of density of planktonic cells when incubated in presence of NPs. Even at the lowest concentration of NPs (~0.25 µg mL^{-1}), significant cell wall deformation and leaching of intra-cellular components, as revealed by the high magnification images [Figs. 7.4(c,f,i)] seem to be very apparent. Furthermore, at high concentrations of NPs (100 µg), it was found that most of the NPs encircle the bacterial outer cell wall [Figs. 7.5(a,b)] indicating that NPs cause mechanical damage to the cell membrane, leading to the release of cytoplasmic constituents, such as DNA, RNA and proteins, elaborate subsequently.

7.3.2.2 Confocal Raman Study:

Typical confocal Raman spectra of untreated *P. putida* cells and that of NPs-treated cells are shown in figure 7.6(a). The corresponding microscopic images of *P. putida* cells are shown in figures 7.6(b-d). Distinct Raman features are observed in the phonon spectra of bacterial cells treated with NPs as compared to that of the untreated cells. The Raman spectrum of untreated bacteria is dominated by broad peaks around 1601 cm^{-1} (COO$^-$ starching antisymmetric), 1448 cm^{-1} [δ (CH$_2$)] and 1361 cm^{-1} (COO$^-$ symmetric), which are

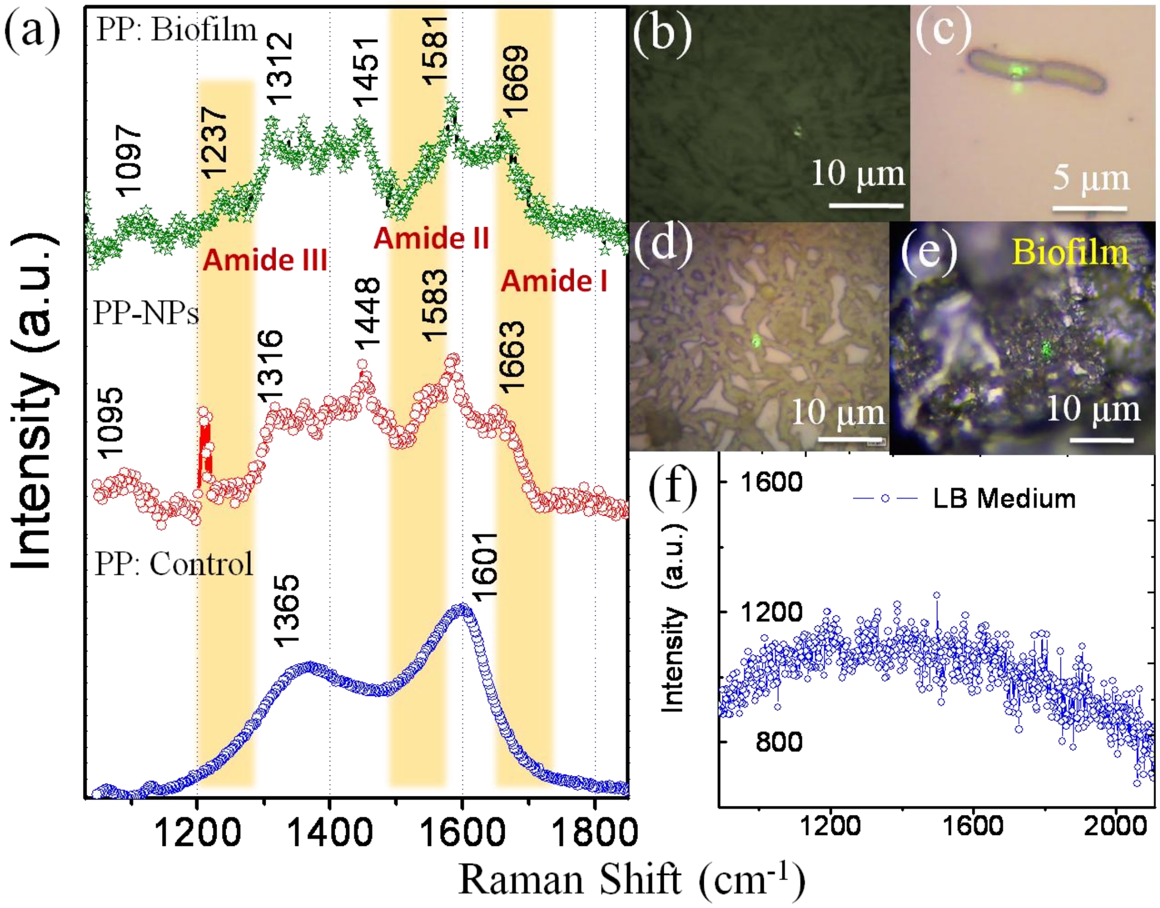

Fig. 7.6 (a) Comparative Raman spectra of *Pseudomonas putida –PP* cells and biofilms incubated in the presence of 1μg of NPs with that of untreated; Typical optical microscopy image of (b) untreated PP cells, (c) single PP cell, (d) PP cells incubated with 1μg of NPs in the culture medium after 24 h, and (e) the corresponding biofilm developed on Si substrate; (f) Typical Rama spectrum of the LB medium in the range of 900 to 2100 cm^{-1}.

mostly attributed to -COO^-stretching vibration.[27-31] These major COO stretching bands and δ-CH_2 scissoring vibrations are characteristic of CH bonding state in lipids, and carbohydrates. On the other hand, the bacteria treated with NPs exhibits many peaks centered at 1669 cm^{-1} (Amide I), 1581 cm^{-1} (Guanine, Adenine), 1575 cm^{-1} (Amide II), 1448 cm^{-1} (CH_2 def.), 1336 cm^{-1} (Adenine), 1237 cm^{-1} (Amide III) and 1095 cm^{-1} (PO_2^- str.). The tentative mode assignment of various functional groups is given in table 7.2.[27-31] These observations reveal that intercellular materials are released upon incubating the planktonic cells with NPs for a duration of 6 h and above. Similar Raman features have been observed with the biofilm of *P. putida* [Fig. 7.6(e)] developed under identical conditions as in the case of incubating

Table 7.2 Raman band assignment of planktonic cells in the frequency range of 1000- 2000 cm^{-1} [Ref. 27-31]

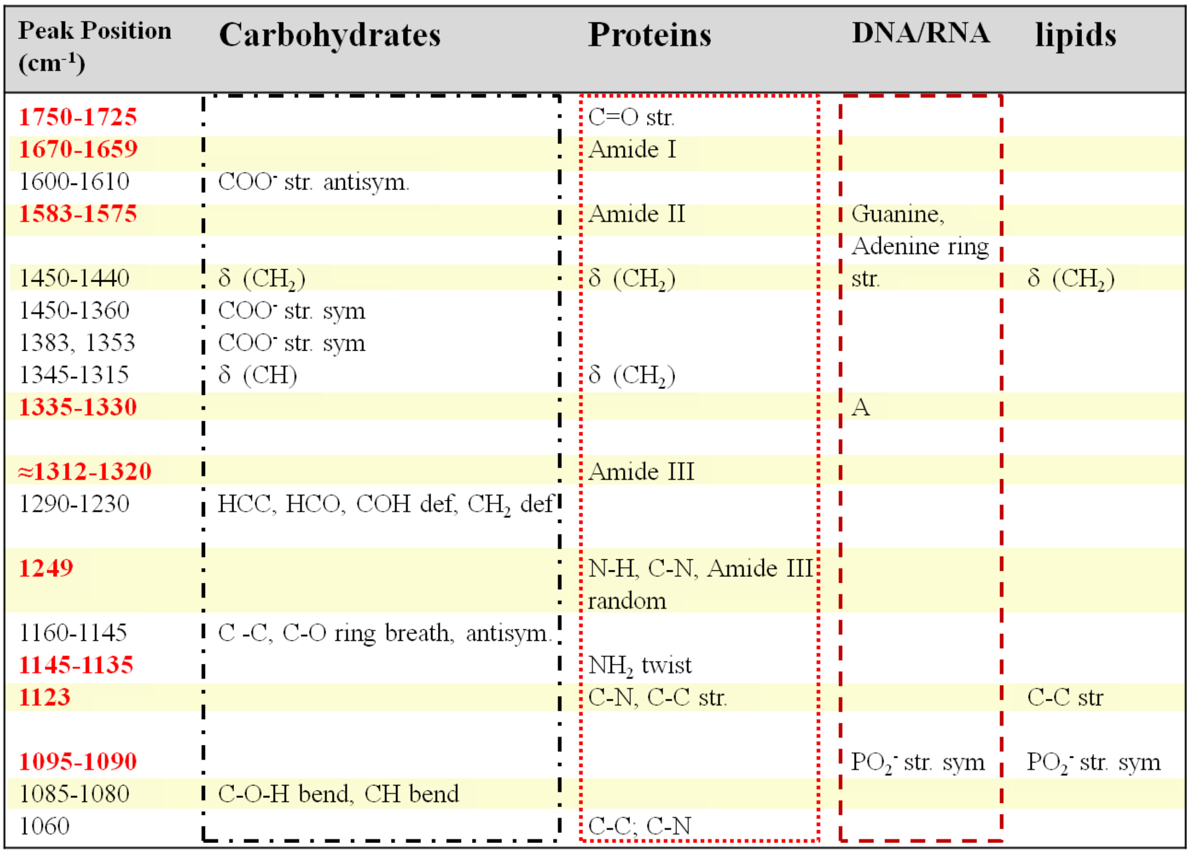

Peak Position (cm^{-1})	Carbohydrates	Proteins	DNA/RNA	lipids
1750-1725		C=O str.		
1670-1659		Amide I		
1600-1610	COO$^-$ str. antisym.			
1583-1575		Amide II	Guanine, Adenine ring str.	
1450-1440	δ (CH$_2$)	δ (CH$_2$)		δ (CH$_2$)
1450-1360	COO$^-$ str. sym			
1383, 1353	COO$^-$ str. sym			
1345-1315	δ (CH)	δ (CH$_2$)		
1335-1330			A	
≈1312-1320		Amide III		
1290-1230	HCC, HCO, COH def, CH$_2$ def			
1249		N-H, C-N, Amide III random		
1160-1145	C -C, C-O ring breath, antisym.			
1145-1135		NH$_2$ twist		
1123		C-N, C-C str.		C-C str
1095-1090			PO$_2^-$ str. sym	PO$_2^-$ str. sym
1085-1080	C-O-H bend, CH bend			
1060		C-C; C-N		

planktonic cells with NPs [Fig. 7.6(a)]. Noticeably, there are no peaks observed in the Raman spectrum of the sterile LB medium in the absence of bacterial cells [Fig. 7.6(f)]. Similar Raman features are also observed in the case of *E. coli*, *P. aeruginosa*, and *S. aureus*, as shown in figures 7.7(a-c), respectively. The Raman peaks of the untreated bacteria are relatively broad and intense as a result of the high density of bacterial cells. However, Raman spectra of bacterial cells, grown in the presence of NPs, comprise of a number of new peaks as compared to the untreated bacteria. Further, the presence of relatively sharp peaks is attributed to the detection of intra-cellular constituents, such as proteins and DNAs. These results are in agreement with the observed density measurements (Fig. 7.3) for biofilms. The results also imply that the bacterial death is directly associated with the damage of bacterial cell membrane and subsequent efflux of intracellular constituents like DNA and proteins.

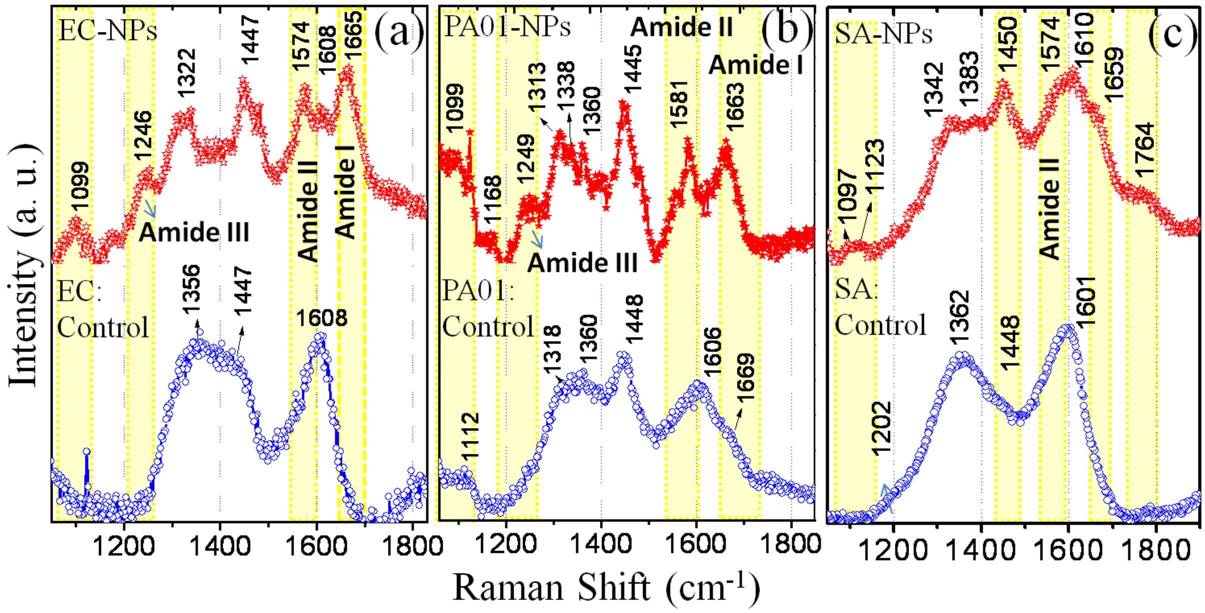

Fig. 7.7 (a) Comparative Raman spectra of untreated cells (blue) and cells incubated in presence of 1μg of NPs (red) (a) *Escherichia coli* -EC, (b) *Pseudomonas aeruginosa*- PA01 and (c) *Staphylococcus aureus*- SA cells.

7.3.2.3 Raman Mapping of Protein Exudation Site:

In order to further explore the underlying mechanism and mode of action of NPs to planktonic cell, Raman mapping studies are performed which provides valuable information about the distribution of various intra-cellular components within a single cell. Figure 7.8(a) shows the optical micrograph of untreated *P. putida* cells supported on a Si substrate. The distribution of *Amide 1* band intensity at the mode frequency of 1663 cm^{-1} is obtained by mapping an area of 40×30 μm with a 0.5 μm step (total 4800 grid point). An acquisition time of 1 s per grid point (total of 80 min for 4800 grid point) for a single spectrum (spectral region from 1000 to 2000 cm^{-1}) is used. The Raman mapping of *Amide 1* band intensity in the case of untreated *P. putida* cells is shown in figure 7.8(b) corresponding to the box region of figure 7.8(a). The optical micrograph [Fig. 7.8(c)] and the corresponding Raman mapping [Fig. 7(d)] of similar *P. putida* cells treated with NPs of 1 μg concentration reveal that the intensity of the 1663 cm^{-1} (*Amide I*) mode frequency increases 30 times as compared to the untreated cells. Raman mapping is performed in similar conditions as in the case of untreated

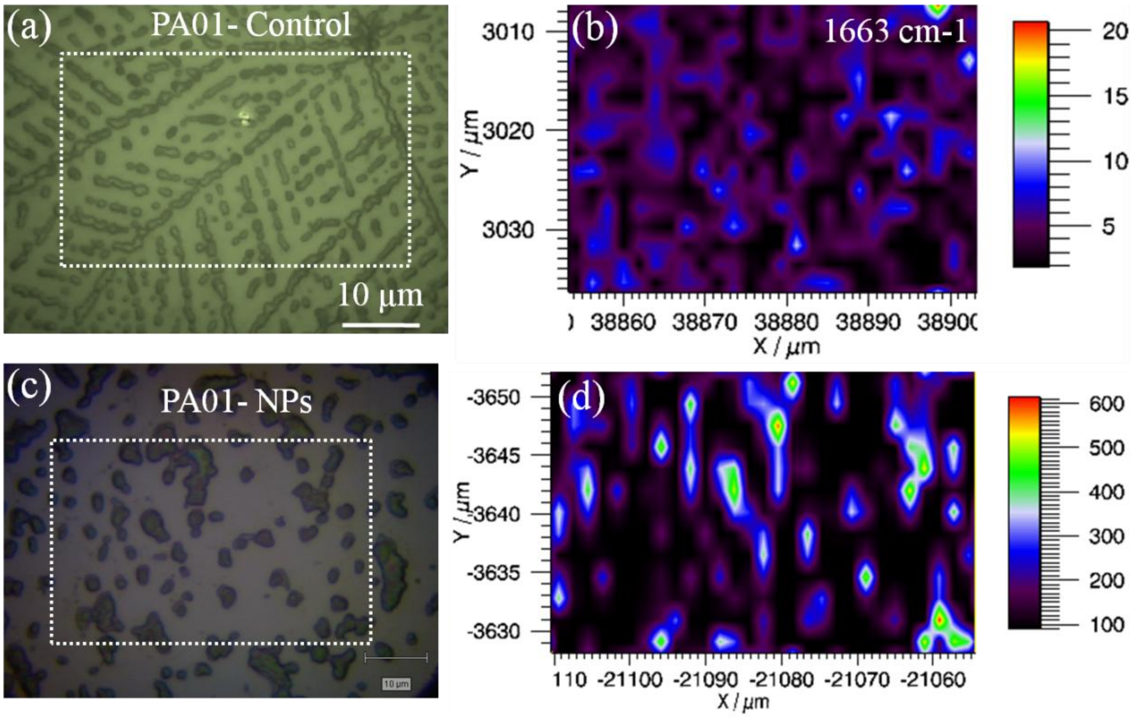

Fig. 7.8 (a) Optical micrograph of the untreated *Pseudomonas aeruginosa*- PA01 and (b) the corresponding Raman mapping of Amide I (1663 cm^{-1}) distribution within the mapped area of 30 X 40 µm [as indicated in the square region in (a)]; comparative (c) optical image and (d) Raman mapping of *Pseudomonas aeruginosa*- PA01 cells incubated with a concentration of 1µg of NPs in the culture medium.

cells. From the optical micrograph, damage to cellular integrity of *P. putida* cells treated with NPs can be clearly observed. Severe changes in the morphology of the cells are also evident. The observed increase in the intensity of *Amide I* is definitely a consequence of cell wall rupture leading to exudation out intra-cellular components from the bacterial cells. Similar Raman mappings of *Amide 1* mode frequency are recorded for other untreated planktonic cells, namely *E. coli* at 1665 cm^{-1} [Fig. 7.9(a), 22×20 µm, 1760 grid point, total 29 min], *P. putida* at 1663 cm^{-1} [Fig. 7.9(c)] and *S. aureus* at 1659 cm^{-1} [Fig. 7.9(e)]. In all these cases, the maximum of 20-30 counts for the distribution of *Amide I* band is observed in the untreated planktonic cells. Raman mappings of plaktonic cells incubated with NPs exhibite strong distribution of the *Amide I* for *E. coli* at 1665 cm^{-1} [Fig. 7.9(b)], *P. putida* at 1663 cm^{-1} [Fig. 7.9(d)] and *S. aureus* at 1659 cm^{-1} [Fig. 7.9(f)]. The maximum peak count of *Amide I* is found to be 30 to 48 times greater than that of untreated cells as revealed from the analysis carried out under identical experimental conditions.

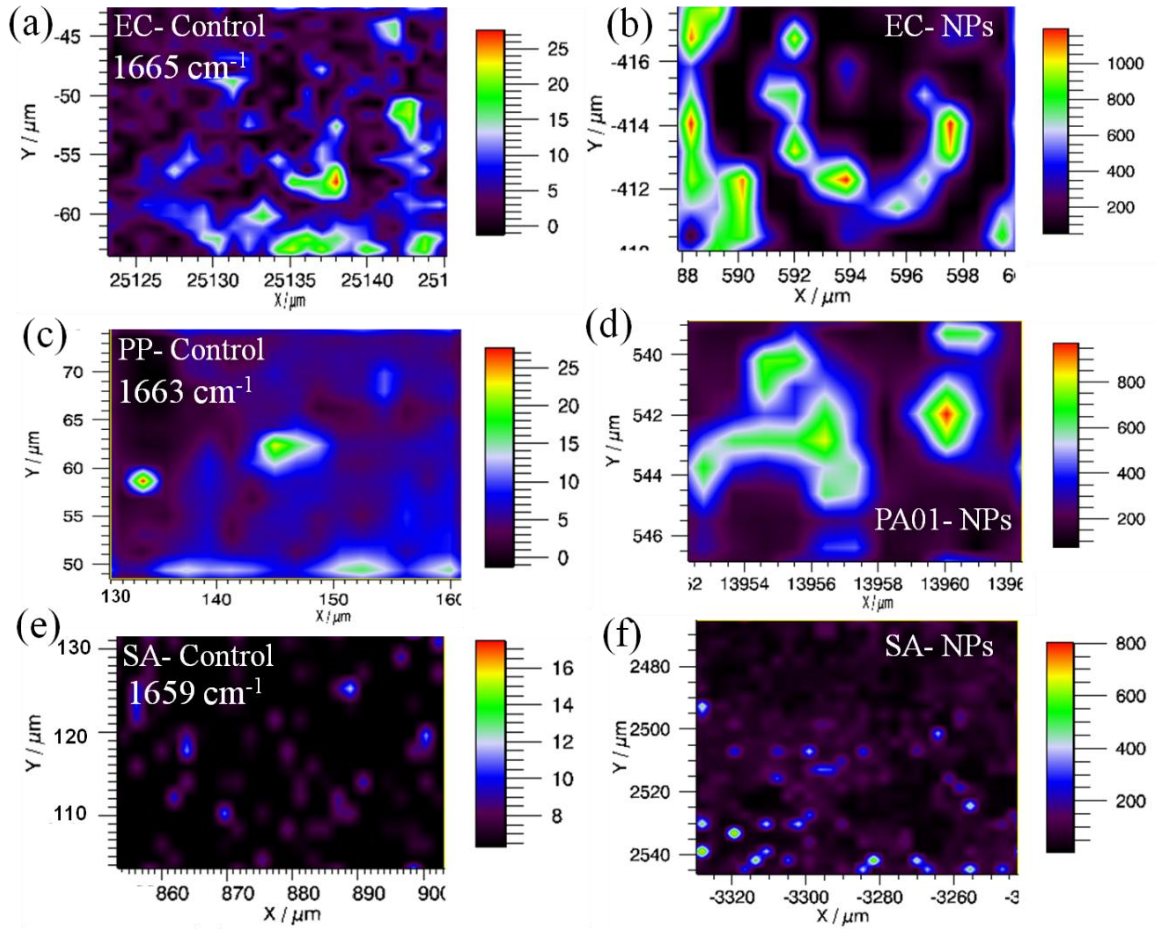

Fig. 7.9 Typical Raman mappings of *amide I* distribution in the untreated planktonic cells and the corresponding cells incubated with 1µg of NPs in the growth medium; (a) and (b) *Escherichia coli* –EC at 1665 cm^{-1}, (c) and (d) *Pseudomonas putida –PP* at 1663 cm^{-1} and (e and f) *Staphylococcus aureus*- SA at 1659 cm^{-1}.

7.3.2.4 Single Cell Analysis:

The effect of NPs interaction with planktonic cells can be further extended to single cellular level by employing confocal Raman spectroscopy in the selected regions of interest. Micrograph of a single *P. putida* cell, incubated in the presence of 1 µg of NPs concentration, is shown in figure 7.10(a). Raman mapping is performed from an area of 10x16 µm with finest step size of 0.3 µm by 0.3 µm (total 1777 grid point). An acquisition time of 1 s per grid point (total 29 min per bacteria) is chosen for the spectral ranges of 1000 to 2000 cm^{-1}.

Figure 7.10(b) shows the typical Raman imaging of a single bacterial cell corresponding to the strongest peaks intensity of *Amide I* (1665 cm^{-1}) mode frequency. Further, the distribution of other intra-cellular protein components in the single cell are mapped by analyzing the sample at different mode frequencies, including 1663 cm^{-1} (*Amide I*), 1581 cm^{-1} (*Amide II*) and 1336 cm^{-1} (*Amide III*) as shown in the figures 7.10(c-e).[27-31] Heterogeneity in the distribution of various protein components in the bacterial cell may appear as a result of localized damage of cell walls after coming in contact with NPs. At a singular point, corresponding to the highest intensity in the Raman map, the intercellular components might have emerged and distributed abruptly. In case of untreated *P. putida* cell, it is however, observed that the intensities of all amide bands are very feeble which is 40 times less than that of cell treated with NPs [Figs. 7.11(a,b)]. Furthermore, the carbohydrates and lipid

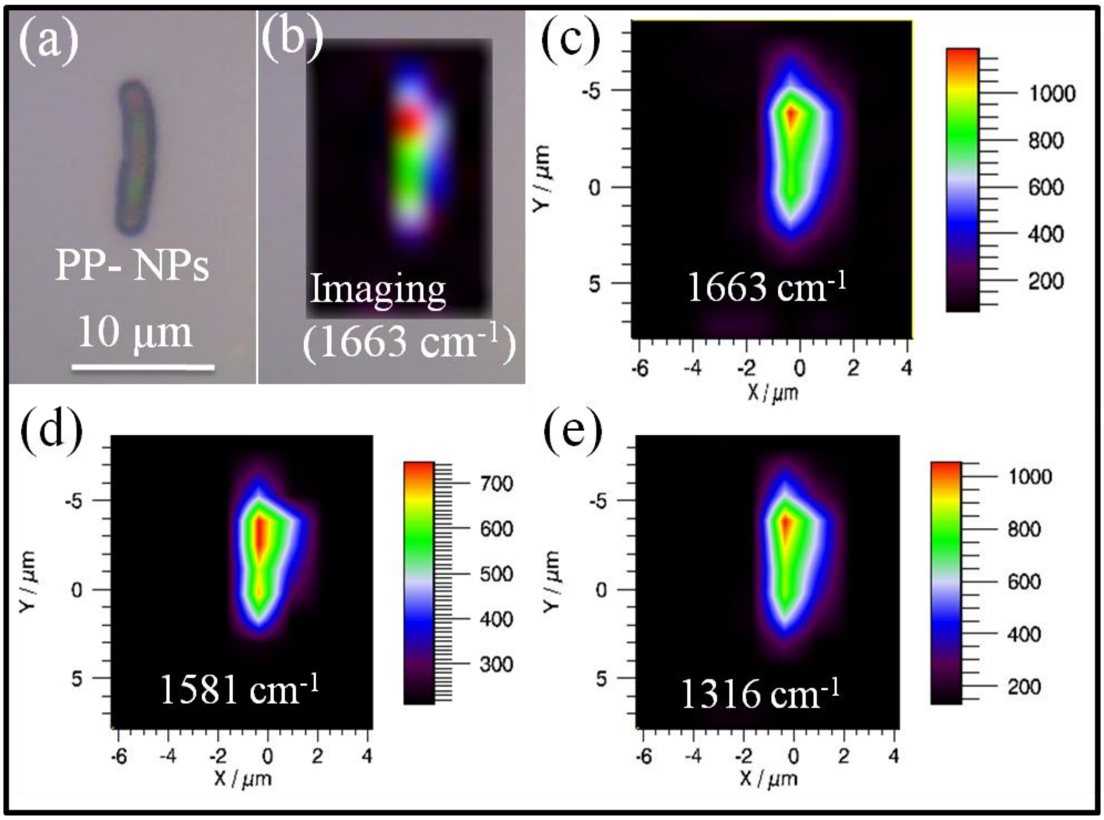

Fig. 7.10 Micrograph of a single *Pseudomonas putida* cell incubated with 1µg of NPs, (b) corresponding Raman imaging at 1663 cm^{-1}; Raman maps for three different protein distribution at frequency (c) 1663 cm^{-1} (Amide I), (d) 1581 cm^{-1} (Amide II) and 1336 cm^{-1} (Amide III).

components are reasonably intense in case of untreated bacterial cells. The detail underlying mechanism has been discussed in succeeding sections.

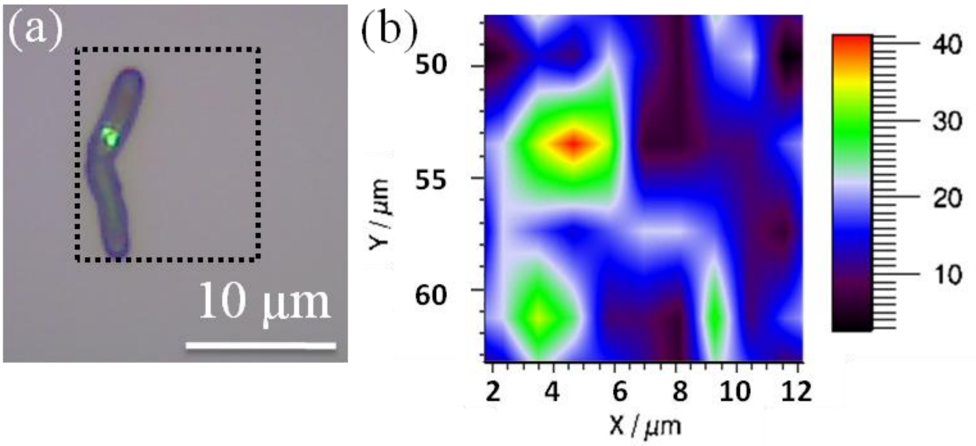

Fig. 7.11 (a) Micrograph of a single untreated *Pseudomonas putida* cell, and (b) the corresponding Raman imaging at 1663 cm^{-1}(Amide I).

A survey of literature shows that there are limited reports on single cell analysis using micro-Raman spectroscopy. Rosch et al.[28] performed Raman mapping of single bacterial cell employing high incident laser power (10 mW) and relatively longer acquisition time of 20 h. However, the appearance of amide bands in their Raman spectra might have emerged as a result of prolonged exposure and high laser irradiation induced damage of cells.[30,31] In some of the earlier studies it took a course of several days to acquire specific data of single bacterial cells.[27] There are a few reports for single bacterial cell analysis employing surface enhanced Raman scattering (SERS) technique.[8,30] In general, SERS technique is based on the use of noble metals, like Au or Ag which enhances the scattered Raman intensities by means of strong electrostatic coupling between incident laser power and surface plasmon of metal NPs. However, in this technique metal particles (e.g., Ag) on their own may possess strong antimicrobial properties, which may further lead to ambiguity in assessing damage to microbes by SERS. In order to overcome these shortcomings, we hope our methodology of analyzing the NP induced cellular damage to planktonic cells by confocal Raman spectroscopy is relatively simple and reliable.

7.4 Molecular Mechanism at the Nano-Bio Interface

Bacterial adhesion and biofilm formation are ubiquitous in nature.[8] Attachment of micro-organisms is a complex process influenced by many variables. The process of biofilm formation involves three steps viz: 1) cell attachment to a surface brought about by electrostatic interaction, which is a weak reversible process, 2) production of exopolymeric substances and irreversible binding to the substrate and 3) formation of micro colonies and subsequent biofilm maturation.

In general, GaN NPs are known to be chemically stable. However, negligible leaching of Ga^{3+} from native and functionalized GaN thin film has been reported.[32] It is difficult to distinguish between bactericidal effects caused by the NPs and ions released by the NPs. The release may be due to interaction of NPs with constituents of the aqueous nutrient media used in such assays. Ga^{3+} has an ionic radius (~ 0.076 nm) similar to that of Fe^{2+} (~ 0.077 nm) and is not differentiated by many biological systems.[19] Fe metabolism is a key factor in bacterial growth and functioning of several important enzymes involved in energy metabolism.[19] However, Ga^{3+} can not be reduced like Fe^{2+} in the metabolic process. Hence, intracellular uptake of Ga^{3+} may interfere with Fe metabolism in bacterial cells, leading to energy starvation and cell death. This may be one of the mechanisms behind toxicity of this metal reported for *E. coli* and *P.* aeuriginosa.[33] Size also may affect the sorption of NPs to cell membrane and intracellular transport that could pierce the lipid bilayer. GaN NPs exhibit high level of inhibition of biofilm formation (60 - 84%) in all the tested strains, similar to metallic Ga reported for *Pseudomonas aeruginosa*.[18] As mentioned earlier, it is hard to differentiate the effects of GaN NPs and leached Ga ions in the assay medium. Leakage of intracellular materials observed through micro-Raman analysis of planktonic cells may be indicative of NP induced damage, while membrane damage and disruption of Fe-dependent processes may be attributable to Ga^{3+}. The high antibiofilm activity observed with GaN NP seems to be identical to those reported for Ga metal.[34-36,18] Studies by Kaneko et al.,[18] have shown that low levels of Ga^{3+} would inhibit growth and biofilm formation in *P. aeruginosa*, whereas higher levels might kill planktonic bacteria and established biofilms. Ga^{3+} internalized by bacterial cells interferes with Fe-dependent processes and may decrease bacterial Fe uptake. Ga ions are known to interfere with many enzymes which require Fe, namely, ribonucleotide reductase (catalyzing the first step in DNA synthesis),[37] superoxide dismutase and catalase (protecting against oxidant stress)[38] and enzymes involved in oxidative phosphorylation such as cytochromes. An implication of these studies is that Ga ions may act simultaneously on several intracellular targets. Therefore, apprehension about possible resistance development due to mutation of any one target seems quite unlikely. GaN NPs seem to have the unique advantage of combination of NP and ionic properties which appear to be responsible for manifestation of enhanced antibacterial and antibiofilm activities.[39] Further studies are required to establish whether GaN NP can be a potential candidate material for wound and implant associated infections.

7.5 Summary:

It was demonstrated that confocal laser Raman spectroscopy (CLRS) has sufficient sensitivity to provide real-time, nondestructive, and quantitative information about the mode of action of NPs in single microbial cells. Such capability and fast analysis in probing the dynamics at the nano-bio interface opens up new possibilities of analyzing cellular process in single microbial cells. Using CLRS and other techniques, we further demonstrate that GaN NPs are very effective in preventing bacterial adhesion and biofilm formation. Species specificity in biofilm inhibition by GaN NPs is observed. GaN NPs are more effective on Gram negative bacterial species viz: *E.coli* > *P. putida* > *P. aeuriginosa* compared to the Gram positive *S. aureus*. CLRS analyses have revealed that GaN NPs induce membrane damage in all the tested bacterial species. It is probable that sorption and passive intake of particles lead to damage of cell membranes. This observation has been substantiated using micro-Raman analysis and protein mapping in individual microbial cells. In comparison, membrane damage (deflation of sessile cells observed through FESEM) and disruption of Fe-dependent processes by Ga ions may also be involved in the inhibition of biofilm formation. GaN seems to be a potential candidate for designing antimicrobial surfaces for implants and catheter devices as well as for combating infections involving biofilms.

7.6 Reference:

1. Gil, P. R.; Oberdorster, G.; Elder, A.; Puntes, V.; Parak, W. J. *ACS Nano* **2010,** 4, 5527.
2. Liu, R.; Liu, J.; Zhou, X.; Jiang G. *Trends in Analytical Chemistry* **2011**, 30, 1462..
3. Krafft, C.; Knetschke, T.; Siegner, A.; Funk, R.H.W.; Salzer, R. *Vibrational Spectroscopy* **2003**, 32, 75.
4. Rosch, P.; Harz, M.; Schmitt, M.; Peschke, K.; Ronneberger, O.; Burkhardt, H.; Motzkus, H.; Lankers, M.; Hofer, S.; Thiele, H.; Popp, *J. Appl. Env. Microbiology* **2005, 71,** 1626.
5. Haka, A. S.; Volynskaya, Z.; Gardecki, J. A.; Nazemi, J.; Lyons, J.; Hicks, D.; Fitzmaurice, M.; Dasari R. R.; Crowe, J. P.; Field, M. S., *Cancer Res.* **2006**, 66, 3317.
6. Saar, B. G.; Zeng, Y. N.; Freudiger, C. W.; Liu, Y. S.; Hummel, M. E.; Xie, X. S.; Ding, S.Y. *Angew Chem. Int. Ed. Engl.* **2010**, 49, 5476.
7. Wagner, M.; Ivleva, N. P.; Haisch, C.; Niessner, R.; Horn, H. *Water Research* **2009**, 43, 63.
8. Premasiri, W. R.; Mori, D. T.; Klempner, M. S.; Krieger, N.; Joness II, G.; Ziegler, L. D. *J. Phys. Chem. B* **2005**, 109, 312.
9. Hall-Stoodley, L.; Costerton, J.W.; Stoodley, P. *Nat. Rev. Microbiology* **2004**, 2, 95.
10. Wingender, J.; Flemming H. C. *Int. J. Hygiene and Environmental Health* **2011,** 214, 417.
11. Hoiby N.; Ciofu, O.; Johansen, K. H.; Song, Z.; Moser, C.; Jensen, P.O.; Molin, S.; Givskov, M.; Tolker-Nielsen, T.; Bjarnsholt, T. *Int. J. Oral Sciences* **2011**, 3, 55.
12. Chen, L. Wen Y-m. *Int. J. Oral Science* **2011**, 3, 66.
13. Bordi, C.; Bentzmann, S-de. *Annals of Intensive care* **2011**, 1, 19.
14. Anselme, K.; Davidson, P.; Popa, A. M.; Giazzon, M.; Liley, M.; Ploux, L. *Acta Biomateriala* **2010**, 6, 3824.
15. Sinha, R.; Karan, R.; Sinha, A.; Khare, S. K. *Bioresource Technology* **2011**, 102, 1516.
16. Zhang, L.; Jiang, Y.; Ding, Y.; Daskalakis, N.; Jeuken, L.; Povey, M.; O'Neill, A. J.; York, D.W. *J. Nanopart. Res.,* **2010,** 12, 1625.
17. Sahoo, P.; Dhara S.; Dash. S.; Tyagi, A.K. *Nanoscience & Nanotechnology-Asia* **2011**, 1, 140.
18. Kaneko, Y.; Thoendel, M.; Olakanmi, O.; Britigan, B. E.; Singh, P. K. *J. Clinical Invstigation,* **2007,** 117, 877.

19. Valappil, S. P.; Ready, D.; Abou, E. A.; Pickup, D. M.; O'Dell, L. A.; Chrzanowski, W.; Pratten, J.; Newport, R. J.; Smith, M. E.; Wilson, M.; Knowles, J. C. *Acta Biomaterialia* **2009,** 5, 1198.
20. Olakanmi, O.; Britigan, B. E.; Schlesinger, L. S. *Infect. Immunity* **2000**, 68, 5619.
21. Yan, G. H.; Wang, G. J.; Li, Y. C. *Acta L Pharmacol. Sin.* **1991**, 12, 530.
22. Sahoo, P.; Dhara, S.; Amirthapandian, S.; Kamruddin, M.; Dash, S.; Tyagi, A. K. *Cryst. Growth Des.* **2012**, 12, 2375.
23. Sahoo, P.; Dhara, S.; Das, C.R.; Das, S.; Tyagi, A. K.; Raj, B. *Int. J. Nanotechnology.* **2010**, 7, 823.
24. Socrates, G. *Infrared and Raman characteristic group frequencies: tables and charts,* John Wiley & Sons, ISBN: 0-470-09307-2.
25. Djordjevic, D.; Wiedmann, M.; McLandsborough, L.A.; *Appl. Env. Microbiology* **2002**, 68, 2950.
26. P. S. Murthy, P. Sahoo, V. P. Venugopalan, S. Dhara, G. Saini, A. Das, A. K. Tyagi, *IEEE Xplore*, **2011**, 490-493, doi: 10.1109/ICONSET.2011.6168010
27. Harz, M.; Rosch, P.; Peschke, K.-D.; Ronneberger, O.; Burkhardt, H.; Popp, J. *Analyst* **2005**, 130, 1543.
28. Rosch, P.; Harz, M.; Schmitt, M.; Peschke, K. D.; Ronneberger, O.; Burkhardt, H.; Motzkus, H. W.; Lankers, M.; Hofer, S.; Thiele, H.; Popp, J. *Appl. Environ. Microbiol.* **2005**, 71, 1626.
29. Sandt, C.; Smith, T. P.; Pink, J.; Brennan, L.; Pink, D. *J. Appl. Microbiology* **2007,** 103, 1808.
30. Chan, J. W.; Winhold, H.; Corzett, M. H.; Ulloa, J. M.; Cosman, M.; Balhorn, R.; Huser, T.; *Cytometry Part A* **2007**, 71A, 468.
31. Ivleva, N. P.; Wagner, M.; Szkola, A.; Horn, H.; Niessner, R.; Haisch, C. *J. Phys. Chem. B* **2010**, 114, 10184.
32. Jewett, S. A.; Makowski, M. S.; Andrews, B.; Manfra, M. J.; Ivanisevic, A. *Acta Biomaterialia* **2012**, 8, 728.
33. Siel, J. R.; Webster, T. J. *Acta Biomaterialia* **2011**, 7, 2579.
34. Chitambar, C. R.; Matthaeus, W. G.; Antholine, W. E.; Graff, K.; O'Brien, W. J. *Blood* **1988**, 72, 1930.
35. Rogan, M. P.; Taggart, C. C.; Greene, C. M.; Murphy, P. G.; ONeill, S. J.; McElvaney, N. G. *J. Infect. Dis.* **2004**, 190, 1245.
36. Singh, P. K.; Parsek, M. R.; Greenberg, E. P.; Welsh, M. J. *Nature.* **2002**, 417, 552.
37. Narasimhan, J.; Ancholine, W. E.; Chitambar, C. R. *Biochem. Pharmacol* **1992**, 44, 2403.
38. Hassett, D. J. *J. Bacteriol.* **1993,** 175, 7658.
39. Sahoo, P.; Murthy, P.; Dhara, S.; Venugopal, V. P.; Das, A.; Tyagi, A. K. (*Under Review*)

CHAPTER 8

BRIEF SUMMARY OF THE THESIS WORK AND FUTURE PROSPECTIVES

In this thesis, the growth of various forms of 1D GaN nanostructures like nanowires, nanotubes, nanotips, microbelts, and nanoparticles have been demonstrated. This exercise aimed at meeting requirements for various applications pertaining to optoelectronics, nanofluidics, gas, chemical and biological sensors. Along with the chapter wise conclusion we briefly outline the future course of action, wherever applicable, to improve the understanding of growth mechanism and material properties of GaN based nanostructures, which will in-turn accelerate their device related applications.

The motivation for the study of 1D-semiconductor nanomaterials along with a brief review of literature is introduced in the chapter 1. The potential research area pertaining to wide band gap GaN nanostructures is presented with current state of idea.

The experimental and characterization techniques used for this thesis work is briefly described in the chapter 2. Indigenously developed chemical vapor deposition reactor, as a part of the curriculum, is depicted.

The important chapter wise findings of this thesis work along with relevant future prospectives are described as follows:

1. In the chapter 3, we observe that the nanowires of varying morphologies can be obtained with a slight variation in the incubation time during the initial stage of nucleation process. However, further efforts are required to achieve nanowires with uniform size and shape distribution in the chemical vapor deposition process. This can effectively reduce the cost required for ultimate realization of a single nanowire based devices. Wurtzite/zinc-

blende biphase homostructure in a single nanowire is an important finding. Such biphase nanostructures of GaN can be utilized to construct a unique quantum well architecture for advanced optoelectronic applications. In addition, the nanotips can be processed suitably by focused ion beam technique for the application as single field emission device. The nanotips will also find usefulness as scanning near field optical microscope tips.

2. As discussed in the chapter 4, core-shell Ga_2O_3 @ GaN microbelts possess distinct shape with self-affirm nanoprotrusions on their surface. These features have been used as ideal materials for humidity sensing and producing suprehydrophobic surface. Further, a single microbelt can be used as a microcantilever, nanofludics device, and as a surface enhanced Raman scattering substrate.

3. Nanotubes are unique for optoelectronic as well as for biomedical applications. As demonstrated in the chapter 5, well faceted GaN nanotubes functionalized with noble metal nanoclusters provide excellent surface sensitive properties suitable towards local oxidation, catalysis, and H_2 sensing. By suitably choosing laser power, catalyst, and local ambience, one can fabricate a single nanotube based CMOS device. The methodology can also be applied to fabricate in-situ gate dielectrics without using any sophisticated techniques. For sensors, we have used percolated mats of GaN nanotube. In fact, a single nanotube can be used to further reduce the detection limit of the present GaN based hydrogen sensor.

4. In the chapter 6, a prototype label-free in-situ electrochemical DNA biosensor is demonstrated by using the dendrimer modified GaN nanowires. An ultra low detection limit down to 0.1 aM target DNA solution has been achieved with excellent selectivity and specificity. Additional study including diameter dependent sensitivity and stability of the functional group over substantial time is required for the practical application of the present study. In addition, we observe a change in luminescence properties of the nanowire sample

after each stage of surface functionalization for DNA sensor. Further study is required to establish its utility at various concentrations of DNA molecules. This will enhance its capability to detect DNA hybridization through low temperature photoluminescence.

5. Finally, a novel methodology to understand the dynamic physicochemical interaction at the nano-bio interface is demonstrated in the chapter 7. It is found that GaN nanoparticles induce severe damage to the bacterial cells leading to the exudation of intercellular constituents. Distribution of protein components in the cell surface is used to substantiate the mode of action of nanoparticles through use of confocal Raman microscopy. However, additional study involving cryo-TEM can be performed to validate the above arguments. We suggest that GaN can be used as a potential candidate for designing antimicrobial surfaces for implants and catheter devices as well as for combating infections involving biofilms.

Journal Publication, Book and Conference Proceedings

Journal publications:

1. Prasana Sahoo, S. Dhara, S. Amirthapandian, M. Kamruddin, S. Dash, A. K. Tyagi, ***Role of surface polarity in self-catalyzed nucleation and evolution of GaN nanostructures,*** Crystal Growth & Design, **2012,** 12, 2375-2381

2. Prasana Sahoo, S. Dhara, S. Dash, I. Manna, B. Raj, A. K. Tyagi, *"**Air trapped nano-cavity induced superhydrophobicity on GaN microbelt**"* Appl. Phys. Lett. **2011,** 98**,** 043103-043105.

   [Featured in ***Nature India highlight*** "Water repelling surface sensor"

   and Virtual J. of Nanoscale Science & Technology, Vol. 23, Issue 5 (**2011**)]

3. Prasana Sahoo, D. S. Oliveira, M. A. Cotta, S. Dhara, S. Dash, A. K. Tyagi, B. Raj, *"**Enhanced surface potential variation on nanoprotrusions of GaN microbelt as a probe for humidity sensing**"* J. Phys. Chem. C, **2011**, 115, 5863-5867**.**

4. Prasana Sahoo, J. Basu, S. Dhara, H. C. Fang, C. P. Lu, T. R. Ravindran, S. Dash and A. K. Tyagi, "***Single step growth dynamics and multi-functional properties of core-shell GaN on Ga_2O_3 freestanding microbelts***", J. Mater. Sci., **2012**, 47, 3447-.3453

5. Prasana Sahoo, S. Dhara, S. Dash, A. K. Tyagi, ***GaN Nanostructures: Growth Kinetics and Applications,*** Nanoscience & Nanotechnology-ASIA, **2011**, 1, 140–161 (Invited Review)

6. Prasana Sahoo, S. Dhara, C. R. Das, S. Dash, A. K. Tyagi, B. Raj, P. Chandramohan, M. P. Srinivasan*, "**Surface optical modes in GaN nanowires**"* Int. J. Nanotech., **2010**, 7, 823-832.

7. Prasana Sahoo, Avinash Patsha, S. Dhara, S. Dash, M. Kamruddin, R. Pandian, A. K. Tyagi, ***Scaling of beaded GaN with pressure in self-catalyzed anisotropic growth technique****,* Int. J. Material Physics, **2012** (In Press**;** not included in thesis**)**

Submitted for review

8. Prasana Sahoo, S. Sumathi, S. Dhara, G. Saini, S. Rangarajan, S. Dash, A. K. Tyagi, ***Directlabel Free Ultrasensitive Impedimetric Genosensor using Dendrimer Functionalized GaN Nanowires,*** Analytical Chemistry, **2012** (Under Review)

9. Prasana Sahoo, P. S. Murthy, S. Dhara, V. P. Venugopala, A. Das, A. K. Tyagi, ***Probing the Dynamics of Cellular Damage and protein expression in Bacterial Cells Induced by GaN Nanoparticles using Confocal Laser Raman spectroscopy,*** J. Phys. Chem. C, **2012** (Under Review)

10. Prasana Sahoo, S. Dhara, S. Dash, S. Amirthapandian, A. K. Prasad, A. K. Tyagi, ***Room temperature H_2 sensing using Pt- functionalized GaN nanotubes,*** J. Phys. Chem. C, **2012** (Under Review)

11. Prasana Sahoo, S. Dhara, S. Dash, A. K. Tyagi, ***Photo-assisted local oxidation, and fragmentation by ultra small Pt nanoclusters functionalized single GaN Nanotubes*,** J. Nanopart. Res. **2012** (Under Review)

Book Chapter:

12. S. Dhara, Prasana Sahoo, A. K. Tyagi, B. Raj *"Surface Optical Modes in Semiconductor Nanowires*, **Nanowires - Implementations and Applications**, Intech- Open Access Book, pp- 1-26, ISBN 978-953-307-318-7; http://www.intechopen.com/books/nanowires-implementations-and-applications/surface-optical-modes-in-semiconductor-nanowires

Manuscript under Preparation:

13. Prasana Sahoo, S. Dhara, S. Amirthapandian, A. K. Tyagi, ***Role of incubation time on the nucleation mechanism of square, hexagonal, and triangular biphase homostructure in GaN nanowires.*** (Manuscript under Preparation).

Conference Proceeding:

1. P. S. Murthy, Prasana Sahoo, V. P. Venugopalan, S. Dhara, G. Saini, A. Das, A. K. Tyagi, ***Ga_2O_3 Nanoparticles Inhibit Bacterial Adhesion & Biofilm Formation,*** IEEE Xplore, Proc. of the "International Conf. on Nanoscience, Engineering and Technology" (ICONSET-2011), Chennai, 2011, 490-493, 978-1-4673-0074-2111.
2. Prasana Sahoo, S. Dhara, A. Patsha, S. Dash, M. Kamruddin, A. K. Tyagi, ***Catalysis Free Growth Of GaN Nanostructures***, DAE Solid State Physics Symposium (DAE-SSPS-2011), Chennai, AIP Conf. Proc. 2011, 1447, 449-450; doi:http://dx.doi.org/10.1063/1.4710073
3. A. Patsha, Prasana Sahoo, S. Dhara, A. K. Tyagi, ***Self-catalyzed Anisotropic Growth Of GaN Spirals***, DAE Solid State Physics Symposium (DAE-SSPS-2011), Chennai, AIP Conf. Proc., 2011, 1447, 1289-1290; doi:http://dx.doi.org/ 10.1063/1.4710484.
4. A. Patsha, Prasana Sahoo, S. Dhara, A. K. Tyagi, ***Growth of GaN nanostructures on graphene,*** IEEE Xplore, Proc. of the "International Conf. on Nanoscience, Engineering and Technology" (ICONSET-2011), Chennai, 2011, 553-555, DOI: 10.1109/ICONSET.2011.6168029

Conference Presentations:

1. Prasana Sahoo, P. Sriyutha Murthy, S. Dhara, V. P. Venugopala, S. Dash, A. K. Tyagi, ***Probing the Dynamics of Cellular Damage in Bacterial Cells Induced by GaN Nanoparticles using Confocal Laser Raman spectroscopy***, Inter. Conf. Nanoscience & Technology (**ICONSAT**), 2012**,** Hyderabad. [**Best Paper Awarded**]
2. Avinash Patsha, Prasana Sahoo, S. Dhara, A. K. Tyagi, ***Probing crystallographic orientation of GaN nanotube by polarized Raman spectroscopy,*** 23rd International Conference on Raman Spectroscopy (ICORS), IISC, Bangalore (Accepted).

3. Prasana Sahoo, S. Sumathi, S. Dhara, S. Bera, S. Rangarajan, S. Dash, A. K. Tyagi, B. Raj, *"**Functional GaN nanowires for label-free Genosensor**"* 3rd Bangalore Nano, Bangalore, India.

4. Prasana Sahoo, Sandeep K., Soumee Chakraborty, S. Dhara, A. Das, S. Dash, A. K. Tyagi, B. Raj, *"**Functionalization of GaN nanowires for label-free biomolecule detection",*** India-Brazil-South Africa (IBSA) Nanotechnology School on Advanced Materials, 2010, Chennai.

5. Prasana Sahoo, S. Dhara, S. Dash, A. K. Tyagi & B. Raj, *"**Surface optical Raman modes of single GaN belt**"*, ICONSAT, 2010, IIT-Bombay.

6. Prasana Sahoo, S. Dhara, S. Dash, A. K. Tyagi & B. Raj, *"**Large Scale Vapor- Phase Synthesis of Gallium Nitrides Nanobelts**"*, International Workshop on Nanotechnology and Advanced Functional Materials (NTAFM), 2009, Pune (*Contributory presentation).*

7. Prasana Sahoo, S. Dhara, S, Dash, A. K. Tyagi, "***Growth of GaN Microbelt for Advanced Applications**",* STEM-2010, Anupuram.

8. S. Dhara, Prasana Sahoo, and A. K. Tyagi, *"**III-V Nitride Nanostructures: Nanoelectronics"***, National Conference on Future Trends in Information & Communication Technology & Applications-2011, Bhubaneswar.

Workshop/Training

1. Cancer Nanotechnology, 2010, IIT-Bombay
2. Indian Nanoelectronics User Program (INUP) and device fabrication, 2009, IIT- Bombay.
3. Indo- US Workshop in "Visible and Ultra violate sources for Solid State Lightening and Water purification", 2009, Anna University, Chennai.
4. "Quantum condensed matter system" 2008, Institute of Mathematical Science, Chennai.

Thank you